This is to certify that the

dissertation entitled

Structure-Property-Processing Relationships and The Effects of Physical Structure on the Hygro-thermal Durability and Mechanical Response of Polyimides

presented by

Jason E. Lincoln

has been accepted towards fulfillment
of the requirements for

Doctor of Philosophy degree in Materials Science and Engineering

Roger J. Morgan
Major professor

Date 12th April 01

STRUCTURE-PROPERTY-PROCESSING RELATIONSHIPS AND THE EFFECTS OF PHYSICAL STRUCTURE ON THE HYGROTHERMAL DURABILITY AND MECHANICAL RESPONSE OF POLYIMIDES

VOLUME I

By

Jason E. Lincoln

A DISSERTATION

Submitted to
Michigan State University
in partial fulfillment of the requirements
for the degree of

DOCTOR OF PHILOSOPHY

Department of Materials Science and Mechanics

2001

Structure

of polyi

applicati

fabricatio

hydrolytic

research a

Car

microcrack

in-situ charact

times at low

threshold in

prevented u

reduction in

interphase.

ABSTRACT

STRUCTURE-PROPERTY-PROCESSING RELATIONSHIPS AND THE EFFECTS OF PHYSICAL STRUCTURE ON THE HYGROTHERMAL DURABILITY AND MECHANICAL RESPONSE OF POLYIMIDES

By

Jason E. Lincoln

Structure-property-processing interrelationships are characterized for a variety of polyimide composite matrices used in advanced aerospace structural applications. The relationships between chemical/physical structure and (i) fabrication conditions, (ii) mechanical, thermal, and physical properties, and (iii) hydrolytic stability, are investigated. Major findings determined from this research are presented below.

Carbon fiber/bismaleimide (BMI) cross-ply composite laminates are microcracked after standard cure and postcure procedures. Using a unique *in-situ* characterization of microcracking, it is demonstrated that extended cure times at low temperatures (177°C) prior to postcure can shift the microcracking threshold in these composites. Ultimately cure induced microcracking can be prevented under standard fabrication postcure temperatures as a result of a reduction in composite residual stress and an improved fiber/matrix interphase.

Stru

(PEI, poly

terminated

thermoplas

deformatio

volume. In

temperature

mechanical

result of liqu

With

be more re

thermoplastic

induced chain

demonstrated

on the chem

Phenylethynyl

hydrolytic sta

hydrolytic att

Compa

thermal, physi

polyamides ba

Structure-property-processing characterization of BMI, polyetherimide (PEI), poly(4,4'-oxydiphenylene pyromellitimide) (POPPI), and a phenylethynyl terminated imide oligomer (PETI-5) demonstrates that deformation in thermoplastic polyimides is controlled primarily by free volume. In thermosets, deformation is controlled by network defects, packing efficiency, and free volume. Interestingly, PETI-5 was shown to crystallize under certain time-temperature cure cycles, which results in dramatic changes in neat resin mechanical properties. The observed crystallization behavior appears to be a result of liquid crystal-like ordering due to the phenylethynyl end groups.

With respect to hygrothermal durability, thermoset polyimides prove to be more resistant to blistering and associated macroscopic damage than thermoplastics under hygrothermal excursions unless hydrolytic degradation induced chain scission has occurred. Accelerated hygrothermal exposure also demonstrated that the hydrolytic stability of polyimides is strongly dependent on the chemical nature of the polyimide and the end caps in thermosets. Phenylethynyl terminated imide oligomers displayed dramatically higher hydrolytic stability than norbornene terminated polyimides as a result of hydrolytic attack of the crosslinks associated with the Michael addition reaction.

Compilation of the results presented provides insight into controlling the thermal, physical, and mechanical properties as well as the hydrolytic stability of polyimides based on chemical structure and processing conditions.

To My Wife

Any large-sc

experimental

from numer

with these pri

and establish

Fundi

Office of Sci

F49620-95-1-

conclusions

interpreted a

Research or t

Michigan Re

Commission,

under L. Sc

UDRI). The

who were fun

From a

advisor, Dr. R

Technology C

ACKNOWLEDGEMENTS

Any large-scale research program cannot be completed without the experimental, theoretical, bureaucratic, training, and monetary contributions from numerous sources. The research presented here is certainly consistent with these principles, and many thanks must be offered to the many individuals and establishments that made this work possible.

Funding for this work was made possible primarily from the Air Force Office of Scientific Research (AFOSR) grant numbers F49620-98-1-0377 and F49620-95-1-0129, under Dr. Charles Lee. Note that the views and conclusions contained herein are those of the author and should not be interpreted as necessarily representing the Air Force Office of Scientific Research or the U.S. Government. Additional funding came from the state of Michigan Research Excellence Funds (REF), Consumer Product Safety Commission, Wright-Patterson Air Force Base, Air Force Research Laboratory, under L. Scott Theibert, and the University of Dayton Research Institute (UDRI). Their support was greatly appreciated by both colleagues and myself who were funded by these sources.

From a personal perspective, I must thank, first and foremost, my advisor, Dr. Roger J. Morgan, who now serves as the Director of the Polymer Technology Center, Department of Mechanical Engineering, Texas A&M

University.

as a sopho

my graduat

knowledge,

offered me

research, bu

interests wi

throughout

time during

A&M Unive

working toge

In add

Research Cer

graduate rese

Engineering

work togethe

My gu

Lucas, and D

learning expe

Michigan Sta

University. I began working for Dr. Morgan as an undergraduate research aid as a sophomore here at Michigan State University, and continued throughout my graduate studies. Dr. Morgan has acted as a mentor and a source of knowledge, opinions, assistance, guidance, and served as a good friend. He offered me a clear set of guidelines and goals with which to conduct my research, but also offered me the freedom to express my own ideas and interests within these guidelines. I cannot thank him enough for his help throughout my research, and especially for looking after me at a complicated time during his transition from Michigan State University (MSU) to Texas A&M University. I look forward to continuing our personal relationship and working together in my capacity as a researcher in the future.

In addition, I would like to thank Dr. E. Eugene Shin of NASA Glen Research Center, for his guidance, support, and assistance throughout my graduate research and years as a Research Aid at the Advanced Materials Engineering Experiment Station (AMEES). Dr. Shin and I will continue to work together in the future.

My guidance committee, Dr. Greg Baker, Dr. Dahsin Liu, Dr. James Lucas, and Dr. David Curliss were instrumental, each in their own way, in my learning experience during both my undergraduate and graduate research at Michigan State University.

Dur

taught by I

in this cour

research ex

of future in

he posed c

additional p

Dr. I

mechanics o

During my g

Teaching Cer

philosophies

materials. Dr

appreciated.

I have

MSU, and ap

me as both a

the opportun

Zhou. In th

twofold, and

During my final year at MSU, I enrolled in a polymer chemistry course taught by Dr. Baker. I learned more new, exciting, and important information in this course than I could have imagined, and his discussions from his personal research experience and polymer chemistry expertise opened many new doors of future interest to me. I am also appreciative of the questions and comments he posed during my Comprehensive Examination that provided me with additional perspectives to my research.

Dr. Liu has helped in my development in the understanding of the mechanics of composite materials and growth in my capacity as a teacher. During my graduate research I had the opportunity to obtain an Engineering Teaching Certification by completing the requirements and studies of teaching philosophies and ultimately teaching an introductory course in composite materials. Dr. Liu's assistance, opinions, and numerous discussions are greatly appreciated.

I have known Dr. Lucas since my early years as an undergraduate at MSU, and appreciate the knowledge, guidance, and friendship he has provided me as both an instructor and committee member. While at AMEES, I also had the opportunity to work with a former Ph.D. student of Dr. Lucas; Dr. Jiming Zhou. In this sense, I had knowledge facilitated to me from Dr. Lucas twofold, and for this I am greatly appreciative.

Dr. I

final stages

him at Wr

polyimide n

am looking

I ap

committee.

helped me t

engineer. I

questions ab

their time, a

committee.

In add

contributed t

describe their

long as this d

past seven ye

Therefo

and Mechanic

assistance; Bo

Simmons, of

Dr. David Curliss was very helpful during my research, especially in the final stages of my program where I had the opportunity to work closely with him at Wright-Patterson Air Force Base on the characterization of a new polyimide material. His assistance and guidance were greatly appreciated, and I am looking forward to working with him in the very near future.

I appreciate the contributions from all members of my advisory committee. Their numerous contributions to my learning experience have helped me to complete and interpret my research as well as develop as an engineer. It is a good feeling to know whom I can call on when I have questions about specific problems I will face in the future. I greatly appreciate their time, assistance, and friendship, and for serving on my guidance committee.

In addition to my committee, there are many more individuals who contributed to my research and learning experiences. Unfortunately, to describe their specific contributions in detail would require a document twice as long as this dissertation. I am indebted to them, and their assistance over the past seven years is greatly appreciated.

Therefore, I would like to thank the Department of Materials Science and Mechanics faculty and staff; Dr. Andre Lee for numerous discussions and assistance; Bob Jurek, Preston Vallad, Jiming Zhou, Jiang Zhou, and Jennifer Simmons, of (or formerly of) AMEES; Dr. L. T. Drzal, Mike Rich, and Jean

Rooney of t

Nicky, and D

live with the

Wright-Patter

Institute, espe

me; my fello

Ben Dorner o

of his help th

from AFRL; a

education and

from all of the

Finally,

this dissertatio

was no doubt

would be impo

I have a lifetim

Rooney of the Composite Materials and Structures Center; Scott, Margie, Nicky, and Ducky Theibert, for their hospitality, support, and allowing me to live with them during my stay at Wright-Patterson Air Force Base; staff of Wright-Patterson Air Force Base and the University of Dayton Research Institute, especially Bill Price who spent countless hours of his time assisting me; my fellow graduate students and colleagues at Michigan State University; Ben Dorner of the University of Ohio; Hua Tang Chen, my office mate, for all of his help through the years; Mark Wilenski from Boeing; Dr. Katie Thorp from AFRL; and all of my family and friends for their support throughout. My education and this dissertation would not have been possible without support from all of these individuals.

Finally, I would like to thank Meagan, who will be my wife by the time this dissertation is published. She stood by me throughout this process, which was no doubt very difficult and I thank her for her support and patience. It would be impossible to repay her for her continuing support and patience, but I have a lifetime to try.

TABLE OF CONTENTS

Chapter 3
Moisture Absorption-Network Structure Correlations in BMPM/DABPA Bismaleimide Composite Matrices

Chapter 4
Fundamental Investigation of Cure Induced Microcracking in Carbon Fiber/Bismaleimide Cross-Ply Laminates

Chapter 5
Critical Parameters that Effect the Deformation and Failure of Thermoplastic and Thermoset Polyimides

Chapter 6
Fundamental Investigation of Polyimide Deformation After Degradation and Plasticization

Chapter 7
Hydrolytic Degradation Mechanisms and Service Environment Durability of Thermoplastic Polyetherimide

LIST OF TABLES

Table 8.4: N
before and af

Table 8.5: N
and AFR700

Table 8.6: C
the initial T_g a
(80°C/100%

Table 9.1: T
for K3B, PE

Table 9.2:
polyimides as
aging effect
color through

Table 9.3: E
based on Tab

Table 9.4: So
(p. 287)

Table 9.5: D
(p. 293)

Table 10.1: M

Table 10.2: D
of three scans

Table 10.3: R

Table 10.4: P
(p. 316)

Table 10.5: C

Table 10.6: M

LIST OF FIGURES

Figure 2.1

Figure 2.1
leading to p

Figure 2.1
hindrance a

Figure 2.1(

Figure 2.1
(hexafluoro
AFR-00B t

Figure 2.18

Figure 2.19

Figure 2.20

Figure 2.21

Figure 2.22
Note that (
D, are activ

Figure 2.23
continuation
shown or a l

Figure 2.24
'ene' molec
connection

Figure 2.25

Figure 2.26
dianhydride
chemical gr

Figure 2.27

Figure 3.5
(p. 100)

Figure 3.6
BMPM:D.

Figure 3.7
plotted as a
systems. p

Figure 3.7
temperature

Figure 3.7
plotted as a

Figure 3.7(
BMI resin sy

Figure 4.1:

Figure 4.2:

Figure 4.3:

Figure 4.4:
Initial cure
molar), and

Figure 4.5:
and 'H2' pos

Figure 4.6
fiber/matrix

Figure 4.6(
debond, and

Figure 4
30μm. T
(p. 126

Figure 4
isotherm

Figure 4
isotherm

Figure 4.
cure temp
highlighte
at the cure
composite

Figure 4.8
cure tempe
5°C/min fo

Figure 4.8
Micrograph
picture was

Figure 4.9(
II, with mar
the surface
cooling cycle

Figure 4.9(
initiates at 5

Figure 4.10
the high str

Figure 4.11
calculated fr

Figure 4.
postcure c
results fro
degradatio

Figure 4.
postcure c
as in Figur

Figure 4.
for lamina
type-I lam
longer. p.

Figure 4.
[0°/90°]$_s$ lo

Figure 4.
the [0°/90°

Figure 4.
the [90°/0°

Figure 4.16
reaction pea

Figure 4.17
BMPM:DA
DSC data an

Figure 4.18
control spec

Figure 4.19
qualitative

Figure 5.1:
POPPI as a

Figure 5.2
slow; b in
p. 170)

Figure 5.3
24 h. Cav
60nm in siz

Figure 5.4
Cavitation i
from therm

Figure 5.5:
packing co
represented
Case A has
BMPM segm

Figure 5.6
stoichiometr

Figure 5.6
stoichiometr

Figure 5.6
stoichiometr

Figure 5.7:
terminating
c permaner
Solid lines re
p. 179)

Figure 5.8
stoichiometr

Figure 5.8
stoichiometr

Figure 8.14(
p. 261)

Figure 9.1:
AFR-00B, a
p. 265)

Figure 9.2:
a) biradical
homocrossl
reaction [11
p. 268)

Figure 9.3:
reactions in

Figure 9.4:
hydrolysis re

Figure 9.5(
control and
p. 278)

Figure 9.5(
instance wh

Figure 9.5(c
endothermic

Figure 9.6(
reduction an

Figure 9.7(
me at vario
p. 283)

Figure 9.7(
residual enth

Figure 9.8:
conditions

Figure 9.
for variou

Figure 9.
bomb for

Figure 9.
177 C hyg

Figure 9.
after 200

Figure 9.1
250 C hyg

Figure 9.1
for 177 –

Figure 9.
AFR700B,

Figure 9.
constant f

Figure 9.
which was
(p. 295)

Figure 10.

Figure 10
oligomers

Figure 10.
(p. 309)

Figure 10.
imide olig
chromatog

Figure 10.5
AFR-PEP-

Figure 10.6
2 at 37 C.

Figure 10.7

Figure 10.
p. 315,

Figure 10.8
PEPA-2, de
p. 316,

Figure 10.9

Figure 10.
determined

Figure 10.1
AFR-PEPA

Figure 10.1
determinati

Figure 10.1
by plotting

Figure 10.1
loss for AF

Figure 10.1
loss for AF

Figure 10.1
loss for AF

Figure A.1:

Chapter

Introducti

1.1 Focus

This dissert

multi-invest

programs u

Fundament

Composites

Characteriza

Composites

98-1-03

principal inv

In ad

the Unive

Technolog

State Univ

Base, and

Chapter 1

Introduction

1.1 Focus of Research

This dissertation and research contained herein represents a portion of two multi-investigator Air Force Office of Scientific Research (AFOSR) funded programs under Dr. Charles Lee, entitled (i) Characterization of Critical Fundamental Aging Mechanisms of High Temperature Polymer Matrix Composites, AFOSR grant number F49620-95-1-0129 and (ii) The Durability Characterization of High Temperature Polymer Matrix – Carbon Fiber Composites for Future Air Force Applications, AFOSR grant number F49620-98-1-0377. Dr. Roger J. Morgan of Texas A&M University served as the principal investigator for these programs.

In addition to Michigan State University, additional collaborators include the University of Michigan, NASA Glen Research Center, Adherent Technologies, University of Dayton Research Institute, Polycomp, Indiana State University, Air Force Research Laboratory / Wright-Patterson Air Force Base, and Texas A&M University.

1.2 Backgr

There is a gr

achieve sim

improvemen

requirement

In the auto

fuel efficie

functions, o

In c

constituent

transfer th

reinforcing

anisotropy

particular

environme

in therm

common

matrix us

significan

glassy sol

1.2 Background

There is a growing need in industry for lighter, stiffer, and stronger materials to achieve simultaneous reductions in weight coupled with performance improvements. Many automotive and aerospace applications are fulfilling new requirements through the application of polymer matrix composite materials. In the automotive industry, the primary driving forces are cost reduction and fuel efficiency. Conversely, aerospace applications, especially for military functions, often take on the perspective that performance outweighs cost.

In composite materials used for structural applications, the matrix constituent has a variety of roles that consist primarily of the following: (i) transfer the applied load to the reinforcing phase (e.g. fibers), (ii) protect the reinforcing phase, and (iii) bind the reinforcements together so that design anisotropy can be achieved. The matrix also limits the applications of a particular composite material in terms of upper use temperature, service environment, fatigue, thermooxidative stability, and toughness. For example, in thermoset polymer matrix composites reinforced with carbon fibers (common aerospace materials) the glass transition temperature (T_g) of the matrix usually defines the upper use temperature of the composite, since significant reductions in stiffness are associated with the transformation from a glassy solid to a rubbery, highly viscous material.

For aerospace environments that require exposure to extreme service environments of synergistic stress-time-temperature-chemical-gaseous conditions, the polymer matrix must demonstrate significant thermooxidative stability, hygrothermal durability, solvent resistance, and high temperature strength. Traditionally, thermoset epoxies were employed for most aerospace composite applications due to their processability, but have drawbacks associated with a limited use temperature (relatively low T_g), moisture absorption and corresponding plasticization, and often a brittle mechanical response, especially after exposure to the aforementioned synergistic exposure conditions.

Polyimides were originally developed in the 1950's at DuPont's Film Department at the Experiment Station in Wilmington, Delaware to obtain thermally stable polymers, which result from their highly aromatic chemical structure [97]. Today, polyimides are available as thermoplastics, thermosets, and as oligomers which can be crosslinked in the melt by the application of energy. There is generally a trade-off, however, between thermal stability and properties, including processability and mechanical toughness. Other drawbacks include toxicity of the starting monomers and hydrolytic stability.

As a result, present and future research related to Air Force aircraft and space applications involves determination of the critical damage mechanisms

and thresho

development

Therm

performance

be processed

to ~350°C.

microcrackin

galvanically

Certa

matrix com

development

severe, syn

dissertation

property-pr

polyimides

future Air

Chapter 2.

and thresholds for polyimides based on chemical structure, and new material development derived from these characterizations.

Thermoset bismaleimide (BMI) resins were developed to bridge the performance and processing gaps between epoxies and polyimides. They can be processed like epoxies, but have T_g values closer to those of polyimides (up to ~350°C). BMI resins suffer from brittleness (which leads to composite microcracking) and carbon fiber/BMI composites have been shown to galvanically corrode in some military service environments.

Certainly, higher speeds cannot be achieved without the use of polymer matrix composite materials, but for future applications this requires the development of new, processable matrix materials that exhibit durability under severe, synergistic service environment conditions. The goals of this dissertation were to contribute to the current understanding of the structure-property-processing relationships of high temperature polymers (predominantly polyimides and bismaleimides) so that new materials may be developed to meet future Air Force military and space needs. A detailed synopsis is presented in Chapter 2.

1.3 Program

High temper
utilized for a
that will be e
service envi
chemical, an
most probal
understandi
credible lon
observed sh
deterioration
meaningful
associated n

With
dissertation
composite
thermooxid
relationship
property-pr

1.3 Program Goals

High temperature polymer matrix-carbon fiber composites are and will be utilized for aerospace structural applications for a whole range of components that will be exposed to prolonged, extreme service conditions. These complex service environment conditions of stress, time, temperature, moisture, chemical, and gaseous environments require a thorough understanding of the most probable critical failure path of the composite component. Such an understanding of the critical fundamental aging mechanisms is necessary for credible long-term composite performance predictions based on experimentally observed shorter time service environment induced composite performance deterioration mechanisms. In addition, this understanding generates meaningful information for mechanics modeling-structural design analyses and associated materials structural optimization at all dimensional levels.

With respect to the aforementioned variables, the contribution from this dissertation involves three primary areas: (i) carbon fiber/bismaleimide (BMI) composite structure-property-processing relationships, (ii) hygrothermal and thermooxidative damage thresholds of polyimide composite matrices and the relationships between chemical structure and durability, and (iii) structure-property-processing interrelationships of polyimides.

1.3.1 Carbo

Carbon fibe
applications
applications
bismaleimid
DABPA,
critical gaps
relations for
two categori

i The
fabri
servi
resul
micr
indu
unk
beli
mod
chen
und
per

1.3.1 Carbon Fiber/Bismaleimide Composites

Carbon fiber/BMI composites are presently used in primary structural applications in Air Force aircraft. The BMI matrices used in these composite applications are based on the thermoset copolymer system composed of 4,4' – bismaleimidodiphenylmethane (BMPM) and 0,0' – diallyl bisphenol A (DABPA). Although this system has been used extensively, there remain some critical gaps in the present understanding of the structure-property-processing relations for this composite and the matrix constituent. These fall namely into two categories, described here:

(i) The BMI cure reactions are incomplete after standard composite fabrication and postcure conditions, and further cure can occur during service environment exposure to elevated temperatures which leads to resulting increases in T_g, mechanical property deterioration, and further microcrack development. Further cure occurs as a result of dehydration induced formation of ether crosslinks which themselves then undergo unknown chemical structure modifications. These chemical changes are believed to account for the observed mechanical and thermal property modifications. The chemistry and kinetics that cause these critical chemical and physical BMI structural modifications are not fully understood and such information is important from a fundamental perspective so that meaningful lifetime models can be developed. A

further understanding of these chemical and physical structural changes may allow a simple, economical chemical structural modification of the DABPA monomer that minimizes or alleviates these further cure reactions.

As a result, the structure-property-processing relationships for the BMPM/DABPA BMI resin system will be explored in this dissertation to improve upon the present understanding of the crosslinked network formation.

(ii) Carbon fiber/BMI composite laminates contain transverse microcracks after standard cure and fabrication conditions, which has been attributed to the poor interfacial integrity in this system, resin shrinkage during cure, and interlaminar residual stresses [5-9]. Attempts to alleviate microcracking in these composite laminates by modification of postcure time-temperature conditions and fiber sizings have been unsuccessful [5-9]. In this dissertation, microcracking will be thoroughly characterized and cure induced microcrack prevention will be attempted in a new approach through initial cure cycle modification rather than postcure cycle variations.

1.3.2 Po

A numbe

research.

the Air F

DuPont's

and Gene

will be cl

mechanis

The fund

herein sh

improvem

processing

Bas

from thes

developed

link from

oligomer

hydrolytic

systematic

1.3.2 Polyimide Characterization

A number of the latest technology polyimides will be investigated in this research, including NASA LaRC® phenylethynyl terminated imide (PETI-5), the Air Force's thermoset AFR700B, Avimid® K3B thermoplastic polyimide, DuPont's® thermoplastic poly(4,4'-oxydiphenylene pyromellitimide) (POPPI), and General Electric's Ultem 1000® polyetherimide (PEI). These materials will be characterized in terms of hydrolytic stability, hygrothermal damage mechanisms and thresholds, and structure-property-processing relationships. The fundamental analysis performed in this research and results contained herein should provide a basis for future composite matrix development and improvement in all areas and interrelationships of structure, properties, and processing.

Based on the results and fundamental degradation mechanisms derived from these studies, a new class of polyimides will be synthesized and developed. These polyimides are synthesized in an attempt to remove the weak link from AFR700B by incorporation of the technology found in the PETI-5 oligomer molecule. Such structural modifications hope to improve the hydrolytic stability and processability compared to AFR700B, and the initial systematic characterization of these materials will be presented.

1.3.3 Cha

Throughou

tools will b

differential

DMA), fu

spectrosco

exposure,

weighing,

scanning

GPC), (

optical mu

magnetic

literature

1.3.3 Characterization Tools

Throughout this dissertation, a variety of common and derived experimental tools will be used for material characterization. These include the following: (i) differential scanning calorimetry (DSC), (ii) dynamic mechanical analysis (DMA), (iii) thermogravimetric analysis (TGA), (iv) Fourier transform infrared spectroscopy (FTIR), (v) moisture absorption, (vi) accelerated pressure bomb exposure, (vii) mechanical testing, (viii) density measurements via hydrostatic weighing, (ix) environmental scanning electron microscopy (ESEM), (x) scanning electron microscopy (SEM), (xi) gel permeation chromatography (GPC), (xii) thermomechanical analysis (TMA), (xiii) physical aging, (xiv) optical microscopy (OM), (xv) thermomechanical analysis (TMA), (xvi) nuclear magnetic resonance (NMR) spectroscopy, and (xvii) various findings from the literature data.

Chapte

Literature

2.1 Introdu

In this ch
composite r
these mater
will be add
current pu
structure-pr
degradation

2.2 Gener

Intense res
Departmen
the primar
resulting fr
all aspects
electronics,
aerospace a

Chapter 2

Literature Review

2.1 Introduction

In this chapter, an overview of the primary high performance polyimide composite matrices for aerospace applications will be presented. The history of these materials, their chemical evolution, and the status of present problems will be addressed. A complete review is neither feasible nor necessary for the current purpose, but an extensive evaluation of the critical fundamental structure-property-processing relationships and environmental induced degradation mechanisms will be presented.

2.2 General Considerations of Aromatic Polyimides

Intense research of aromatic polyimides began in the 1950's at DuPont's Film Department at the Experiment Station in Wilmington, Delaware [97]. One of the primary attractions of these polymers was their inherent thermal stability resulting from their highly aromatic structures. Today, polyimides are found in all aspects of the technological community, ranging from applications in electronics, photosensitive devices, and wire insulation, to high performance aerospace adhesives and composite matrices.

The p

polyimides u

degradation

polyimides.

reactive end

PMR-type p

among the r

E

where:

E =

E =

E =

E =

Figure 2.1

The primary focus of this dissertation lies in the area of aerospace grade polyimides used as composite matrices, although the chemistry, properties, and degradation mechanisms to be discussed generally include a wide range of polyimides. These polyimides can be generically classified in terms of their reactive end group chemistry, shown in Figure 2.1. The first three in the figure: PMR-type polyimides, bismaleimides, and phenylethynyl terminated imides, are among the most widely used in high performance composites.

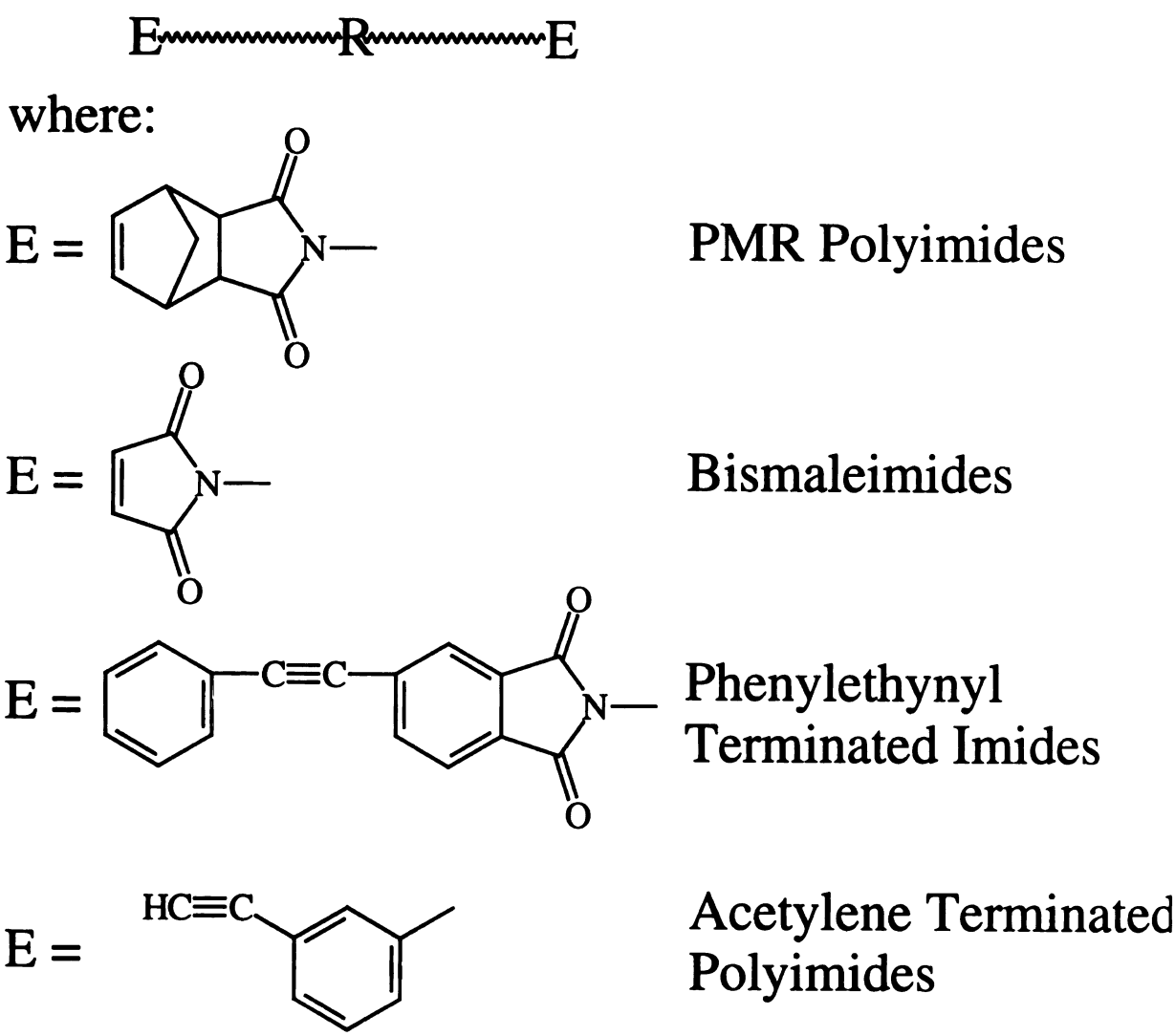

Figure 2.1: End group chemistry of polyimides.

PMR

conditions

Monomer

Lightsey at

monoalkyl

aromatic c

low-boilin

used to ir

end grou

composit

temperat

Figure
used to
group

PMR-type polyimides acquired their name from the processing conditions used to manufacture composite components: Polymerization of Monomer Reactants. In this process, developed by Serafini, Delvigs, and Lightsey at NASA Lewis in 1972 [98], an alcohol solution is prepared from the monoalkyl ester of 5-norbornene-2,3-dicarboxylic acid (nadic ester, NE), an aromatic diamine, and a dialkyl ester of an aromatic tetracarboxylic acid in a low-boiling alkyl alcohol (methanol or ethanol). This monomeric solution is used to impregnate the reinforcing fibers; polymerization through the nadic end group in the resin occurs directly on the fiber surfaces, producing a composite with excellent thermal and mechanical properties for use as high temperature aerospace structural components [98].

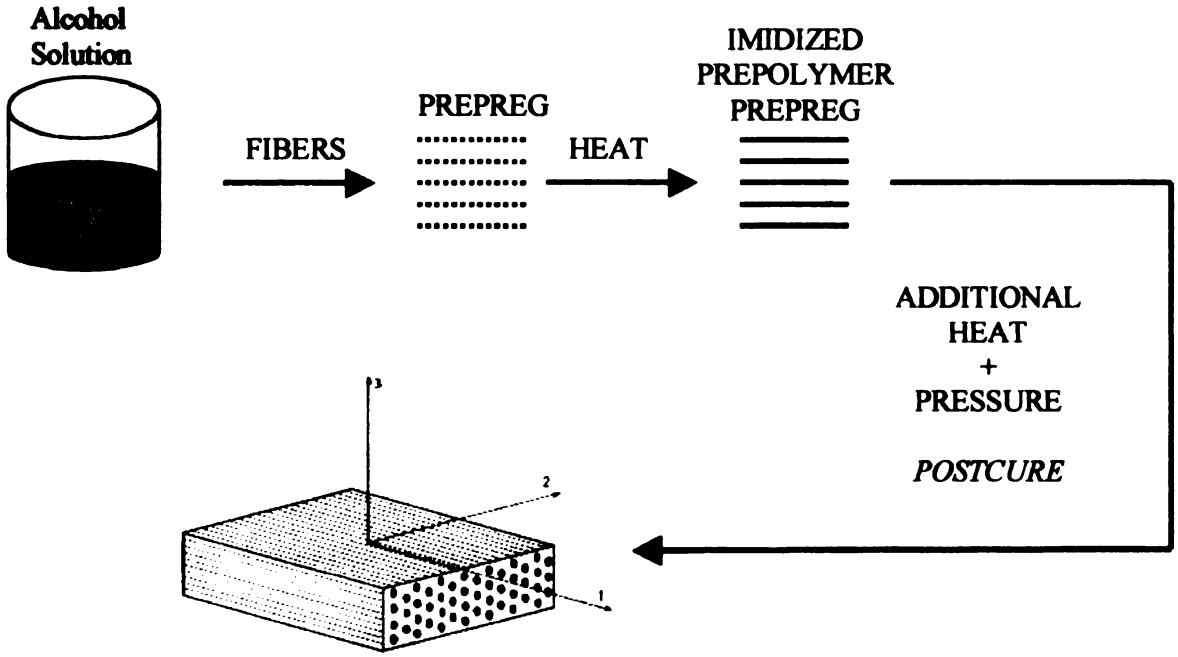

Figure 2.2: PMR processing conditions. The monomeric alcohol solution is used to impregnate the fibers; in-situ polymerization through the nadic end group occurs directly on the fiber surfaces.

Bismaleimides bridge the gap between polyimides and epoxies because of their high temperature capabilities and relatively easy processing, respectively. These crosslinked glassy matrices have also been shown to possess excellent hot/wet properties, which are required for aerospace applications, but have the drawback of brittleness. Usually, these matrices are blended with a toughening agent prior to manufacture of structural components.

Polyimide composite matrices are generally reinforced with carbon fibers and can be of thermoplastic or thermoset form, depending on their synthesis. The majority of polyimides contain extended rigid planar aromatic and heteroaromatic structures and are infusible and insoluble. Formation begins with a dianhydride or dianhydride derivative which is added to a diamine in a dipolar aprotic solvent. A high molecular weight polyamic acid is rapidly formed at ambient temperatures, which can then be transformed into the polyimide by the process known as imidization (a cyclodehydration reaction).

Imidization of the polyamic acid generally takes place in the solid state, and occurs in the 250-350°C temperature range, depending on the stability and glass transition temperature of the polymer. The reaction mechanisms are often complex and can be difficult to model [98], and differ slightly with different polyimides, as discussed later.

As

temperat

research

other ph

discussec

extended

temperat

need to b

In

must be

high stre

and aircr

stripping

and futu

fundame

between

an under

predictio

As mentioned, polyimides were primarily developed for their high temperature properties, and over the past 50 years an extensive amount of research has been conducted to couple the high temperature capabilities with other physical, thermal, chemical, and mechanical properties, which will be discussed below. Many polyimides are being used, or considered for use, for extended times (60,000 h) at elevated temperatures (371°C). Besides high temperatures, there are numerous synergistic environmental mechanisms that need to be addressed before a polyimide matrix can be employed.

In the case of military aircraft for example, the polyimide composite must be able to withstand combined effects of high temperature, high air flow, high stress levels, impact damage, thermal cycling, and exposure to moisture and aircraft fluids. Such fluids include hydraulic fluid, deicing chemicals, paint stripping solvents, high pH cleaning solutions, and aircraft engine fuels. Recent and future research on these materials involves determination of the critical fundamental damage mechanisms and thresholds, and the relationships between polyimide structure and the environmental parameters. Only through an understanding of these mechanisms can material improvements and lifetime predictions be developed.

2.3 Preser

In order to
improvemer
to understar
respective c
of polyimid
their associ

Many
Transport
HSR, whic
Administra
program, th
capable of
dimension.
5000 naut
anticipated
flying over
instead of
estimated s
balance of
useful for

2.3 Present/Future Military and Civilian Aerospace Applications

In order to make accurate lifetime model predictions and material design improvements based on the environmental exposure conditions, it is necessary to understand the actual lifetime exposure conditions and applications of the respective composite components. Here, some current and future applications of polyimides and polyimide matrix composites will be discussed, along with their associated exposure conditions.

Many of the polyimides developed arose from the High Speed Civil Transport (HSCT) program (also known as the High Speed Research program, HSR) which was canceled in 1999. The National Aeronautic and Space Administration (NASA) and the Boeing Company funded a portion of this program, the focus of which was on the development of a commercial aircraft capable of Mach 2.4 (1600 mph) speeds, about the length of a football field in dimension, and capable of transporting up to 400 passengers for a length of 5000 nautical miles while flying at an altitude of 12 miles [99]. Several anticipated benefits were used to promote the program: (i) the time saved in flying over large bodies of water, such as San Francisco to Tokyo in 4.5 h instead of the current subsonic airplane time of 10.5 h, (ii) the influence of an estimated $250 billion market for high-speed commercial airplanes on the U.S. balance of trade, and (iii) the spin-off technology that would evolve and be useful for subsonic and military airplanes [99].

Unde

160°C but,

177°C for 6

the wings, v

reasons, ho

HSR progr

NASA follo

To th

has proven

terminated

polyimides

In a

military air

stealth figh

Also

and/or po

has applica

tubes, and

commercia

polyimide

airliners [1

Under the above conditions, the surface of the aircraft would be about 160°C but, as a safety margin, the program required material performance at 177°C for 60,000 h. Some inner portions of the airplane, including fuel tanks in the wings, would also reach high temperatures [99]. Due in part to economic reasons, however, the Boeing Company announced in October 1998 that the HSR program would be postponed for 10 years, and in late September 1999, NASA followed.

To this date, the anticipated benefit (iii) mentioned two paragraphs ago has proven to be valid, most notably with the development of phenylethynyl terminated imide oligomers and polyimides therefrom. These unique classes of polyimides and their technology are described in a later section.

In addition, polyimide composites are also widely used in present military aircraft, including the Advanced Tactical Fighter (ATF), the F-117A stealth fighter, the Navy F-18 Strike Fighter, F-16XL, and AV-8B.

Also, many civilian aircraft components are composed of polyimides and/or polyimide carbon fiber composites. For example, the GE-90 engine has applications for carbon/polyimide ducts, engine casings, stator vanes, vent tubes, and fuel lines. Also, Kapton wire insulation is employed in many commercial aircraft, and has recently been a subject of interest due to polyimide wire degradation observed in over half of the world's commercial airliners [100].

As

payloads,

maneuver

manifest

replaced v

severe syn

gaseous-cl

effects of

perspectiv

As

composite

Polyimides

but other

the fuel t

considera

cycling re

The latter

the tanks

is that rap

moisture

the comp

As a result of weight savings, airplanes can increase passenger and cargo payloads, improve on fuel efficiency, and fly at greater speeds with increased maneuverability. Employing lighter structural materials in the design can manifest these weight savings, and more and more components are being replaced with organic matrix composites. Such replacements can lead to more severe synergistic exposure requirements of combined stress-time-temperature-gaseous-chemical environments. In the following section, some of the general effects of environmental degradation will be examined from a fundamental perspective, and detailed problems with specific materials will follow.

As a final note, it should be pointed out that carbon/polyimide composites are not the only composites used in aerospace applications. Polyimides and BMIs are the most notable for high temperature applications, but other composites are being considered for cryogenic applications, such as the fuel tanks on the X-33 Reusable Launch Vehicle (RLV). The primary considerations for these composites will be their cryogenic toughness, thermal cycling resistance, and the possibility to be fabricated by electron beam curing. The latter is necessary due to the size of the tanks; building a furnace to house the tanks is financially unreasonable. A problem with e-beam curing, however, is that rapid heating rates (>200°C/min) can be reached during the process. If moisture is present, an essential thermal spike can lead to interface damage in the composite and/or matrix blistering.

2.4 Fundar

2.4.1 Topi

The critica
mechanism
composites
severe hyg
and exam
perspectiv
subsequen
cracking, g
and therm

2.4.2 The

Since the
different,
are chara
crosslink
crosslink
deforma

Th
crystallin

2.4 Fundamentals of Hygrothermal Degradation

2.4.1 Topics of Interest

The critical fundamental synergistic damage initiation and propagation mechanisms of advanced high temperature polymer matrix-carbon fiber composites (bismaleimides and polyimides) resulting from prolonged and/or severe hygrothermal service environment exposure are reported in this section and examined systematically from physical, chemical, and thermodynamic perspectives. Damage mechanisms discussed include composite blistering and subsequent delamination, matrix plasticization, composite micro- and macro-cracking, galvanic corrosion, hydrolysis, molecular moisture 'lock-in' theory, and thermooxidative degradation.

2.4.2 Thermoplastics and Thermosets

Since the polymer physical structures for thermosets and thermoplastics are different, the mechanisms of hygrothermal degradation also differ. Thermosets are characterized by parameters such as network structure, covalent bonding, crosslink density, and defects in the form of chain ends, unreacted groups, and crosslink heterogeneities. Network extensibility and defects control deformation.

Thermoplastics can be amorphous and/or have some degree of crystallinity, and are characterized by parameters such as average molecular

weight, mol

chains. De

the polymer

degradation

As a

polymer co

excursions

fundament

Phys

Therm

Damage

W

High Te

High

Pr

Co

Damag

Furthe

Moisu

High Va

Ice F

Figure 2.

behavior

weight, molecular weight distribution, and van der Waals bonding between chains. Deformation is strongly controlled by the amount of free volume in the polymer. These differences are important to keep in mind when looking at degradation mechanisms and susceptibility.

As an example, consider the behavior of a thermoset and a thermoplastic polymer composite that has absorbed water and is then subjected to thermal excursions to high and low temperatures. Figure 2.3 demonstrates the fundamental differences between the two resin matrix types.

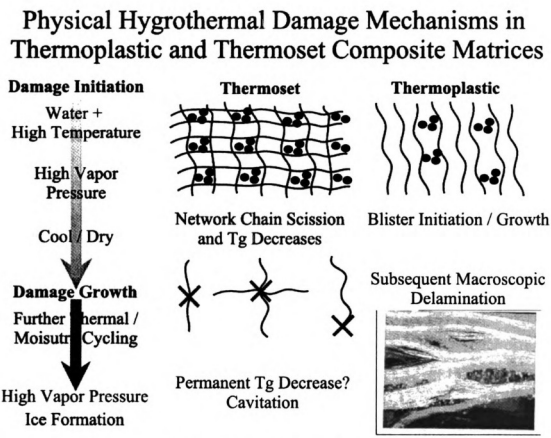

Figure 2.3: Schematic of differences is thermoplastic versus thermoset matrix behavior during hygrothermal cycling.

2.4.3 The

Hygrother

moisture

material.

For

aircraft ap

of 500°C

coefficient

which will

repeated th

composite

unacceptab

Clea

temperatur

physical su

improving

science is

The

temperatu

terms of

2.4.3 Thermal Considerations

Hygrothermal environments, by definition, include combined temperature and moisture conditions, but either of the two alone can be deleterious to a material.

For example, bismaleimide carbon fiber composites are used for military aircraft applications that require exposure to heating and cooling rates in excess of 500°C/min (thermal spikes) up to 250°C. There will be a dramatic coefficient of thermal expansion mismatch between the fiber and the matrix, which will produce a significant stress field in the vicinity of the fiber. During repeated thermal cycles, this can cause fiber-matrix debonding, and subsequent composite delamination resulting in component performance depletion and unacceptable damage.

Clearly, poor interfacial adhesion is unacceptable for future high temperature composites. Interface improvement by fiber chemical and physical surface modifications and fiber sizings is of primary importance in improving advanced polymer composites, but a discussion of this particular science is outside the scope of this review.

The following three sections describe the primary effects of high temperature exposure on the respective polymer matrix composite materials in terms of (i) physical aging, (ii) chemical aging, and (iii) thermooxidative stability.

2.4.3.1 Phys

Physical agin

temperature.

density increa

Aging results

molecular pa

chemical rea

temperature

volume to be

The c

physical agin

affect the tim

and rate depe

2.4.3.2 Che

Chemical ag

or neat re

environmen

ultimately d

form of fur

oxidation.

2.4.3.1 Physical Aging

Physical aging occurs in amorphous glassy polymers below the glass transition temperature. This phenomenon is a thermo-reversible process that leads to a density increase, a decrease in creep compliance, and an increase in brittleness. Aging results in a reduction in molecular mobility due to thermally induced molecular packing conformations and restrictions. In the absence of any chemical reactions, raising the temperature above the glass transition temperature increases the molecular mobility enough to allow equilibrium volume to be maintained, therefore relieving any physical aging effects.

The change in mechanical properties and volume associated with physical aging is often very small (often less than ~10%) but can dramatically affect the time-dependent mechanical properties (creep and stress relaxation) and rate dependent failure properties (such as yield stress) [102].

2.4.3.2 Chemical Aging

Chemical aging occurs when the high temperature polymer matrix composite or neat resin is exposed to extreme temperatures and/or a reactive environment. Irreversible chemical structural modifications take place, which ultimately degrade the material's mechanical response. These can be in the form of further crosslinking, chain scission, other chemical reactions, and oxidation.

Many p

degradation is

conditions is

released duri

spectroscopy

Many

thermolysis

primary off-g

carbon mon

site for initial

When

observed fro

properties. S

induced co

environment

load from o

stresses at t

locked-in st

high temper

Crack

composites

Many properties may be monitored to determine the nature of chemical degradation in a polymer matrix. Weight loss as a function of time-temperature conditions is one method commonly employed. Monitoring the volatiles released during high temperature exposure by mass spectrometry or infrared spectroscopy is extremely useful in identification of chemical aging reactions.

Many polyimides, for example, release CO_2, CO, and H_2O from thermolysis at high temperatures [97]. Below 350°C exposure, CO_2 is the primary off-gas whereas above 400°C, homolytic bond rupture occurs and carbon monoxide is released. From this, one may postulate that the primary site for initial degradation in polyimides is the imide ring.

When high temperature crosslinking reactions occur they may be observed from an increase in T_g, change in density, modulus, and other material properties. Such matrix chemical changes can lead to resin shrinkage stress induced composite microcrack formation during high temperature environmental exposure. In cross-ply laminates, a shear stress transfers the load from one layer to the next, causing a combination of macroscopic shear stresses at the ply interface and tensile stresses at the ply midplane. These locked-in stresses drive towards a lower energy state during postcure and/or high temperature environmental exposure by matrix microcrack formation.

Cracks tend to be larger in cross-ply laminates than in unidirectional composites, since the latter do not have any interlaminar thermal expansion

stresses. In a

by mechanica

oxygen and n

other synergi

2.4.3.3 The

Thermooxid

polymer con

opposed to i

oxygen. On

polyimides a

i) Oxidat
oxidati
origin
occurs

ii) If the
produ

iii) Over
to for
for mi

iv) Micro
menti
compo
to a
oxidat

stresses. In any respect, microcracking leads to composite deterioration, both by mechanical property degradation and by creating fast diffusion paths for oxygen and moisture, which can then degrade the composite by a number of other synergistic mechanisms.

2.4.3.3 Thermooxidation

Thermooxidation is probably the most studied form of chemical aging in polymer composites. Since true service environments are usually in air as opposed to inert atmospheres, the degradation is accelerated by the presence of oxygen. One can summarize this synergistic degradation mechanism for polyimides as follows:

(i) Oxidation begins at the surface of the polymer matrix, forming an oxidation layer that has a different chemical composition than the original matrix and can be seen in the microstructure. Weight loss occurs primarily in the surface layer.

(ii) If the temperature is high enough chemical degradation or reaction by-products and volatiles will diffuse out of the resin.

(iii) Over time, the surface layer increases and microcracks and voids begin to form at the surface. Voids increase in size, density, and act as points for microcracks to grow.

(iv) Microcracks also form in the composite interior due to the mechanisms mentioned earlier. Cracks in the laminate enhance oxidation of the composite by providing additional paths for oxygen penetration, leading to a vicious circle, with oxidation promoting cracking, allowing more oxidation, and so on.

Figure 2.4

neat specir

on the sur

thermooxic

Figure 2.4:
crack of a P

Figure 2.4 displays an optical micrograph of the cross-section of a PMR-15 neat specimen that was aged in air for 200 h at 300°C. Note the oxidative layer on the surfaces of the specimen. Also, Figure 2.5 outlines the process of thermooxidation as observed for PMR-15 [20].

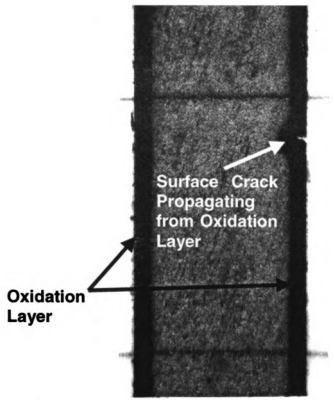

Figure 2.4: Stereo-micrograph of oxidative layer and macroscopic surface crack of a PMR-15 specimen cross-section aged at 300°C for 200h.

t_1

t_2

t_3

t_4

t_5

Figure
propos

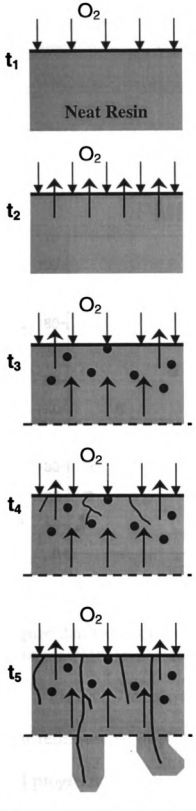

At temperatures greater than 300°C, oxidation (thermal degradation) begins to occur at the surface of the polymer matrix.

Over time, weight loss occurs releasing a mixture of volatile and non-volatile products from the resin chemistry.

Vapors released from the resin cause voids to form in a diffusion controlled manner. Chemical and physical structural changes including thermal decomposition and chain scission take place.

Microcracks form at the surface and penetrate, damaging the material severely. These are the effects of true service environments.

Mechanisms compete in terms of crack growth and oxidation penetration. If fibers are present, the interfaces may act as high diffusion paths increasing the degradation kinetics.

Figure 2.5: Schematic summary of thermooxidative degradation mechanism proposed by Morgan *et al.* [20].

Morgan *et al.*

as a function

me, oxidat

microcracking

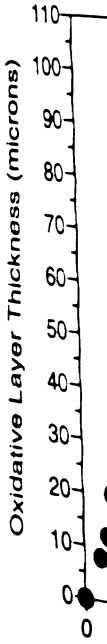

Figure 2.6
in air for P

Figu

neat resin

and progr

60 µm aft

Morgan *et al.* [20] monitored the oxidative layer thickness in PMR-15 neat resin as a function of the exposure time isothermally at 300°C (Figure 2.6). Over time, oxidation proceeds deeper into the composite, coupled with microcracking, void formation, and weight loss.

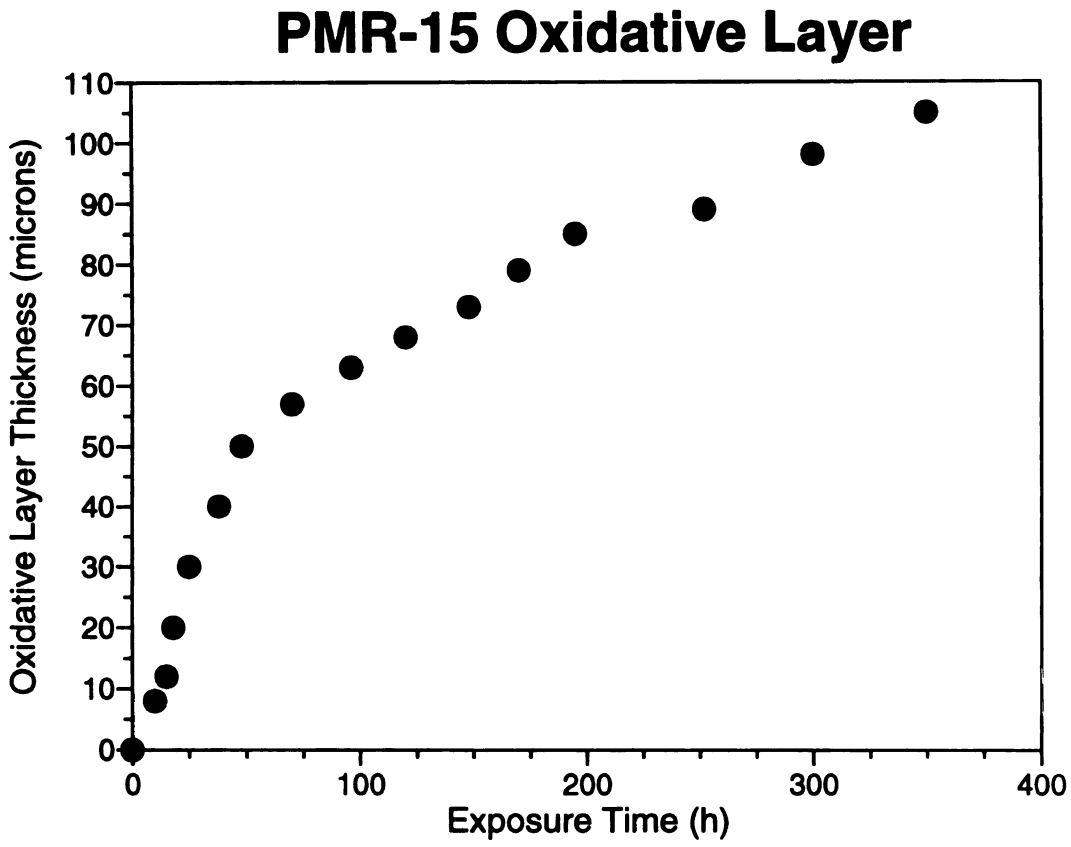

Figure 2.6: Oxidative layer thickness as a function of exposure time at 300°C in air for PMR-15 neat resin [20].

Figure 2.7 displays the microstructure (cross-sectional) for the PMR-15 neat resin sample displayed in Figure 2.6 at two aging times. The formation and progression of the oxidative layer is clear, as the thickness increases from 60 μm after 50 h exposure to 92 μm after 250 h.

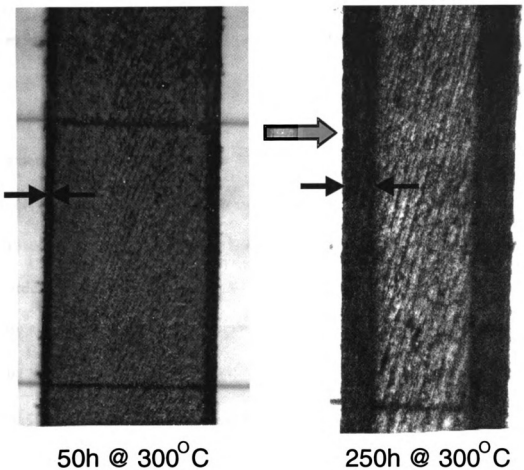

Figure 2.7: Stereo-micrographs at same magnification of oxidative layer in a PMR-15 specimen cross-section aged at 300°C for 50 h and 250 h. Layer thicknesses are 60 μm and 92 μm, respectively.

In the composite, more degradation occurs along the fiber-matrix interface, accelerating growth of surface layers in the axial direction [103]. As mentioned, laminated composites tend to degrade faster than unidirectional composites. Oxidation of the fiber surface can also occur at elevated temperatures, implementing an additional overall composite deterioration mechanism.

Like m

modeled usin

where τ is th

energy for th

absolute tem

order of ~13

by simple m

by thermogr

of controver

by determin

1-C, where

Points repr

The slope

can be writ

The model

arguments

kinetic dat

Like many thermally activated processes, oxidation may be properly modeled using the Arrhenius equation

$$\tau = A\exp\left(\frac{-E}{RT}\right) \tag{2.1}$$

where τ is the rate of change, A is a proportional constant, E is the activation energy for the oxidation process, R is the universal gas constant, and T is absolute temperature [104]. For most polyimides, the value of E is on the order of ~130 kJ/mol [102, 104-111]. The activation energy can be determined by simple mathematical extrapolation if the other two variables are known, or by thermogravimetric analysis (TGA), however the latter technique is a subject of controversy [102]. By monitoring weight loss at various heating rates, β, and by determining the temperatures at which different percent weight loss points (1-C, where C is the fraction of the original mass remaining) are reached. Points representing different 1-C values are plotted on a log β vs. T^{-1} curve. The slope of the line is proportional to the oxidation activation energy, which can be written as

$$E \quad \alpha \quad \frac{d(\log\beta)}{d\left(\frac{1}{T}\right)} \tag{2.2}$$

The model may further be generalized for different reaction orders. Most arguments against this method warn that diffusion effects may influence the kinetic data, leading to inaccurate determination of the activation energy.

The ex

thermooxidat

above, it is d

kinetics, whe

In or

reaction mec

examined a c

Above, E is

is the diffusi

the reaction

The parame

diffusion pr

this parame

small value

speed.

The

depending

The exact mechanism for weight loss, often the most used indication of thermooxidation for engineering purposes, is difficult to discern, but, as shown above, it is dependent on two main dynamic properties: diffusion and reaction kinetics, where often the reaction rates are controlled by diffusion.

In order to compare the relative importance of the diffusion and reaction mechanisms of thermooxidation, McManus and Cunningham [112] examined a dimensionless parameter, ζ:

$$\zeta = \frac{kh^2}{D_o} \exp\left(-\frac{E}{RT}\right) \tag{2.3}$$

Above, E is the activation energy for the mass loss degradation mechanism, D_o is the diffusion coefficient for oxygen diffusion, h is the sample dimension, k is the reaction rate constant, T is temperature, and R, the universal gas constant. The parameter, ζ, is the ratio of the rate determining terms of the reaction and diffusion processes, normalized by the specimen dimension. Large values of this parameter indicate that the mass loss will be limited by diffusion, whereas small values for ζ indicate that the mass loss will be limited by the reaction speed.

The value of ζ can range from very small (about 0.1) to very large (10^5), depending on the material and conditions of interest. The shape of the mass

loss cure

shown sc

Figure 2
T as a fur

As

mechanis

many of t

to combi

loss cure will vary, depending on the numerical value of this parameter. This is shown schematically in Figure 2.8.

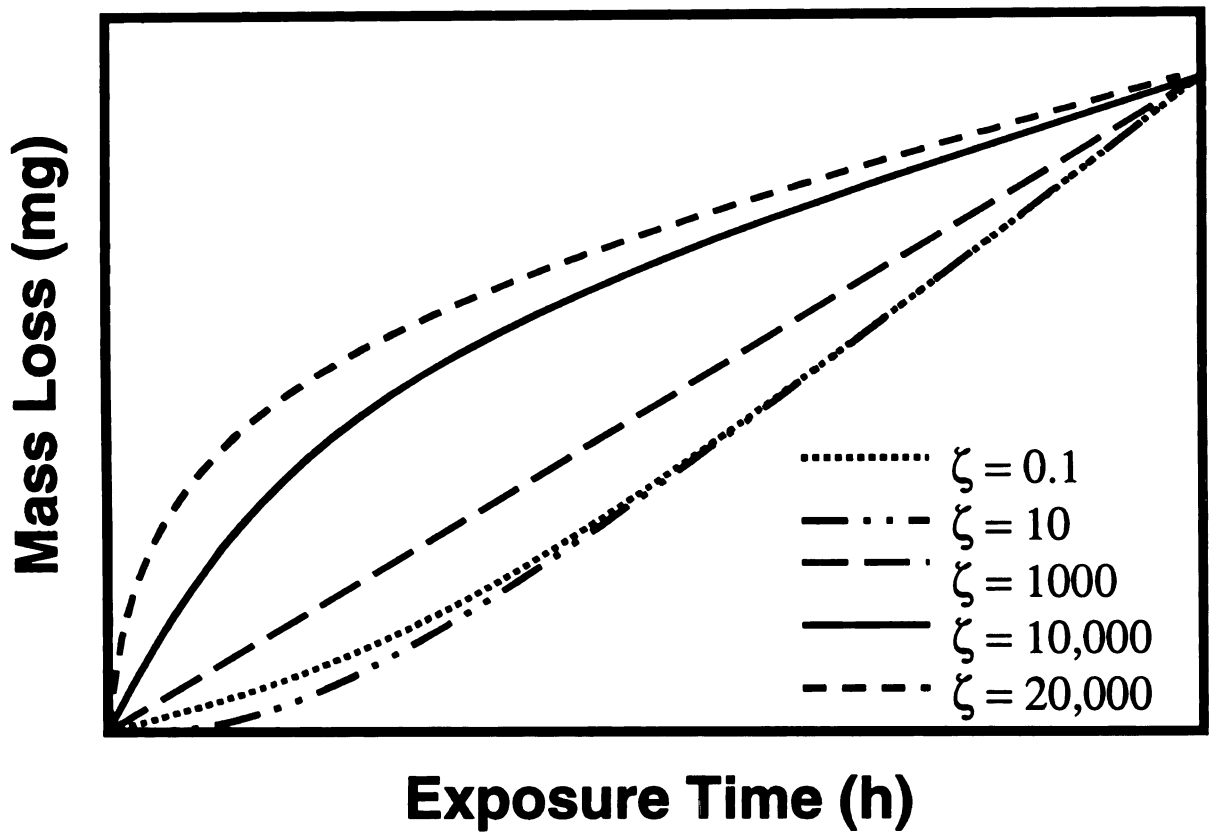

Figure 2.8: Hypothetical mass loss curves versus exposure time at temperature T as a function of the ζ parameter [112].

As discussed, thermooxidation is an extremely complex degradation mechanism. Polyimides are the most thermally stable polymer matrices, but many of these materials degrade rapidly by various mechanisms when subjected to combined high temperature and moisture.

Many

improve the

Methods su

concentratio

Jange

thermooxid

found that

composites

along the fi

by addition

stability cou

For

monomers

electron-de

from the

backbone

facilitating

In a

polymer cl

'chain sto

limit mole

Many techniques in terms of chemical modifications are employed to improve the high temperature stability of polyimide-carbon fiber composites. Methods such as partial fluorination of the matrices and reduction in the concentration of nadic end caps usually enhance oxidative stability [97].

Jangchud *et al.* [105], sought improvement of PMR-15 composite thermooxidative stability by an investigation of the fiber-matrix interface. They found that fiber-matrix dipolar interactions govern the stability of these composites at high temperatures. By inhibiting the development of cracks along the fiber-matrix interface, the mass loss was significantly reduced. Thus, by addition of polar components to the matrix, the composite thermooxidative stability could be enhanced from the resulting improved interfacial adhesion.

For polyimide matrix high temperature stability, electron-deficient monomers are usually preferable, although polymers derived from certain electron-deficient dianhydrides may not be as oxidatively stable as predicted from the usual trend. This is because charge transfer along the polymer backbone increases the net electron mobility of a polyimide system, thus facilitating oxidation [97].

In addition, for some polyimides, including PMR-15 and AFR700B, the polymer chain end groups may also assist in controlling the stability. Terminal 'chain stoppers' are frequently employed in the preparation of polyimides to limit molecular weight for ease of processing, to cap reactive functionality for

melt stability

Amine grou

stability. Us

therefore oft

at elevated t

stoppers is t

Some additi

biphenylene

In ge

or nadic anh

biphenylene

oxidation is

employed [1

2.4.4 Hyg

When a p

temperatur

temperatur

but also th

attack res

threshold

melt stability, or to incorporate reactive chain ends for crosslinking [97]. Amine groups ($-NH_2$) are generally regarded as detrimental to polyimide stability. Use of a slight excess of anhydride in formulating the polyimide is therefore often desirable. Anhydrides, however, are susceptible to degradation at elevated temperatures via hydrolysis. Capping with monofunctional chain-stoppers is therefore generally the best way to avoid end group degradation. Some additional reactive end groups include maleimides, nadimines, acetylenes, biphenylenes, and phenylethynyl.

In general, polyimides capped with aliphatic end groups such as maleic or nadic anhydrides are usually less stable than those capped with acetylene or biphenylene moieties [97]. In these PMR-type systems, stability toward oxidation is, to an extent, inversely proportional to the amount of end group employed [113].

2.4.4 Hygrothermal Damage

When a polymer composite is exposed to conditions of combined high temperature and moisture, the results can be devastating. At high temperatures, not only are the aging mechanisms discussed above operating, but also the presence of moisture leads to additional and accelerating modes of attack resulting in overall composite degradation. These unacceptable damage thresholds can be achieved through moisture induced microcrack formation,

hydrolytic de

subsequent c

from hydrol

ambient ter

performance

certain comp

aeropulsi

2.4.4.1 Ge

Polymer m

temperature

freely. Th

composite

degrade th

include m

formation.

temperatu

Ma

cure, cros

Exposure

the polym

hydrolytic degradation, molecularly 'locked-in' water, blister formation and subsequent composite delamination, and a variety of mechanisms resulting from hydrolysis and galvanic attack. The presence of moisture, even at ambient temperatures, can dramatically reduce a composite's in-service performance. Poor hot-wet properties are often the primary drawback in using certain composites for specific applications, including wing skins and in various aeropropulsion components.

2.4.4.1 General Effects of Moisture

Polymer matrices differ from other structural materials in that, at ambient temperatures, low molecular weight substances can easily migrate in them freely. The diffusion of water into a polymer matrix or polymer matrix composite is an immensely investigated phenomenon, since moisture can degrade the matrix and the fiber-matrix interface. Degradation mechanisms include matrix plasticization, micromechanical damage, cavitation, craze formation, glass transition temperature depression, hydrolysis, and at high temperatures, macroscopic blistering and delamination.

Many thermoset matrices have an inhomogeneous morphology. During cure, crosslink heterogeneities form due to glassy state diffusion restrictions. Exposure to humid environments induces different morphological changes of the polymer structure, depending on the affinity and mode of sorption. When

water molecule

different cross

craze when sub

Depend

network, mois

et al. [115] a

hydrophilic si

microcavities.

As a

absorption

Plasticization

lower glass

increase the

molecular 'e

depress T_g

expansion,

In o

relationship

of interest

hydrogen

the syster

water molecules cluster, significant swelling stresses can develop in regions of different crosslink density. Less crosslinked resins will therefore more readily craze when subjected to swelling stresses.

Depending on the morphology and chemical nature of the polymer network, moisture can be absorbed in a variety of ways, generalized by Apicella *et al.* [115] as: (i) forming a polymer-water solution, (ii) absorbed on hydrophilic sites, or (iii) absorbed on the surface of free volume elements or microcavities.

As a result of these various mechanisms, a measure of moisture absorption does not necessarily represent the degree of plasticization. Plasticization refers to an increase in free volume in the polymer that leads to a lower glass transition temperature. Water molecules present in the material increase the ability of long-term segmental motion by allowing for additional molecular 'elbow room'. The same amount of sorbed water, for example, will depress T_g differently for systems having different coefficients of thermal expansion, hydrogen bond capacity, or crosslink homogeneity.

In order to model the absorption of moisture in a polymer, a variety of relationships can be developed, depending on the nature of the polymer matrix of interest. For systems which contain negligible influence of polar or hydrogen bond groups, (i.e. amines, hydroxyl, sulfones, or tertiary nitrogen), the system can be viewed as a molecular solution, and treated with a liquid

lattice appro

correlates the

Above, a is

the water-p

consider the

fraction wou

rather than

constant, k

These relat

of water or

Glas

free volum

during pro

amount of

can craze

polymers

be defined

lattice approach based on the Flory-Huggins theory. The below equation correlates the water activity and the composition of the solution [115]:

$$\ln a_{H_2O} = \ln(1 - V_P) + V_P^2 + \chi_{H_2O} V_P \tag{2.4}$$

Above, a is the water activity, V_P is the polymer volume fraction, and χ_{H_2O} is the water-polymer interaction parameter. This could also be modified to consider the absorption of a gas, such as oxygen, since the polymer volume fraction would approach unity. Changing the subscripts to account for oxygen rather than water simplifies the expression to the limiting Henry's Law constant, k_d^{-1}:

$$\begin{aligned} a_{O_2} &= V_{O_2} \exp(1 + \chi_{O_2}) \\ k_d^{-1} &= \exp(1 + \chi) \end{aligned} \tag{2.5}$$

These relationships have been shown to give good results for dilute solutions of water or oxygen in a non-polar, homogenous polymer [115].

Glassy polymers are able to absorb water and gas molecules in 'holes' or free volume regions, which develop due to molecular packing irregularity during processing. When the temperature of a polymer containing a significant amount of moisture is increased, parts of the polymer (less crosslinked regions) can craze and form microcavities, which can then absorb more moisture. In polymers where this morphological modification occurs, the sorption, C, can be defined by the equation [115]:

Here, τ a

capacity,

is useful

As

the polyn

this influ

network

volume d

If

in T_g with

where T_g

represent

fraction

generally

systems

defined

$$C(T,\tau,a,\alpha)=k_d a+\frac{C_h'(\tau,\alpha)b(T)a}{(1+b(T)a)} \tag{2.6}$$

Here, τ and α are the thermal and activity histories, C_h' is the preexisting hole capacity, and b is the time dependent moisture affinity constant. This equation is useful only for relatively small concentrations of absorbed moisture.

As mentioned, the absorbed moisture results in a plasticization effect of the polymer matrix. The glass transition temperature will decrease as a result of this influence, with the magnitude of decrease depending on the polymer network characteristics; that is, if the network dependent function is free volume dominated or displays configurational entropy dominance [115].

If changes in free volume are considered the dominant mode, the change in T_g with absorbed moisture ('wet' T_g) can be estimated by

$$T_g^w=\frac{T_g^P V_P \alpha_P}{V_P\alpha_P+V_{H_2O}\alpha_{H_2O}}+\frac{T_g^{H_2O} V_{H_2O}\alpha_{H_2O}}{V_P\alpha_P+V_{H_2O}\alpha_{H_2O}} \tag{2.7}$$

where T_g^w is the wet glass transition temperature, and the P and H_2O scripts represent the polymer and water components, respectively. V is the volume fraction and α the coefficient of thermal expansion. The proposed theory generally applies to systems whose T_g and α are well defined, but fails for systems and temperature ranges where these values need to be arbitrarily defined [116]. It also does not apply to systems with strong polar groups. For

the above

transition

value nea

similarly f

For

temperat

Values a

and r =

of the wa

sites with

per gram

gram of

relations

as an ep

molecula

In

presence

kinetics

the above equation, it is interesting to note that a term is needed for the glass transition temperature of water, $T_g^{H_2O}$. This term is generally replaced by a value near the freezing temperature of water (4°C at maximum density) and similarly for the thermal expansion, $\alpha = 3.66 \times 10^{-3}/°C$ [116].

For the other case, where configurational entropy is assumed the temperature dependent function, the expression for the wet T_g is [117]:

$$T_g^w = T_g^P\left(1 - \frac{Ry(r)}{M_s \Delta c_p}\right) \tag{2.8}$$

Values are the same as above, in addition to $y(r) = r\ln(1/r) + (1-r)\ln(1/(1-r))$ and $r = (M_s/M_w)f$, R is the universal gas constant, M_w is the molecular weight of the water, $M_s = N_a/N_s$ is the effective formula weight of the hydrogen bond sites with N_a Avagadro's number and N_s the number of hydrogen bond sites per gram of polymer. Also, f represents the number of grams of moisture per gram of dry resin. The Δc_p term is the change in the specific heat at T_g. This relationship for determining the wet T_g has been proposed for polymers (such as an epoxy) in which water may be absorbed by localization at strongly polar molecular groups, i.e. a hydrogen bond.

In addition to understanding the mechanisms associated with the presence of moisture in the material, it is crucial to understand the absorption kinetics since hygrothermal degradation is a function of polymer chemistry,

compor

obtaine

fairly w

enginee

the forr

Above,

maximu

This eq

weight

gravim

by grap

latter

knowle

component geometry, and moisture diffusion. A Fickian diffusion model, obtained by solving Fick's second law can model most polymer composites fairly well. Slight deviations from the solution may exist, but from an engineering standpoint the model is usually sufficient. The approximation of the form below is commonly used [118]:

$$\frac{M_t}{M_\infty} = 1 - \exp\left[-7.3\left(\frac{Dt}{h^2}\right)^{3/4}\right] \tag{2.10}$$

Above, M_t is the moisture content after some time t, M_∞ is the equilibrium or maximum moisture content, h is the thickness, and D is the mass diffusivity. This equation allows for the determination of D and M_∞ by monitoring the weight gain in a given moisture exposure condition as a function of time via gravimetric analysis. Diffusivity and equilibrium moisture can be determined by graphical methods (Figure 2.9) or by non-linear regression analysis. The latter method gives more consistent results since the former requires knowledge (an approximation in many cases) of M_∞.

Figur

but dep

D_0 is a

T is ten

was rep

polymic

absorbs

usually

AFR

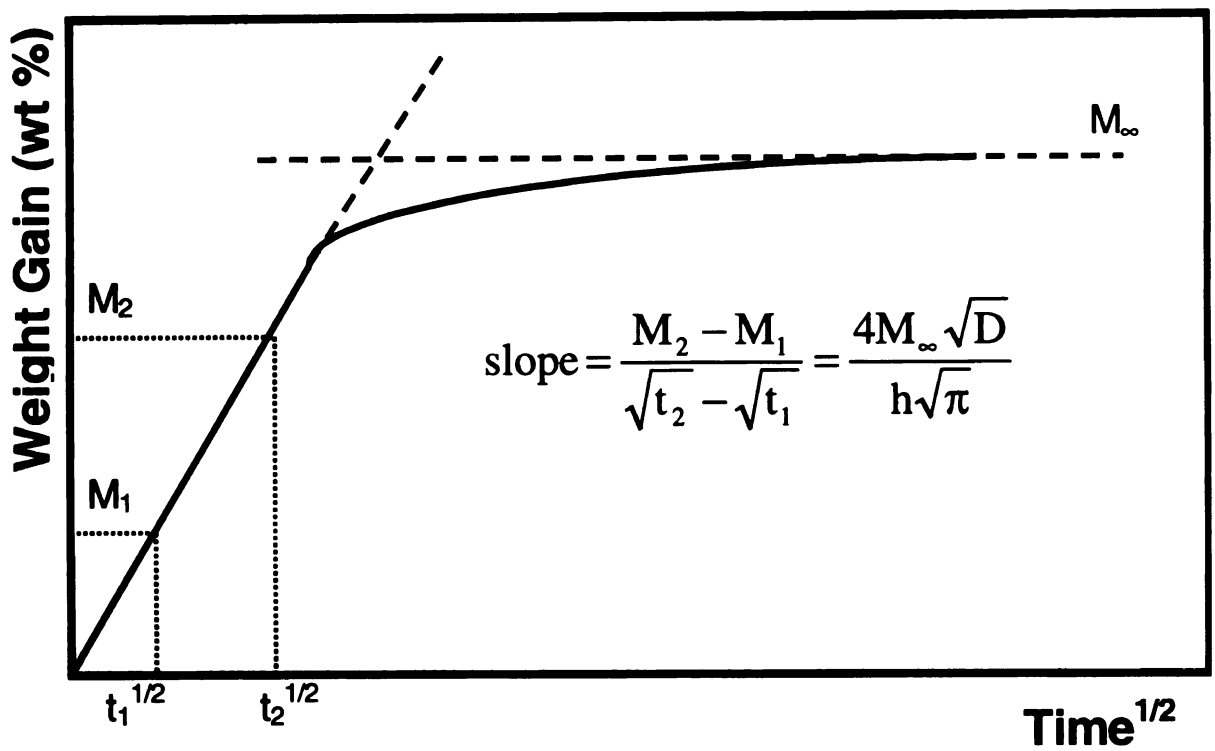

Figure 2.9: Graphical determination of D and M_∞ [118].

Also, the diffusivity is assumed independent of stress and concentration but depends on temperature by the Arrhenius equation

$$D = D_0 \exp\left(-\frac{Q}{RT}\right) \tag{2.11}$$

D_0 is a pre-exponential factor, Q is the activation energy for moisture diffusion, T is temperature, and R is the universal gas constant. For AFR700B, the value was reported to be about an order of magnitude smaller than for other polyimides, suggesting that under experimental conditions this polyimide absorbs water more readily [119]. Q for the majority of thermosetting resins is usually observed to be more in the range of 20-50 kJ/mole, where the value for AFR700B was reported at 2.77 kJ/mole. VanLandingham *et al.* [120] observed

activation ene

which include

network struct

A scher

some polyme

temperature d

moisture con

equilibrium

composites h

environment

dependency i

epoxy resins

absorption w

volume and

certain mois

absorption oc

The m

vapor-induce

in Figure 2.1

dependent o

activation energies for some thermoplastic polyimides of about 40 kJ/mol, which included K3B. In any case, D, M_∞, and Q are all dependent on the network structure of the respective polymer matrix.

A schematic model has been proposed to explain the observation that some polymers show a decrease in M_∞ with temperature, some show no temperature dependence, while others display an increase in the maximum moisture content with a temperature increase [5, 9]. For example, the equilibrium moisture content in BMPM/DABPA BMI-carbon fiber composites has been shown to decrease with increasing moisture-temperature environment (95% RH, 80° versus 20°C). The observed inverse temperature dependency is opposite that observed for many epoxy resin systems. Many epoxy resins generally show a slight increase to no change in moisture absorption with increased temperature as a result of increased glassy-state free volume and enhanced access to polymer hydrogen bonding sites. Under certain moisture-temperature conditioning, however, additional moisture absorption occurs at lower temperatures.

The moisture absorption behavior was explained in terms of moisture vapor-induced elastic cavity formation. Shin *et al.* [5] developed the schematic in Figure 2.10 to aid in the understanding. Notice that the schematic is dependent on the concentration of moisture accessible hydrogen bond sites

within the network structure and the residence time of water molecules on the hydrogen bond sites, noted as a thermodynamic effect.

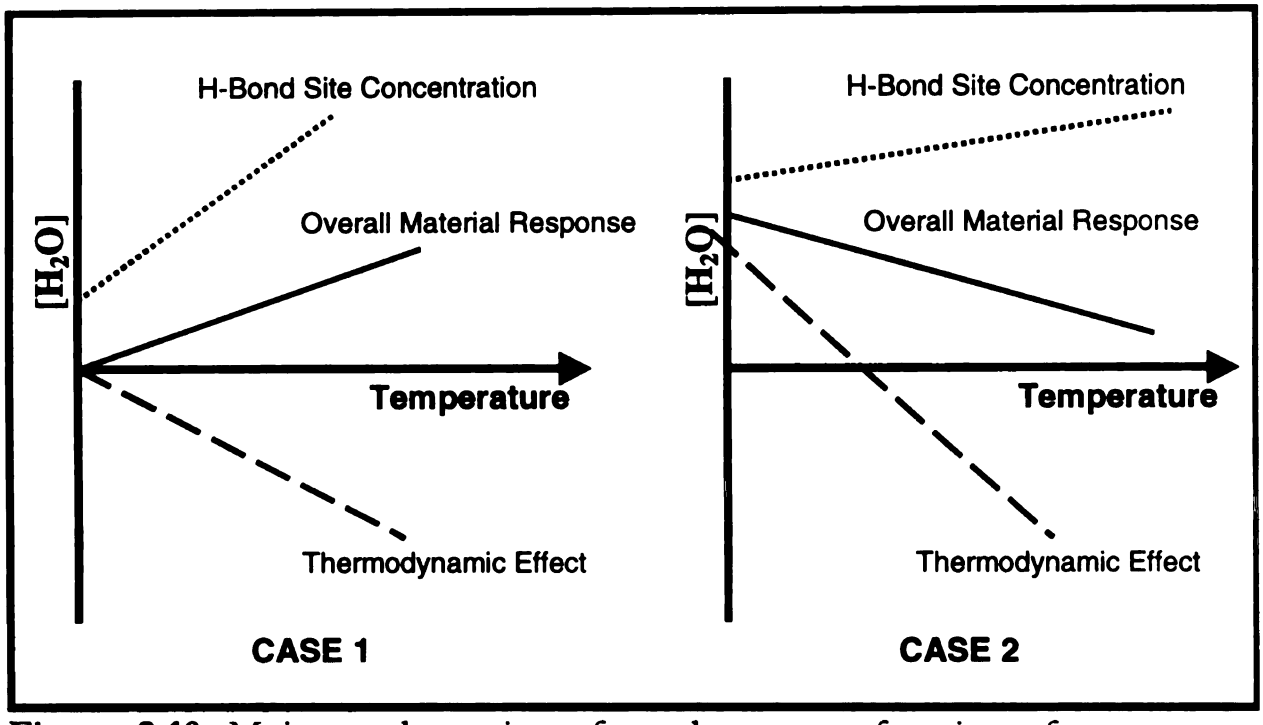

Figure 2.10: Moisture absorption of a polymer as a function of temperature for two different behaviors [5].

This illustrates that the equilibrium moisture absorption is controlled by both thermodynamic and kinetic reactions of water molecules to the polymeric system, and offers an explanation of how M_∞ can vary differently between two different polymer matrices with temperature. Epoxy resins often show more of a hydrogen bond concentration influence due to the presence amine groups, whereas the moisture behavior in BMIs is controlled more by the thermodynamic influence of molecular residence time due to the absence of highly polar molecules.

As mo

prediction of

composites.

impermeabilit

not be discus

The al

information r

often a mea

thermoset m

polyimide tha

the moisture

Studies

less moisture.

cause microc

unreacted gr

deformation.

processing t

dependent tr

match the co

As mentioned, the aforementioned diffusion models give a fair prediction of the diffusion of moisture into most polymers and polymer matrix composites. More precise equations have been developed to account for the impermeability of the fibers, fiber volume fraction, etc. [118, 121], but they will not be discussed here.

The absorption of moisture into a polymer matrix can give useful information in terms of network structure characteristics. For example, T_g is often a measure of the degree of cure (extent of crosslinking) for many thermoset materials. It has been show [119] for AFR700B fluorinated polyimide that the degree of cure (measured by T_g) is directly proportional to the moisture diffusivity and equilibrium moisture content:

$$T_g \quad \alpha \quad D, M_\infty \tag{2.14}$$

Studies also indicate [21-24] that a less crosslinked network will absorb less moisture, but at elevated temperatures could continue to cure and possibly cause microcracks to form and propagate. Also, incomplete cure may leave unreacted groups that may be attacked by moisture or act as defects during deformation. It may be beneficial to cure these materials to a lower T_g during processing to reduce the moisture absorption. Clearly there is a material dependent trade-off that needs to be addressed during fabrication in order to match the composite properties with the desired application.

2.4.4.2 Mole

Permanent dr

thermoplastic

20]. This is d

resin upon dr

In a h

availability fo

molecular str

down, water

may only dif

molecularly

conditions,

lowering the

This p

in occurring

and ⊗ are st

structure of

2.4.4.2 Molecular Lock-In Theory

Permanent dry T_g decreases have been observed for many thermosetting and thermoplastic polyimides after exposure to a hygrothermal environment [1-10, 20]. This is due in part to the inability to remove all of the moisture from the resin upon drying.

In a hygrothermal environment, high temperatures allow for increased availability for hydrogen boding sites to be susceptible to moisture, as the molecular structure expands with temperature. During a relatively rapid cool-down, water molecules become trapped or 'locked-in' to molecular 'cages', and may only diffuse out upon subsequent exposure to high temperatures. The molecularly locked-in water molecules cannot escape under low temperature conditions, and upon higher temperature exposure may act as plasticizers, lowering the measured T_g of the resin.

This process is shown schematically in Figure 2.11, with molecular lock-in occurring between T_1 and T_2. X represents water that is able to diffuse out, and ⊗ are sites where water molecules that become 'trapped' in the molecular structure of the resin.

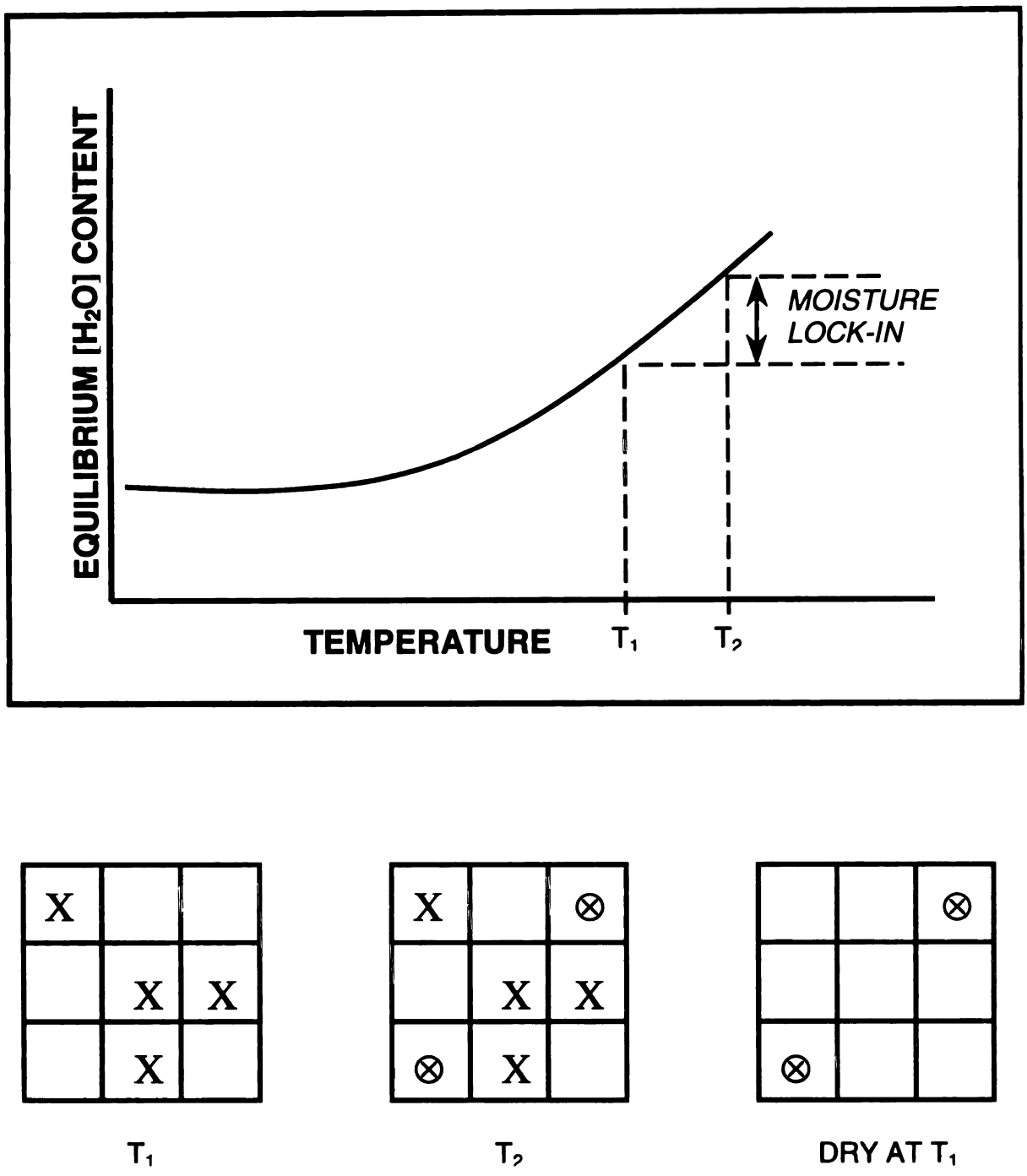

Figure 2.11: Schematic of molecular 'lock-in' theory. X represents H_2O molecules able to diffuse out, whereas ⊗ are molecularly locked-in hydrogen bonding sites [6].

This inability to remove moisture after hygrothermal exposure reduces the upper use temperature of the composite and may lead to blistering under

rapid tempera

190 H_2O mol

to temperatur

consequential

increases [6].

2.4.4.3 Hyg

Microcrackin

composites

microcracks

the accelerat

a reduction i

More

interlaminar

diffusion p

Under high-

to freeze-t

adhesion fa

increase wi

increase dr

certain com

rapid temperature increases. Besides high temperature exposure, if greater than 190 H_2O molecules are able to form clusters in these so-called 'cages', cooling to temperatures below the freezing point of water can lead to ice formation and consequential irreversible damage resulting in ice formation induced volume increases [6].

2.4.4.3 Hygrothermal Microcracking

Microcracking is usually the first form of damage to manifest itself in composites under hygrothermal cycling and extended exposure. These microcracks can then propagate other forms of damage and form pathways for the accelerated ingress of moisture and chemicals into the material, resulting in a reduction in the residual material properties and hence, a reduced lifetime.

More specifically, microcracks reduce the bearing strength, modulus, and interlaminar shear strength of the composite [122]. They also act as fast diffusion paths for moisture, thereby increasing the measured diffusivity. Under high-low temperature cycling, moisture trapped in microcracks can lead to freeze-thaw delamination, skin-core debonding, and/or fiber-matrix adhesion failures. Microcrack size and density (measured in cracks/ply/cm) increase with hygrothermal fatigue, and diffusion coefficients can, over time, increase dramatically; a fivefold increase in diffusivity has been observed for certain composite laminates after hygrothermal fatigue [122].

simple

examp

schem

Moisture Content (wt %)

Figure
microc

time, w

Microc

distribu

The dramatic effect of microcracks has even been observed under simple isothermal soaking conditions in pure water for some polyimides. For example, refer to Figure 2.12, which displays the moisture absorption curve in a schematic sense for a polymer matrix composite [123].

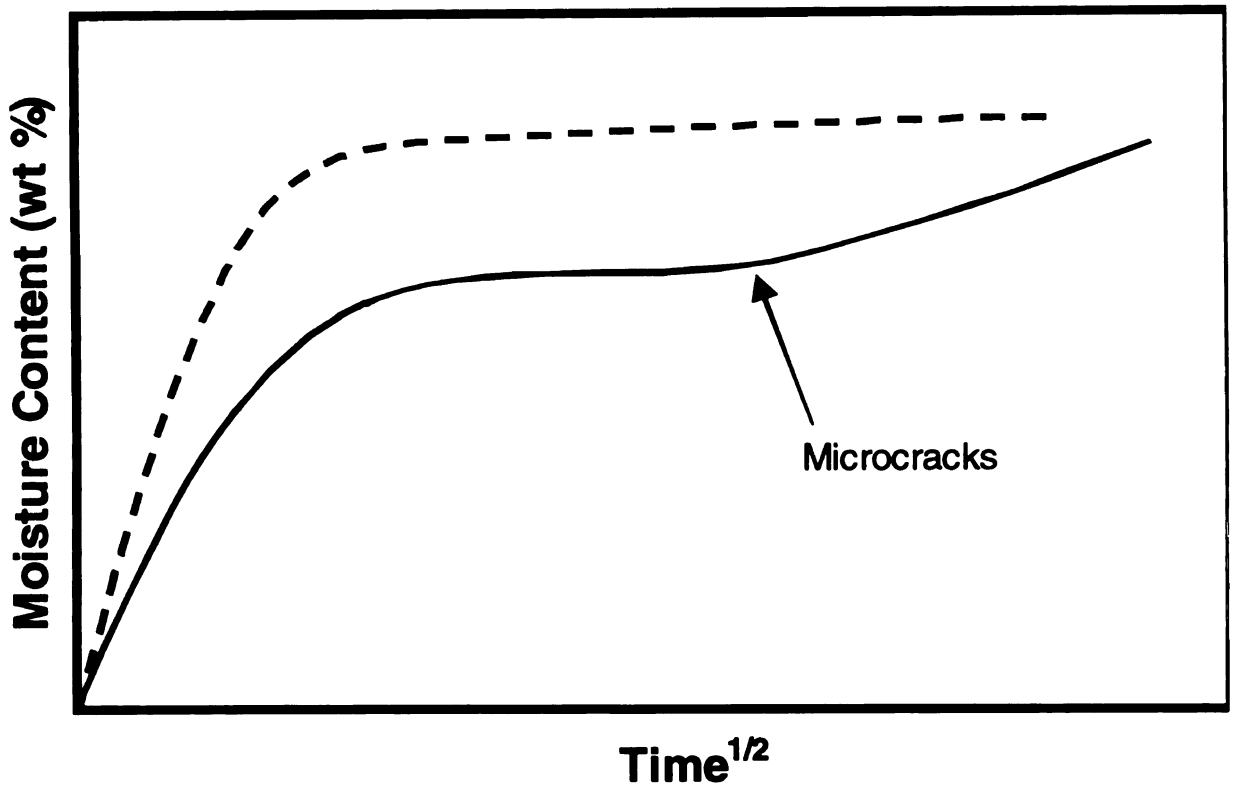

Figure 2.12: Schematic curve of dual-mode moisture absorption resulting from microcrack formation.

Above, note that the absorption is Fickian up to some characteristic time, where after a dual-mode absorption occurs due to microcrack formation. Microcracks form due to swelling stresses resulting from a non-uniform distribution of moisture in the material. Also, if any chemical degradation

occurs, such

propagation

microcracks a

behavior. If

as elastic cav

absorbing m

Figure 2.12.

2.4.4.4 Hyd

One of the

stability. M

especially w

extremely d

Hydr

degradation,

thickness, a

depolymeriz

all material p

Polyi

polymer cha

defects pres

occurs, such as hydrolysis, this can further accelerate the formation and propagation of microcracks. After microcracks form, moisture penetrates the microcracks and can thereby further propagate them, leading to the observed behavior. If the microcracks are permanent, (rather than a phenomenon such as elastic cavity formation or self-healing cracks), drying the material and re-absorbing moisture under the same conditions will yield the dashed curve in Figure 2.12.

2.4.4.4 Hydrolysis and Depolymerization

One of the primary concerns associated with polyimides is their hydrolytic stability. Many polyimides chemically degrade in the presence of water, especially when the pH varies from 7, even at low temperatures, leading to extremely deleterious and often irreversible damage to the composite.

Hydrolysis of polyimides (Figure 2.13) can lead to varying degrees of degradation, depending on such factors as resin chemistry, component thickness, and diffusivity. In the worst case scenario, hydrolysis can lead to depolymerization and reversion to the monomers, resulting in a loss of nearly all material properties [20].

Polyimides are susceptible to acid or alkaline catalyzed hydrolytic polymer chain scission as a result of (i) scission of any inherent amide group defects present as a result of non-ring closure to the imide ring and (ii) imide

ring opening t

Hydrolytic att

resulting in th

associated m

in regeneratio

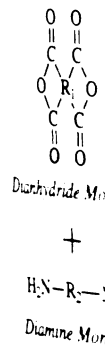

Dianhydride Mon

+

$H_2N-R_2-NH_2$

Diamine Mon

Figure 2.13:

The h

high temper

127]. Amid

polymer ch

molecular

mechanism

three order

ring opening to amide formation followed by scission of the amide group. Hydrolytic attack of the imide ring actually reverses the polymerization reaction resulting in the formation of polyamic acid, followed by chain scission and associated molecular weight and strength decreases. This can ultimately result in regeneration of the monomers; complete degradation [20].

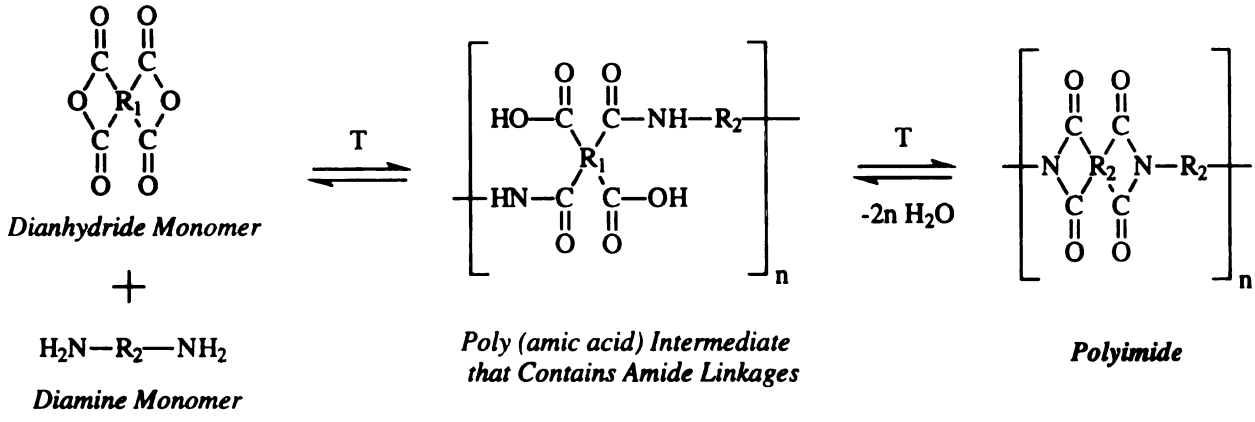

Figure 2.13: Polymerization and depolymerization of a polyimide [20].

The hydrolytic degradation of amide linkages in polymers, particularly at high temperatures in the presence of moisture is well-documented [97, 124-127]. Amide linkages are severed by this degradation mechanism, creating new polymer chain ends in the form of additional defects in the polymer, lower molecular weight, and lower strength (Figure 2.14). This degradation mechanism is accelerated by up to five orders of magnitude in acidic media and three orders of magnitude in alkaline media [19].

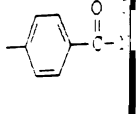

Figure 2.14: leading to pol

Openi

and resultan

associated

environment

polyimide o

reported tha

the imide hy

sulfuric aci

phthalanil, [

It wa

polyimides

advanced ai

of dramatic

become tra

as discusse

Final

often reve

Figure 2.14: Hydrolytic attack of amide linkages in the presence of a catalyst leading to polyimide degradation.

Opening of the imide ring by acidic H^+ protons or alkaline OH^- groups and resultant hydrolytic chain scission, lowering of molecular weight, and associated polymer strength loss occurs in aggressive humid-acidic environments. Molecular weigh decreases are further accelerated by the polyimide oxidative degradation mechanisms discussed earlier. It has been reported that between the above two hydrolytic mechanisms of degradation, the imide hydrolysis is 550X slower than the amide hydrolysis in concentrated sulfuric acid (from model compound studies of phthalanilic acid and phthalanil) [10].

It was originally assumed [125] that since AFR700B and some other polyimides were being used in components near the engine regions of advanced aircraft that the parts would dry quickly enough to prevent any form of dramatic degradation. For thick components however, moisture can become trapped leading to significant property reductions by rapid hydrolysis (as discussed above), plasticization, and blistering.

Finally, it should be noted that some portion of hydrolytic degradation is often reversible. For example, refer back to the polymerization-

depolymerization reaction in Figure 2.13. Water reverses the condensation reaction at elevated temperatures, but high temperatures can also result in repolymerization after the moisture has diffused out, again releasing water as a result of the reaction. As will be discussed, however, even though repolymerization may occur, the secondary water released from this reaction can lead to hygrothermal damage by way of blistering.

2.4.4.5 Galvanic Corrosion

Not all polymer composites are susceptible to this corrosion mechanism, but included are imides (bismaleimides and polyimides), triazines, and polycyanates. Those not affected include many epoxies, Radel-X, and polybenzimidazole [10].

According the Gaskell [128], a system which is capable of performing electrical work as the result of the occurrence of a chemical reaction is called a galvanic cell, with the overall chemical reaction being represented by a half-cell reaction. From the Nernst equation, the Gibb's free energy (ΔG) can be related to the half-cell EMF (ξ), at a constant temperature and pressure:

$$\Delta G = -zF\xi \tag{2.15}$$

Above, z is the valence of the ions transported by some voltage difference and F is Faraday's constant. Similarly, it can be shown that the change in molar

entropy and enthalpy can also be related to ξ at constant temperature and pressure by Equations 2.16 and 2.17, respectively [128].

$$\Delta S = zF\left(\frac{\partial \xi}{\partial T}\right)_P \tag{2.16}$$

$$\Delta H = -zF\xi + zFT\left(\frac{\partial \xi}{\partial T}\right)_P \tag{2.17}$$

In the case of imides, galvanically driven hydrolytic degradation has been traced to the electrolytic cell established between the graphite fibers and the metal in contact with the saline solution (seawater), generating hydroxide ions which diffuse into the polymer matrix and cleave the imide linkage via nucleophilic attack, reverting the resin to the polyamic acid then to the monomers [129].

The anodic reaction consists of the oxidation of a metal (aluminum in this case) which increases its valence state through the production of electrons. The electrons are then consumed by the cathodic reaction in which water is reduced in the presence of oxygen, producing hydroxide ions that diffuse into the matrix. The critical area of degradation is observed to be under an electrolyte film, which is in contact with the graphite and bulk electrolyte [130]. This thin film provides a short diffusion path for the reactant oxygen but a long diffusion path for the hydroxide concentration to the bulk electrolyte. As a result, a high region of hydroxide concentration is formed that can approach

saturation under some conditions, as manifested by severe resin loss and delamination of the composite a short distance above the waterline [129].

Rommel *et al.* [130] has shown that temperature is the greatest accelerator of galvanic attack. Also, an increase in chemical potentials between the polymer matrix composite and the metal in contact increase the degradation rate. From their study, they determined that a necessary condition for galvanic corrosion is a potential difference of at least 250 mV between the two materials.

Current protection technology of galvanic corrosion for high temperature structural applications depends mostly on the use of barriers or coatings on the composites or sizings on the fibers to disrupt the electrolytic cell between the fiber and matrix [129]. This approach, however, requires a 100% reliable barrier coating for the life of the component and thus becomes unworkable as the coating ages and develops cracks. An alternate method to prevent galvanic degradation would be to replace aluminum with titanium or other galvanically compatible (inactive) metals. Unfortunately, the latter approach incurs weight and cost penalties to the structure.

More reasonable means to prevent or delay hydrolytic attack are by (i) modifying the electronegativity and steric shielding of neighboring substituents, and (ii) incorporation of 'hydroxide scavenger' species into the polymer matrix.

Leung *et al.* [129], for example, reported that galvanic degradation of the polymer matrix (imides) could be dramatically reduced by modifying the chemical structures in terms of attaching bulky substituents to the amines and/or anhydrides, steric hindrance and shielding around the imide carbonyls reduced the rate of polymer degradation by the hydroxide ions. Of the thirteen model compounds studied, the best improvement came from a combination of steric hindrance and elimination of one of the carbonyl groups in the imide (Figure 2.15). This can be visualized from a physical perspective in that there is restricted space for water molecules to attack the imide linkages.

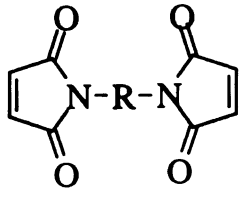

GENERIC IMIDE

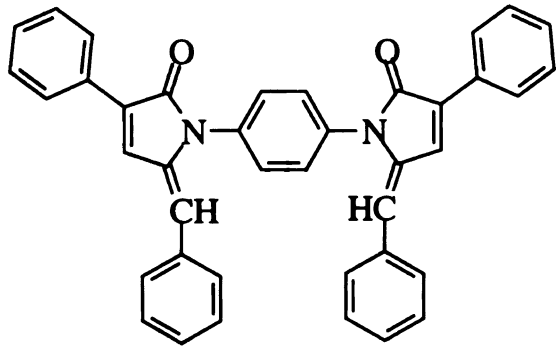

REDUCTION IN GALVANIC CORROSION BY (i) STERIC HINDRANCE AND (ii) ELIMINATION OF ONE OF THE CARBONYL GROUPS IN THE IMIDE

Figure 2.15: Reduction in galvanic attack by chemical modifications of steric hindrance and removal of a carbonyl group for an imide polymer [129].

In addition, Morgan *et al.* [10] reported that certain organic acids act as counterions with the imbibed hydroxide anion, preventing or impeding the hydrolytic attack on the imide group. One such class of materials is the triarylsulfonium hexafluoroantimonate salts, which are miscible with the imide monomers and are easily blended into the polymer matrix.

From the above discussion, it appears to be possible that with certain combinations of polymer microstructural and/or formulational modifications, total damage can be reduced to an acceptable level for the lifetime of a composite component. The discussed *in-situ* protection mechanisms may eventually replace present parasitic coatings or fiber sizings [20].

2.4.4.6 Blister Initiation and Growth

When physically trapped and/or chemically evolved moisture vapor pressure exceeds the matrix yield stress during dynamic hygrothermal exposure, matrix cavitation will occur in the form of macroscopic blistering, leading to subsequent delamination of the composite.

Vapor pressure-induced blistering and associated delamination has been shown to be a function of a number of variables: (i) previous humidity-time temperature exposure and associated moisture concentration profiles, (ii) component thickness, and (iii) rapid heat-time service environment exposures, such as thermal spikes [20]. Variations in blistering susceptibility also depend

on the polymer physical and/or chemical structure. For example, a thermoset is generally more resistant to cavitation and associated blistering than a thermoplastic because thermoset cavitation requires rupture of covalent crosslinked molecular segments.

For polyimides, the imide linkages formed during postcuring are highly strained because of water released during the cure reactions. These linkages may be more vulnerable to hydrolysis, resulting in a likely link between blistering and hydrolytic degradation.

Blisters can form in pores or microvoids, from cracks, or from water and/or volatiles released during polymerization or depolymerization reactions. The vapor pressure in the blister can cause the blister to expand, or, depending on the heating rate and matrix material, burst. The vapor pressure in the cavity will drive to expand the size of the blister. Elastic cavitation will occur until the yield stress of the matrix is exceeded, at which point plastic cavitation will cause blistering, cracking, and/or composite delamination. In some composites, blisters have been shown to readily form around the fibers due to increased moisture diffusion into these regions [131]. Microcracks also may act as blister initiation sites, but since blisters can lead to microcracks this mechanism is somewhat uncertain.

2.5 PMR-15

PMR-15 was one of the earlier polyimides to be used for composite matrix aerospace applications, and at the time of its development in the 1970's had the best combination of processablity, thermooxidative stability, and retention of strength at high temperatures for extended periods of time.

The '15' used in the nomenclature refers to the formulated molecular weight of 1500 g/mol for the imide prepolymer. It is prepared from the combination of the following three monomers: (i) monomethyl ester of 5-norbornene-2,3-dicarboxylic acid (NE), (ii) 4,4'-methylene dianiline (MDA), and (iii) 3,3',4,4'-benzophenonetetracarboxylic acid (BTDE) in 2.000:3.087:2.087 molar ratio [103]. The reaction is shown schematically in Figure 2.16.

PMR-15 itself has a number of attractive properties, including relatively easy processing, good mechanical properties and excellent retention of mechanical strength at elevated temperatures (288°C–316°C) for an extended period of time (1000-10,000 hours, depending on the service temperature) [103]. PMR-15 has four notable shortcomings: (i) inadequate resin flow for the manufacture of thick and complicated parts, (ii) microcracking during and after fabrication, (iii) health and safety concerns arising from the use of carcinogenic 4,4'-methylene dianiline, and (iv) a lack of thermooxidative stability at 371°C (700°F).

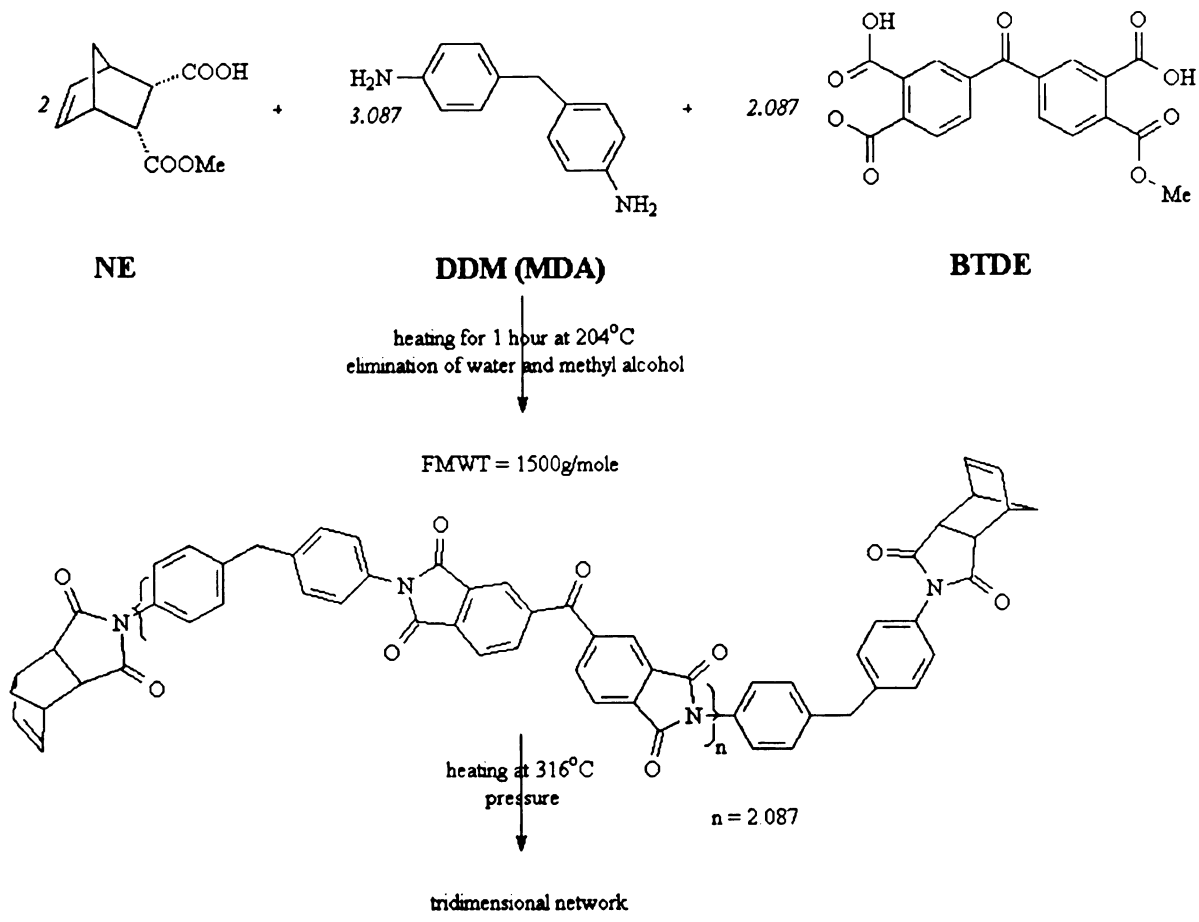

Figure 2.16: Synthesis of PMR-15 thermosetting resin.

In order to overcome the aforementioned problems associated with the PMR-15 class of polyimides, other PMR thermosetting polyimides have subsequently been developed and commercialized. Some of these systems include LaRC®-160, PMR-II, V-CAP, AFR700B, and LaRC®-46. The reader is referred to a review by Pater [98] for a more detailed comparison of the material properties, fabrication techniques, applications, and synthesis of these PMR polyimides. Most notable of the developed 'replacement' polyimides is the Air Force's AFR700B, which will be discussed next.

2.6 AFR700B

When developing AFR700B, the following development goals based on PMR-15 were established: (i) 371°C service temperature, (ii) thermooxidative stability of less than 2% weight loss of a 60 volume % fiber composite after 100 hours at 371°C, (iii) mechanical properties at 371°C equal to the mechanical properties of PMR-15 at 288°C, (iv) autoclave processablity at 1.38 MPa, and (v) low toxicity [113, 114].

PMR-15 was found to degrade at high temperatures through the dimethyl ester of BTDE and MDA components and most importantly through the decomposition of the aliphatic monomethyl ester of NE. AFR700B fulfilled the aforementioned material design requirements by (i) replacing BTDE with 4,4'-(hexafluoroisopropylidene)-bis(phthalic acid) dimethyl ester (6FDE) to improve thermal stability, (ii) replacing MDA with para-phenylenediamine (*p*-PDA) to reduce toxicity and (iii) reduce the amount of NE to reduce the aliphatic content compared to the amount in PMR-15 (i.e. the diester-diacid:diamine:NE molar ratio was changed from 2.087:3.087:2 in PMR-15 to 8:9:1 in AFR700B) (Figure 2.17) [113].

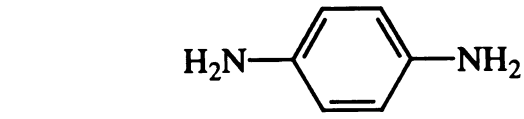

PPDA

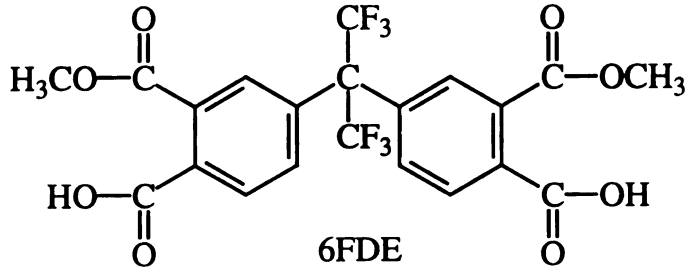

6FDE

Figure 2.17: Chemical structures of phenylenediamine (*p*-PDA) and 4,4'-(hexafluoroisopropylidene)-bis(phthalic acid) dimethyl ester (6FDE) used in AFR700B thermosetting resin.

The interesting chemistry of AFR700B can be seen in Figure 2.18, beginning with the monomers 6FDE, *p*-PDA, and NE in the molar ratio 8:9:1, respectively. Following the PMR approach, these monomers are combined in a methanol solution having typically 70 weight percent monomers. As the solution is heated, the monomers react to form oligomers of polyamic acid and 17 moles of methanol per mole of oligomer. End groups on these oligomers are a norbornene group, which limits the chain length, and an amine group. The norbornene end group, by controlling the chain length, can dramatically affect the overall material properties by influencing the network structure. Next, polyamic acid reacts to form polyimide oligomers and 17 moles of water per mole of oligomer. The water and methanol reaction byproducts and residual solvent (methanol) must be removed to produce void-free composites.

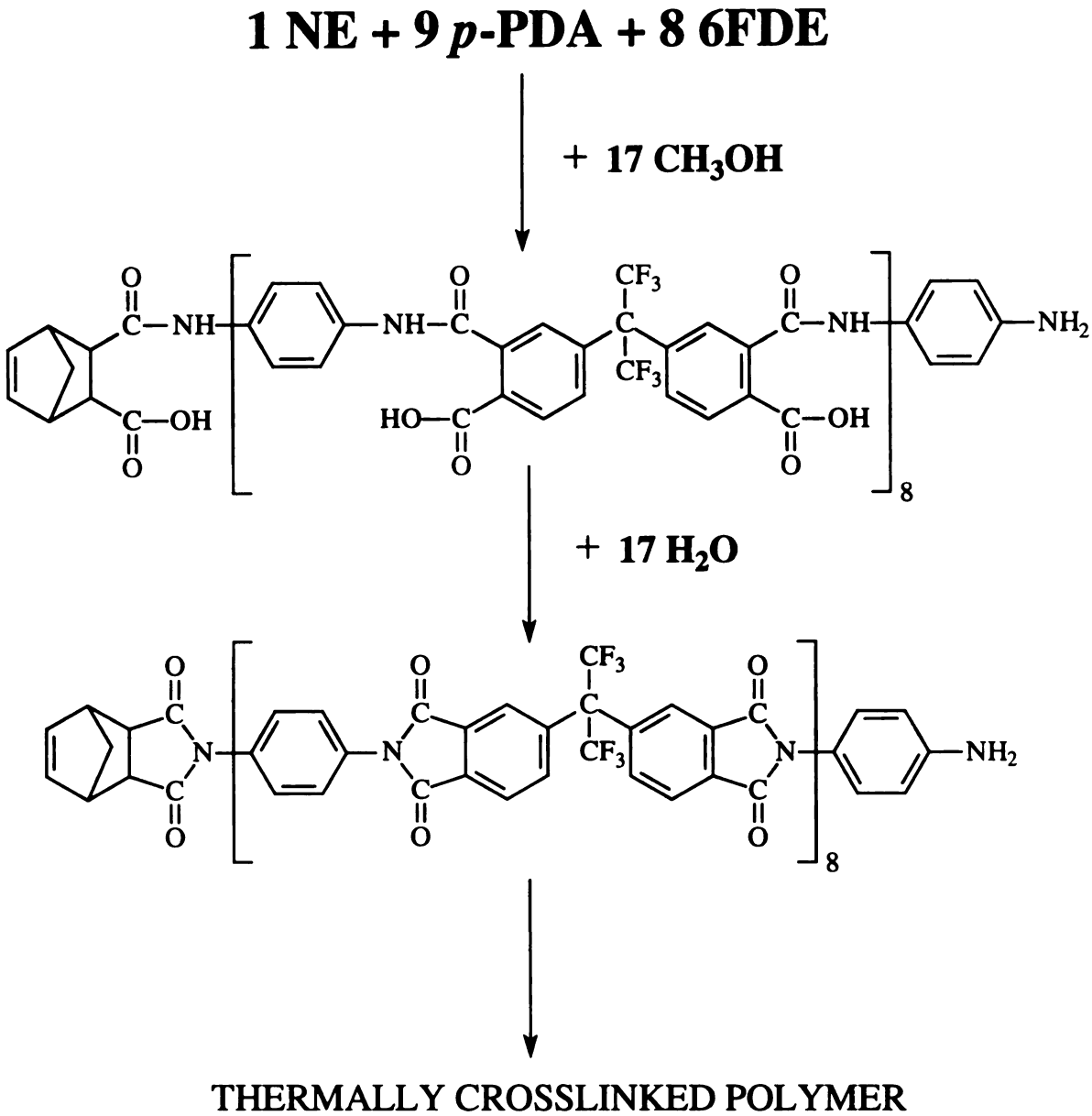

Figure 2.18: Synthesis of AFR700B thermosetting polyimide.

Upon further heating at higher temperatures, crosslinking reactions take place in the system. Russell and Kardos characterized the crosslinking reactions in AFR700B, and the reader is referred to two references for a complete discussion of the cure reactions [113, 114]. Variations in the

monomer compositions are also possible, which can yield extremely high values for T_g (>400°C).

As a result of the excellent thermooxidative stability of the AFR700B polyimide matrix, in early 1999, the Air Force Research Laboratory, Materials and Manufacturing Directorate (ML) completed what has been termed by the Air Force to be one of the most successful part replacement projects on record [132]. A recurring heat damage problem with the F-117A stealth fighter's fuselage trailing edges was addressed by replacing the respective components with AFR700B, which provided an increased heat tolerance of an additional 150°C. A total of 450 separate components were fabricated, with the last component being assembled in January 1999. The success of the aforementioned project earned the first Lieutenant General Thomas R. Ferguson, Jr. Award for Excellence in Technology Transition.

Although the high temperature performance of AFR700B appears to be excellent, the material performance in the presence of moisture has been shown to be the opposite. Hydrolysis has been reported to lead to significant reductions in the glass transition temperature and mechanical properties after prolonged exposure to hot/wet environments [6, 7].

There is another interesting point that needs to be considered while evaluating these polyimides: the physical geometric location of the hydrolytic-induced scission will have a dramatic influence on the degradation kinetics. For

example, Morgan *et al.* [10, 20] has shown that in the case of thermoplastics, one random chain scission per molecule --which is a scission of <1% of the total inherent initial imide rings-- causes the strength to decrease by 50%. If the hydrolytic attack occurs on the ends of the macromolecules, (macromolecules that result in acid or amine monomer formation) then no significant decrease in mechanical properties will be observed.

In the case of thermoset polymers, however, hydrolytic chain scission at a crosslink rather than in an inter-crosslink segment of the network would lead to serious mechanical property deterioration because crosslink scission generates 1.5 to 2 times greater of disconnected network defects, (these segments can no longer support a load, leading to a decrease in network extensibility), depending on if the crosslink has 3 or 4 network interconnections, respectively. This is shown schematically in Figure 2.19.

Finally, although AFR700B may no longer be used in hygrothermal exposure applications, many components already exist in aerospace applications, leading to the conclusion that accurate service lifetime predictions are still necessary, as are an understanding of the critical fundamental degradation mechanisms.

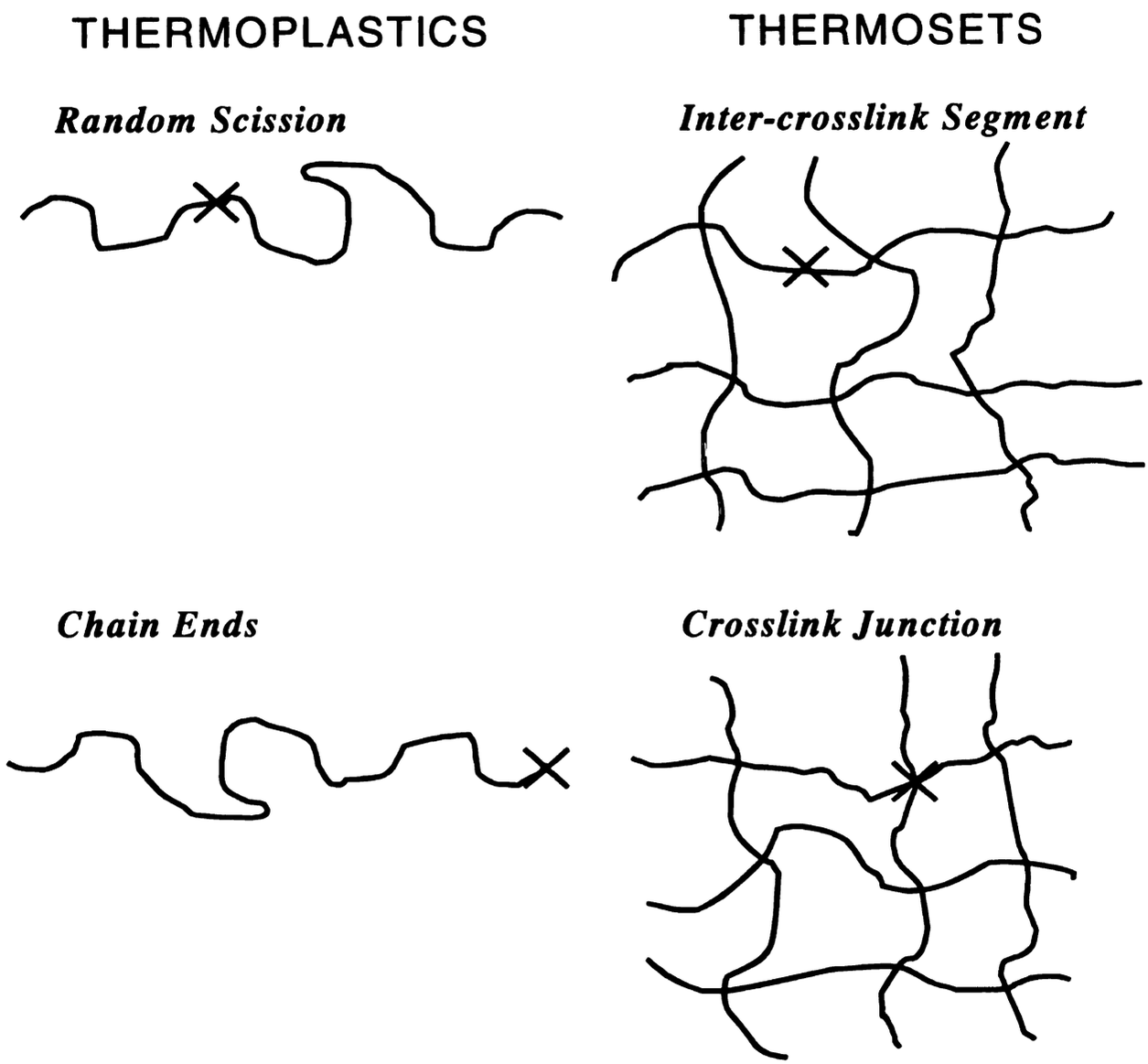

Figure 2.19: Geometric hydrolysis possibilities for polyimide matrices.

2.7 Bismaleimide (BMI)

Bismaleimide thermosetting resins are among the most widely used of all polyimide composite matrices. The most common, such as 5250-4, are primarily based on the fundamental copolymer composed of 4,4'-bismaleimidodiphenylmethane (BMPM) and 0,0'-diallyl bisphenol A (DABPA), shown in Figures 2.20 and 2.21, respectively. This system is commercially available as Matrimid® 5292 from Ciba-Geigy.

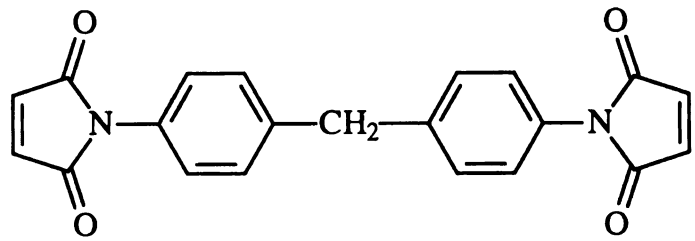

Figure 2.20: 4,4'-bismaleimidodiphenylmethane (BMPM) monomer.

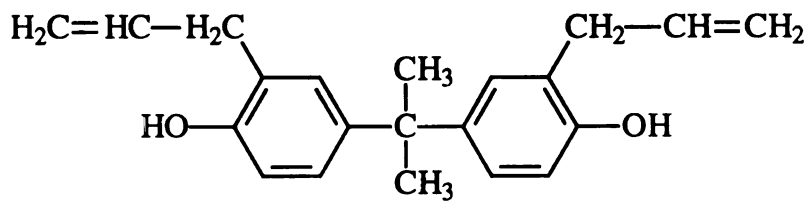

Figure 2.21: 0,0'-diallyl bisphenol A (DABPA) monomer.

BMPM/DABPA bismaleimide cure reactions are incomplete after standard composite fabrication and postcure conditions, and further cure can occur during service environment exposure resulting in glass transition temperature increases and associated composite mechanical property

deterioration [7]. Certainly these network structure-controlling reactions will determine the mechanical, physical, and thermal properties of the matrix constituent, therefore an understanding of these reactions is essential to this research. Cure reactions associated with the resin system have been thoroughly characterized by Morgan *et al.* [3], but further development of the high temperature cure reaction mechanisms needs to be developed.

Morgan *et al.* [3, 5-10, 27], have conducted systematic Fourier transform infrared spectroscopy (FTIR) and differential scanning calorimetry (DSC) studies of the cure reactions for the BMPM/DABPA BMI resin system as a function of chemical composition (initial BMPM:DABPA monomer ratio) and time-temperature cure conditions, from which the following mechanistic path for the cure reactions has been proposed.

Beginning near 100°C, the maleimide bond of BMPM (Figure 2.20) and the allyl bond of the DABPA monomer (Figure 2.21) react by addition to from the 'ene' adduct prepolymer (Figure 2.22). The 'ene' molecule is pentafunctional due to the presence of three C=C double bonds capable of chain extension and crosslinking, and two hydroxyl groups capable of etherification by hydroxyl dehydration. From Figure 2.22, the double bond appellations are (A) allyl, (B) propenyl, (C) maleimide, and (D) hydroxyl. The 'ene' reaction occurs at significant rates above ~180°C.

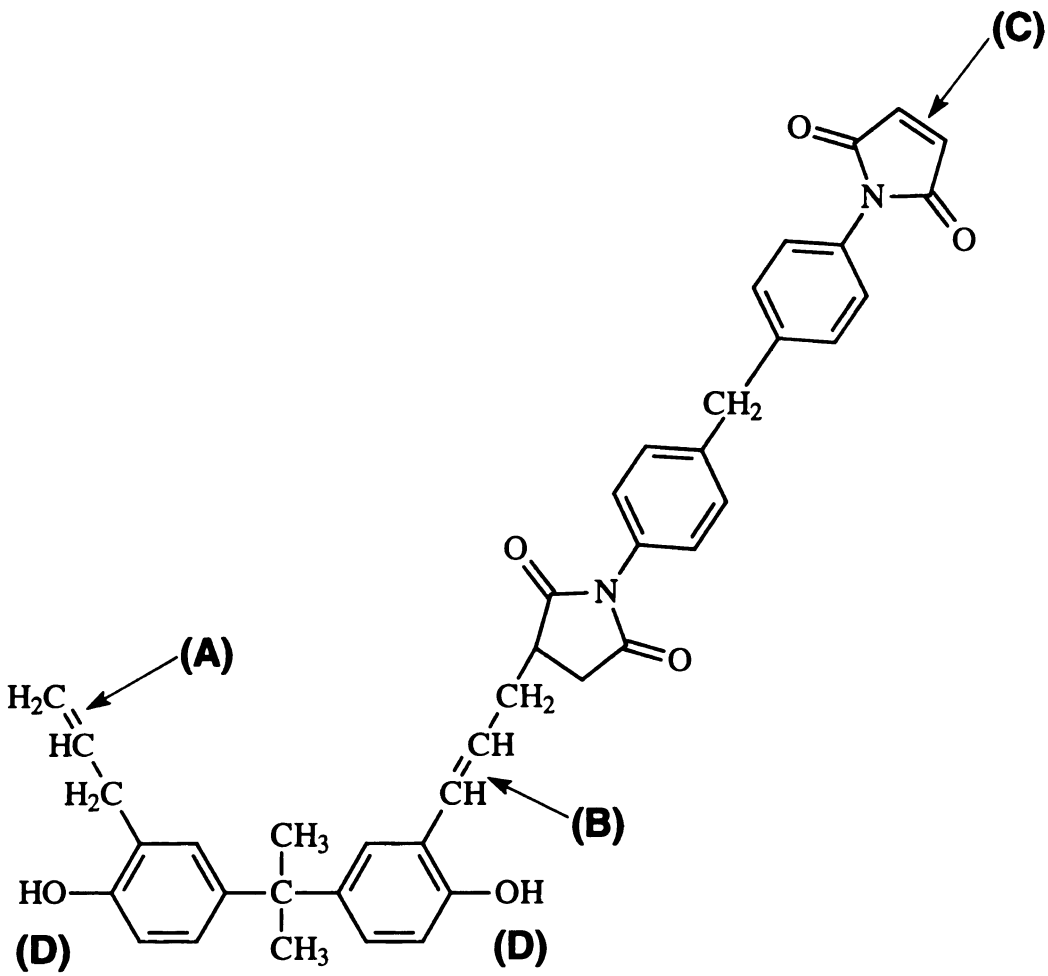

Figure 2.22: Chemical structure of BMPM/DABPA 'ene' adduct prepolymer. Note that (A), (B), and (C) are double bonds capable of polymerization, and (D) are active hydroxyl groups.

At temperatures between 200-300°C, the principal crosslinking reactions occur via the C=C double bonds of the 'ene' molecule, with etherification occurring above 240°C at DSC heating rates of 10°C/min. In this temperature regime, the cure reactions generally occur in the following order: (i) homopolymerization of the maleimide groups of the BMPM monomer, (ii) homopolymerization of the allyl groups, (iii) Diels-Alder ('ene'-BMPM double

bond crosslinking polymerization) reaction, and (iv) hydroxyl dehydration. The 'ene' reaction has been shown [3] to be favored over either homopolymerization reaction. Structurally, a ladder-type network develops from the Diels-Alder reaction process and an anionic imide oligomerization, and the product in Figure 2.23 is often referred to as the Diels-Alder adduct.

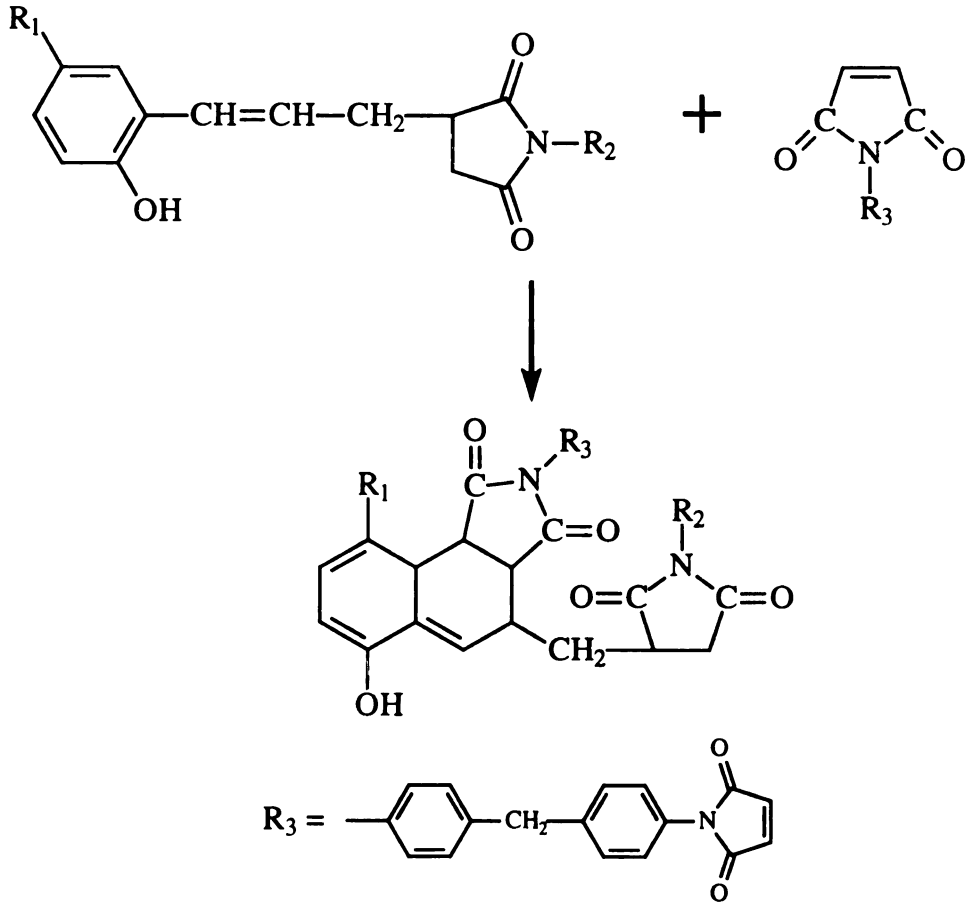

Figure 2.23: Diels-Alder polymerization reaction. Here, R_1 and R_2 represent continuations of the prepolymer formed in the 'ene' reaction, and R_3 is as shown or a longer chain 'ene' reaction product.

As cure proceeds and the viscosity increases, intramolecular reactions become favored over intermolecular reactions. Consequently, the allyl and propenyl bonds of the 'ene' molecule may react to form the cyclization structure shown in Figure 2.24, which is considerably more reactive than the maleimide double bond.

From the above reaction regime, it is critical to note two important factors: (i) the principal cure reactions via the C=C bonds of the 'ene' molecule are complete after a cure of 3 h at 250°C and (ii) ether crosslinks formed via dehydration of the hydroxyl groups of the 'ene' molecule decrease in concentration in the 240 – 300°C temperature range as a function of cure time. The latter reaction is only 50% complete after cure at 250°C for 9 h.

At the highest postcure temperature of 300°C, the ether linkages dissociate and rearrange to form less flexible segments with neighboring groups. The respective dehydration induced ether crosslink formation and subsequent rearrangement to stiffer crosslinked segments plays a critical role in the chemical and physical network structural changes of BMPM/DABPA BMI resins at high service environment temperatures and long times. These changes can significantly modify the BMI resin thermal and mechanical response and composite resin shrinkage induced microcrack characteristics [3-10]. Dramatic property changes have been attributed to the ether crosslink formation and

subsequent rearrangement to less flexible crosslinks, such as –C–C– linkages, and a possible overall increase in the crosslink density.

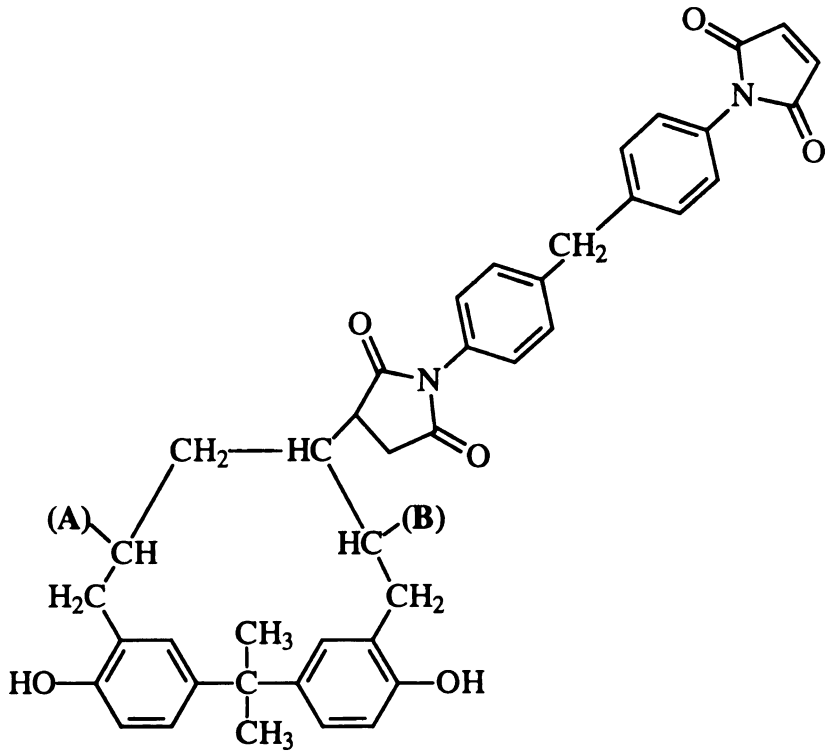

Figure 2.24: Intramolecular cyclization through (A)-(B) double bonds of an 'ene' molecule. The (A) and (B) indicate the structural intermolecular connection to neighboring 'ene' molecules.

It is important to briefly note the implications of the above discussion. Complete cure is only attained after an additional postcure of 2 h at 300°C beyond recommended standard fabrication conditions, leading to a final T_g of about 350°C. Although standard cure conditions may avoid some of the detrimental effects of the ether formation, dissociation, and subsequent rearrangement, complete cure is necessary to remove defects in the form of

unreacted groups, since these segments can support no load. Neighboring segments will have to account for this additional stress during deformation, and chain scission will occur at lower stress levels (decreased network extensibility) and lead to embrittlement [10].

For the BMPM/DABPA BMI matrix system, the following problems still exist: (i) carbon fiber/BMI cross-ply laminates are microcracked after standard fabrication and postcure conditions and (ii) further evidence is needed as to the physical state of the network structure; in particular, further evidence on the role of the ether crosslinks and their dissociation at elevated cure temperatures.

2.8 Polyetherimide (PEI)

Polyetherimide (Ultem 1000®, General Electric) is a low cost, extremely tough thermoplastic that has the drawbacks of poor solvent resistance, questionable hydrolytic stability, and relatively low maximum use temperature for aerospace applications ($T_g \approx 215°C$). The chemical structure is shown in Figure 2.25.

Besides composite matrix applications, the low cost and excellent properties of PEI have lead to its use in consumer applications. As a result of recent consumer law suits involving the use of PEI in flue pipes, questions have arisen regarding the hydrolytic stability (especially in the presence of alkali

or acidic media) and the structure-property-processing relationships of this polyimide. Both of these topics will be addressed in this research from the fundamental perspectives of hydrolytic stability and thermal history of polyimides.

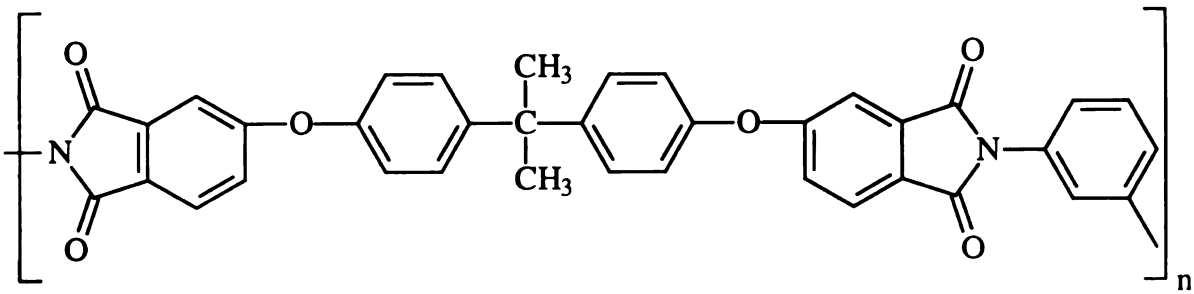

Figure 2.25: Chemical structure of Ultem 1000® polyetherimide.

2.9 DuPont Avimid® K3B

K3B is an amorphous thermoplastic polyimide in the form of a distribution of high molecular weight polymers that are entangled, not linked, resulting in its ability to be melt-processed. Like other condensation polyimides, K3B is derived from anhydride derivatives and amines.

The intermediate polyamic acids are produced by a series of step-growth reactions at room temperature, which control the final molecular weight of the polymer [136]. The general process of condensation polymerization of thermoplastic polyimides is shown below in Figure 2.26. Crosslinked thermoset polyimides are generally derived from preformed imide monomers

or oligomers, such as bismaleimides or PMR-15. The chemical structure of K3B is shown in Figure 2.27.

Like other polyimides, K3B is susceptible to hydrolysis and associated physical degradation mechanisms, such as blistering. As a result, this polyimide will be investigated comparatively to polyimides of different chemical structures.

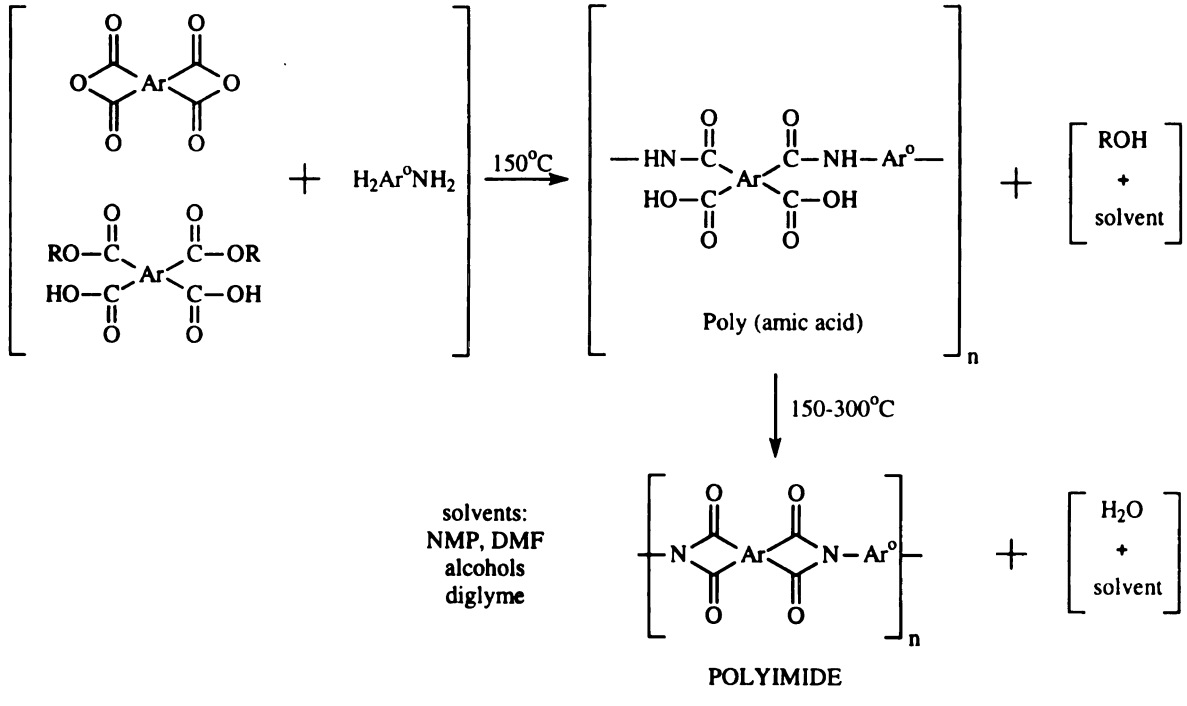

Figure 2.26: Generic description of condensation polyimide synthesis from dianhydride and diamines. Ar and Ar^o can be of a multitude of possible chemical groups [136].

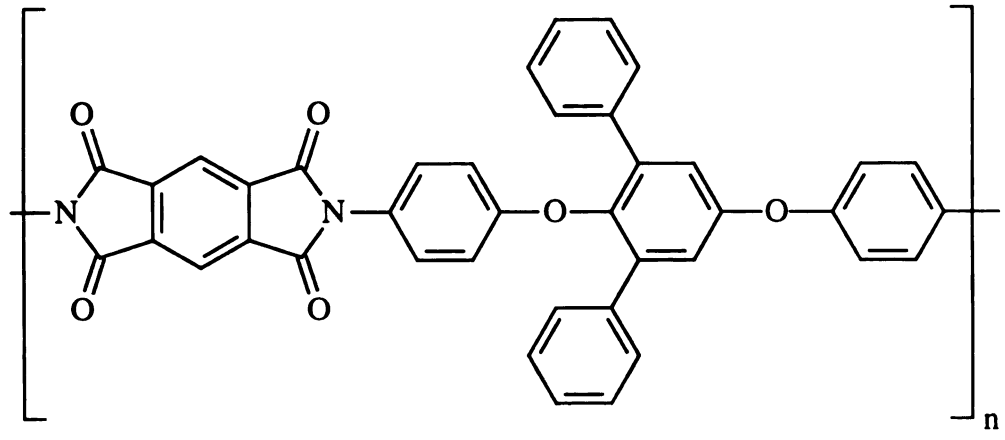

Figure 2.27: Chemical structure of K3B thermoplastic polyimide.

2.10 Poly(4,4'-Oxydiphenylene Pyromellitimide) (POPPI)

Poly(4,4'-oxydiphenlyene pyromellitimide) is fundamentally among the most interesting polyimides from a historical perspective because it is the primary component in DuPont's commercially available Kapton® film. The chemical structure of POPPI is shown in Figure 2.28.

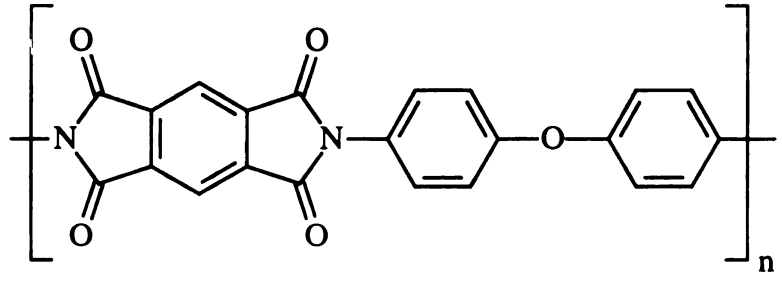

Figure 2.28: Chemical structure of poly(4,4'-oxydiphenylene pyromellitimide) (POPPI) thermoplastic polyimide.

Fundamental studies on the hydrolytic degradation in various pH environments and thermally induced repolymerization of POPPI have been conducted by researchers as early as 1971 [140-144].

DeIasi and Russell [140] investigated the effects of various temperatures and pH exposures on the tensile mechanical response of POPPI polyimide films. The authors report an 87% reduction in strain to failure and a 39% reduction in tensile strength after immersion in distilled water at temperatures ranging from 25°C to 100°C for times of 1 h to several hundred hours. In the pH range of 2.0-12.0, degradation was found to occur primarily by hydrolysis of uncyclized amic acid linkages or diamide functional groups present in the polyimide. For highly acidic conditions (pH < 2.0) degradation was found to occur via hydrolysis of both imide and amide bonds.

In a later publication [141] DeIasi demonstrated that nearly complete regeneration (81-97%) of the tensile properties of the hydrolytically degraded POPPI films was possible upon heat treatment temperatures of 310°C by way of repolymerization. The kinetics of regeneration indicated that the reaction corresponds to the two-step recombination of the hydrolytically attacked amide linkages that were initially present in the as-received polyimide film. Also, the regenerated polyimide exhibited a much-improved hydrolytic stability over the untreated material and specimens heat treated directly without prior aqueous degradation.

In effect, the above publications and more recent research on imide and amide hydrolysis of POPPI based polyimides [142-144] has provided a basis for which to investigate the degradation of polyimides of more complex chemical structures. The most important findings discussed above relative to the current dissertation are (i) the mechanism of polyimide hydrolysis via scission of amide linkages and (ii) the finding that not all of the degradation is permanent, as evidenced by regeneration of the tensile properties of hydrolytically degraded polyimide films [141].

Due to the quantity of data available on POPPI with respect to hydrolytic stability, thermal stability, deformation behavior, etc., this polyimide serves as a useful basis from which more complex polyimide structures can be understood.

2.11 Phenylethynyl Terminated Imide Oligomers

Based on an understanding of polyimide hydrolytic degradation and the structural factors that control processability, researchers have shown that preparation of low molecular weight imide oligomers end capped with terminal functional groups can provide high temperature, hydrolytically stable, tough, processable polyimides [20].

Most notably, investigators have demonstrated these properties by application of the end capping agent 4-phenylethynyl phthalic anhydride (PEPA) to various polyimide backbones. NASA's PETI-5, for example, received enormous attention during development of the High Speed Civil Transport program. This polyimide (Figure 2.29), which can be crosslinked with heat (350-371°C) and pressure (~1 MPa), has demonstrated excellent hot/wet properties, improved hydrolytic stability, high toughness (strain to failure = 32%), excellent mechanical strength (130 MPa), and a respectable glass transition temperature (270°C) relative to other polyimides. Various molecular weights are fabricated (1250-5000 g/mol) to control processability, and some of these polyimides can be processed by resin transfer molding (RTM).

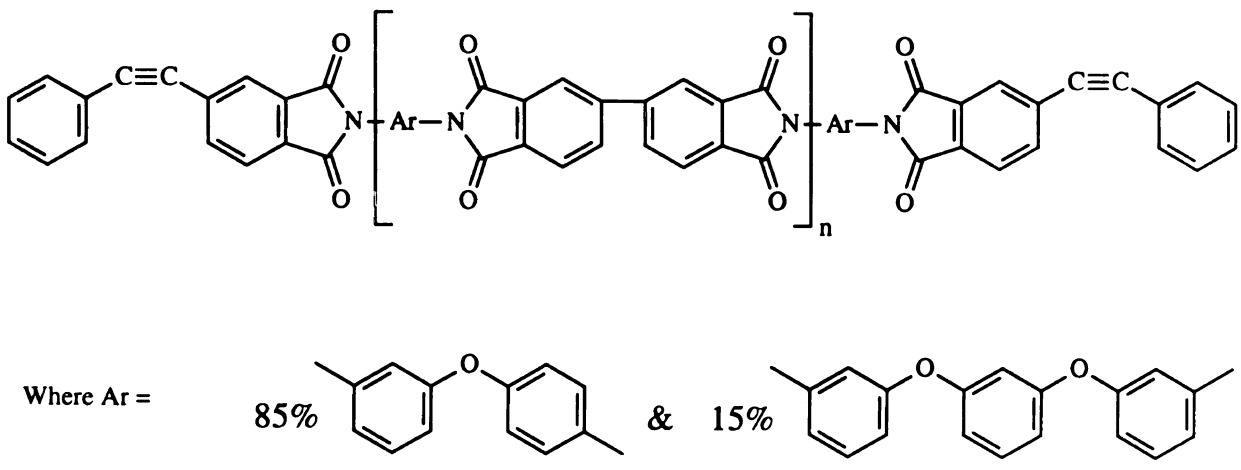

Figure 2.29: NASA LaRC® PETI-5 imide oligomer.

Although the concept is not new, the high cost of the PEPA component (currently $600-$1000 per pound) often discourages work in this area. In instances where performance outweighs cost, the technology could be critical to future material improvements. More research is currently needed to investigate the application of PEPA to other polyimide structures.

Chapter 3

Moisture Absorption-Network Structure Correlations in BMPM/DABPA Bismaleimide Composite Matrices

3.1 Introduction

Bismaleimide-carbon fiber composites are utilized for present commercial and military aerospace structural applications that involve exposure to prolonged extreme service conditions, and are being considered for future applications, which consist of equivalent or more synergistic environments. These complex service exposures of stress, time, temperature, moisture, chemical, and gaseous environments require a thorough understanding of the physical, chemical, and mechanical phenomena that control the most probable critical failure path of the composite. Therefore, an understanding of the critical fundamental aging mechanisms and network structure-property correlations are necessary for long-term composite performance predictions and fabrication optimization.

This chapter represents additional efforts to those completed previously [1-10] to identify structural characteristics with respect to the moisture diffusion behavior of BMI resins. Recently [4-9], there has been an attempt to correlate network structure-property interrelationships with physical, thermal, and mechanical properties, where network structure alterations are controlled

by initial monomer ratios and cure cycles derived from the current understanding of the cure chemical reactions.

The primary objective of this particular study was to further correlate the same critical structure-property interrelationships by monitoring the effects of moisture in 50°C and 70°C water bath environments. Specifically, moisture absorption behavior dependence on the following properties is presented: (i) monomer composition, (ii) cure time-temperature schedules, and (iii) physical and thermal interrelationships also dependent on these critical network structure-controlling variables; T_g and room temperature density.

3.2 Experimental Techniques

3.2.1 Materials and Fabrication

The BMI resin system utilized was the Matrimid® 5292, Ciba-Geigy copolymer system composed of BMPM and DABPA monomers in various stoichiometric ratios, shown in Figures 2.20 and 2.21, respectively. The DABPA amber viscous liquid monomer of appropriate amount was poured into a magnetic stir-activated beaker and heated on a hot plate at 130°C until the viscosity decreased, then the corresponding amount of yellow BMPM crystalline powder was added slowly and mixed until a homogeneous solution was achieved.

Next, the respective prepolymer solution was degassed in full vacuum at 130°C for 10-20 minutes.

Finally, BMI resin panels were prepared by pouring the mixture into two preheated (90°C) clamped tempered glass plates coated with release agent and separated by a high temperature silicone gasket. The panels were fabricated by systematically varying the monomer ratio and cure time-temperature conditions corresponding to Table 3.1. One stoichiometric and three off-stoichiometric (one BMPM deficient and two BMPM rich) systems were formulated with six different cure conditions. Post-cure at 250°C and above was performed in a nitrogen atmosphere.

Table 3.1: Monomer compositions and cure conditions for BMI resins.

BMPM:DABPA RATIO pbw *molar*		SYSTEM A 87:85 *1:1.13*	SYSTEM B 100:85 *1:1*	SYSTEM C 113:85 *1:0.87*	SYSTEM D 120:85 *1:0.82*
Cure Cycle	Lower Temperature Cure	177°C / 1h + 200°C / 1h			
		177°C / 1h + 200°C / 3h			
	Standard Temperature Cure	177°C / 1h + 200°C / 2h + 250°C / 1h			
		177°C / 1h + 200°C / 2h + 250°C / 6h*			
	Higher Temperature Cure	177°C / 1h + 200°C / 2h + 250°C / 6h + 300°C / 1h			
		177°C / 1h + 200°C / 2h + 250°C / 6h + 300°C / 6h			

*Industry standard cure cycle

3.2.2 Specimen Preparation

Resin samples were sized to desired specifications using a diamond blade saw, slow traverse head speed, and running water. Release agent and surface porosity were removed by standard metallographic polishing techniques, using a sequence of 320, 400, 600, 800 grit paper on a Buehler Ecomet IV polishing wheel at 300 rpm angular velocity and head pressure. Approximately 1 mm of material was removed from each side of a given specimen, resulting in a final specimen thickness of about 1 mm. All samples were then cleaned briefly with de-ionized water and dried in full vacuum at 80°C until no weight change occurred (~2 weeks). Thickness was measured at five locations along the rectangular specimen and the average recorded.

3.2.3 Glass Transition Temperature (Modulated DSC)

Glass transition temperature measurements were made using 10-25 mg BMI samples in a TA Instruments® 2920 modulated DSC, heating rates of 5°C/min, and a N_2 atmosphere. Data was recorded and analyzed using a TA Instruments® 2200 data acquisition system, and T_g determined from the inflection point of the reversing heat flow (heat capacity component) versus temperature curve.

3.2.4 Room Temperature Density (Hydrostatic Weighing)

Room temperature density was determined at 23°C by hydrostatic weighing (ASTM D798-86) with a distilled water test liquid medium and wetting agent on a Mettler balance with a 0.1 mg resolution. Specimen dimensions were 10 mm x 80 mm x ~4 mm. Five specimens per condition were tested.

3.2.5 Moisture Absorption

Specimens were dried for 72 h at 80°C in addition to aforementioned preconditioning treatment. The moisture absorption was determined by submerging the samples (10 mm x 50 mm x ~1 mm) in de-ionized water baths of 50°C and 70°C and monitoring the water up-take (in weight percent) gravimetrically by the relationship

$$M_t = \left(\frac{W - W_d}{W_d} \right) \times 100 \qquad (3.1)$$

where W is the weight of the sample after time t, W_d represents the weight of the specimen after completion of the preconditioning ('dry' weight), and M_t represents the percent weight gain at the same time, t.

Samples, originally secured in glass specimen support racks, were removed from the water bath and excess water removed by gently wiping with lint-free paper towels. Weight was recorded to 0.1 mg precision on a Mettler balance. The average of two samples was used to determine one data point.

In order to model the diffusion of moisture in the resin, Fick's Second Law can be solved by considering a plate of thickness b exposed on two sides to identical environments. The estimation is made that the plate's dimensions in the orthogonal directions are large enough when compared to the thickness that they may be assumed infinite, reducing the problem to one dimension. Thus, the differential equation and respective boundary conditions are

$$D\frac{\partial^2 c}{\partial x^2} = \frac{\partial c}{\partial t} \tag{3.2}$$

$$c = c_i \qquad 0 < x < b \qquad t \le 0$$

$$c = c_a \qquad x = 0, x = b \qquad t > 0$$

Above, c is the concentration of the moisture, t is the diffusion time, x is the thickness direction, c_i represents the moisture concentration inside the plate before the sample is exposed to the hygrothermal environment, D is the diffusion coefficient or diffusivity (assumed not a function of concentration), and c_a is the moisture concentration at the interface after the sample is exposed. Solving the differential equation with the above assumptions and boundary conditions, then integrating over the entire plate thickness yields the total weight ratio of the moisture in the material:

$$\frac{M_t}{M_\infty} = 1 - \frac{8}{\pi^2}\sum_{j=0}^{\infty}\frac{1}{(2j+1)^2}\exp\left[-(2j+1)^2\pi^2\left(\frac{Dt}{h^2}\right)\right] \tag{3.3}$$

Here, M_t represents the water content absorbed in the system after time t and M_∞ is the saturated (equilibrium) water content at $t = \infty$. Since Equation 3.3 is tedious to apply, the approximation of this equation (Equation 2.10) was used.

For the sake of consistency and minimization of error, the diffusivity and equilibrium moisture content were determined by regression analysis of the data fitted to Equation 2.10. Other methods require knowledge of M_∞, which may incorporate external error into the calculation.

In addition to determining M_∞ and D, the activation energy, Q, and diffusion constant, D_o, were obtained by performing absorption experiments at two temperatures (50°C and 70°C) and solving the Arrhenius relationship in Equation 2.11.

Plots of percent weight gain as a function of the square root of time divided by thickness were constructed to account for variations in specimen thickness, and to display the interrelationships between cure schedule and monomer composition.

3.3 Results and Discussion

3.3.1 Resulting BMI Network Structure

3.3.1.1 Room Temperature Density

Hydrostatic weighing was a simple and useful test to display the qualitative trends, which have been verified in other studies by *in-situ* specific volume measurements during cure, weight loss during cure [8], and Positron Annihilation Lifetime Spectroscopy (PALS) studies on these resins [11].

Evidenced from Table 3.2 and Figure 3.1, the room temperature density increased with concentration of the BMPM monomer and decreased with increasing degree of cure. It has been reported for BMI systems copolymerized with methylenedianilene (MDA) that decreasing BMPM concentration and increasing cure results in an increase in density [17,18], however the findings here display anomalous behavior for the BMPM/DABPA BMI resin system. The latter relationship may be attributed to further crosslinking resulting in increased three-dimensionality of the structure (increasing the structural volume) thereby leaving more regions available for nanopores or voids. As cure proceeds, increasing crosslink density imposes geometric constraints on segmental packing by the crosslinked network geometry. Molecular modeling of many thermosets indicates that as the crosslink density of the network increases, the packing efficiency decreases [21], i.e. the lower crosslinked glass is more compact. Also, since the mass density of the BMPM monomer was 1.4

g/cm^3 whereas the DABPA monomer was only 1.08 g/cm^3, the higher initial BMPM concentration showed higher overall BMI density.

In addition to the effects of curing, excess BMPM monomer resulted in (i) stiffer network segments that inhibited molecular conformation and (ii) higher crosslink density that lead to a more open, less well-packed structure (also evidenced by moisture absorption results below and data presented in Chapter 5).

Gordon and Ravve [24] studied the oxygen transmission of highly crosslinked polymers of varying structure produced by the reaction of poly(glycidyl acrylate) and methacrylate with a variety of anhydride crosslinking agents. It was reported that molecular packing efficiency decreased when one component of the system was much more rigid and/or bulky, creating stiff crosslinks that prevented optimum space filling to occur during crosslinking reactions. Flexible chains (less stiff segments) were able to pack more efficiently on a molecular scale. As a result of these network structure details, highest permeabilities were obtained when a very bulky and stiff crosslinking agent was reacted to very high crosslink densities with a relatively flexible backbone polymer. This stiffness-steric hindrance structural dependence was observed with these BMI resin systems, and might help to partially explain the reverse behavior observed when the BMPM was copolymerized with MDA rather than the DABPA monomer [17,18].

The data presented in this chapter and that obtained from previous investigations [1-10, 20] suggests that the primary structural network modification mechanisms associated with this BMPM/DABPA BMI system are the crosslinking density and molecular segment stiffness influences described above.

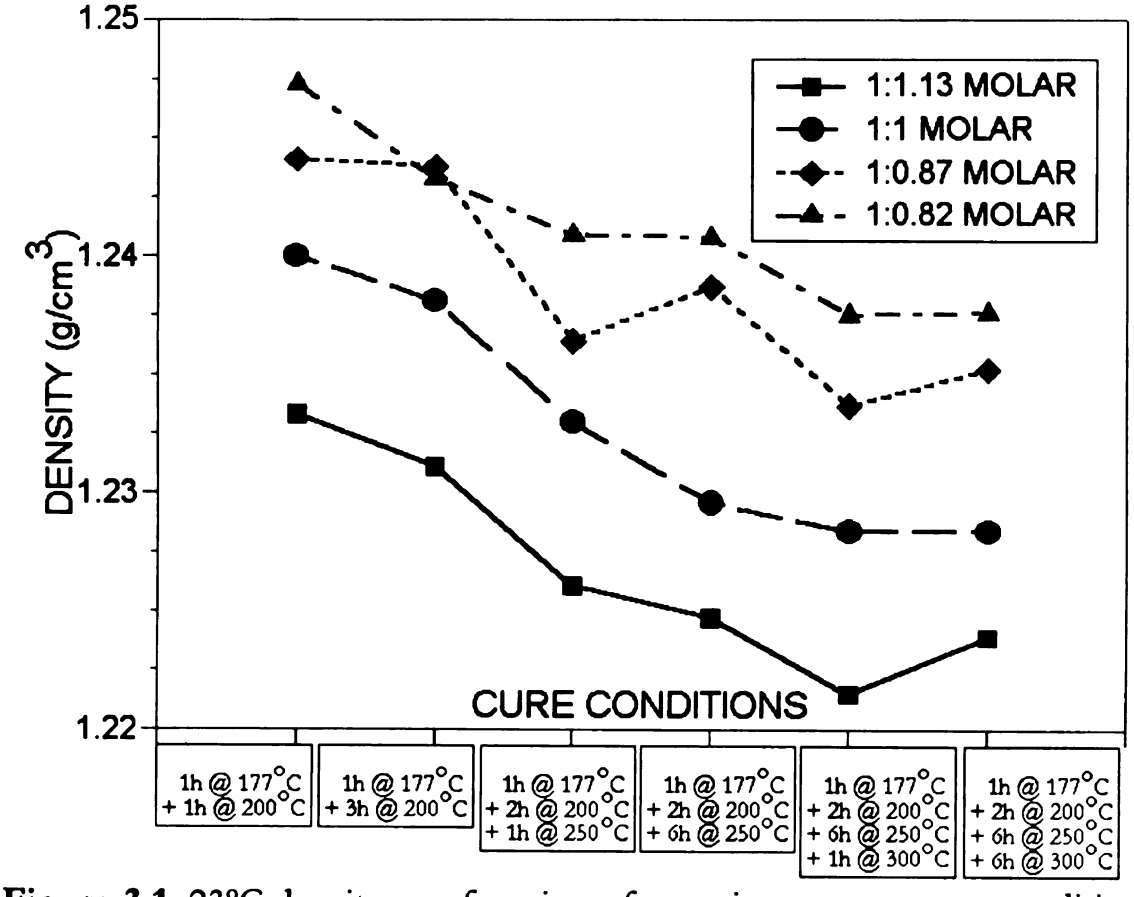

Figure 3.1: 23°C density as a function of cure time-temperature conditions and initial BMPM:DABPA monomer ratio.

3.3.1.2 Glass Transition Temperature

T_g results are tabulated with room temperature density in Table 3.2, and shown schematically as a function of cure conditions in Figure 3.2; T_g increased with increasing cure time-temperature conditions, producing a final T_g of about 350°C after the highest post-cure treatment of 6h at 300°C. This was expected based on previous investigations of BMI cure reactions and kinetics, in which it has been suggested that additional T_g increase was due to further cure via hydroxyl dehydration induced ether crosslinks and their subsequent rearrangement to stiffer crosslinks [2,3]. Differences in monomer ratios over the compositions studied did not influence the final T_g at standard or extended cure cycles, but did influence associated kinetics of the respective cure reactions.

These network structure-T_g relationships can be attributed to the ether crosslink rearrangement to stiffer crosslinked segments, noting that the ether crosslinks decrease in concentration in the 240-300°C range as a function of time [20]. Previously, researchers have examined the network physical and structural changes at high temperatures and/or long times [1-10] where these service environments significantly modify the BMI resin mechanical response.

Table 3.2: Density and T_g numerical results for BMI resins.

BMPM:DABPA RATIO *molar*		SYSTEM A *1:1.13*		SYSTEM B *1:1*		SYSTEM C *1:0.87*		SYSTEM D *1:0.82*	
		density (g/cm^3)	T_g (°C)	density (g/cm^3)	T_g (°C)	density (g/cm^3)	T_g (°C)	density (g/cm^3)	T_g (°C)
Cure Cycle	177°C / 1h + 200°C / 1h	1.2333	151	1.2400	180	1.2441	199	1.2473	200
	177°C / 1h + 200°C / 3h	1.2311	177	1.2381	197	1.2438	220	1.2433	223
	177°C / 1h + 200°C / 2h + 250°C / 1h	1.2261	247	1.2330	262	1.2364	259	1.2409	275
	177°C / 1h + 200°C / 2h + 250°C / 6h	1.2247	318	1.2296	313	1.2387	311	1.2408	305
	177°C / 1h + 200°C / 2h + 250°C / 6h + 300°C / 1h	1.2215	344	1.2284	343	1.2337	342	1.2375	342
	177°C / 1h + 200°C / 2h + 250°C / 6h + 300°C / 6h	1.2239	347	1.2284	351	1.2352	350	1.2376	350

For example, the following property changes were observed: a ~0.3 % weight loss during cure, a 10% modulus decrease, and a 25-40% ductility loss in the 25-177°C temperature range as a function of initial monomer composition, with an associated 0.2% density decrease and a ~100°C increase in T_g after further cure in the 250-300°C temperature range (Chapter 5).

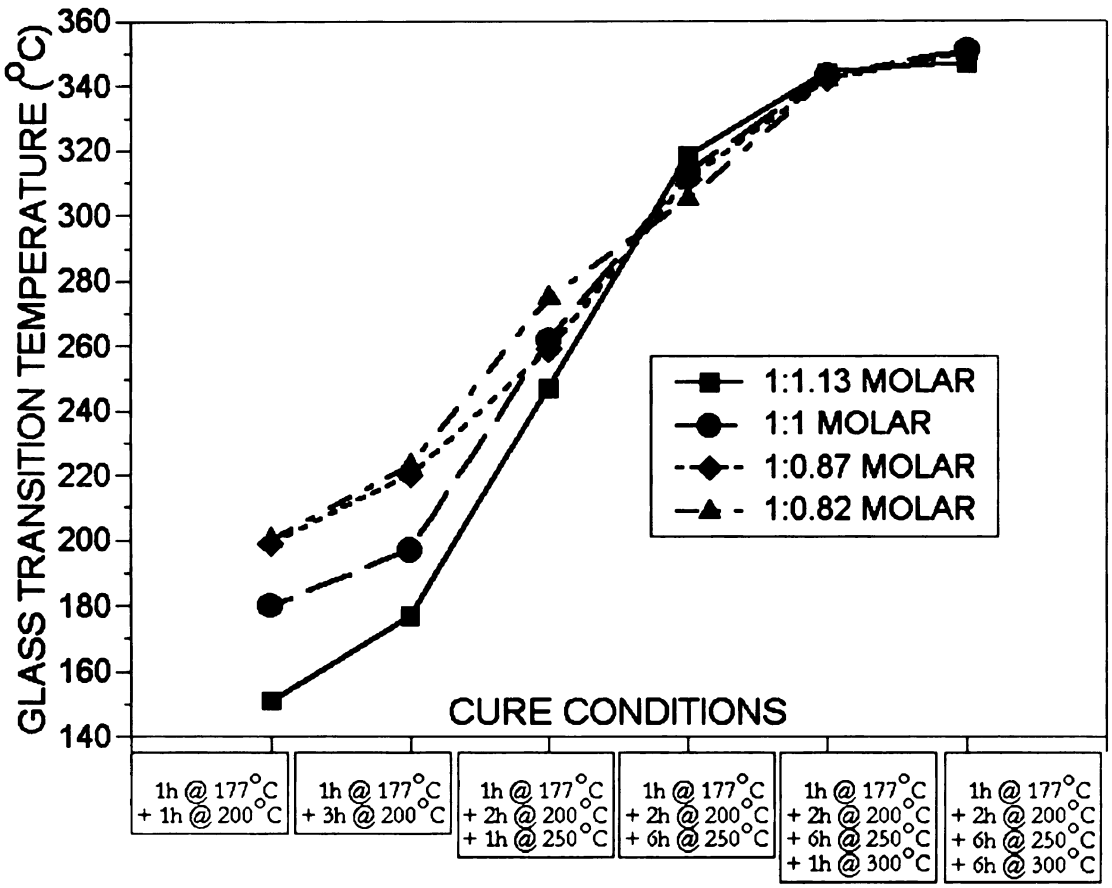

Figure 3.2: Glass transition as a function of cure conditions and BMPM:DABPA initial monomer ratio.

These property changes occur after all of the C=C double bonds of the 'ene' molecule (Figure 2.22) have been consumed. Therefore, the chemical and physical mechanisms associated with these BMI resin property modifications must involve thermal dissociation of the ether linkages followed by formation of less flexible crosslinks, such as –C–C– linkages, and a possible overall increase in crosslink density [20].

3.3.2 Moisture Absorption Characterization of the BMI Network Structure

Moisture absorption at 50°C and 70°C followed Fickian-type behavior and displayed similar trends in the data between the two temperatures (Table 3.3). To avoid unnecessary repetition and confusion, analysis will include only the 70°C moisture absorption behavior since the observed trends mirror the 50°C data.

Before continuing with the analysis, it must first be noted that the 50°C generally possessed higher values (1-9%) for the equilibrium moisture content than observed upon exposure to 70°C. Only the two lowest cure cycles in Systems A and B deviated from this trend, which showed a slight increase to no change in M_∞. Also, although there was scatter in the data, the qualitative differences in equilibrium moisture content at the two temperatures may be summarized by stating that the magnitude of the percent decrease in M_∞ generally (i) increased with increasing degree of cure and (ii) displayed no apparent dependence on the initial monomer stoichiometry.

This 'reverse thermal' behavior has been observed for a variety of crosslinked systems, but the precise mechanism(s) involved are still subject of debate [4,5,8,9]. The results obtained in this investigation suggest that the thermodynamic effect associated with the residence time of water molecules on hydrogen bond sites is more influential on the overall material response in

terms of equilibrium moisture content than the concentration of moisture accessible sites within the polymer structure, which increase at higher temperatures. Thus, water molecules tend to have shorter residence times at higher temperatures, as discussed in Chapter 2.

Figures 3.3 and 3.4 display water uptake curves as a function of the square root of time normalized to the specimen thickness at various cure conditions for four different initial monomer compositions. Cure cycle designations are low ('L'), standard ('S'), and high ('H') temperature cure consistent with Table 3.1. Within a given stoichiometry, the equilibrium moisture content and diffusivity increased with increasing degree of cure, but dropped off slightly at the higher cure regimes. For a given cure condition, the value of M_∞ generally increased with increasing initial concentration of the BMPM monomer.

Table 3.3: Moisture absorption results for BMI resins as a function of stoichiometry and cure conditions.

Cure Conditions	Effects Of Moisture	BMI NEAT RESIN COMPOSITIONS BY BMPM:DABPA RATIO (molar)							
		SYSTEM A (1:1.13)		SYSTEM B (1:1)		SYSTEM C (1:0.87)		SYSTEM D (1:0.82)	
		Bath Temperature		Bath Temperature		Bath Temperature		Bath Temperature	
		50°C	70°C	50°C	70°C	50°C	70°C	50°C	70°C
177°C / 1h + 200°C / 1h	M_∞ (%)	2.48	2.74	2.78	2.83	3.00	3.09	3.22	3.14
	D (cm^2s^{-1}) x 10^{-8}	.847	1.79	1.03	2.67	1.07	2.51	1.48	2.52
	Q ($kJmol^{-1}$) $D_o(cm^2s^{-1})$	34.4 *3.18 x 10^{-3}*		43.7 *1.20 x 10^{-1}*		39.3 *2.43 x 10^{-2}*		24.7 *1.443 x 10^{-4}*	
177°C / 1h + 200°C / 3h	M_∞ (%)	2.82	2.82	3.11	3.09	3.37	3.30	3.36	3.34
	D (cm^2s^{-1}) x 10^{-8}	.958	2.08	1.12	2.68	1.24	2.93	1.60	2.97
	Q ($kJmol^{-1}$) $D_o(cm^2s^{-1})$	35.9 *6.08 x 10^{-3}*		40.2 *3.53 x 10^{-2}*		39.8 *3.34 x 10^{-2}*		28.4 *6.33 x 10^{-4}*	
177°C / 1h + 200°C / 2h +250°C / 1h	M_∞ (%)	3.70	3.58	4.16	3.89	4.34	4.11	4.31	4.08
	D (cm^2s^{-1}) x 10^{-8}	1.48	3.83	1.81	3.82	1.67	4.11	1.84	4.00
	Q ($kJmol^{-1}$) $D_o(cm^2s^{-1})$	43.7 *1.73 x 10^{-1}*		34.4 *6.65 x 10^{-3}*		41.6 *9.03 x 10^{-2}*		35.7 *1.10 x 10^{-2}*	
177°C / 1h + 200°C / 2h +250°C / 6h	M_∞ (%)	4.41	4.06	4.63	4.21	5.13	4.78	4.61	4.32
	D (cm^2s^{-1}) x 10^{-8}	2.30	4.84	2.04	4.80	2.34	5.58	2.28	4.71
	Q ($kJmol^{-1}$) $D_o(cm^2s^{-1})$	34.4 *8.23 x 10^{-3}*		39.4 *4.85 x 10^{-2}*		40.1 *7.26 x 10^{-2}*		33.5 *5.92 x 10^{-3}*	
177°C / 1h + 200°C / 2h +250°C / 6h + 300°C / 1h	M_∞ (%)	4.60	4.32	5.16	4.73	5.34	4.89	5.37	4.95
	D (cm^2s^{-1}) x 10^{-8}	2.54	5.03	2.25	5.64	2.66	5.63	3.39	5.71
	Q ($kJmol^{-1}$) $D_o(cm^2s^{-1})$	31.5 *3.16 x 10^{-3}*		42.3 *1.57 x 10^{-1}*		34.6 *1.04 x 10^{-2}*		24.1 *2.65 x 10^{-4}*	
177°C / 1h + 200°C / 2h +250°C / 6h + 300°C / 6h	M_∞ (%)	4.58	4.37	--	--	5.16	4.85	5.18	4.93
	D (cm^2s^{-1}) x 10^{-8}	2.91	4.85	--	--	2.39	5.20	3.55	5.70
	Q ($kJmol^{-1}$) $D_o(cm^2s^{-1})$	23.6 *1.88 x 10^{-4}*		-- --		35.8 *1.46 x 10^{-2}*		21.8 *1.21 x 10^{-4}*	

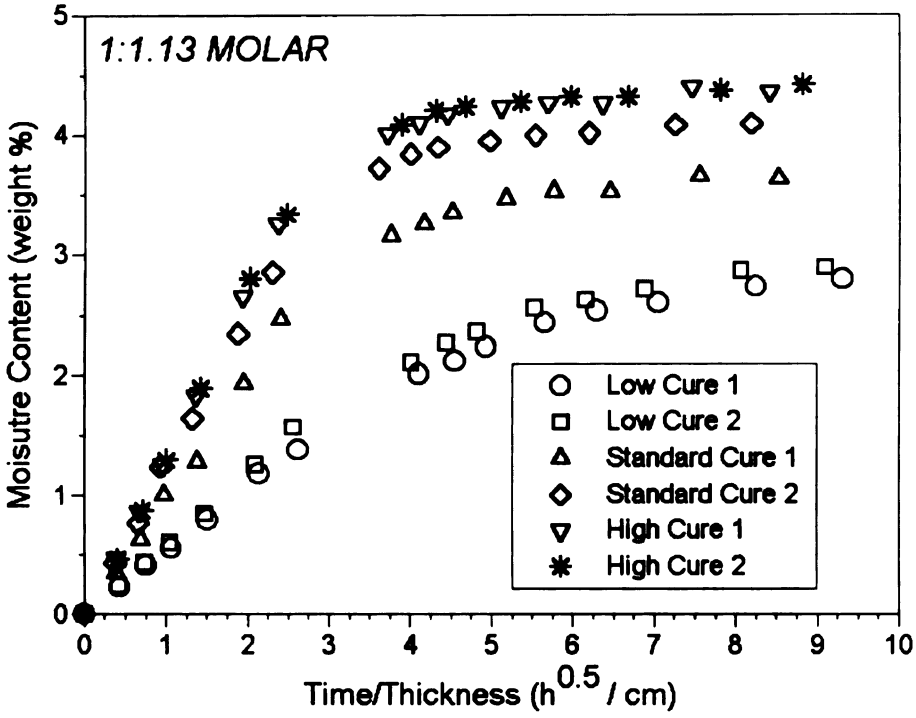

Figure 3.3(a): Moisture absorption curves at 70°C as a function of BMPM:DABPA ratio and cure conditions for 1:1.13 molar.

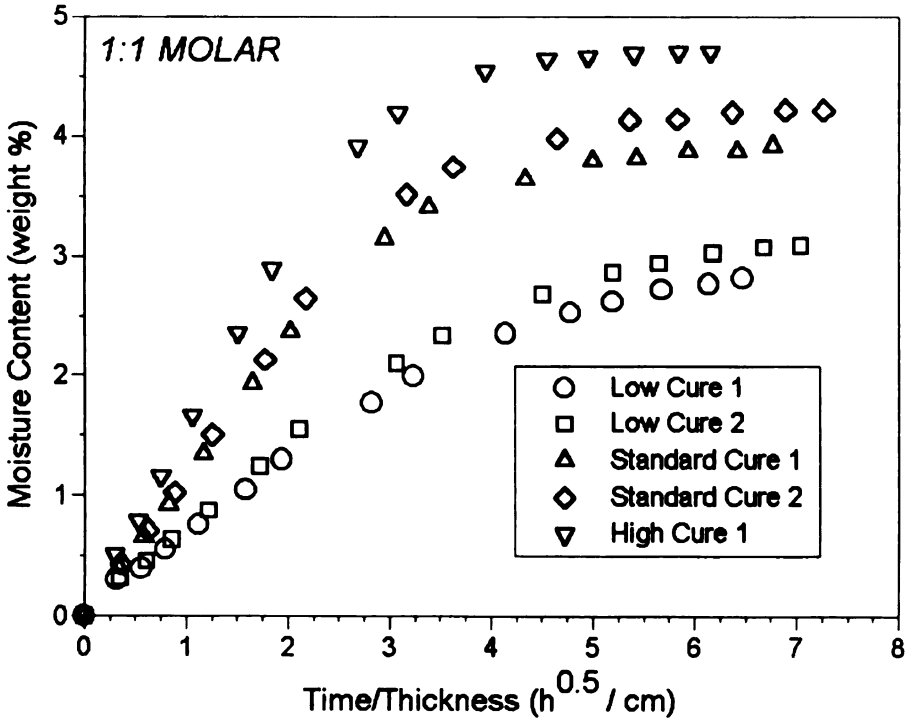

Figure 3.3(b): Moisture absorption curves at 70°C as a function of BMPM:DABPA ratio and cure conditions for 1:1 molar.

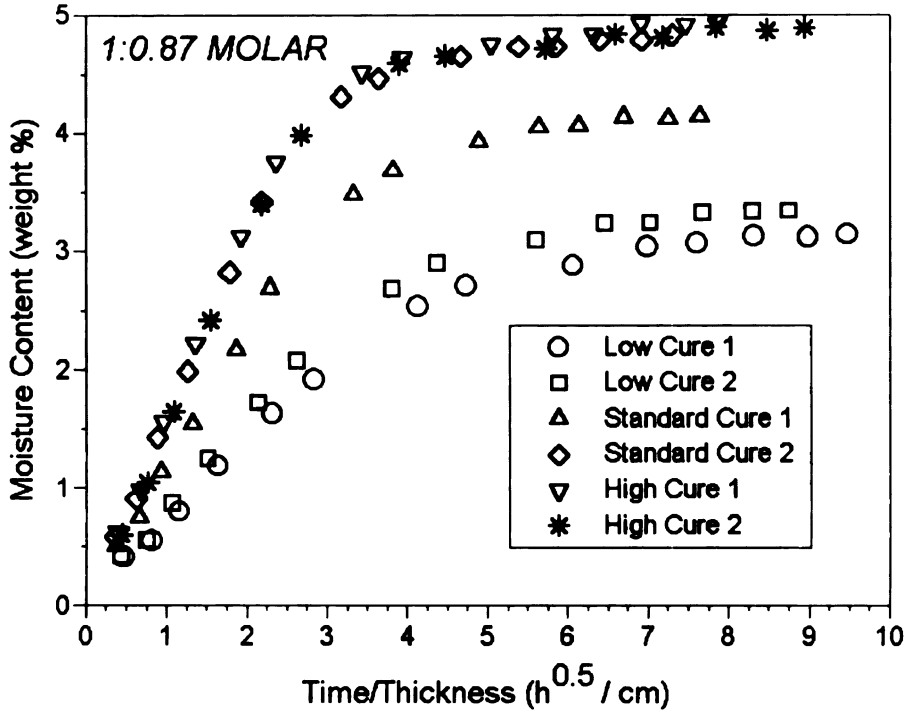

Figure 3.3(c): Moisture absorption curves at 70°C as a function of BMPM:DABPA ratio and cure conditions for 1:0.87 molar.

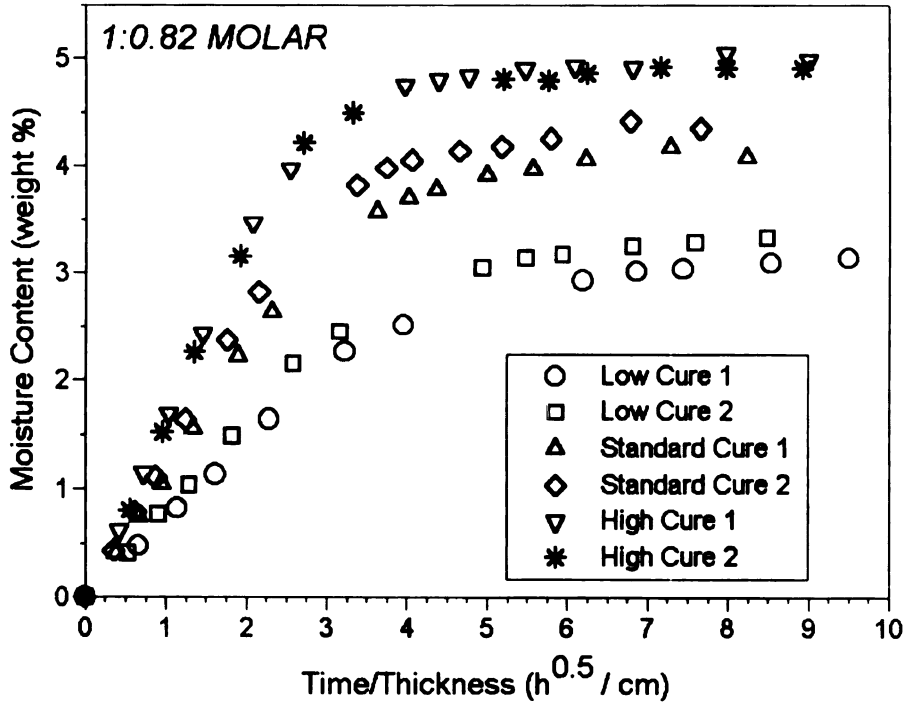

Figure 3.3(d): Moisture absorption curves at 70°C as a function of BMPM:DABPA ratio and cure conditions for 1:0.82 molar.

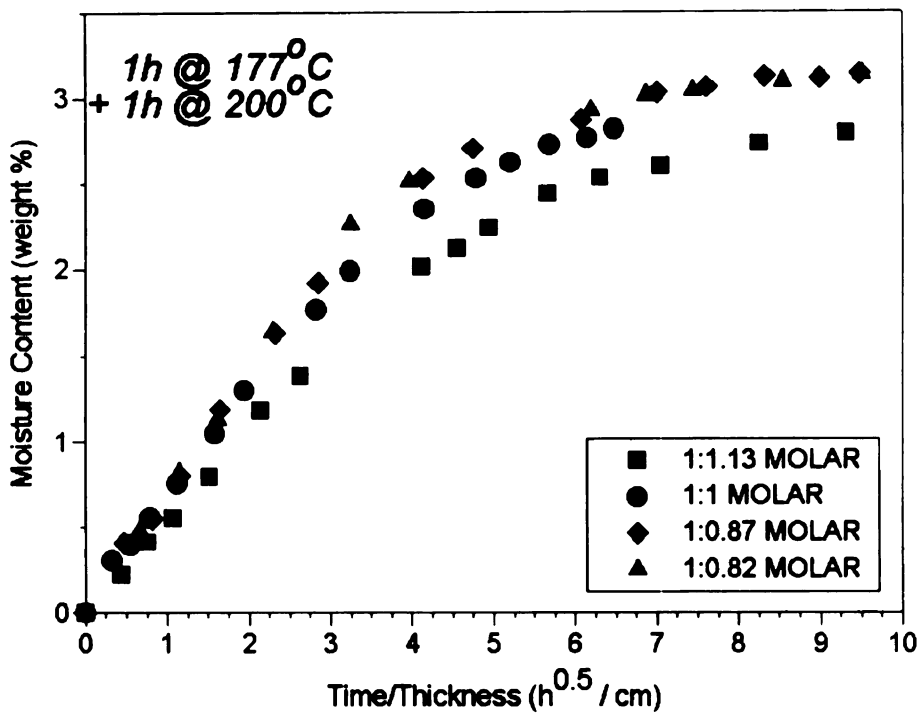

Figure 3.4(a): Moisture absorption curves as a function of cure and BMPM:DABPA ratio for the 'L1' cure cycle.

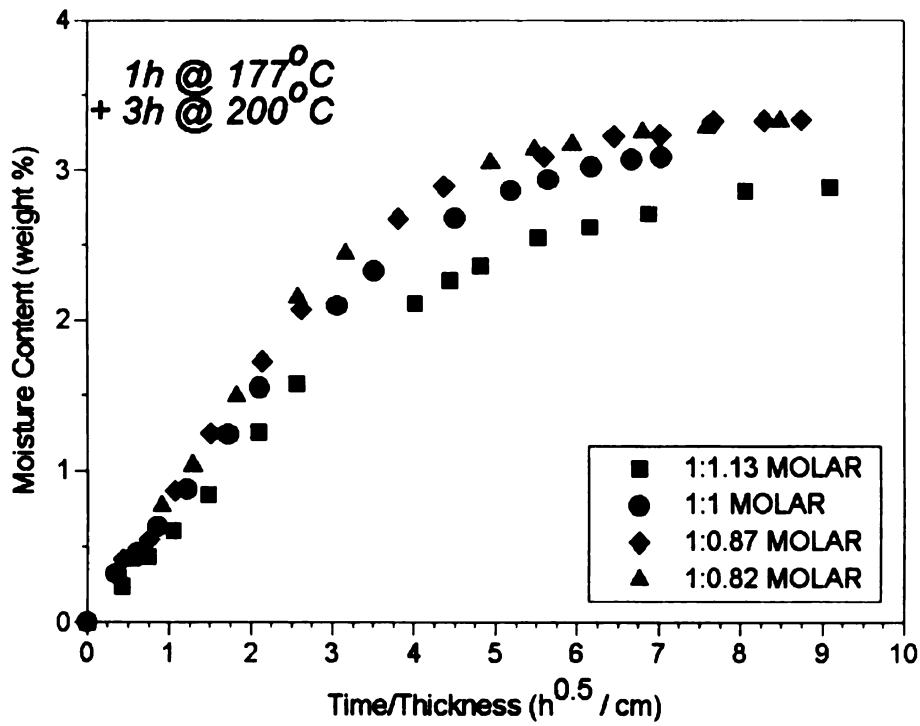

Figure 3.4(b): Moisture absorption curves as a function of cure and BMPM:DABPA ratio for the 'L2' cure cycle.

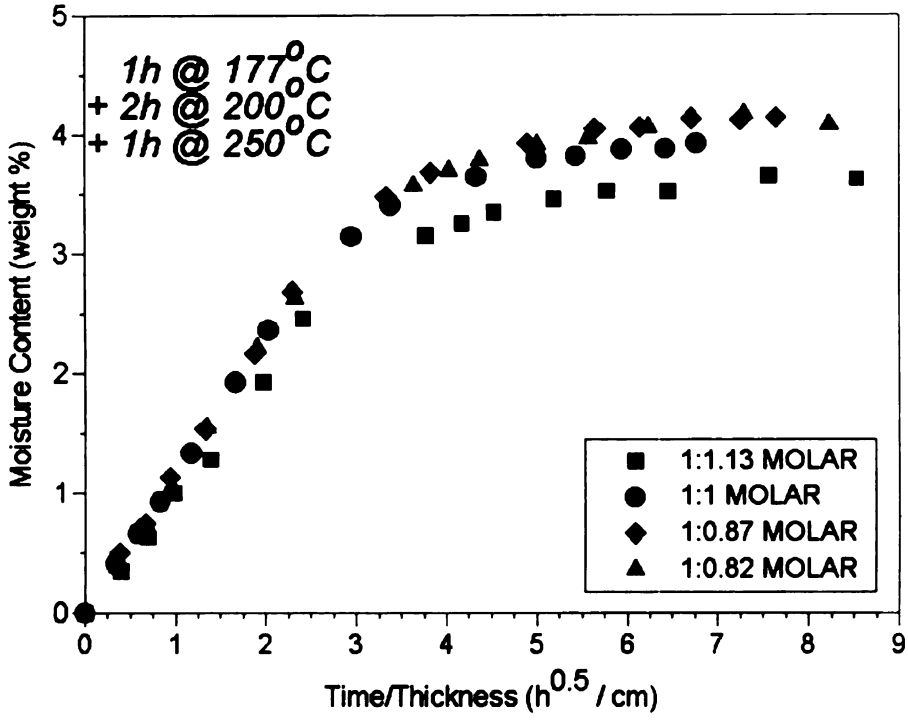

Figure 3.4(c): Moisture absorption curves as a function of cure and BMPM:DABPA ratio for the 'S1' cure cycle.

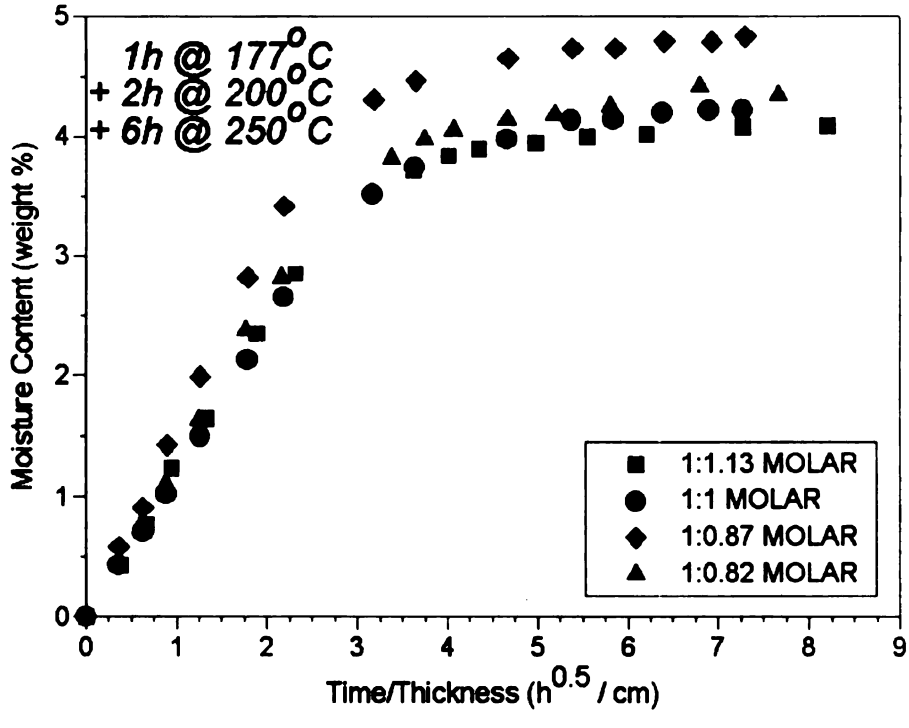

Figure 3.4(d): Moisture absorption curves as a function of cure and BMPM:DABPA ratio for the 'S2' cure cycle.

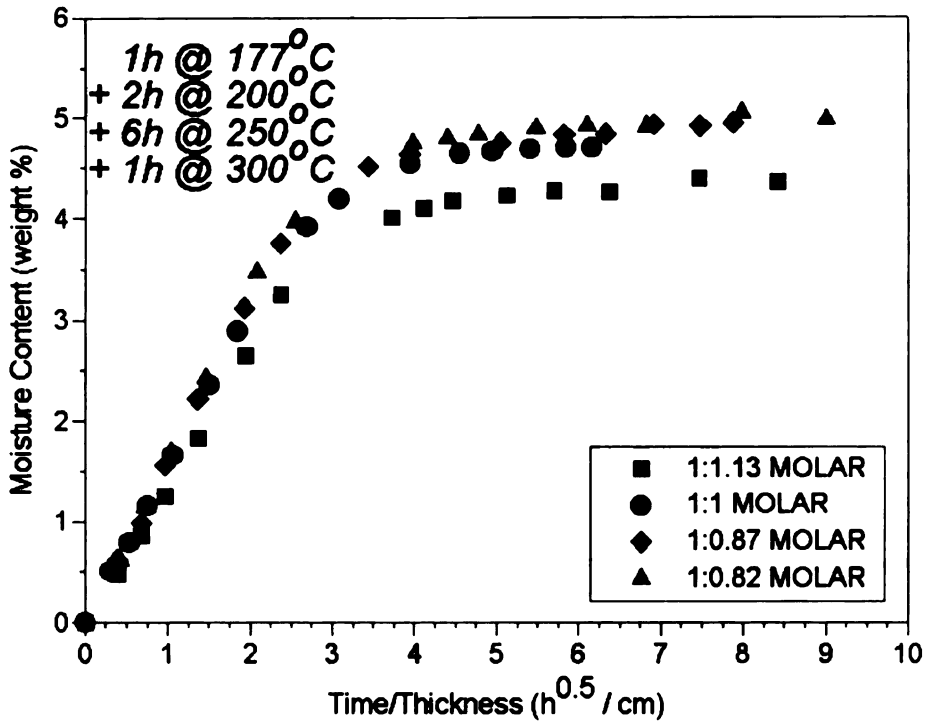

Figure 3.4(e): Moisture absorption curves as a function of cure and BMPM:DABPA ratio for the 'H1' cure cycle.

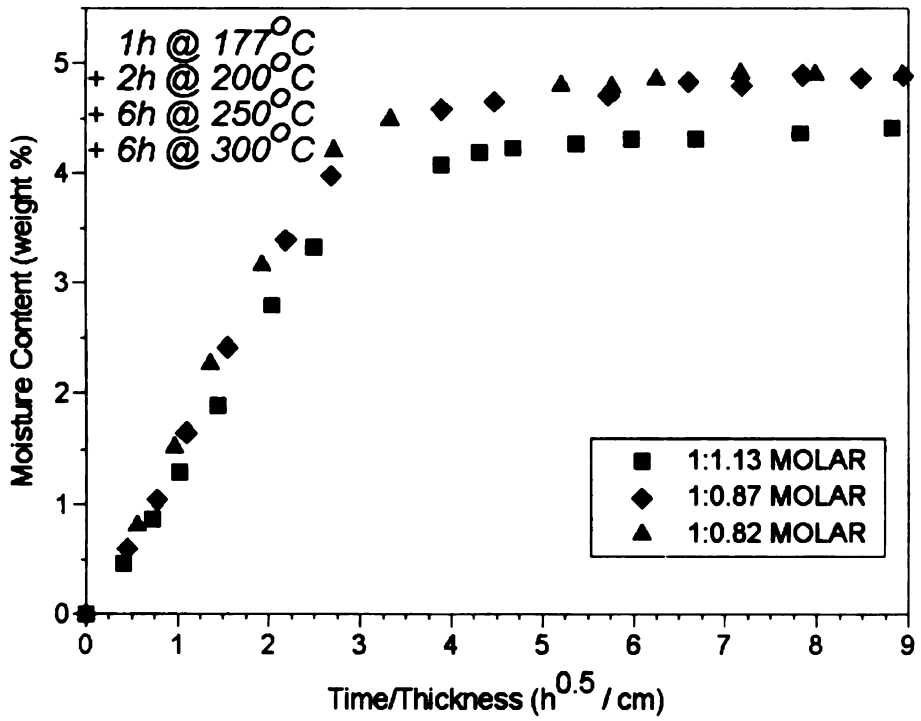

Figure 3.4(f): Moisture absorption curves as a function of cure and BMPM:DABPA ratio for the 'H2' cure cycle.

In order to develop network structure-property interrelationships in terms of the BMI network and the moisture absorption properties, M_∞ and D were plotted as a function of cure conditions (Figures 3.5 and 3.6), T_g, and room temperature density (Figure 3.7), obtained earlier in this investigation. The maximum moisture content increased linearly with T_g with the exception of high cure conditions when the values tended to level off. Room temperature density showed a fairly linear decrease of M_∞, supporting density data that increasing degree of cure results in increased availability of regions for molecular residence in these BMI resin systems.

Similarly, diffusivity increased with increasing cure, leveling-off at higher cure time-temperature conditions, and increased linearly with T_g. Plotted as a function of room temperature density, the diffusivity showed a linear decrease as a result of increased density within a system. Also, D displayed only a slight increase with additional BMPM. Thus, the monomer concentration did not dramatically affect the moisture flux of water molecules into the resin, but the degree of curing did, as would be predicted from previous data [1-10] and that reported above in this investigation, since the time-temperature cure conditions primarily control the network crosslink density.

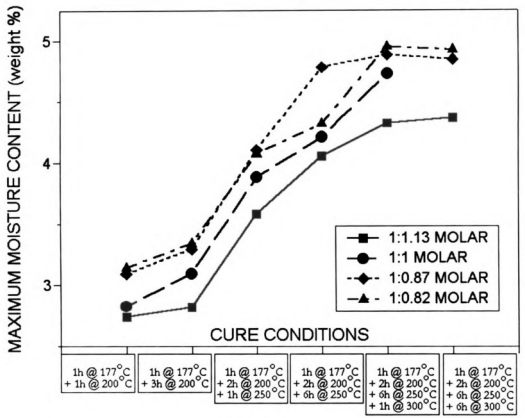

Figure 3.5: Maximum moisture content as a function of cure conditions.

In addition, this data reinforces the previously speculated and present understanding of this BMI network in terms of stiffer segments and increased crosslink density reducing the molecular packing efficiency. Diffusion studies of H_2O and O_2 in crosslinked glasses indicate that permeabilities will exhibit a maximum at the highest crosslink density if the units that form the network inhibit close packing because of steric restrictions [20-24], and Barton [22] observed for a variety of glassy polymers that the most highly crosslinked

polymers have the highest equilibrium moisture content. Certainly the multitude of research from this work is supportive of these findings.

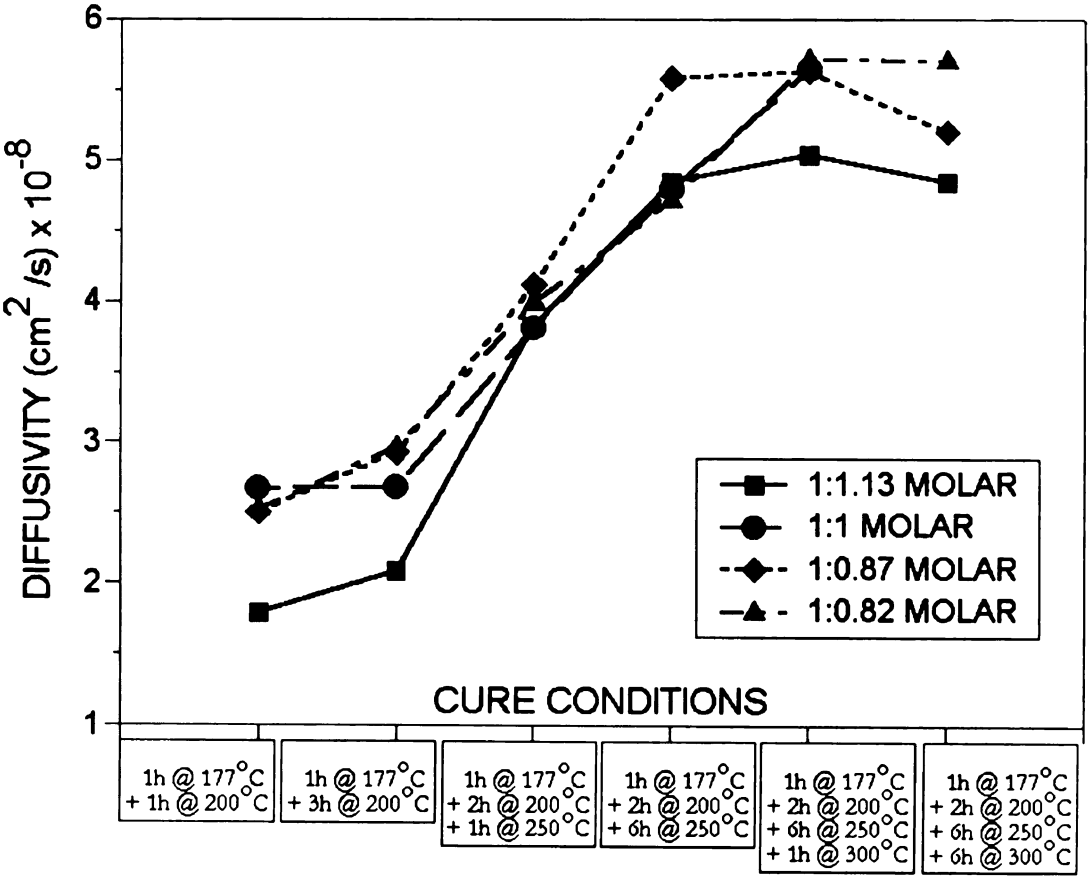

Figure 3.6: Diffusivity plotted as a function of cure conditions for four initial BMPM:DABPA ratios.

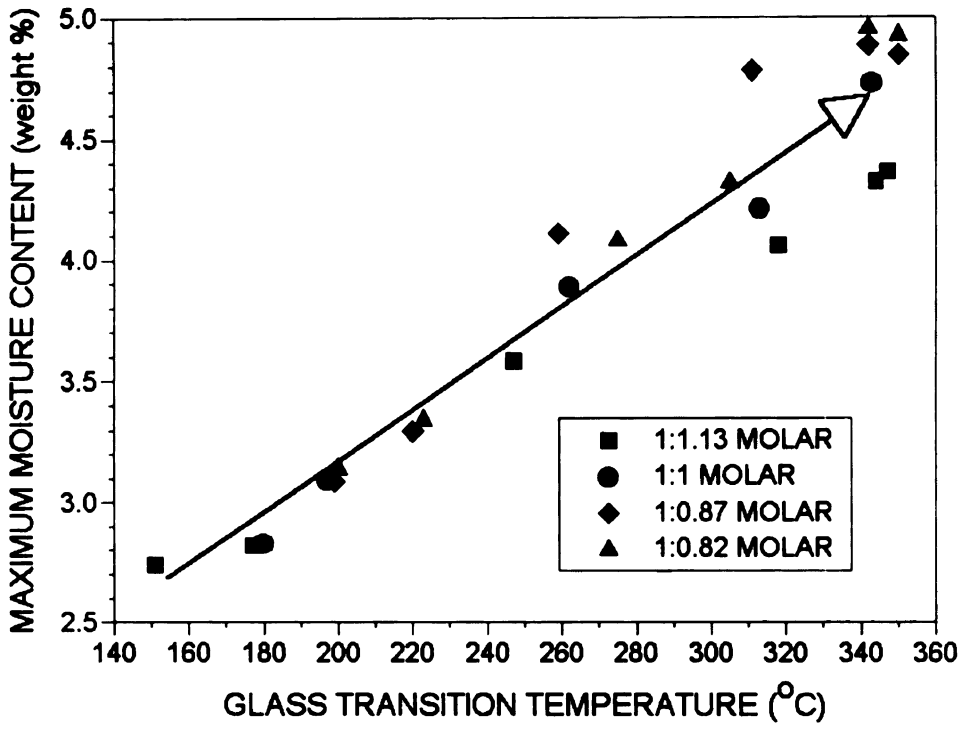

Figure 3.7(a): Equilibrium moisture content (maximum moisture content) plotted as a function of the glass transition temperature for the four BMI resin systems.

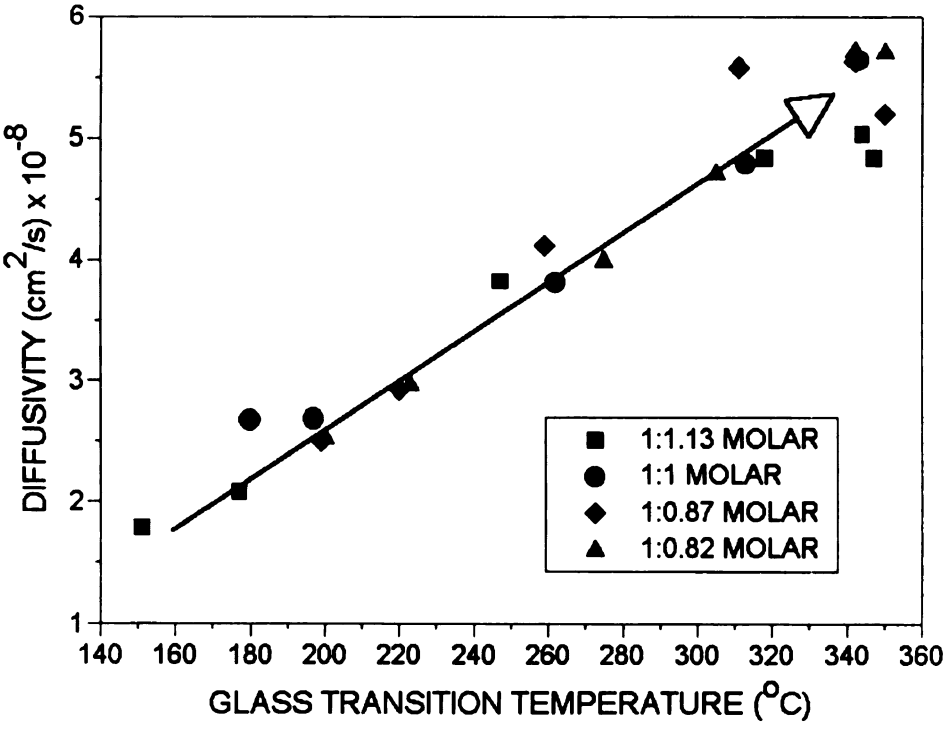

Figure 3.7(b): Diffusivity plotted as a function of the glass transition temperature for the four BMI resin systems.

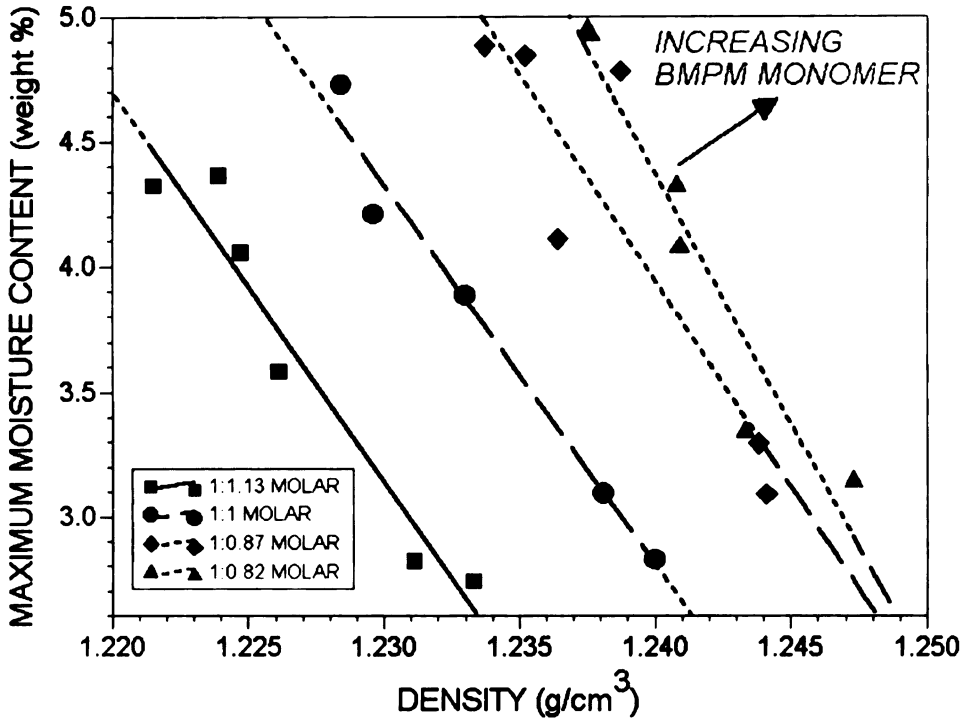

Figure 3.7(c): Equilibrium moisture content (maximum moisture content) plotted as a function of mass density for the four BMI resin systems.

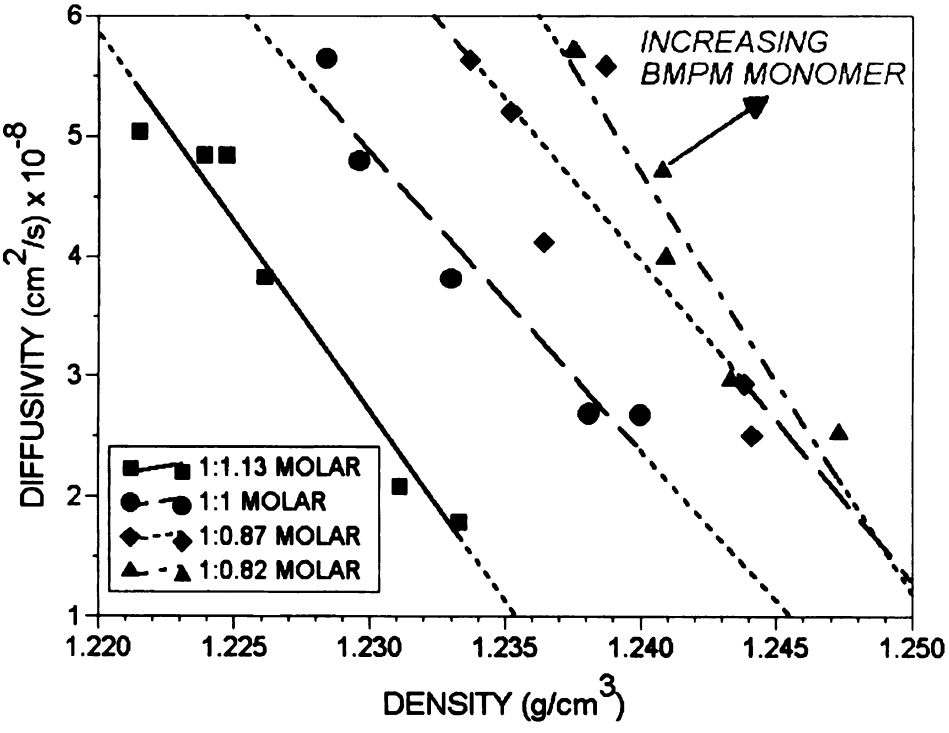

Figure 3.7(d): Diffusivity plotted as a function of the mass density for the four BMI resin systems.

Consistent with T_g and density data above, evidence of etherification and subsequent rearrangement of the ether crosslinks to less flexible segments is again observed for samples cured in the 250 – 300°C temperature range. On average (of four monomer compositions) a ~20% increase in equilibrium moisture content and ~36% increase in diffusivity are observed after all of the C=C double bonds of the 'ene' molecule have been consumed.

Finally, activation energies displayed a variety of values in the range from ~23-44 kJ/mole for monomer composition-cure schedules, but no definite or meaningful trends could be ascertained from the data.

3.4 Conclusions

The major findings of this investigation involve the critical structure-property interrelationships in terms of room temperature density, glass transition temperature, and moisture absorption behavior based on (i) initial BMPM:DABPA monomer composition and (ii) cure time-temperature conditions.

Precisely, higher concentration of the BMPM monomer resulted in (i) higher room temperature density, (ii) higher equilibrium moisture content, (iii) higher diffusivity within a given cure schedule condition, and (iv) was influential on controlling the cure reaction kinetics and overall network structure (via segmental packing restrictions), but did not influence the final T_g.

Increasing cure time and temperature showed the following structure-property relationships: (i) a lower observed room temperature density, displaying a higher crosslinked network structure with more void space, (ii) increased diffusivity, (iii) increased equilibrium moisture content, and (iv) higher T_g values. For the 300°C postcure conditions, the values for M_∞ and D leveled-off for all compositions, which will require a further future understanding of the cure reactions in this temperature regime to thoroughly develop the associated network-moisture diffusant relationship.

After all of the C=C double bonds of the 'ene' molecule have been consumed, a ~0.2% density decrease, a ~100°C increase in T_g, a ~20% increase in equilibrium moisture content, and a ~36% increase in the diffusion coefficient were observed. These property changes are evidence of the significant role played by ether crosslinks and their rearrangement at high temperatures to form less flexible segments.

Further curing appears to be a more influential factor in terms of overall network structure-material property relationships than the initial monomer composition, since the former mechanism is the dominant variable controlling both crosslink density and ether crosslink formation and subsequent rearrangement to stiffer segments.

Chapter 4

Fundamental Investigation of Cure Induced Microcracking in Carbon Fiber / Bismaleimide Cross-Ply Laminates

4.1 Introduction

Microcracking in polymer matrix composites is a topic of considerable interest to researchers in the field of advanced composite materials, and a large amount of work has been published in the areas of prevention, characterization, microcrack-material property relations, modeling, and prediction [1-10, 20, 25-54]. Microcracks can be deleterious to overall composite properties, leading to reduced stiffness and strain to failure, composite delamination, a decrease in compressive strength, reduction of fatigue life, and increased oxidative weight loss during high temperature exposure. Also, composite microcracks may reduce the material's hygrothermal and environmental durability by acting as fast diffusion paths for moisture, oxygen, and/or other chemical species that may have synergistic effects on the fibers and/or resin matrix [20, 32-34].

Through extensive research over the past ten years, Morgan and Shin *et al.* [1-10, 20, 25-27] have identified the critical network structure-property interrelationships and most likely environmental induced damage mechanisms for these carbon fiber/BMI composites. After standard fabrication and cure

conditions these cross-ply laminates are microcracked, which has been attributed primarily to (i) resin shrinkage stresses that develop during cure and subsequent postcure, (ii) coefficient of thermal expansion (CTE) mismatch between the fibers and matrix, (iii) interlaminar residual stresses due to the CTE mismatch between individual laminae, and (iv) hydroxyl dehydration induced ether crosslink formation and subsequent rearrangement to stiffer crosslinks, which leads to glass transition temperature increases and matrix embrittlement [20, 25-27]. The fiber/matrix interfacial integrity is extremely poor in these composites (interfacial shear strength values are less than 10% of the values for standard carbon fiber/epoxy systems [20]) and, as a result, primary thermal and mechanical failure modes are interfacial.

Previously, attempts have been made [4-10, 20, 25-27] to prevent cure-induced microcracking in $[0°/90°]_S$ laminates using a variety of techniques, including both cure cycle modifications and fiber/matrix interfacial integrity improvements, but both attempts were unsuccessful. For the latter case, the improvement approaches fall into four primary categories: (i) modification of fiber surface energy, (ii) increase in fiber surface functional group concentration, (iii) resin toughening, and (iv) fiber sizing additions. Significant improvements in the mechanically weak interface were not observed due to a variety of factors. The wide temperature range between the composite fabrication conditions and lower extremes of service environment use

temperatures produces high fiber/matrix interfacial stresses. Also, since full cure of carbon fiber/BMI composites requires a postcure temperature of 300°C, carbon fiber surface functional groups, such as carboxyl and hydroxyl groups, are lost from the fiber surface (these groups are lost above 270°C). Similarly, the necessary long time-high temperature fabrication conditions and service environment temperature exposures are too extreme for many thermoplastic sizings [20, 26].

In addition to the interfacial deficiency problem, efforts to alter the cure time-temperature conditions have been unsuccessful because the exact onset time-temperature thresholds in terms of thermal loading have not been established. Finite element models and microcrack predictions based on the stress free temperature (temperature at which no residual thermal stresses exist) have been shown to be inadequate for this composite system, possibly due to the measurement of the stress free temperature and thermal residual stresses in the cross-ply laminates [27, 45-54]. Also, models based on classical laminate theory do not yield good results primarily because (i) microcracks redistribute the ply stress and (ii) the theory breaks down at the free edge of the composite [38-44]. For the carbon fiber/BMI system used in the present study, the stress free temperature is significantly lower than the cure temperature (20 – 80°C, depending on thermal history), which greatly influences the magnitude of the stress calculated by any model based upon thermal expansion mismatch [26].

During manufacturing, gelation and vitrification lead to abrupt, orders of magnitude changes in the viscoelastic and strength properties that make mechanical phenomena accompanying the curing of composites difficult to simulate [56]. As a result, residual stress calculations of composite defect formation, crack propagation, and defect-type characterization during cure are often difficult to correlate to experimental data [57-59].

Alternative approaches have been developed to predict microcracking based on thermodynamics [38], linear elastic fracture mechanics [40], and analytical variational models [42-44], which have been shown to be accurate in specific applications. All models that predict mechanical properties of microcracked samples also have simplified assumptions as to the physical nature, growth mechanisms, dimensions, and distributions of the microcracks within the laminate [33-37]. The sum of these factors, in addition to the complexity of the BMI network structure-property relationships makes microcrack prevention by cure cycle design difficult.

Scola *et al.* [28] examined the effects of cure cycle on microcracking in [0°/90°] graphite/BMI cross-ply laminates composed of a variety of commercial bismaleimide resins. Their results for the composite systems studied demonstrated that (i) alteration of the cure cycle was not effective in preventing microcracking in most balanced configurations, (ii) cracking could be prevented, irrespective of the cure or postcure cycle in composites

consisting of a multiple of $[0^\circ_4/90^\circ_2/0^\circ_4]$ in a completely balanced configuration, indicating that internal stresses in this configuration were sufficiently low to prevent matrix fracture, (iii) microcracking occurred after the cool down from the 177°C cure temperature, and (iv) increasing the postcure temperature by 100°C did not influence the microcracking tendency. Finite element models used in their investigation were inadequate for predicting the observed microcracking tendencies.

In a similar investigation, Wilson *et al.* [29] studied the effects of cure temperature on microcracking in graphite/PMR-15 composites. They demonstrated that a low temperature cure (280 – 290°C as opposed to the standard 330°C) could reduce the tendency to microcrack in these composites when subsequently exposed to thermal cycling at higher temperatures. The improved resistance to microcracking of PMR-15 laminates cured at low temperatures was attributed to a combination of two primary factors. First, residual thermal stresses were reduced in the laminate by about 15% when curing at 280°C versus 330°C. Second, the resin modulus was most likely reduced by the low temperature cure, which was attributed to the type and quantity of crosslinks. At low temperatures the polymer network became modified by the preferential formation of relatively flexible crosslinks of reduced density, leading to a reduction in resin modulus.

Korotkov, Chekanov, and Rozenberg *et al.* [56-58] examined the effects of cure schedule on resin shrinkage induced defect formation for epoxy resins constrained in a tubular glass vessel. They divided defect types into a variety of temperature regimes for epoxy cure, and subsequently developed a cure cycle that could alleviate shrinkage induced defects. At cure temperatures above the glass transition temperature of a fully cured polymer, the gelation transition occurs and cohesive shrinkage defects (including debonding) were shown to arise in the system. When the cure temperature was less than T_g for the fully cured composite, shrinkage defects developed in the rubbery state (physically similar to the defects that formed above T_g), but at the instant of vitrification abrupt increases in strength terminated defect development. In the intermediate temperature regime, the wide transition of vitrification occurs immediately after gelation, which is the cause of solidification. Under these temperatures, the increase in strength imposed by vitrification was shown to significantly hinder defect formation in the rubbery state.

As a result of these physical and thermodynamic processes, the investigators were able to prevent defects by inducing solidification at the lowest possible temperature within the intermediate temperature regime. After solidification, the temperature could be subsequently increased to a higher value to achieve full cure of the composite. In the intermediate temperature

region, the liquid-rubber transition does not actually cause shrinkage defect development, and hence defects could be prevented by cure cycle modification.

The primary aims of this study are to examine and characterize microcracking in carbon fiber/BMI composite laminates on a fundamental level, and to offer an additional initial cure step that alleviates microcracking upon subsequent completion of standard postcure time-temperature cycles. The composite system utilized is composed of the commercially available BMI resin system based on 4,4'-bismaleimidodiphenylmethane (BMPM) / 0,0'-diallyl bisphenol A (DABPA) (Matrimid® 5292, Ciba-Geigy), and IM7 graphite fibers (Hexcel) in a $[0^{o}/90^{o}]_{S}$ configuration. Sequentially, this investigation will proceed with the following goals:

(i) characterize microcracking in terms of onset time-temperature thresholds, microcrack growth and formation mechanisms, and physical characteristics as a function of cure conditions;

(ii) investigate the modified cure cycle that prevents microcracking (extends the microcracking threshold), and characterize microcracking for this cure cycle;

(iii) determine the effects of initial BMPM:DABPA monomer stoichiometry on microcracking tendencies, mechanisms, and physical characteristics;

(iv) evaluate the thermal and dynamic mechanical properties of the composites cured under standard fabrication procedures and compare these properties to the laminates fabricated with the extended cure cycle;

(v) incorporate the above to explain the most likely network structural modifications induced by the extended cure step and summarize the critical parameters that control microcracking on all dimensional levels.

4.2 Experimental Techniques

4.2.1 Composite Fabrication

The composite constituents used in this investigation were BMPM/DABPA bismaleimide resins and 12k IM7-G graphite fibers. The DABPA viscous liquid monomer of appropriate amount was poured into a magnetic stir-activated beaker and heated on a hot plate at 130°C until the viscosity decreased, then the corresponding amount of BMPM crystalline powder was added slowly and mixed until a homogeneous solution was achieved. Stoichiometries of 1:1 and 1:0.87 molar BMPM:DABPA were prepared. Next, the respective prepolymer solution was degassed under vacuum at 130°C for 15 minutes, then poured into the heated resin pot of the prepregging unit. IM7 fibers were run through a 250°C burn-off in air prior to being drawn through the resin pot and onto a release paper-coated rotating drum. Prepregs with good tack and drape properties were obtained, and cut into 32 cm^2 square prepreg laminae which were stacked in a $[0°/90°]_S$ configuration using the hand lay-up technique.

These prepreg laminates were cured in a miniclave at 177°C for either 1.5 h or 8 h, and removed upon cooling to room temperature. This procedure resulted in three different initial composites with a fiber volume fraction, V_f = 0.66 ± 0.015. All heating and cooling rates were 5°C/min during fabrication. Postcure of the laminates was performed in a specially designed oven with a small sample chamber such that the sample temperature could be controlled to within ±1°C. Postcure cycles used in previous studies [1-10, 20, 25] were also used here for consistency, and are defined by Figure 4.1.

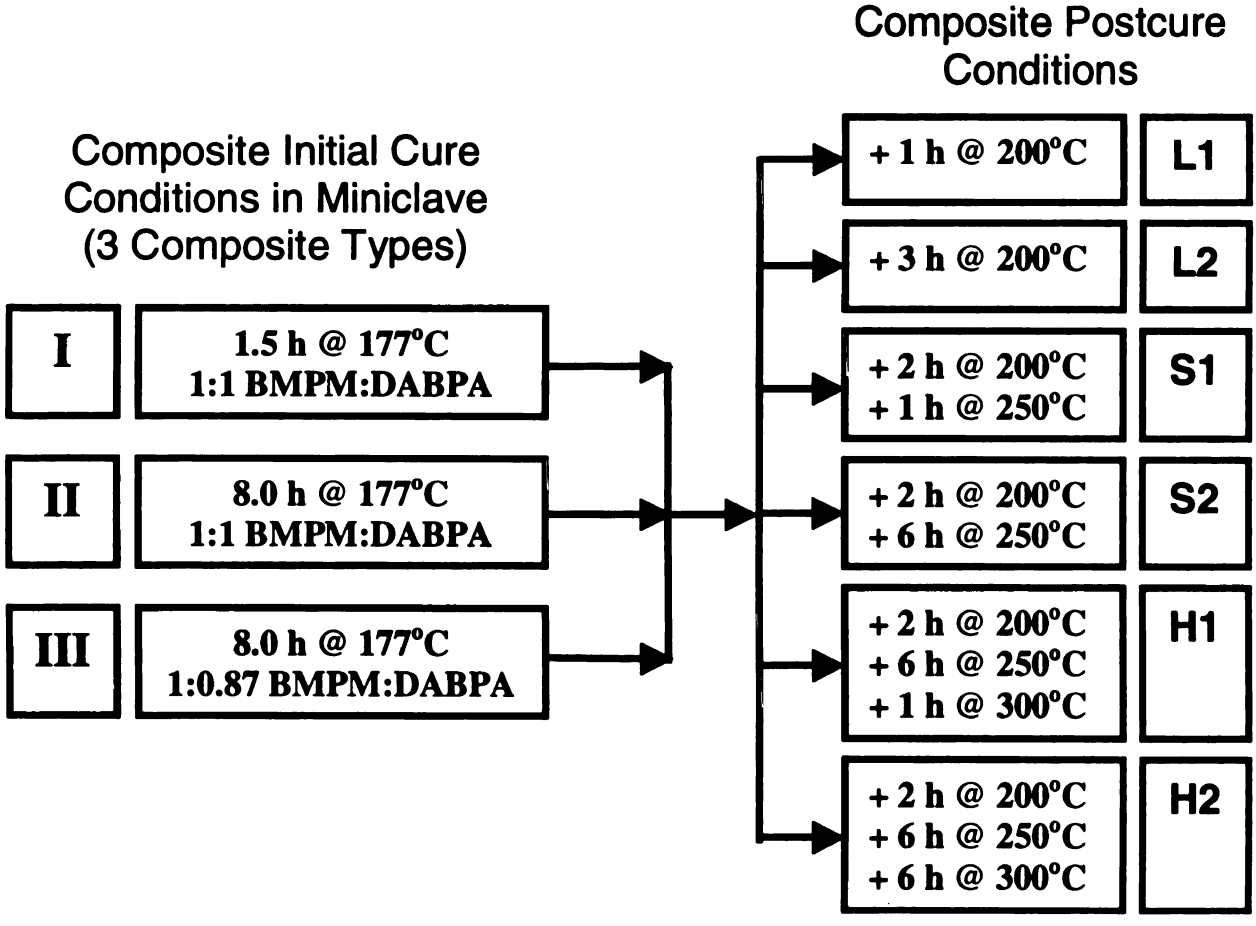

Figure 4.1: Laminate cure and postcure cycles.

Where necessary, laminates were cut to desired dimensions using a slow speed diamond blade saw and running water, then the desired edges polished using standard metallographic techniques with increasing grit to 0.05 μm powder. Laminate thickness was approximately 0.6 mm.

4.2.2 Microcrack Density Characterization

Specimens of 25 cm x 15 cm were examined along the longer edge, which revealed the longitudinal direction of the middle layers (90°). Optical microscopy and a Philips ElectroScan 2020® Environmental Scanning Electron Microscope (ESEM) were used to observe any transverse microcracks. No microcracks were observed in any of the initially cured composites (177°C), and microcracked samples (after postcure) were characterized in terms of the number of transverse microcracks per unit length.

4.2.3 Microcrack Width Characterization

Microcrack widths were measured using the software available on the ESEM. The average of at least ten crack widths constituted a single data point for a particular sample type.

4.2.4 In-Situ Postcuring Experiment

Samples were cut and polished to 3 mm x 5 mm and attached to a small metallic plate using carbon paint. The sample and holder were then placed into a heating unit located inside the chamber of the ESEM. Using an accelerating voltage of 20 kV and high temperature electron detector, the 90° free edge of the composite was observed while performing the postcure *in-situ*. As determined by the microcrack density and width results above, the following postcure experiments were performed under observation in the ESEM: (i) after 1.5 h initial cure at 177°C the 1:1 molar laminate was cured for 3 h at 200°C, and (ii) after an 8 h initial cure at 177°C plus sequential curing at 200°C for 2 h, 250°C for 6 h, and 300°C for 1 h, both the 1:1 molar and 1:0.87 molar were postcured for an additional 5 h at 300°C. All heating and cooling rates were 5°C/min.

4.2.5 Dynamic Mechanical Analysis

DMA specimen dimensions were 35 mm x 8 mm, and tested using a TA Instruments 2980® Dynamic Mechanical Analyzer in single cantilever beam bending mode, 1 Hz frequency, and heating rate of 3°C/min to 400°C. Samples were cut and tested in two different loading directions: one loading direction indicative of the fiber/interphase dominated properties ($[0°/90°]_S$)

and the other $([90°/0°]_S)$ with more influence from the matrix (Figure 4.2). Dynamic mechanical spectra yielded the storage modulus, E', and damping factor, tan δ, as a function of temperature. T_g was taken as the maximum in the tan δ peak.

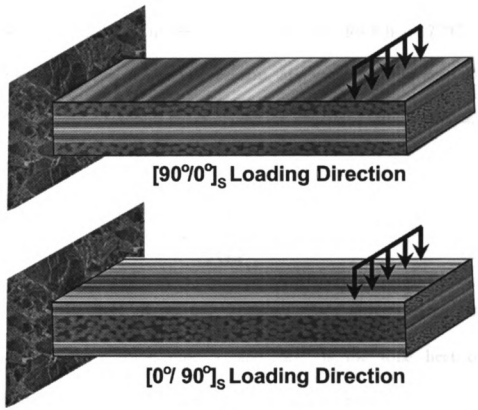

Figure 4.2: Loading conditions used in the DMA experiment.

4.2.6 Differential Scanning Calorimetry

Neat resin samples were prepared as discussed above (prior to insertion into the resin pot), and poured into DSC aluminum pans in ~20 mg amounts. The

following experiments were conducted using a TA Instruments® 2920 Modulated DSC and a nitrogen purge of 50 mL/min: (i) an isothermal scan for 18 h at 177°C of the 1:1 molar resin, (ii) dynamic scans at 10°C/min on control (uncured) 1:1 and 1:0.87 molar samples, (iii) dynamic scan at 10°C/min on 1:1 molar resin initially cured for 1.5 h at 177°C, and (iv) dynamic scans at 10°C/min on 1:1 and 1:0.87 molar resins initially cured for 8 h at 177°C. From the aforementioned data, the heat of reaction, ΔH, was calculated from the area under the exothermic reaction peaks. Also, the degree of conversion, α_t^T, was determined from the equation

$$\alpha_t^T = \frac{\Delta H_t^T}{\Delta H_\infty} \tag{4.1}$$

where ΔH_t^T is the heat of reaction obtained from an isothermal scan at temperature, T, after some time, t, and ΔH_∞ is the total heat of the polymerization reaction determined from dynamic experiments.

4.3 Results and Discussion

4.3.1 Microcrack Prevention

In previous studies [26, 27] using finite element modeling of microcracking thresholds and experimental observations via electron microscopy, it was reported that extended postcures at temperatures greater than 200°C offered

only a moderate reduction in the stress free temperature and were insufficient in microcrack alleviation. Therefore, in this investigation, the initial recommended cure step at 177°C was extended from 1.5 h to 8 h, and compared the composite laminates as a function of postcure and BMPM:DABPA initial monomer ratio (Figure 4.1).

Upon observation by optical microscopy and ESEM analysis of the polished free edge of cured and postcured composite laminates, it was determined that (i) none of the samples were microcracked after the initial cure at 177°C, (ii) transverse microcracks were first observed in the standard fabrication samples (type-I) after the 'L2' postcure cycle of 3 h at 200°C and all other postcures except 'L1', and (iii) microcracks were not observed in extended initial cured laminates (type-II and type-III) until a postcure of 2 h at 200°C + 6 h at 250°C + 6 h at 300°C; the 'H2' postcure. Note the use of the term 'microcrack' in this investigation refers to cracks that span the thickness of the 90° layer. Microcrack precursors are small microcracks from which complete transverse microcracks initiate. The remaining experiments of this investigation were performed to determine the mechanisms associated with the observed microcrack alleviation.

4.3.2 Microcrack Physical Characteristics

Average transverse microcrack width and density plots as a function of cure conditions are shown in Figures 4.3 and 4.4, respectively. As expected, microcrack width increased with extent of cure time-temperature conditions for standard type-I laminates, reaching an average width of 2.86 $\pm$ 0.73 μm after the highest postcure treatment. This progression is shown in Figure 4.5, and note that the failure mode is primarily interfacial. The only microcracked samples in the case of the type-II and type-III laminates had average widths also within this standard deviation.

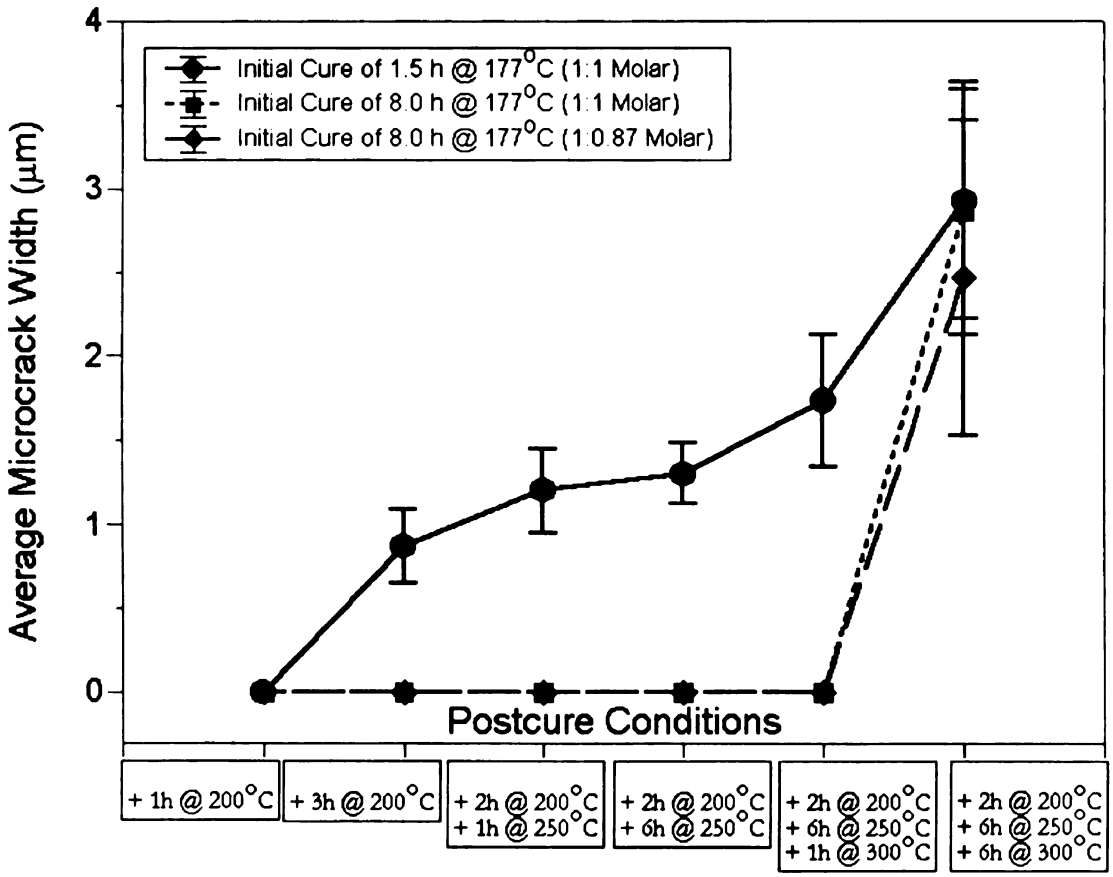

Figure 4.3: Microcrack width as a function of postcure conditions.

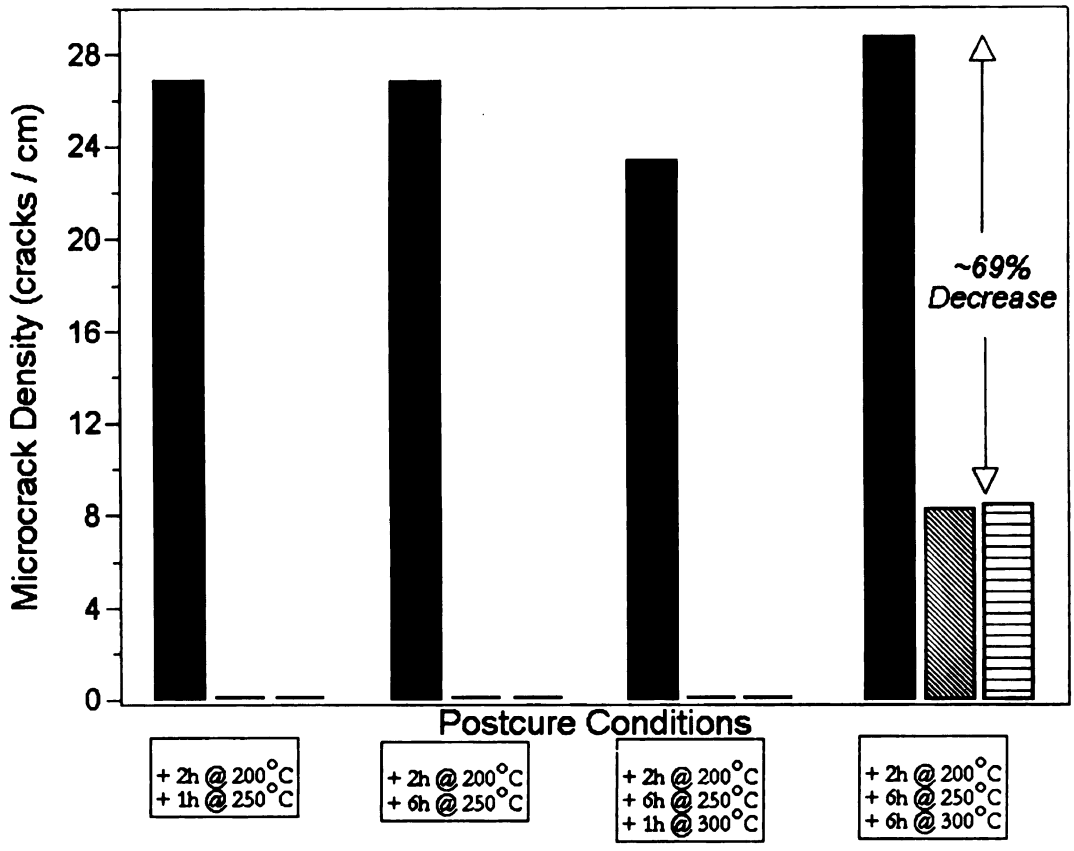

Figure 4.4: Transverse microcrack density as a function of cure conditions. Initial cure cycle of: ■ 1.5 h at 177°C (1:1 molar), ■ 8.0 h at 177°C (1:1 molar), and ■ 8.0 h at 177°C (1:0.87 molar).

The most significant physical attribute observed was the dramatic 69% decrease in microcrack density between the initial 1.5 h and 8 h cured laminates after the same 'H2' postcure (Figure 4.4). That is, even though the type-II and type-III samples finally microcrack after the 'H2' postcure, their microcrack density was still significantly lower than the standard type-I initial cured laminates. This microcracking tendency was independent of chemical composition for the two stoichiometries examined, and suggests a reduction in residual stress resulting from the extended initial cure time.

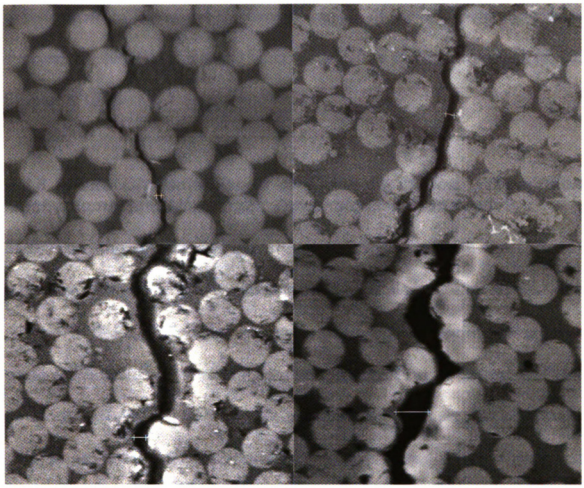

Figure 4.5: Increase in crack width with increased postcure for 'L2', 'S2', 'H1', and 'H2' postcure cycles from left to right, respectively.

Also, since microcracks do not form until 6 h at 300°C in the type-II laminates, the resin shrinkage stresses responsible for these particular microcracking tendencies can be attributed to the ether crosslink formation and subsequent rearrangement during this long postcure cycle. This is supported by the observation of an increase in resin modulus and density, and a decrease

in resin strain to failure and mechanical strength of the 'H2' postcure cycle as opposed to the 'H1' cycle, the latter of which is not microcracked [8, 25, Chapter 3, Chapter 5].

4.3.3 In-situ Characterization of Crack Formation, Propagation Mechanisms, and Microcrack Threshold Determination

Many experimental methods have been used to characterize the onset of transverse microcracking in symmetric cross-ply laminates. For example, the research of Talreja [37] stated that mechanically induced microcracking onset could be identified by a knee in the load-displacement curve. Pagano *et al.* [44] however, demonstrated from acoustic measurements that microcracking occurs prior to the knee in the load-displacement curve. Using DMA, Vallely and Gillham [32] observed hysteresis between cooling and subsequent heating in a glass/epoxy composite and attributed it to microcracking. They defined the onset of microcracking as the temperature at which the modulus began to decrease with further cooling.

Here, in this *in-situ* approach, microcracking onset is characterized as the time-temperature condition at which microcracks are physically observed to form on the free edge of the laminate. As observed in the ESEM, the general process of microcracking during cure in the $[0°/90°]_S$ laminates occurs as follows:

(i) initial processing defects are present in the form of (Figure 4.6),
(a) voids,
(b) small microcrack precursors,
(c) debonded fiber/matrix interfaces,
(d) broken fibers;

(ii) during the isothermal hold step, (b) and (c) may form as a function of time, but are stable and do not propagate as the temperature remains constant;

(iii) microcracks may form in 'defective' regions during the isothermal step, such as in regions that are extremely resin rich, but these cracking modes are rare and do not result in full span microcracks (Figure 4.7);

(iv) upon cooling from the cure temperature, transverse interfacial microcracks form rapidly from small microcrack precursors, debonded interfaces, or some other defect not visible from the free surface, to span the entire 90° layers until becoming constrained by the 0° plies (Figures 4.8 and 4.9);

(v) although the failure propagation mode is predominantly interfacial and through the matrix between fibers, cracks may also propagate through as a result of the high stress intensity at the crack tip (Figure 4.10);

(vi) microcracks formed in (iv) generally grow in width during further cool down to room temperature (Figure 4.8).

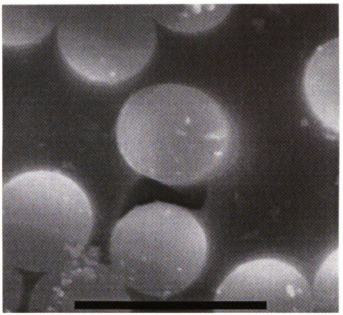

Figure 4.6(a): Micrograph showing an initial processing defect of a fiber/matrix debond. Marker bar is 10μm.

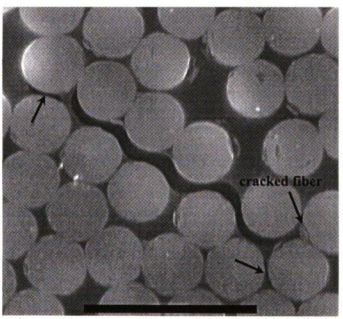

Figure 4.6(b): Initial processing defect of a cracked fiber, fiber/matrix debond, and large microcrack precursor. Marker bar is 15μm.

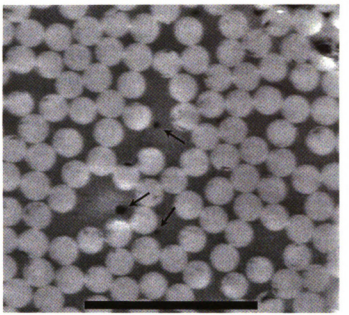

Figure 4.6(c): Initial processing defects of resin matrix voids. Marker bar is 30μm. The overall void content for the composites was less than 0.1%.

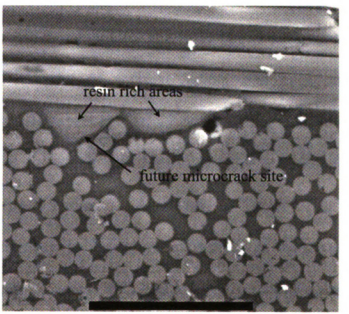

Figure 4.7(a): ESEM micrograph (114°C) of microcrack formation during the isothermal hold in a defective resin rich region. Marker bar is 45μm.

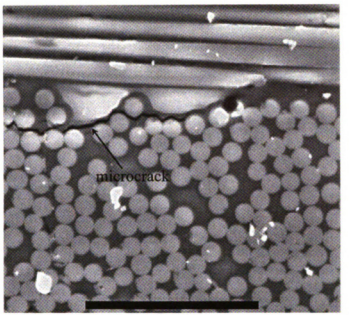

Figure 4.7(b): ESEM micrograph (200°C) of microcrack formation during the isothermal hold in a defective resin rich region. Marker bar is 45μm.

Microcracking thresholds for the three composites studied are shown in Table 4.1 as a function of thermal history and cool down. The off-stoichiometric type-III specimen could not be characterized precisely due to experimental difficulties, but the thresholds were qualitatively similar to the stoichiometric type-II laminate. As shown in Table 4.1, a thermal load of ~250°C was necessary to cause microcracking in laminate type-II, but a temperature change of only ~50°C lead to microcracking in the type-I laminate, again evidence of a decrease in residual stress resulting from the extended initial cure time at 177°C.

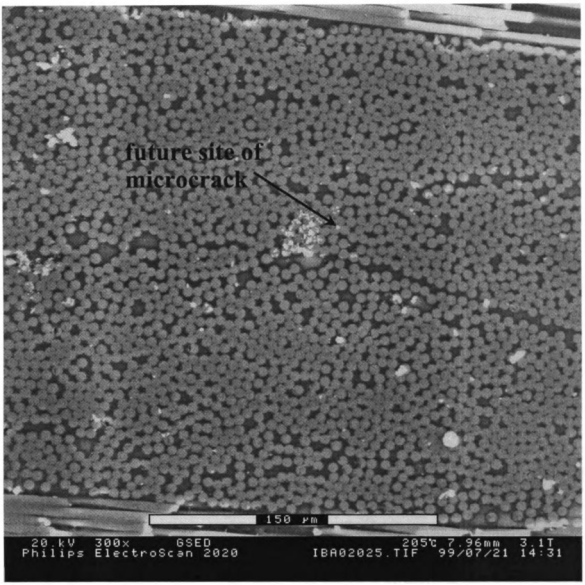

Figure 4.8(a): Progression of microcrack formation and propagation from the cure temperature during cooling at 200°C. Above, future site of microcrack is highlighted with an arrow. Marker bar is 150µm and the micrograph was taken at the cure temperature of 200°C. Note that no initial defect is visible from the composite surface.

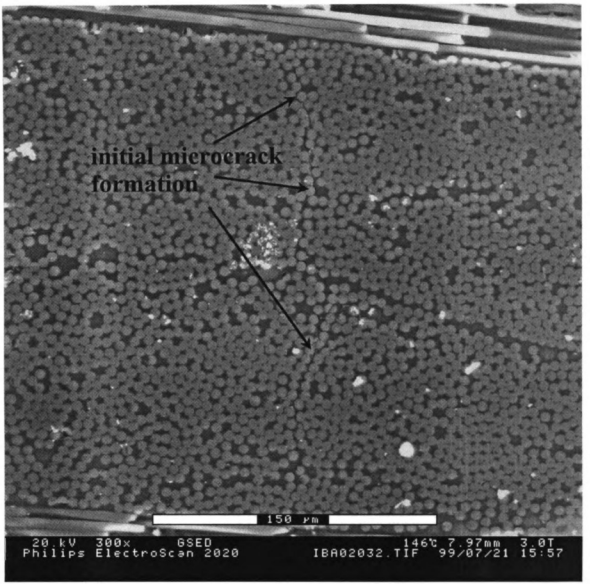

Figure 4.8(b): Initial formation of the microcrack during cooling from the cure temperature. Crack first appears at 146°C during cooling from 200°C at 5°C/min for this type-I laminate specimen. Marker bar is 150µm.

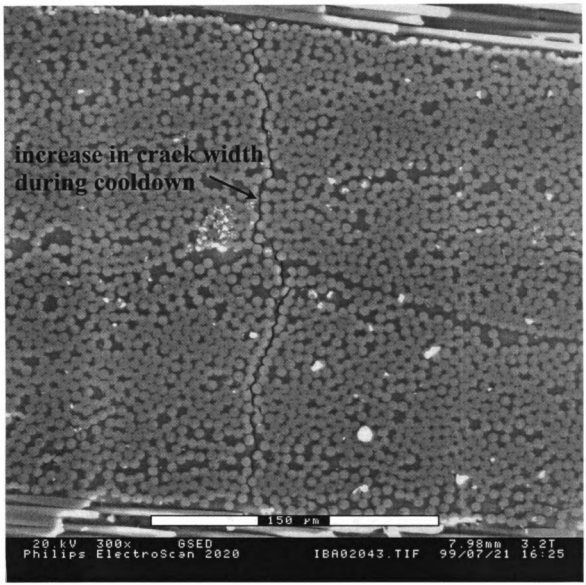

Figure 4.8(c): Increase in crack width during cooling to room temperature. Micrograph conditions are the same as in (b) and (c), except that the above picture was taken at 23°C. Marker bar is 150µm.

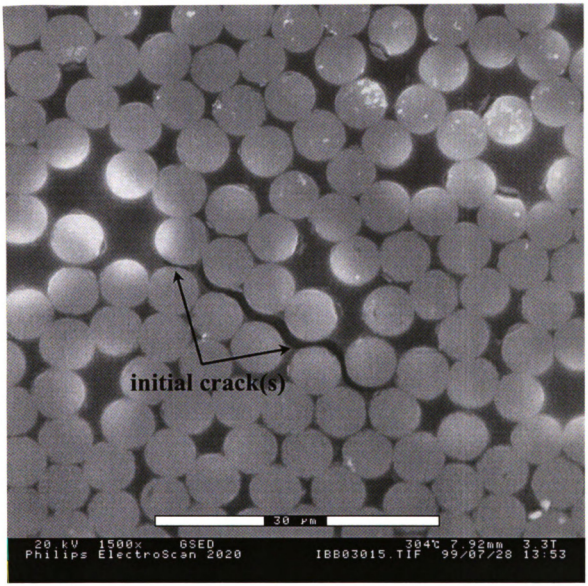

Figure 4.9(a): Initial microcrack precursor present at 300°C for specimen type-II, with marker bar of 30µm. Unlike Figure 4.8, the defect here is visible from the surface and the microcrack will initiate here and propagate during the cooling cycle, as shown in Figure 4.9(b).

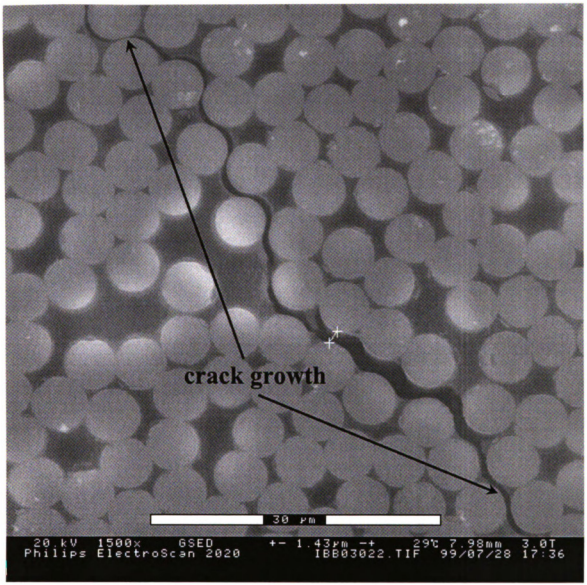

Figure 4.9(b): Crack growth from the microcrack precursor, which first initiates at 50°C for the type-II laminate. Marker bar is 30µm.

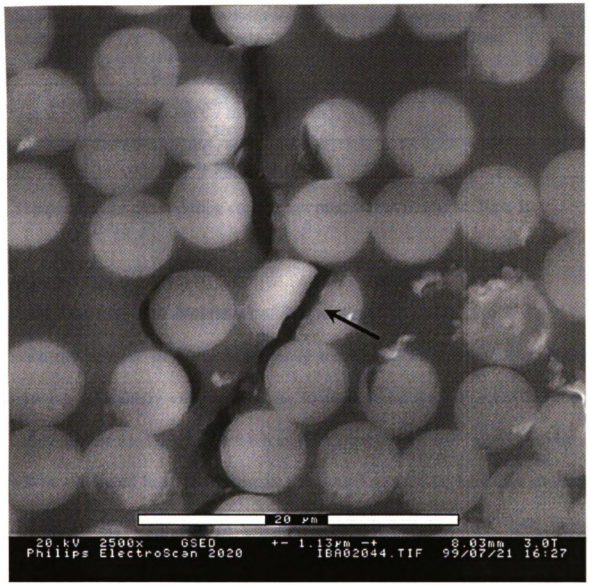

Figure 4.10: Propagation of a microcrack through an IM7 fiber as a result of the high stress intensity at the crack tip. Marker bar is 20µm.

Table 4.1: Microcracking threshold results from *in-situ* experiment.

Laminate	Postcure Cycle (Heating/Cooling Rates = 5°C/min)	Microcracking Onset Temperature	ΔT
Type-I	200°C / 3h ('L2')	146°C	**54°C**
Type-II	200°C / 2h + 250°C / 6h + 300°C / 6h ('H2')	50°C	**250°C**
Type-III*	200°C / 2h + 250°C / 6h + 300°C / 6h ('H2')	--	--

*Temperature of onset during cooling not precise, but similar to Type-II

4.3.4 Thermal and Mechanical Properties

Since the primary objective of dynamic mechanical analysis and differential scanning calorimetry experiments was to understand the difference between curing initially for 1.5 h versus 8.0 h at 177°C, only type-I and type-II laminates will be compared here. Experiments performed on type-III laminates showed similar trends to the type-II composites, which was expected since these specimens differed only in initial monomer stoichiometry.

4.3.4.1 Dynamic Mechanical Analysis

DMA has traditionally been utilized to understand molecular motion in polymers [59-62], but in recent years has developed into a tool for characterizing composite materials. An extensive amount of research has been published regarding damping predictions and modeling, damage quantification,

cure kinetics, and interphase/interface analysis [63-93]. Although the quantity of variables involved in this investigation (microcracks, fiber/matrix debonds, cure schedule variation, loading directions, composite lay-up, temperature effects, and initial monomer stoichiometry) make quantitative predictions and model development unreasonable, one can reflect upon the literature data to make conclusions of the results from a variety of perspectives.

In order to properly interpret the data, it is necessary to understand the loading conditions used in the experiment and the general distribution of stresses in the laminate. Due to the geometry of the laminate, there is no bending-stretching or shear coupling during deformation for either loading condition, and the equation for the effective flexural modulus can be written as follows [95]:

$$E_f = \frac{8}{N^3} \sum_{j=1}^{N/2} (E_x)_j \left(3j^2 - 3j + 1\right) \tag{4.2}$$

Note that this equation applies only to the specific loading conditions, laminate lay-up, and geometry. Above, j is the ply number measured in the z-direction from the ply midplane, E_x is the modulus in the x-direction (along the beam) and E_f is the effective modulus (see Appendix).

Similarly, the normal and shear stresses were determined from the equations below, with the variables defined as follows: M is the bending

moment, N is the total number of plies, I is the beam moment of inertia, V is the transverse shear forced defined by V = dM/dx, b and h are the beam cross-sectional dimensions, and j and k are laminate counters [95].

$$(\sigma_x)_j = \frac{Mz}{I_{yy}}\left[\frac{(E_x)_j}{E_f}\right] \tag{4.3}$$

$$(\tau_{xz})_k = \frac{3V}{2bh}\left[\frac{S}{E_f}\right] \tag{4.4}$$

$$S = \frac{4}{N^2}\sum_{j=k}^{N/2}(E_x)_j(2j-1) \tag{4.5}$$

Figure 4.11 displays the normal (σ_x) and interlaminar (τ_{xz}) stress distributions as calculated from classical laminate theory for static loading of a single cantilever beam, where h is the distance from the center of the laminate and Z and K are constants. Elastic-viscoelastic correspondence shows the same qualitative distributions of the complex stresses in the laminate [88]. Note that in both the $[0°/90°]_s$ and $[90°/0°]_s$ loading directions, the largest normal stresses are observed in the 0° plies, but the magnitude of the stress is roughly 90% smaller for the latter. Also, the properties measured in the $[0°/90°]_s$ loading direction are more indicative of the fiber/matrix interface than the $[90°/0°]_s$ direction. It has been shown [79] that flexural deformation of laminates provides a more sensitive detection of interfacial properties than other modes, such as tension

or compression, which is the reason for choosing the single cantilever beam deformation mode.

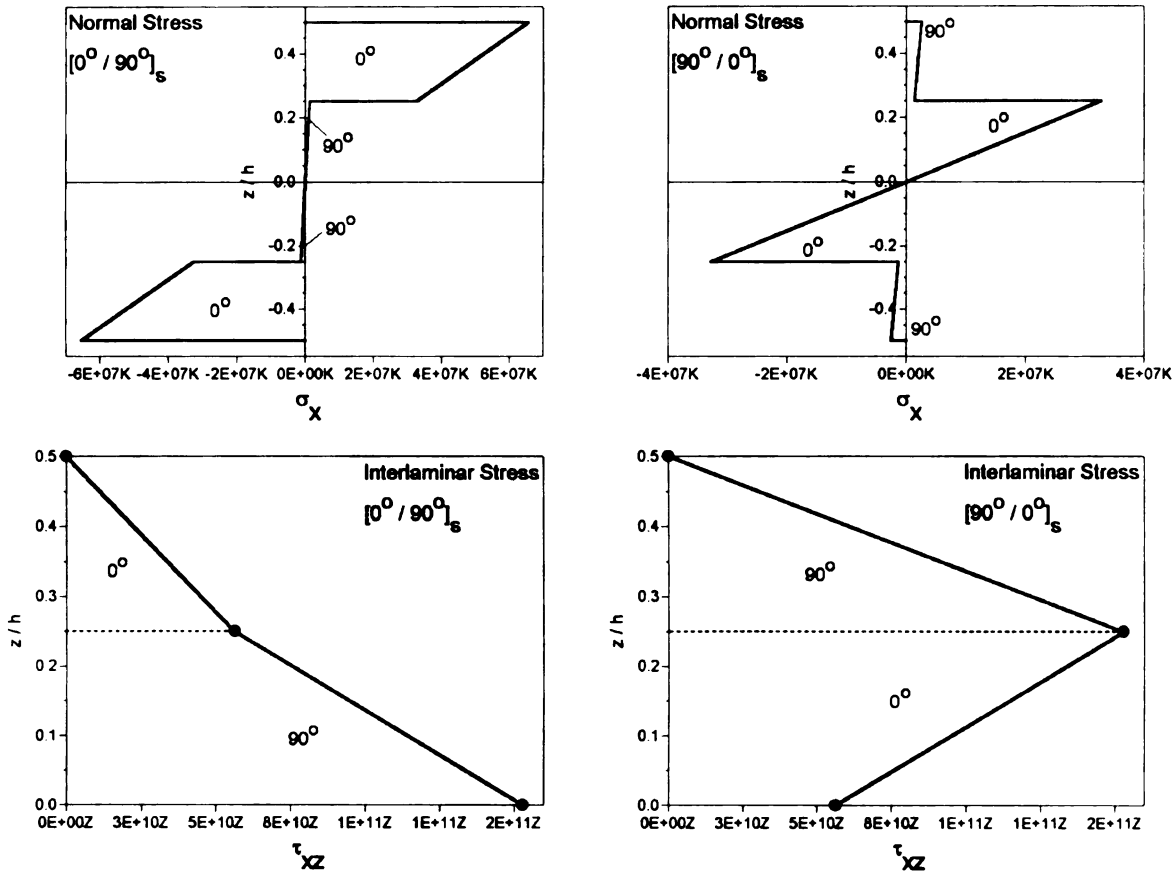

Figure 4.11: Stress distributions for both DMA laminate loading conditions as calculated from Equations 4.3 and 4.4. See Appendix for derivation.

Representative DMA spectra are shown in Figure 4.12 for two specimen types loaded under the $[0°/90°]_s$ condition. Experiments conducted under the $[90°/0°]_s$ loading direction show similar results. The first spectrum, Figure 4.12(a), is for a 1.5 h at 177°C initial cure and a subsequent 'L1' postcure. Since this specimen has not been cured completely, a knee appears in both the tan δ and E' curves at temperatures greater than T_g (designated α).

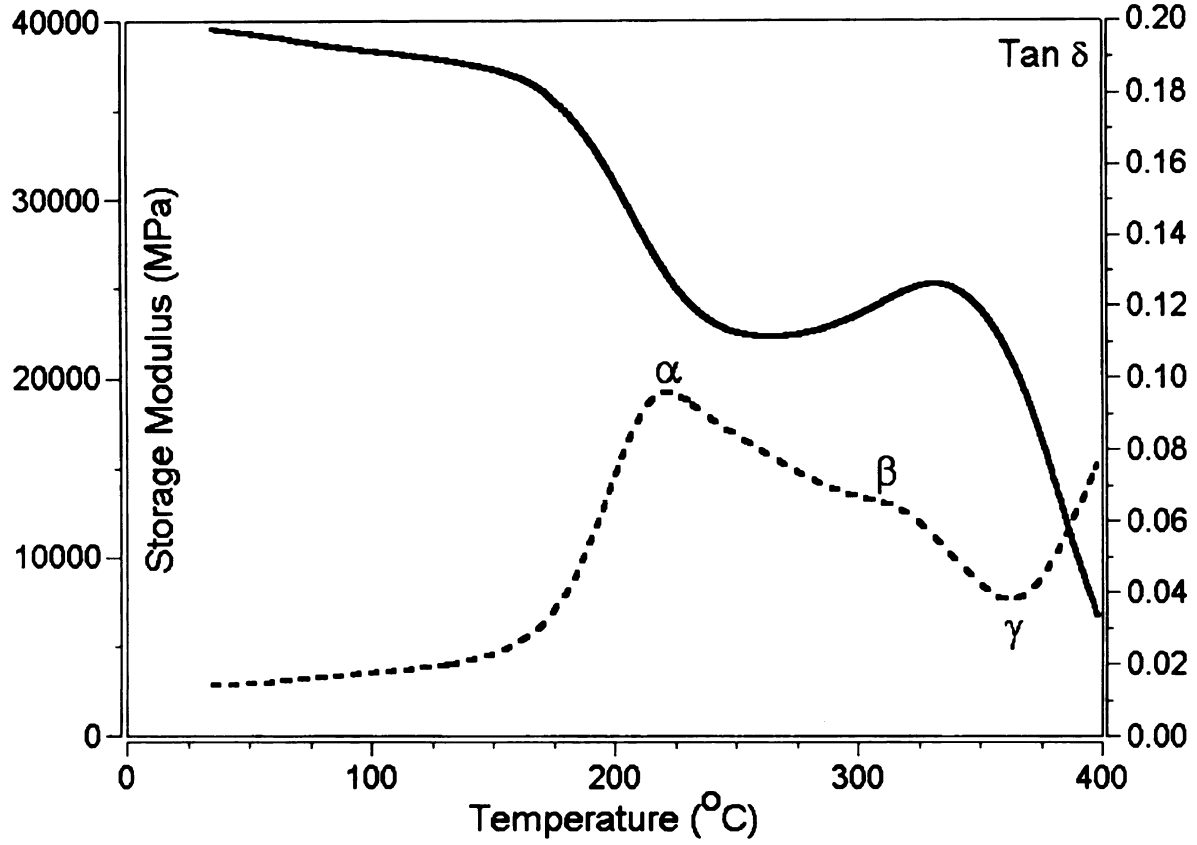

Figure 4.12(a): DMA spectrum for the 1.5 h at 177°C followed by the 'L1' postcure cycle. Heating rate was 3°C/min, and peak designations are α is T_g, β results from incomplete cure from the 'L2' postcure, and γ is associated with degradation.

Further crosslinking during heating results in an increase in the modulus above T_g. The second peak, β, most likely results from additional cure leading to a second, 'experimental induced T_g'. Previous investigators have attributed the second (β) peak above T_g to an interphase glass transition temperature or matrix heterogeneities [73, 75-79]. In a detailed study by Thomason [74], however, this second peak was shown to be artificial, resulting from a complex interaction of the instrument, the sample thermal conductivity, the heating rate,

and the sample modulus above T_g, and the peak manifested from additional cure of the composite. For the present investigation, the latter explanation is also supported by Figure 4.12(b) for a completely cured laminate. In this case, the β peak does not appear, nor does an increasing modulus above T_g; only the glass transition temperature (α) and the degradation onset peak (γ) are observed in the spectrum.

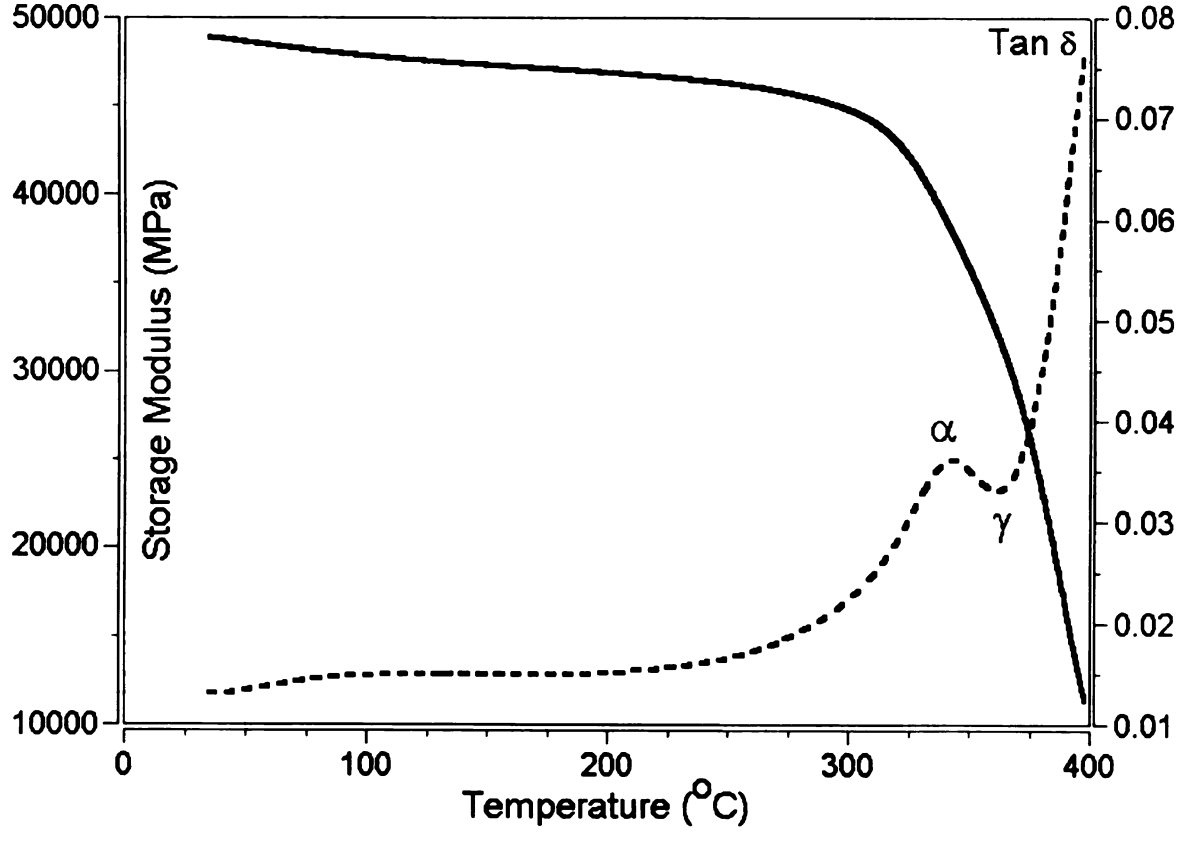

Figure 4.12(b): DMA spectrum for the 1.5 h at 177°C followed by the 'H2' postcure cycle. Heating rate was 3°C/min, and peak designations are the same as in Figure 4.12(a). Note the disappearance of the β peak.

Interesting results were observed for the glass transition temperature, shown in Figure 4.13. Irrespective of postcure conditions, laminates initially cured for 1.5 h at 177°C displayed a higher value for T_g than those initially cured for 8 h at 177°C, with the difference between the two laminate types decreasing with increasing postcure. Thus, the specimen cured for longer time showed a lower glass transition temperature.

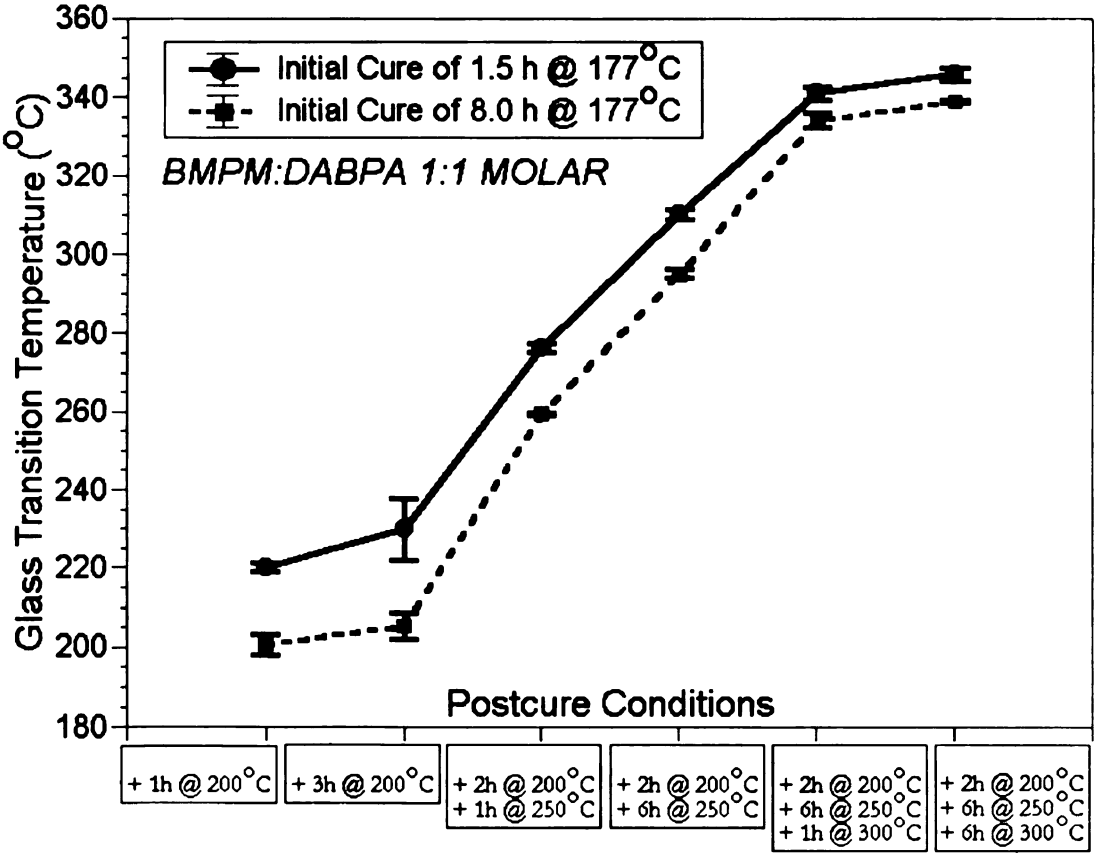

Figure 4.13: Glass transition temperature as a function of postcure conditions for laminates type-I and type-II. Note the higher value measured for T_g for type-I laminates, even though the total cure time of type-II laminates was longer.

From an initial, molecular perspective, one might suggest that the network structure has been significantly modified by the extended cure time at 177°C. Previous work, however, has shown that the final network structure is independent of the initial cure sequence [3]. For example, in Chapter 3, a constant T_g of ~350°C was observed for a variety of initial cure sequences and BMPM/DABPA monomer stoichiometries ranging from 1:0.82 to 1:1.13 molar.

Recall that in the 177°C temperature regime, the primary reaction is the 'ene' reaction, with BMPM homopolymerization and crosslinking of the allyl and maleimide double bonds occurring at moderate rates. The relative rates of the allyl and maleimide double C=C bonds can be complex and depend on the cure history sequence. Under certain cure schedules, one observes nearly the same reaction rates for allyl and maleimide crosslink formation, but under other conditions Morgan *et al.* [3] have reported up to a 10% difference in the reaction rates. Stiffer and/or bulkier segments can lead to a higher observed glass transition temperature as defined by molecular motion in the DMA experiment [59, 60, 62]. Both Wilson *et al.* [29] and Hay *et al.* [94] have attributed a decrease in composite microcrack tendency for PMR-15 composites to cure schedule alteration induced network structural modifications.

Based on the current understanding of the complex cure reactions however, a dramatic modification of the network structure for this system is unlikely for the cure sequences examined. The contribution from a small chemical structural variation is insignificant to be responsible for either the observed decrease in T_g or the observed microcracking response.

In addition to the glass transition temperature, significant differences were observed in the composite stiffness (as measured by E') between laminate types I and II. These results are shown in Figure 4.14, measured at 23°C and plotted as a function of postcure conditions for the $[0°/90°]_s$ loading direction. Recall that this loading direction is, in part, an indication of the interface/interphase properties of the laminate. The ~38% higher storage modulus observed for the type-II laminates most likely results from a contribution of factors, and indicates an improved interface in the type-II laminates. Stiffness reduction is manifested from microcracks in the transverse plies, but this is not the only mechanism involved. Recall that 'H2' postcured specimens of both sample types are microcracked, but the large difference in modulus is still observed. The only other possible variables are the cure cycle modification, an improved interface, or an improved resin modulus, which are interrelated through a reduction in residual stress.

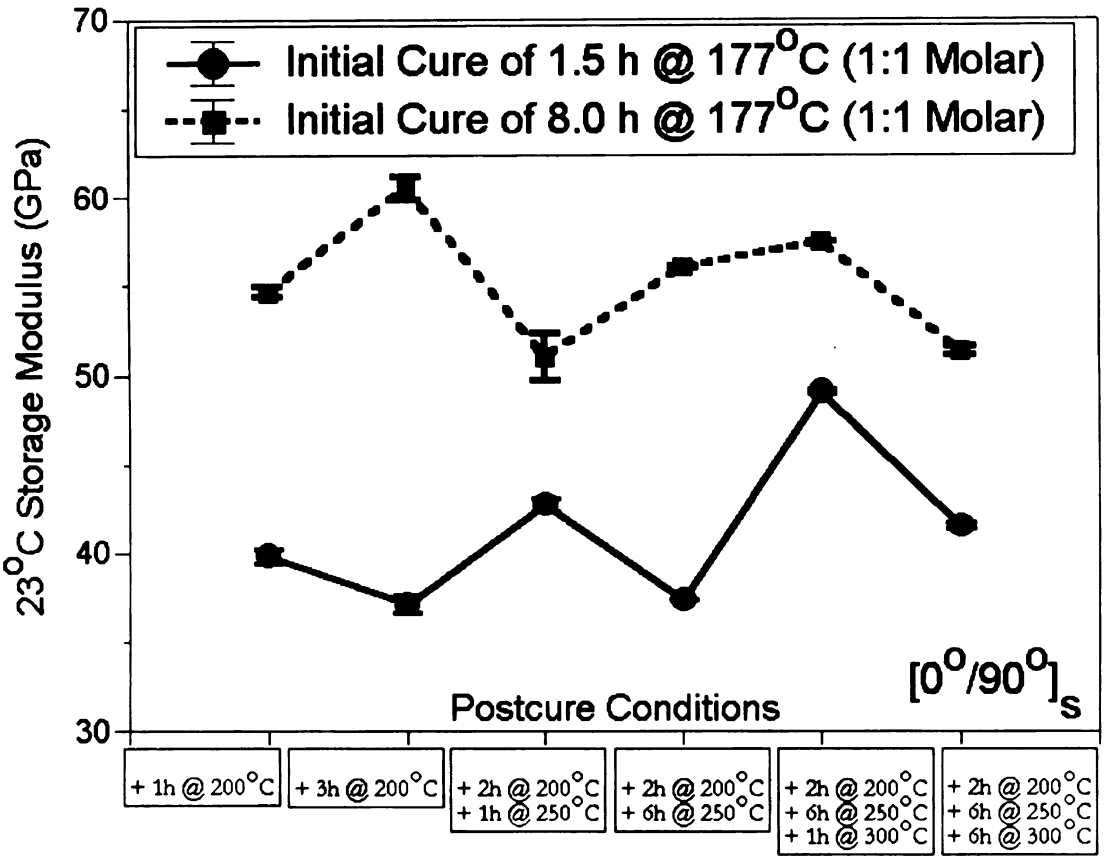

Figure 4.14: Storage modulus as a function of postcure conditions for the $[0°/90°]_S$ loading condition at 23°C.

An improved resin modulus is not likely based on the current understanding of these BMI network structure-property relationships and the damping data discussed below. Damping, primarily due to shear deformation, has been shown to increase when the mismatch between the fiber and matrix modulus is increased [60]. Also, a lower resin modulus would be more likely in explaining the reduction in residual stress observed from the microcracking tendencies.

The final point of interest concerning the DMA results is the composite damping factor, tan δ. Many investigators have attempted to correlate tan δ of

polymer matrix composites with delamination [65], fiber/matrix interfacial Coulomb friction [66], the interphase and adhesion [73, 74, 77-79], interfacial microcracking [75, 80], transverse tensile strength [76], and degradation [93], although there is still some disagreement as to the proper interpretation of the results (see 'Discussion' of Reference 89). For the case of a variety of unidirectional composites, it has been shown that the interfacial shear strength is inversely proportional to tan δ measured at the glass transition temperature [78-80, 89]. For this study, this value is plotted for both loading directions in Figure 4.15.

In both cases, the non-microcracked type-II laminates show a higher value for the damping factor, which may appear to be in disagreement with the aforementioned studies. However, since these samples are cross-ply laminates, damping contributions can not be modeled as simply as they can for the unidirectional case and require complex evaluation and interpretation to quantify [63, 64, 66, 67, 81-83, 87].

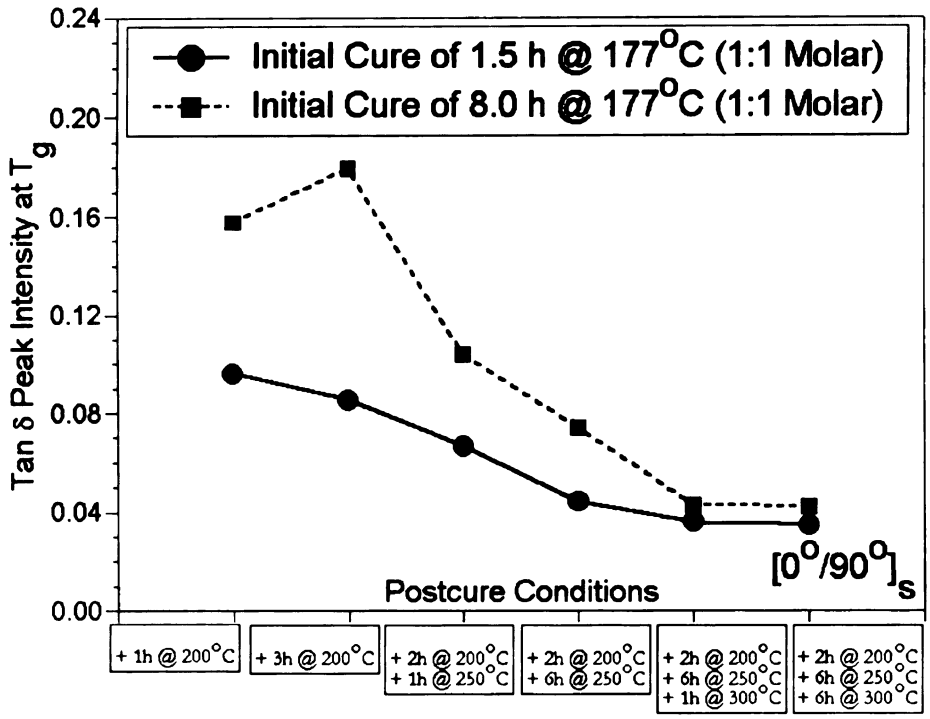

Figure 4.15(a): Damping peak intensity at the glass transition temperature for the $[0°/90°]_S$ loading direction.

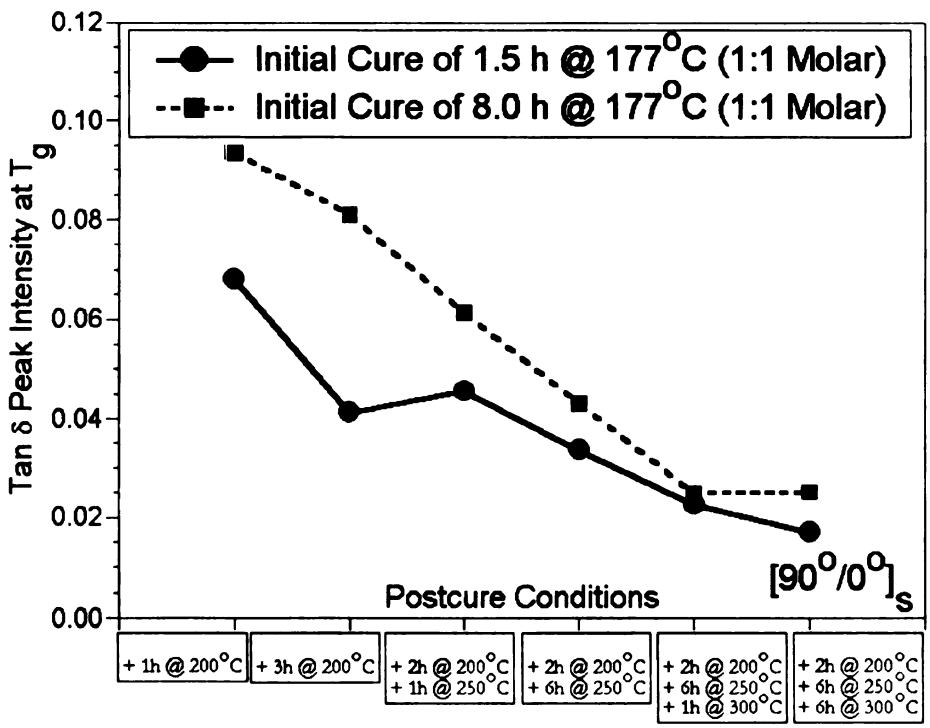

Figure 4.15(b): Damping peak intensity at the glass transition temperature for the $[90°/0°]_S$ loading direction.

Additionally, one may expect excess energy dissipation due to the presence of microcracks, but the results here indicate the reverse behavior. This can be understood by considering the entire mechanisms involved in energy dissipation in a polymer matrix composite. These can arise from (i) cracks or delamination, (ii) Coulomb friction at the fiber/matrix interface, (iii) viscoelastic molecular motion in the matrix and fiber constituents, (iv) fiber-polymer chain molecular motions, especially in high stress regions, and (v) a variety of other possible mechanisms. Because the type-II laminates are not microcracked, they will have more viscoelastic damping in both interfacial regions and in the matrix compared to type-I laminates, since the latter contain microcracks which do not allow for viscoelastic flow. In a previous study, Morgan *et al.* [9] showed that microcracks in these IM7/BMI cross-ply laminates open and close during cyclic deformation via a hinge mechanism. Therefore, the energy dissipation associated with matrix and interfacial flow at T_g must be higher than that of the microcracks minus the energy dissipated from the lost viscoelastic flow. This can be realized by a simple qualitative equation, where the aforementioned components constitute the subscripts and tan δ is the value measured during a dynamic mechanical experiment.

$$\tan\delta = \tan\delta_{MATRIX} + \tan\delta_{INTERFACE} + \tan\delta_{MICROCRACK} + \tan\delta_{OTHER} \quad (4.6)$$

In other words, for a fixed value of $\tan\delta_{OTHER}$, the decrease in $\tan\delta_{MATRIX} + \tan\delta_{INTERFACE}$ resulting from the presence of microcracks in type-I laminates must be larger than $\tan\delta_{MICROCRACK}$, which may in part to explain the apparent anomaly observed in Figure 4.15.

4.3.4.2 Differential Scanning Calorimetry Results

The DSC results provide further insight to the mechanisms associated with microcracking in these composites. Dynamic DSC scans are shown in Figure 4.16, where ξ represents the main reaction peak and ψ is the diffusion-controlled portion of the reaction. Note the decrease in the main reaction peak as a function of initial cure (prior to the dynamic scan); after 8 h the ξ peak has completely been consumed and thus no detectable exothermic reaction appears in the main reaction regime. Figure 4.17 displays the degree of conversion as a function of time, and demonstrates that the degree of cure is 23% larger for 8 h at 177°C versus 1.5 h. In Figure 4.18, the reaction peaks ξ and ψ are quantified.

Interestingly, the above data indicates, at least from an engineering perspective, that the 8 h cured BMI resin (type-II) has both a higher initial T_g and higher degree of cure. Recall, however, the discussion regarding the composite T_g values determined from DMA: after a given postcure, the

measured T_g relationship is reversed. Although the previous discussion and reasoning regarding the reaction kinetics may be valid, one must also consider the reaction enthalpy values determined here.

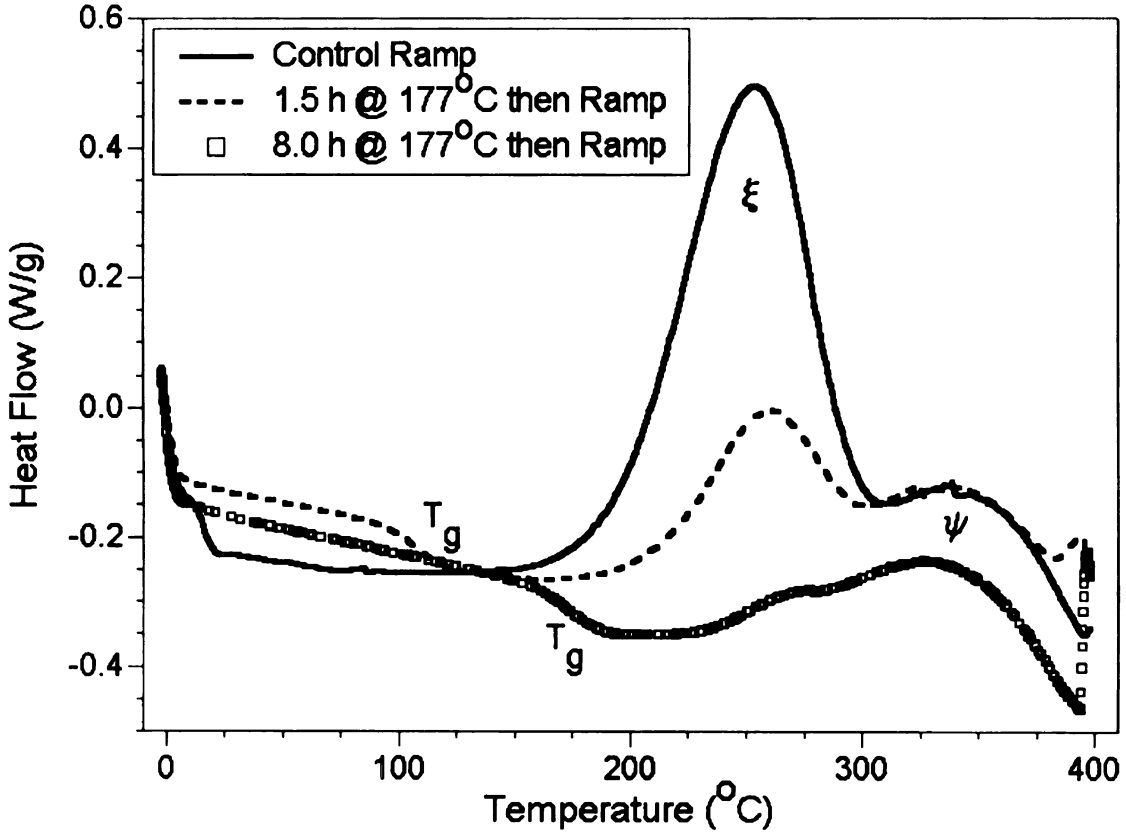

Figure 4.16: Dynamic DSC scan at 10°C/min, where ξ is the main crosslinking reaction peak and ψ is the diffusion controlled portion of the reaction.

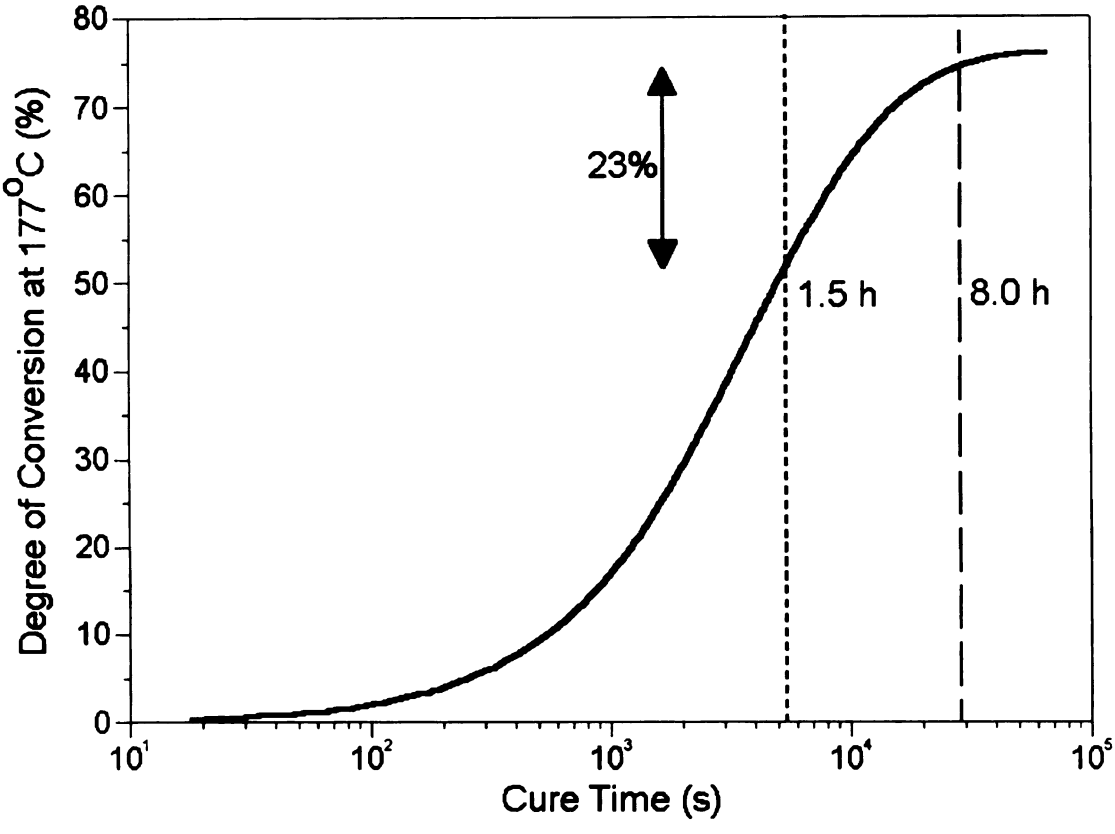

Figure 4.17: Degree of conversion as a function of time at 177°C for 1:1 molar BMPM:DABPA monomer ratio as calculated from isothermal and dynamic DSC data and Equation 4.1.

Specifically, consider Figure 4.18, and note the larger value for $\Delta H(\xi)$ at 1.5 h versus 8 h (type-I compared to type-II, respectively). During a DMA temperature scan, the intrinsic reaction heat evolved during the experiment could raise the local temperature of the sample, thereby accelerating the heating rate. If the temperature increase were sufficient, this could lead to a higher heating rate and higher measured value of T_g. Since samples already cured for 8 h (type-II) show a negligible ξ reaction peak, this heating-rate phenomena would only be significant for type-I material, and therefore may offer another

possible contribution to the observed composite glass transition temperature behavior.

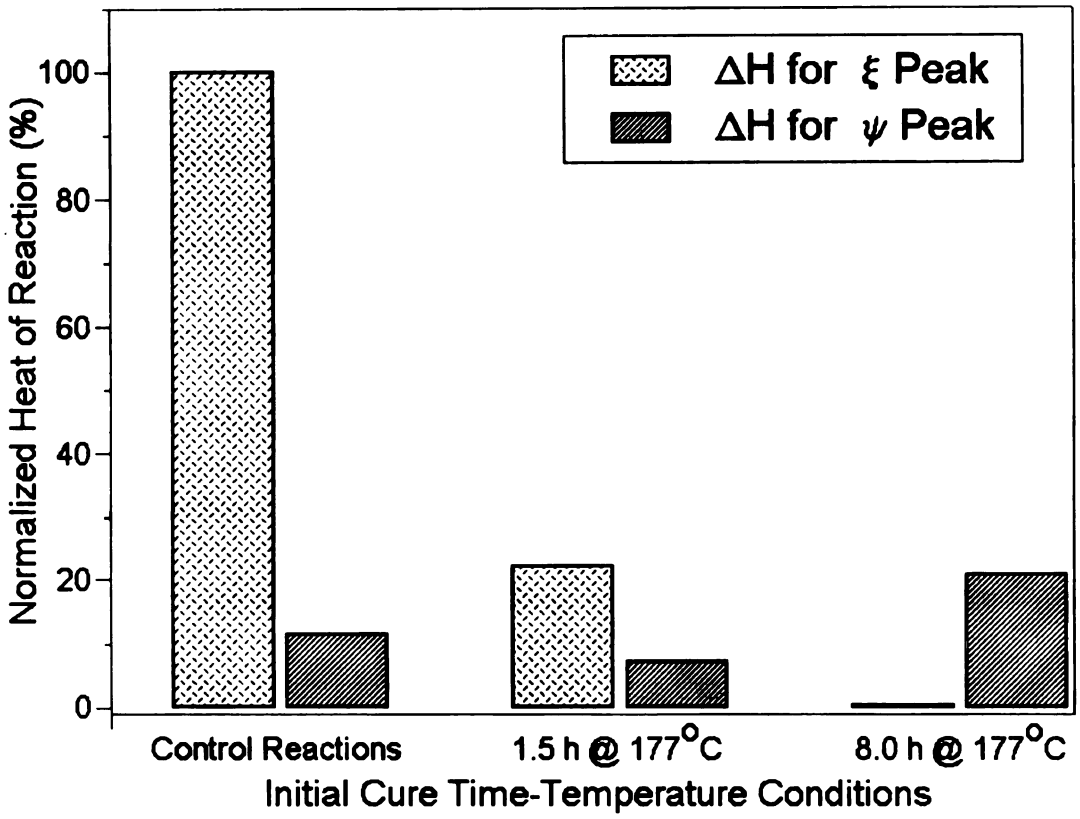

Figure 4.18: Quantification of the reaction enthalpy for initially cured and control specimens as calculated from Figure 4.16.

Performing the above calculation, however, indicates that the reaction enthalpy itself is insufficient in magnitude to account for the lower T_g in type-II laminates. Since the network is not dramatically different as a result of the initial cure cycle, the primary mechanism for T_g reduction must be due to a reduction in composite residual stress, which enhances molecular mobility and thereby results in a decreased T_g for equivalent postcures to type-I laminates.

This physical relaxation is a composite phenomenon, as previous work shows that the neat resins do not exhibit this behavior [3]. The above conclusion is consistent with all of the data presented here as well as the previous work on these BMI resins and composites [3-10, 20, 25-27].

For a further discussion of this phenomenon the reader is referred to a paper by Chow [137] that provides a theoretical expression of the glass transition temperature as a function of the stress state. In principle, the measure of the *in-situ* T_g is an indirect measure of the overall stress state. The competing mechanisms of structural relaxation (leading to an increased stress level) and the stress relaxation (leading to a lower stress level) are difficult to address [138], but in this study it is clear that the latter dominates for the cure and postcure sequences presented.

4.3.5 Critical Fundamental Microcracking Mechanisms and Thresholds

Compilation of the above data, corresponding discussions, and previous studies allows one to draw the following conclusions that appear to be the critical parameters that control microcracking in this composite system on all dimensional levels:

(i) Transverse microcracks form during cooling from the cure temperature.

(ii) Microcrack width is a function of the postcure time-temperature conditions, and the microcrack onset point and density can be controlled by the initial cure time-temperature conditions. Microcracking is not a function of initial BMPM:DABPA monomer stoichiometry for the two ratios examined.

(iii) Microcracks can be prevented by an extended initial cure of 8 h at 177°C prior to postcure, and no microcracks are observed until an additional postcure for 6 h at 300°C for these composite laminates.

(iv) The extended initial cure cycle that prevents microcracking does so by a reduction in overall composite residual stress as evidenced by the following:
   (a) A 69% decrease in microcrack density for type-II laminates as opposed to type-I laminates after the same postcure of 6 h at 300°C;
   (b) A 38% increase in the $[0°/90°]_s$ storage modulus resulting from the extended cure time (improved interface);
   (c) A ~200°C higher thermal load required to initiate microcracks in type-II laminates;
   (d) An increase in damping in type-II laminates;
   (e) A slightly lower T_g in type-II laminates.

Figure 4.19 is offered as a simple qualitative summary to the mechanisms discussed in this research for microcracking as a function of initial cure time at 177°C. Using x-ray and optical measurements, Geldermans *et al.* [139] measured the residual stress of different polyimide films cured on a ceramic substrate as a function of different cure history sequences. Complex residual stresses (measured at 25°C) were observed as a function of different curing cycles for different materials. Similarly, (Figure 4.19) the following qualitative explanation for the residual stresses resulting from resin shrinkage and stress

relaxation is proposed: after 1.5 h at 177°C, the stresses are higher (due to initial resin shrinkage) than after 8 h at 177°C, which is in the relaxation regime. As mentioned earlier, beyond this initial cure a decrease in the resin density is observed as a function of postcure conditions, except for a slight increase from the 'H1' to the 'H2' postcure cycle.

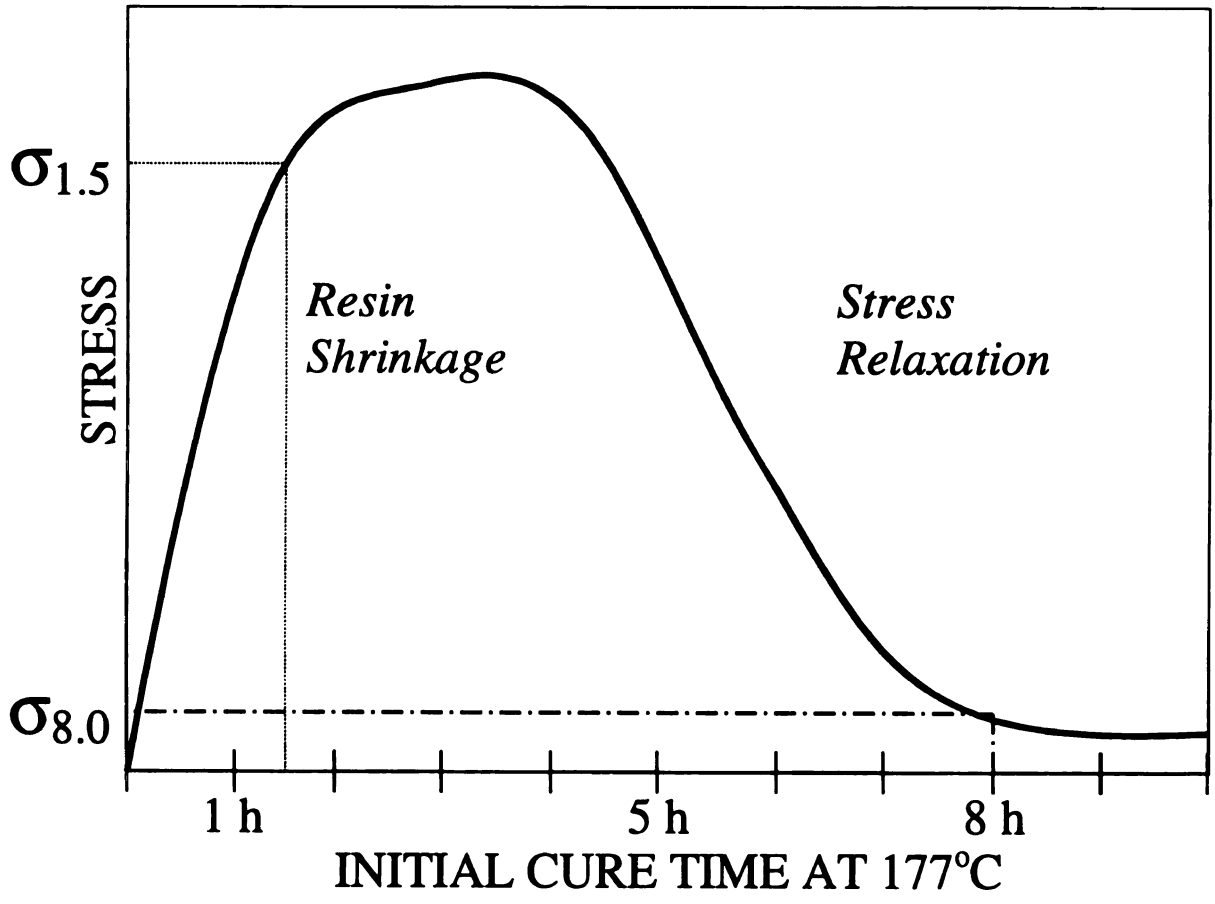

Figure 4.19: Resin shrinkage stresses as a function of initial cure time at 177°C (qualitative).

4.4 Conclusions

The critical parameters controlling cure induced microcracking on all dimensional levels have been reviewed and examined in this investigation for IM7/BMI cross-ply laminates. It was determined by an *in-situ* microscopy technique that microcracks form during the cool down to room temperature from the cure temperature, and their width is a function of the postcure conditions. From these results and a review of the literature data, a cure cycle modification was employed that prevented microcracking under standard fabrication conditions. The effects of this cure cycle on the composite properties were then examined by DMA and DSC, and these results correlated to the physical microcracking characteristics to determine the critical mechanisms involved in microcrack prevention.

As a result of the above experiments, it was determined that an extended initial cure step for 8 h at 177°C prevents microcracking under standard subsequent postcure conditions by a reduction in residual stress and an improved interface, leading to a laminate with higher damping at T_g, a lower value for T_g, and an increased dynamic modulus in the $[0°/90°]_s$ loading direction. The observed composite property improvements are manifested on the molecular, microscopic, and macroscopic levels by a physical relaxation of the processing induced residual stresses imposed on the resin network.

It should be emphasized that this study was fundamental in nature, but a more comprehensive analysis could extrapolate the results obtained here to meet certain experimental or design criteria. For example, different initial cure times at 177°C, additional monomer compositions, or modifications of the laminate thickness and/or stacking sequence could be examined, based on the important fundamental parameters and mechanisms reported here.

DATE DUE	DATE DUE	DATE DUE
NOV 0 3 2000 FEB 1 3 2002		
1 1 0 5 1 2		

ST
RELATIO
STRUCTU
AND MI

STRUCTURE-PROPERTY-PROCESSING RELATIONSHIPS AND THE EFFECTS OF PHYSICAL STRUCTURE ON THE HYGROTHERMAL DURABILITY AND MECHANICAL RESPONSE OF POLYIMIDES

VOLUME II

By

Jason E. Lincoln

A DISSERTATION

Submitted to
Michigan State University
in partial fulfillment of the requirements
for the degree of

DOCTOR OF PHILOSOPHY

Department of Materials Science and Mechanics

2001

C

C
F

5.

Chapter 5

Critical Parameters that Effect the Deformation and Failure of Thermoplastic and Thermoset Polyimides

5.1 Introduction

Significant progress has been made in efforts to tailor polyimide molecules, not only for environmental stability, but also for ease of processing, toughness improvements, and thermooxidative stability. For example, numerous researchers [6, 149, 157, 159, 160-174] have demonstrated that termination of various imide oligomers with reactive phenylethynyl end groups can lead to dramatic improvements in hygrothermal durability, processability, solvent resistance and toughness.

In this chapter, the effects of processing conditions and thermal history on the structure and deformation behavior of the following polyimides are identified: (i) thermoplastic poly(4,4'-oxydiphenylene pyromellitimide) (POPPI), (ii) thermoset bismaleimide (BMI), (iii) thermoplastic polyetherimide (PEI), and (iv) a thermoset phenylethynyl terminated imide (PETI-5).

5.1.1 Poly(4,4

POPPI, shown

the principal c

behavior is inve

are compared

degradation in p

Kapton® films

thermoplastic a

additives [176].

5.1.2 Bismalei

Bismaleimide res

because i) they

and epoxies. It

hot/wet propert

have been cond

BMI resin syste

variety of comm

resin system co

bis(4-diallyl bisphe

5.1.1 Poly(4,4'-Oxydiphenylene Pyromellitimide)

POPPI, shown in Figure 2.28, is among the first commercial polyimides and the principal component of materials such as Kapton® film. The deformation behavior is investigated here, as it is often a basis from which other polyimides are compared. For example, the current understanding of hydrolytic degradation in polyimides is based on work conducted in the early 1970's on Kapton® films [174-175]. This polymer is in the form of an amorphous thermoplastic and proprietary versions may vary in molecular weight and additives [176].

5.1.2 Bismaleimide

Bismaleimide resins have developed rapidly in the past two decades primarily because (i) they bridge the temperature performance gap between polyimides and epoxies, (ii) have similar processability to epoxies, (iii) display excellent hot/wet properties, and (iv) possess a versatile chemistry. Numerous studies have been conducted on structure-property-processing interrelationships of BMI resin systems composed of different bismaleimide monomers and a variety of comonomer curing agents [98, 177-184]. Here, the BMI copolymer resin system composed of 4,4'-bismaleimidodiphenylmethane (BMPM) and 0,0'-diallyl bisphenol A (DABPA), Figures 2.20 and 2.21, respectively, is

investigated wh

studies perform

Recently

studies of BMP

cure kinetics

weight loss d

moisture abso

IMT BMI com

5.1.3 Polyethe

PEI Figure 2

disadvantageous

and a relatively

both a composite

molding.

investigated which compliments the moisture absorption and microcracking studies performed in Chapters 3 and 4.

Recently [Chapter 3, Chapter 4, 3, 148-151], the results of systematic studies of BMPM/DABPA network formation have been reported by way of (i) cure kinetics and mechanisms, (ii) mass density changes during cure, (iii) weight loss during cure, (iv) glass transition temperature progression, (v) moisture absorption-network structure correlations, and (vi) carbon fiber (IM7)/BMI composite cure induced microcracking.

5.1.3 Polyetherimide

PEI (Figure 2.25) is a tough, amorphous thermoplastic but has the disadvantageous characteristics of hydrolytic instability, poor solvent resistance, and a relatively low glass transition temperature [160]. It has applications as both a composite matrix and as a structural plastic, often processed by injection molding.

5.1.4 Phenyle

Phenylethynyl to

Figure 2.29 a

through the eth

crosslinking. St

understand the

formed by the

materials exhib

reported from

understanding o

structure-proper

Studies b

terminated imid

reported in the

occurs during n

rubber elasticity

and relationship

properties of a

Center Soluble

network state c

5.1.4 Phenylethynyl Terminated Imide (PETI-5)

Phenylethynyl terminated imide oligomers, such as NASA LaRC® PETI-5 (Figure 2.29) are generally crosslinked in the 350-371°C temperature range through the ethynyl C≡C triple bond, which is capable of chain extension and crosslinking. Significant research has been conducted recently in an attempt to understand the crosslinking reactions and physical structure of the network formed by the cure reactions of phenylethynyl terminated oligomers. These materials exhibit extremely high toughness (strain to failure for PETI-5 reported from 14-84% in the 23-177°C temperature range) and an understanding of the network formation will provide crucial insight into the structure-property relationships [160-174].

Studies based on model compounds and similar phenylethynyl terminated imide oligomers suggest that the excellent toughness values reported in the literature are a result of a high degree of chain extension that occurs during network formation. For example, Nicholson *et al.* [185] used rubber elasticity theory, the DiMarzio relationship for crosslink density [186], and relationships from Miller and Macosko [187] to characterize the mechanical properties of a phenylethynyl containing imide oligomer (Langley Research Center Soluble Imide, LaRC®-SI). Their findings suggest that the physical network state consists of a high degree of chain extension and low degree of

crosslinking. T

groups will prod

In addition

compound studi

possible structur

for PETI-5 the r

to a reaction ord

mechanisms are

structures, such

reactions to for

reactions to for

unsaturated stru

Glaser coupling

regime above 9

system based on

Besides

terminated imid

temperature is

detailed study o

or below

morphology th

crosslinking. The authors state that only half of the reactive crosslinking groups will produce 'effective' crosslinks.

In addition to the above research, other scientists have conducted model compound studies on phenylethynyl terminated polyimides and suggested possible structures for the network. Fang *et al.* [173], for example, found that for PETI-5 the reaction was first order up to 90% degree of cure, then changed to a reaction order of 1.5. Their results suggest that complicated cure reaction mechanisms are involved which include crosslinking reactions of polyene-like structures, such as intramolecular and bimolecular double bond addition reactions to form a more highly crosslinked polymer. Cyclotrimerization reactions to form crosslinked aromatic structures and condensed polycyclic unsaturated structures derived from Diels-Alder, Friedel-Crafts, Straus and Glaser coupling reactions were postulated to account for the complex cure regime above 90% cure. The investigators proposed a fused ring polymer system based on their findings [173].

Besides physical network characteristics, some of the phenylethynyl terminated imides will crystallize via a liquid crystal mechanism if the cure temperature is insufficient because crosslinking inhibits crystallization. In a detailed study of PETI-5 processing, Hou *et al.* [188] demonstrated that curing at or below 350°C resulted in a partially crosslinked, semicrystalline morphology that could not be removed upon annealing below the melting

temperature. U

obtained and cr

The aforc

the resin mecha

increase in frac

compared to cor

Here, it

control the defo

roles played by

deformation and

The overa

that control th

environments a

interrelationships

absorption, glas

mechanical prop

temperature. Upon curing at 371°C, a completely amorphous material was obtained and crystallization could no longer be reproduced upon annealing.

The aforementioned morphological differences can significantly modify the resin mechanical response. For example, Connell [189] reported a 10% increase in fracture toughness (G_{IC}) of semicrystalline PETI-5 (2500 g/mol) compared to completely amorphous PETI-5.

Here, it is sought to determine the physical structural parameters that control the deformation of PETI-5 neat resin. Of particular interest are the roles played by free volume, polymer morphology, and thermal history on the deformation and failure mechanisms.

The overall goals of this chapter are to identify the critical parameters that control the deformation of polyimides with respect to service environments and processing conditions. In order to characterize these interrelationships, the following were monitored: thermal history, moisture absorption, glass transition temperature, melting points, mass density, mechanical properties, and fracture surfaces.

5.2 Experimen

5.2.1 Poly(4,4

POPPI Vespel

dogbone coup

circulating oven

temperature. Spe

ice water. Mech

machine at strain

under the stress

using a Coates &

Morgan perform

AFOSR program

5.2.2 Bismale

BMPM-DABP s

according to the

time-temperature

Postcure temper

Panels were cut

and then tested

5.2 Experimental Techniques

5.2.1 Poly(4,4'-Oxydiphenylene Pyromellitimide)

POPPI (Vespel®, DuPont) molded sheets, 0.75 mm thick, were cut into dogbone coupons (five specimens per condition) and annealed in an air-circulating oven between 300-500°C for 24 h, then cooled at 2°C/min to room temperature. Specimens were also heated to 450°C for 1 min then quenched in ice water. Mechanical tensile tests were performed on an Instron, TTDM® machine at strain rates of 3 x 10^{-2}/min. Toughness was recorded as the area under the stress versus strain curve and fracture topographies were analyzed using a Coates & Welter® scanning electron microscope (SEM). Dr. Roger J. Morgan performed the above experiments for POPPI as portion of the overall AFOSR program discussed in Chapter 1.

5.2.2 Bismaleimide

BMPM/DABPA resins (Matrimid® 5292, Ciba-Geigy) were prepared according to the technique outlined in Chapter 3. Monomer ratios and cure time-temperature conditions were systematically varied according to Table 3.1. Postcure temperatures of $\geq$ 250°C were performed in a nitrogen atmosphere. Panels were cut into rectangular bars, polished, dried at 80°C for two weeks and then tested in flexure (three point bending) at 23°C, 177°C and 250°C,

cording to AS

Density and glass

included in the a

5.2.3 Polyethe

PEI Ultem 1

Samples were d

Additional spec

temperature T_g

2C/min. Tensi

equipped with an

gage length was 5

according to AST

Moisture a

conditions for

absorption is se

absorption was

Equation 3.1. T

In order

content, M_∞, th

according to ASTM D790 with an UTS® mechanical testing instrument. Density and glass transition temperature were reported in Chapter 3, but will be included in the analysis here where appropriate.

5.2.3 Polyetherimide

PEI (Ultem 1000®) pellets were injection-molded into dogbone coupons. Samples were dried at 80°C for one week and considered control specimens. Additional specimens were annealed after drying at the glass transition temperature (T_g = 215°C) for 30 min, using heating and cooling rates of 2°C/min. Tensile tests were performed at 23°C using an UTS® instrument equipped with an optical extensometer. Strain rates were 40 x 10^{-2}/min and the gage length was 5.08 cm. Mass density was determined by hydrostatic weighing according to ASTM D798-86.

Moisture absorption was conducted under 95°C/100% relative humidity conditions for both annealed and control specimens because moisture absorption is sensitive to changes in free volume. Weight gain due to water absorption was recorded by weighing on a Mettler® balance and the applying Equation 3.1. The average of two specimens constituted a data point.

In order to determine the diffusivity, D, and equilibrium moisture content, M_∞, the weight gain curves were fitted to Equation 2.10 by nonlinear

regression anal

Philips Electros

5.2.4 Phenyle

Thin, ~0.5 mm

mer powde

mold were used

coated with rel

semicrystalline m

Table 5.1. Dog

645 cm^2, of s

chamber with a n

morphous PE

DSC, TA Instru

peaks.

Tensile t

conducted in the

5.25 x 10^{-3}/min

according to AS

was used to comp

regression analysis. Fracture surface topographies were characterized using a Philips Electroscan® 2020 Environmental Scanning Electron Microscope.

5.2.4 Phenylethynyl Terminated Imide (PETI-5)

Thin, ~0.5 mm thick panels were molded from imidized 5000 g/mol PETI-5 oligomer powder obtained from Imitec®. A 100 cm^2 stainless steel frame and mold were used and the powder was placed between two aluminum sheets coated with release agent. Cure schedules resulting in amorphous and semicrystalline morphology were used, as were different cooling rates, shown in Table 5.1. Dogbone coupons (2.54 cm gage length) and density specimens (6.45 cm^2) of semicrystalline PETI-5 were cut then annealed in a sealed chamber with a nitrogen atmosphere at 177°C, T_g–30°C, and T_g–10°C for 24 h. Amorphous PETI-5 was not annealed. Differential scanning calorimetry (DSC, TA Instruments® 2920) was used to measure T_g and observe melting peaks.

Tensile tests and fracture surface topography examination were conducted in the same manner as discussed for PEI, except that a strain rate of 5.25 x 10^{-2}/min was used for the tensile tests. Density was determined according to ASTM D798-86. The average of five specimens per condition was used to constitute a single data point.

Table 5.1: Ther

Cure Cycl
3
+ 3
3
+ 3
3
3
+ 3
3
+ 3

5.3 Results an

5.3.1 Poly(4,4

Toughness is plo

displayed in the

Note that the

annealed cont

by the ice quench

into three zones

for POPPI.

First, in t

induced glassy st

Toughness compa

to the ice-quenche

Table 5.1: Thermal history conditions for the processing of PETI-5.

Cure Cycle	Cooling Rate	Morphology
350°C / 3 h + 360°C / 1 h	1.1°C/min	semicrystalline
350°C / 8 h + 360°C / 1 h	1.1°C/min	semicrystalline
371°C / 1.5 h	1.1°C/min	amorphous
350°C / 3 h + 360°C / 1 h	8.7°C/min	semicrystalline
350°C / 3 h + 360°C / 1 h	ice quench	semicrystalline

5.3 Results and Discussion

5.3.1 Poly(4,4'-Oxydiphenylene Pyromellitimide)

Toughness is plotted as a function of annealing temperature in Figure 5.1. Also displayed in the figure is the control toughness for the ice-quenched material. Note that the ice-quenched state exhibits a higher toughness than the unannealed control material due to a higher content of free volume locked in by the ice quench. The deformation mechanisms for POPPI can be divided into three zones as a function of annealing temperature. Note that $T_g \approx 365°C$ for POPPI.

First, in the 300-323°C regime, annealing leads to physical relaxation induced glassy state free volume decreases as evidenced by a 15% decrease in toughness compared to the unannealed control and a 46% decrease compared to the ice-quenched material after annealing at 323°C for 24 h.

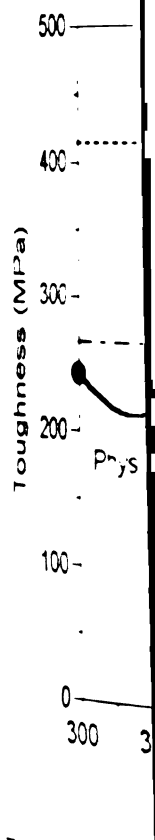

Figure 5.1: To
POPPI as a func

Polymer

23-375 C resu

ONeal [196] ob

of a copolyma

Through exten

ides of the fr

pon annealing

microvoids of

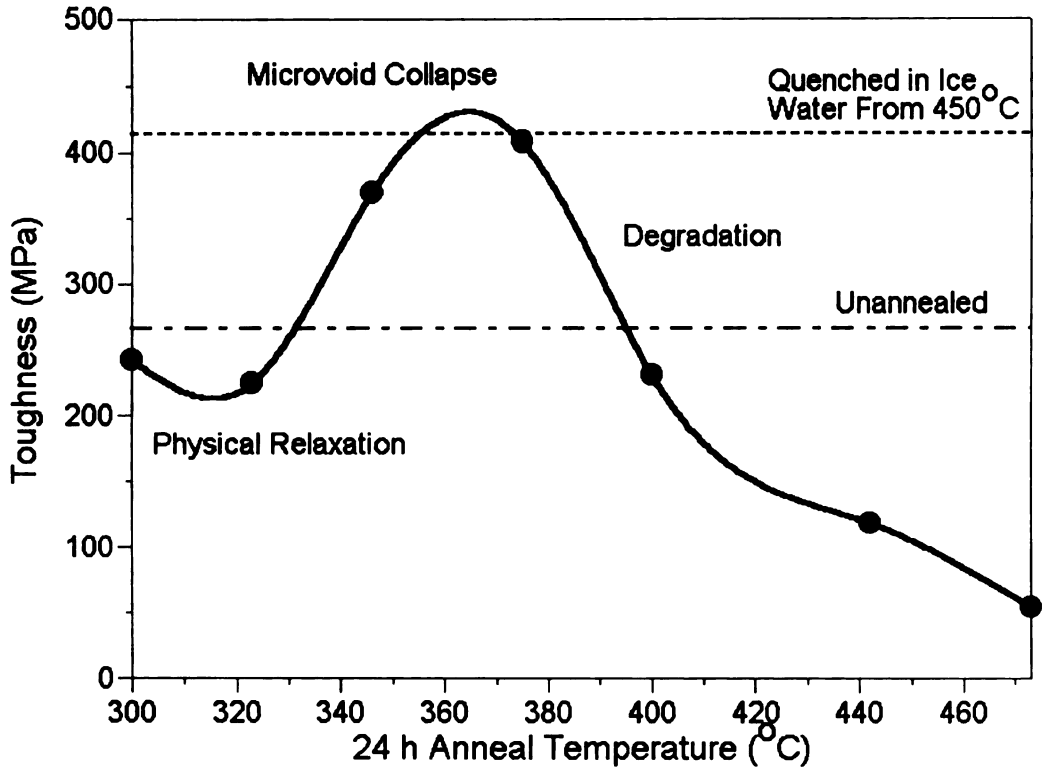

Figure 5.1: Toughness (from area under the stress versus strain curve) for POPPI as a function of 24 h anneal temperature.

Polymer modifications occurring in the second temperature regime of 323-375°C result in significant improvements in toughness. Morgan and O'Neal [190] observed similar trends in the study of the deformation behavior of a copolyimide based on benzophenone tetracarboxylic acid dianhydride. Through extensive optical, SEM, and transmission electron microscopy (TEM) studies of the fracture topographies, the authors attributed improved toughness upon annealing at high temperatures to collapse of microvoids. Inherent microvoids of 1 – 15 nm in diameter were observed by Bright-field TEM.

Prior to high te
displayed a high
as stress concen
temperatures le
toughness. It is
responsible for
regime for PCI

Above 3
increases in d
embrittlement.
MPa only 20

Fracture
resulted in the h
Figures 5.2 and
are divided into
intermediate, 5-1
the cavitation a
magnification.
fluids range from

Prior to high temperature annealing, fracture surfaces of the glassy polyimide displayed a high number of craze initiation sites as a result of microvoids acting as stress concentrators. Elimination of the microvoids by annealing at high temperatures led to markedly different fracture topographies and improved toughness. It is believed that microvoid collapse is the dominant mechanism responsible for the improved toughness observed in the 323-375°C annealing regime for POPPI observed here.

Above 375°C thermooxidative degradation begins, and the mechanism increases in dominance as the annealing temperature is increased, leading to embrittlement. Upon annealing for 24 h at 473°C, the toughness drops to 54.4 MPa, only 20% of the unannealed control value.

Fracture surface topographies for the 375°C annealed POPPI, which resulted in the highest value of toughness achieved (408.5 MPa), are shown in Figures 5.2 and 5.3. In Figure 5.2, characteristic fracture propagation regions are divided into (a) slow, with 5-30μm microfracture plane diameter (MPD), (b) intermediate, 5-100μm MPD, and (c) fast, 5-150μm MPD. Figure 5.3 displays the cavitation and fibrillation features of the fracture surface at higher magnification. Cavities are on the order of 0.1-1μm in diameter, while the fibrils range from roughly 30-60 nm.

Addition
shown in Figu
observed. The
a result of n
Comparison of
between the tw
The con
crazing proces
observed from
evidence that
predominates a
result of incom
compression m
In polym
tensile failure st
rate [204]. This
lower stresses
macroscopic st
observed that
topographies of

Additionally, the fracture topography for the 473°C annealed POPPI is shown in Figure 5.4. Recall that this represents the most brittle failure observed. The MPD values range from only 5-15μm for all fracture regions as a result of numerous crack sites and lack of cavitation development. Comparison of Figures 5.2 and 5.4 demonstrates the significant differences between the two failure modes.

The compression molded POPPI specimens deformed by a massive crazing process across the whole of the failed specimen cross-section, as observed from the fracture topography studies discussed above. There was no evidence that shear banding occurred in these POPPI samples. Crazing predominates as a result of numerous nanoscale voids in the specimens as a result of incomplete fusion of these relatively rigid macromolecules during the compression molding fabrication process.

In polyimides that deform predominately by crazing, the macroscopic tensile failure strain decreases with increasing temperature and decreasing strain rate [204]. This is because softening of the craze fibrils causes them to fail at lower stresses that allows the development of critical flaws earlier in the macroscopic stress-strain process. Consistent with this hypothesis it is observed that the craze fibrils are not as well developed in the fracture topographies of specimens that fail at higher temperatures or lower strain rates.

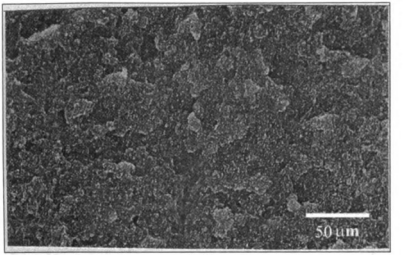

(a)

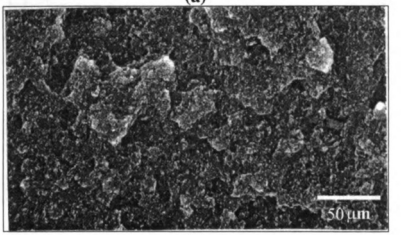

(b)

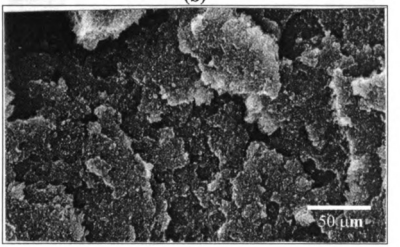

(c)

Figure 5.2: Fracture topography of POPPI annealed at 375°C / 24 h for (a) slow, (b) intermediate, and (c) fast fracture regions. All marker bars are 50μm.

Figure 5.3: Ca
24 h. Carry
from in size.

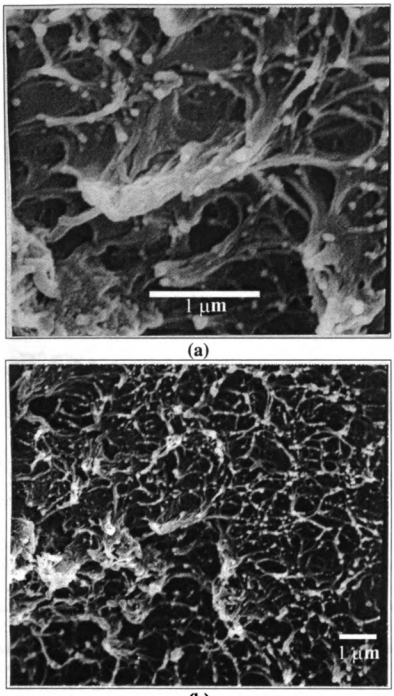

Figure 5.3: Cavitation and fibrillation structure of POPPI annealed at 375°C / 24 h. Cavity diameter ranges from 0.1 – 1.0μm and fibrils range from 30 – 60nm in size. Marker bars are 1μm.

Figure 5.4:
Cavitation is
from thermo

A sim
annealed and
such as thos
from a lowe
density due
that lead to c

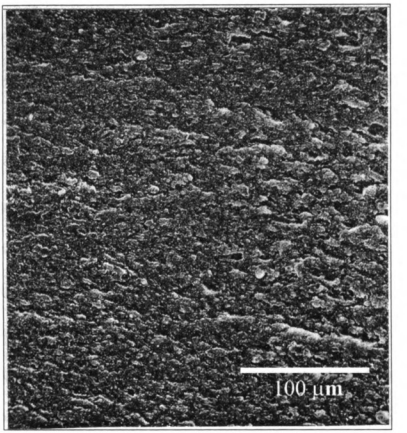

Figure 5.4: Fracture topography of POPPI annealed at 473°C / 24 h. Cavitation is less well developed due to embrittlement of craze fibrils resulting from thermooxidative degradation and possible crosslinking.

A similar phenomenon is observed for the specimens that have been annealed and oxidized above the T_g and then tested at ambient temperatures, such as those discussed in this research. These property modifications result from a lowering of the molecular weight and/or an increase in the crosslink density (due to thermooxidative induced crosslinks and chemical degradation) that lead to craze fibril embrittlement and associated decrease in toughness.

5.3.2 Bismale

Mass density a

four BMPM:D

and 3.2, respec

both additional

case, the obse

BMPM mono

g cm^3, but the

Studies o

reported an inc

of further cros

opposite trend

more crosslin

BMPM MDA

result of the M

crosslinked g

crosslinked g

observations

and the diff

resin system

barely cros

5.3.2 Bismaleimide

Mass density and T_g as a function of cure time-temperature conditions for the four BMPM:DABPA initial monomer compositions are shown in Figures 3.1 and 3.2, respectively. The most notable feature is the decrease in density with both additional cure (crosslink density) and DABPA monomer. For the latter case, the observed trend results from the 29% higher mass density of the BMPM monomer (1.4 g/cm^3) as opposed to the DABPA monomer (1.08 g/cm^3), but the former case requires some interpretation.

Studies of BMPM copolymerized with 4,4'-methylene dianiline (MDA) reported an increase in mass density with increasing degree of cure as a result of further crosslinking and resin shrinkage [17-18]. In this study, exactly the opposite trend is observed because as the three-dimensional network becomes more crosslinked, the packing efficiency decreases. The structure of the BMPM/MDA resin was shown to contain a high degree of chain extension as a result of the Michael addition reaction [17-18]. It has been reported for highly crosslinked glassy polymers, which contain stiff segments, that the more highly crosslinked glass is less compact [21, 24]. This also supports previous observations of a directly proportional increase in equilibrium moisture content and the diffusion coefficient as a function if increased crosslinking for this BMI resin system (Chapter 3). Similar relationships have been reported for other highly crosslinked glasses in inert gas diffusion studies [24] and additional

evidence has be

PALS experim

As expec

degree of cure.

of the 'ene' m

dissociation and

appears to be

monomer stoich

poor to comp

prepolymer, th

concentration.

excess BMPM

the higher rigid

[183-184]. In

content, diffu

supports the l

As a re

tem system.

ha inhibit m

to a more

molecular pa

evidence has been obtained from Positron Annihilation Lifetime Spectroscopy (PALS) experiments [191] on BMI resins.

As expected, the glass transition temperature increases with increasing degree of cure, with a ~100°C increase in T_g after all of the C=C double bonds of the 'ene' molecule have been consumed as a result of ether crosslink dissociation and rearrangement to stiffer crosslinked segments. The final T_g appears to be independent of cure thermal history sequence [3] or initial monomer stoichiometry, leading to a final value of roughly 350°C. However, prior to complete consumption of the C=C double bonds of the 'ene' prepolymer, the T_g increases with increasing initial BMPM monomer concentration. It has been proposed [17-18] that this phenomenon arises from excess BMPM monomer resulting in a higher overall crosslink density and/or the higher rigidity of the BMPM segments compared to the DABPA segments [183-184]. In Chapter 3 a linear relationship between equilibrium moisture content, diffusivity, and BMPM concentration was reported, which further supports the latter argument.

As a result of the differences between the two monomers of this BMI resin system, excess BMPM monomer results in (i) stiffer network segments that inhibit molecular conformation and (ii) higher crosslink density that leads to a more open, less well-packed structure. In this particular BMI resin, molecular packing efficiency decreases because the BMPM component is more

igid than the

optimum space

less stiff DAB

scale. Figure 5

composition

represented by

coils rope

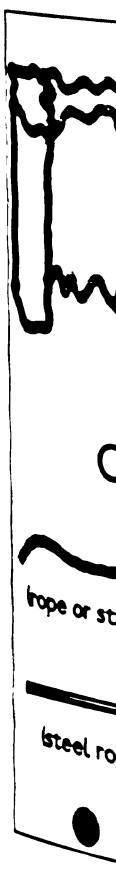

Figure 5.5: S
packing con
represented b
Case A has ex
BMPM segme

rigid than the DABPA monomer, creating stiff crosslinks that prevented optimum space filling to occur during crosslinking reactions. Flexible chains (less stiff DABPA segments) are able to pack more efficiently on the molecular scale. Figure 5.5 is a schematic representation of the influence of monomer composition on molecular packing efficiency, with BMPM segments represented by rigid rods (steel bars) and DABPA segments signified by flexible coils (rope).

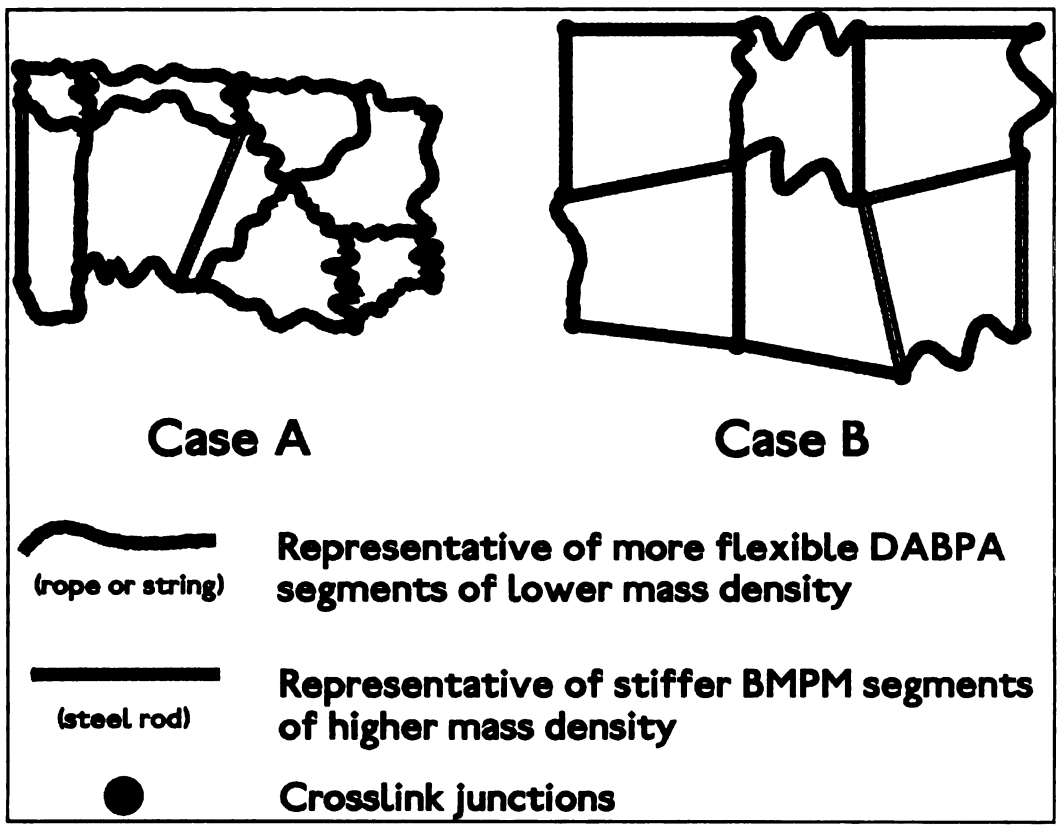

Figure 5.5: Schematic two-dimensional representation of geometric network packing constraints in the BMI resin network. BMPM segments are represented by a rigid rod (steel) and DABPA segments by flexible coils (rope). Case A has excess DABPA segments and Case B represents an excess of stiffer BMPM segments.

Mechan

flexural modu

equivalent to t

and E, signific

straightforward

increasing with

As a resu

significant scat

statistical in na

defects can be

modes. Figure

structure-prop

chain ends ca

concentration

understandin

during the fo

Mechanical test results are summarized in Table 5.2, where E is the flexural modulus of elasticity, σ_f represents the ultimate flexural strength (equivalent to the failure strength for the observed brittle mechanical response), and ε_f signifies the strain to failure. The effect of test temperature is straightforward, with modulus and strength decreasing and elongation to break increasing with increasing temperature.

As a result of the brittle failure mode of this BMI resin system, there is significant scatter in the strength data, and the numerical results are mostly statistical in nature (Figure 5.6). In a highly crosslinked glass, many structural defects can be responsible for heterogeneities in crosslink density and failure modes (Figure 5.7) which often leads to difficulties in the determination of structure-property relationships. For example, unreacted groups in the form of chain ends can support no load during deformation, and may act as stress concentration sites to initiate cracks, ultimately leading to failure [10, 193]. This understanding of deformation in glassy polymers should be kept in mind during the following discussion.

Table 5.2: Flexural test results for BMI resins as a function of initial monomer stoichiometry, cure conditions, and test temperature.

Cure	Flexural	BMI NEAT RESIN COMPOSITIONS BY BMPM:DABPA RATIO (molar)			
		SYSTEM A (1:1.13)	SYSTEM B (1:1)	SYSTEM C (1:0.87)	SYSTEM D (1:0.82)

Table 5.2: Flexural test results for BMI resins as a function of initial monomer stoichiometry, cure conditions, and test temperature.

Cure Conditions	Flexural Properties	BMI NEAT RESIN COMPOSITIONS BY BMPM:DABPA RATIO (molar)											
		SYSTEM A (1:1.13)			SYSTEM B (1:1)			SYSTEM C (1:0.87)			SYSTEM D (1:0.82)		
		Temperature (°C)			Temperature (°C)			Temperature (°C)			Temperature (°C)		
		23	177	250	23	177	250	23	177	250	23	177	250
177°C / 1h + 200°C / 1h	E (MPa)	4454	-	-	4368	-	-	4369	-	-	4122	-	-
	σ_f (MPa)	131	-	-	150	-	-	124	-	-	149	-	-
	ε_f (%)	3.14	-	-	3.80	-	-	2.70	-	-	3.77	-	-
177°C / 1h + 200°C / 3h	E (MPa)	4410	-	-	4009	-	-	3925	-	-	3927	-	-
	σ_f (MPa)	178	-	-	159	-	-	173	-	-	168	-	-
	ε_f (%)	4.50	-	-	4.34	-	-	4.97	-	-	4.63	-	-
177°C / 1h + 200°C / 2h +250°C / 1h	E (MPa)	3967	-	-	3665	2527	-	3732	2580	-	3702	-	-
	σ_f (MPa)	162	-	-	143	101	-	169	110	-	199	-	-
	ε_f (%)	4.49	-	-	4.09	7.64	-	4.65	8.93	-	7.10	-	-
177°C / 1h + 200°C / 2h +250°C / 6h	E (MPa)	3886	2234	1603	3573	2432	1965	3779	2431	1894	3794	2531	1781
	σ_f (MPa)	152	94	59	113	100	75	164	114	67	157	120	63
	ε_f (%)	4.55	5.51	5.38	3.15	4.91	5.55	5.10	7.41	7.38	4.77	6.64	8.59
177°C / 1h + 200°C / 2h +250°C / 6h + 300°C / 1h	E (MPa)	3443	2468	1759	3965	2415	1628	3511	2810	1962	3553	2728	1986
	σ_f (MPa)	137	110	79	138	108	80	156	131	88	150	123	90
	ε_f (%)	4.37	5.99	7.71	4.13	6.39	7.80	5.20	7.23	8.52	4.99	6.78	8.47
177°C / 1h + 200°C / 2h +250°C / 6h + 300°C / 6h	E (MPa)	3988	2072	1602	3846	2416	1723	3960	2344	1760	3741	2334	1860
	σ_f (MPa)	137	78	74	107	106	79	133	108	87	132	106	92
	ε_f (%)	4.02	4.47	7.14	2.98	5.95	6.63	3.87	6.00	6.65	4.27	5.76	7.65

The gene

increase in stre

network are c

bonds, the stre

at 300 C. Wh

rearrange to f

high temperat

to microcrack

significant fac

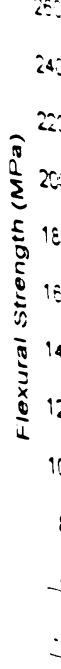

Figure 5.6
stoichiome

The general trend of strength as a function of cure conditions shows an increase in strength as the 'ene' C=C double bonds and unreacted groups in the network are consumed. Upon conversion of all of the 'ene' C=C double bonds, the strength decreases with further cure, reaching a minimum after 6 h at 300°C. When cured at 300°C for long times, the unstable ether crosslinks rearrange to form stiffer, more aromatic-like segments [134]. These complex high temperature rearrangement reactions have been postulated to contribute to microcracking in IM7/BMI laminates (Chapter 4), and are most likely a significant factor to the observed decrease in strength with further cure.

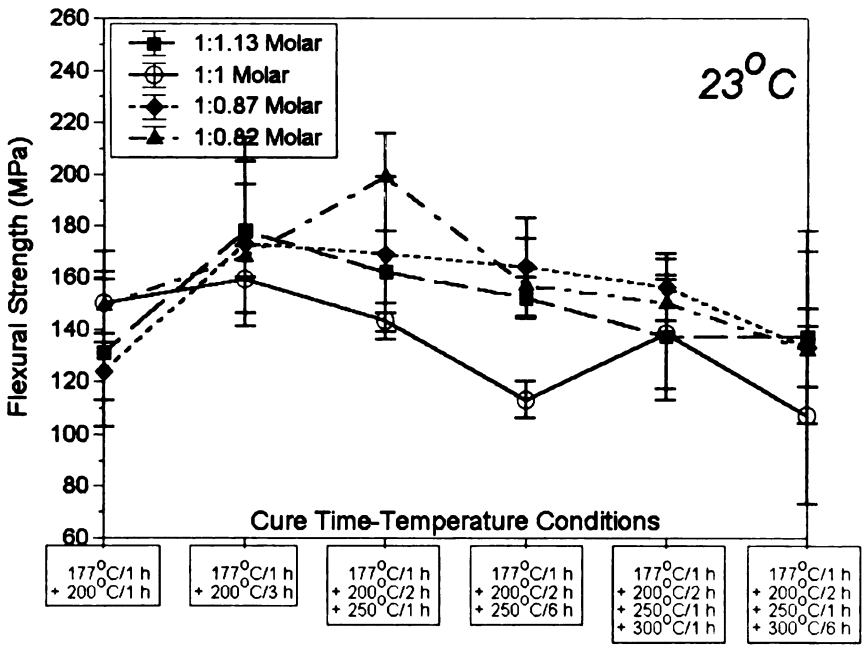

Figure 5.6(a): Flexural strength as a function of cure and monomer stoichiometry for flexural test temperature of 23°C.

Figure 5.6(b
stoichiometry

Figure 5.6(
stoichiometry

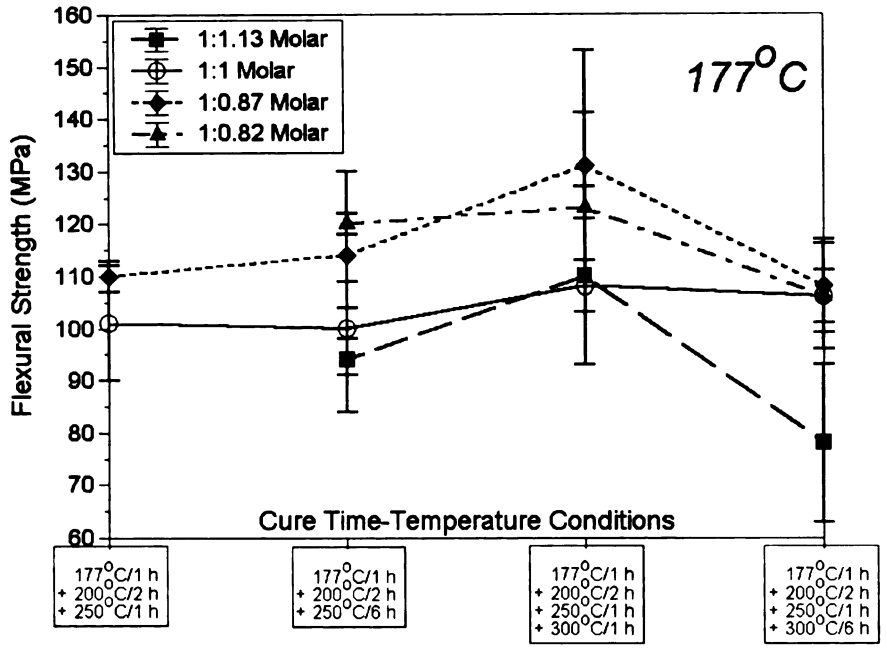

Figure 5.6(b): Flexural strength as a function of cure and monomer stoichiometry for flexural test temperature of 177°C.

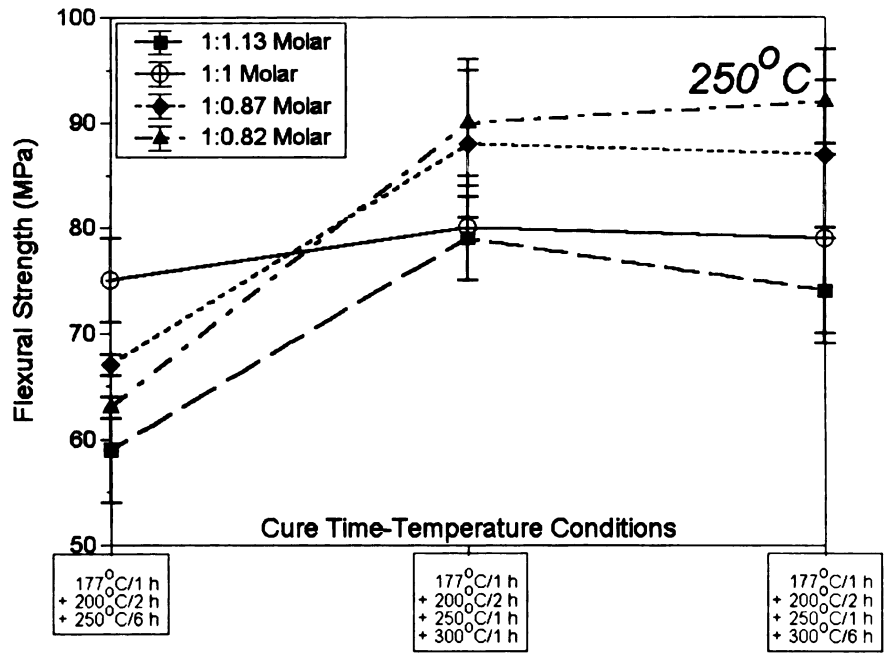

Figure 5.6(c): Flexural strength as a function of cure and monomer stoichiometry for flexural test temperature of 250°C.

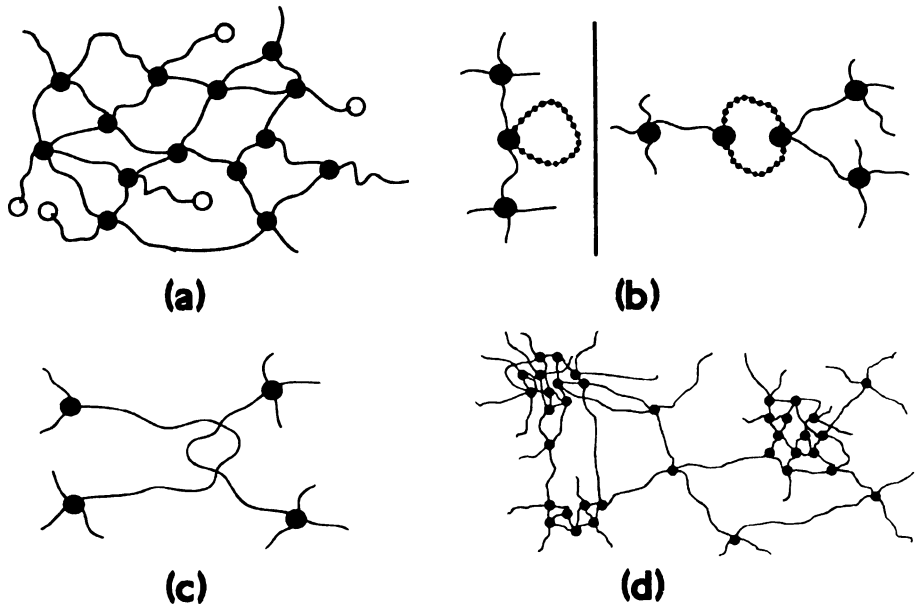

Figure 5.7: Schematic of common defects in crosslinked glassy polymers: (a) terminating chain ends (open circles), (b) intramolecular reactions (dashed line), (c) permanent entanglements, and (d) a heterogeneously crosslinked network. Solid lines represent polymer chains and solid circles signify crosslink junctions.

As a result of both the complex high temperature rearrangements and resin T_g, the mechanical tests at 250°C deviate from the trend, displaying a maximum in strength for the highest temperature cured (and thus highest T_g) systems. Also, the strength at 250°C increases with increasing BMPM monomer concentration, possibly due to the higher rigidity of these molecules yielding an increased thermal stability. A more perfect network structure contains less defects and thus an improved ability to undergo plastic flow near the T_g. In the case of a network consisting of numerous defects, a corresponding decreased network extensibility results in lower failure strains and flexural strength.

Flexur

except for t

observed fr

same trend a

identical p

later cure c

the C=C d

reduction in

For

modulus t

efficiency

3 C flexu

at 300 C d

formation

As

observed

BMPMD

bonds o

Observe

compos

Flexural modulus generally decreases with increasing cure (Figure 5.8), except for the final cure schedule, where a ~17% increase in modulus is observed (from 300°C/1 h to 300°C/6 h final cure temperature), which is the same trend as mass density. IM7/BMI composite laminates fabricated with the identical postcure cycles used here displayed processing microcracks for the latter cure conditions, but not for the former [184]. Also, overall, after all of the C=C double bonds of the 'ene' molecule have been consumed, a 10% reduction in stiffness occurs.

For resins cured ≤ 250°C, the mechanism responsible for the observed modulus trend appears to be primarily related to the molecular packing efficiency [192], and a quasi-linear relationship is observed when plotting the 23°C flexural modulus as a function of density (Figure 5.9). BMI resins cured at 300°C deviate from this trend, again most likely due to the ether crosslink formation and subsequent rearrangement.

As expected, the trends in failure strain (Figure 5.10) mirror those observed for flexural strength. No significant tendencies with respect to the BMPM:DABPA ratio could be determined. Again, after the C=C double bonds of the 'ene' molecule have all reacted, significant property changes are observed; a 25-40% ductility loss as a function of temperature and monomer composition.

Figure 5.8(a
stoichiometry

Figure 5.8
stoichiometry

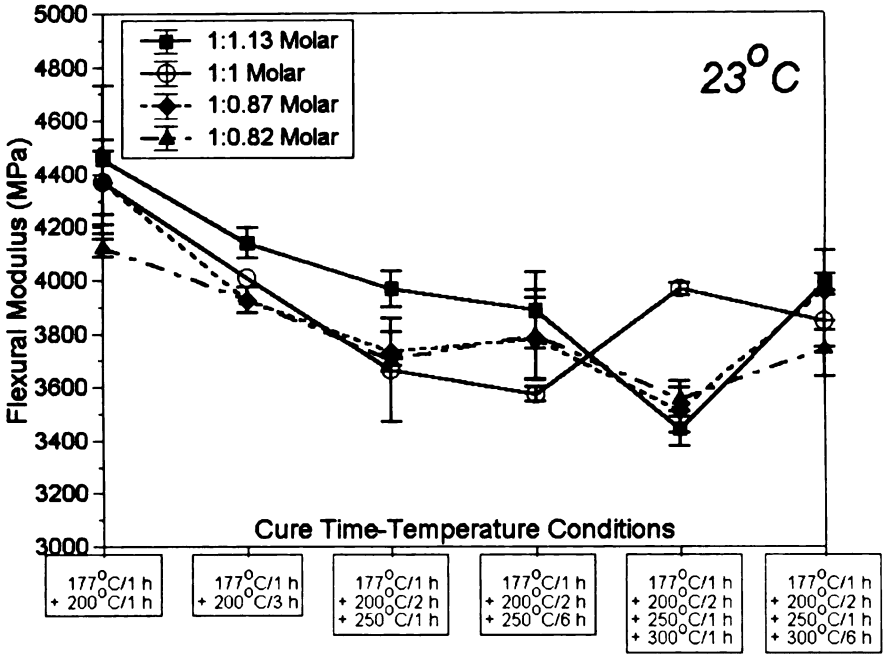

Figure 5.8(a): Flexural modulus as a function of cure and monomer stoichiometry for test temperature of 23°C.

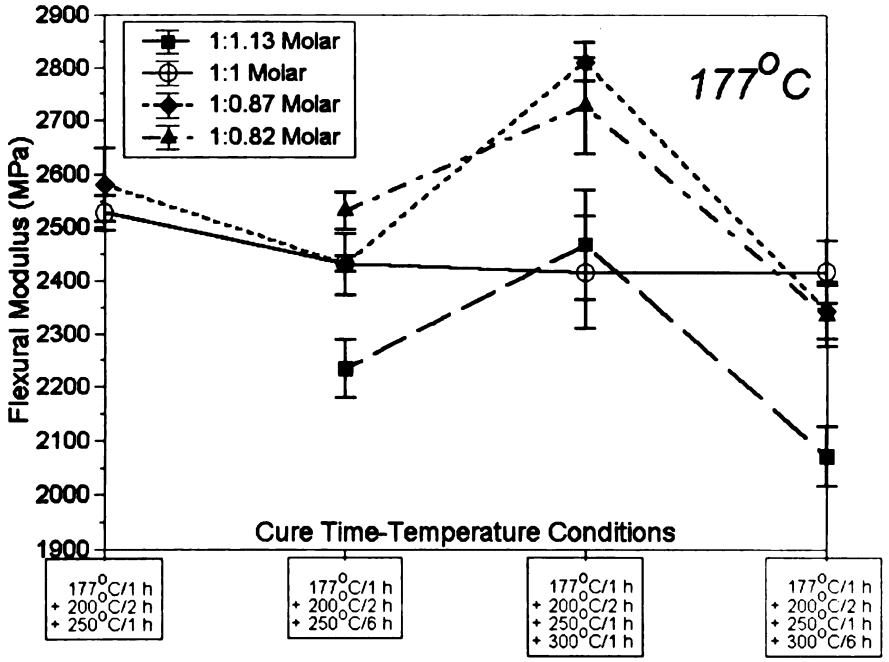

Figure 5.8(b): Flexural modulus as a function of cure and monomer stoichiometry for test temperature of 177°C.

Figure 5.8(
stoichiometry

Figure 5.9
cured at roo

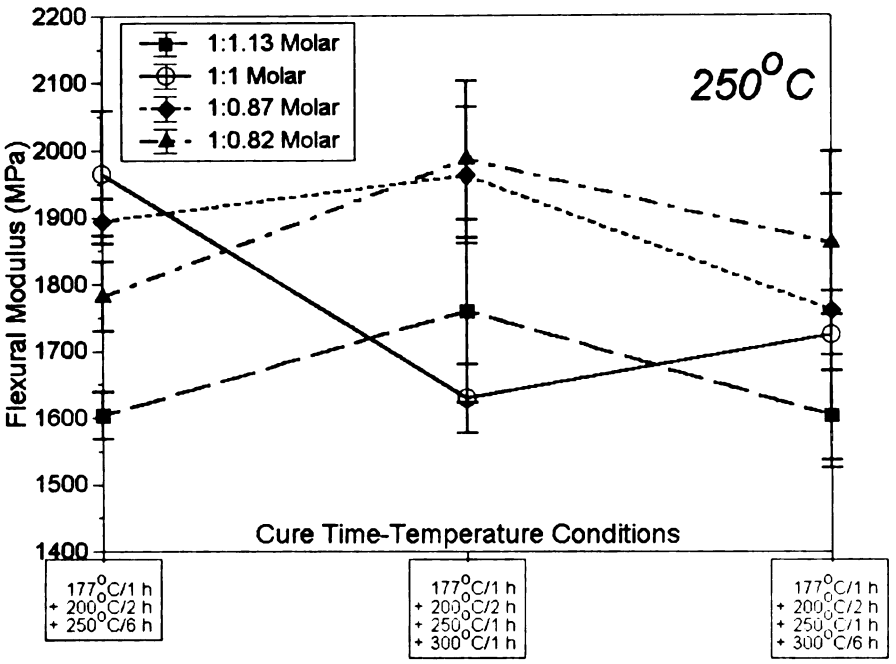

Figure 5.8(c): Flexural modulus as a function of cure and monomer stoichiometry for test temperature of 250°C.

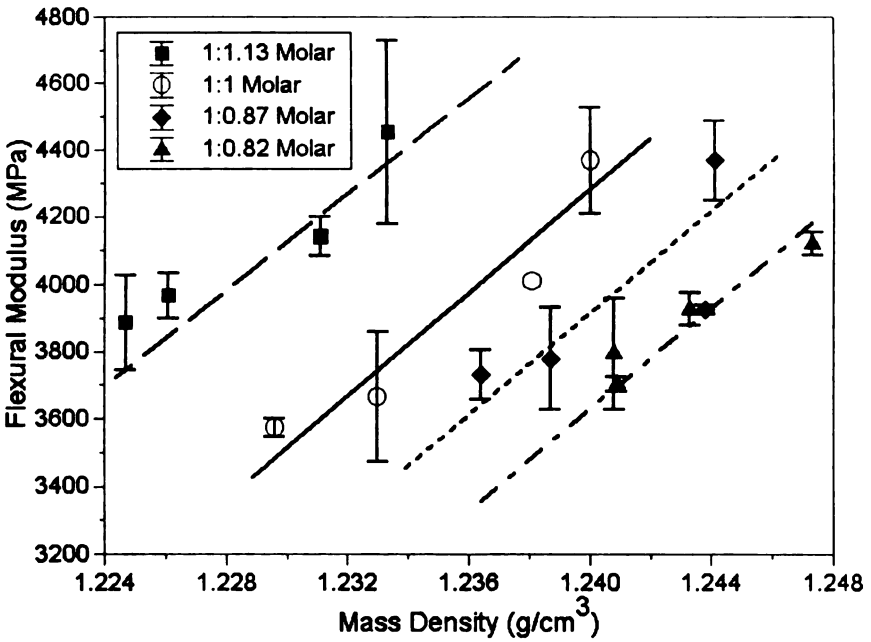

Figure 5.9: Flexural modulus as a function of mass density at 23°C for resins cured at temperatures ≤250°C.

5.3.3 Polyeth

The principal

behavior of P

and strain to

For the conte

but after anne

increasing th

reduction in

a 23% increa

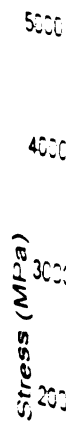

Figure

5.3.3 Polyetherimide

The principal controlling parameters responsible for the observed deformation behavior of PEI is free volume. Figure 5.10 displays the modulus, strength, and strain to failure of control (injection molded) and annealed polyetherimide. For the control polymer, deformation occurs via macroscopic shear banding, but after annealing deformation occurs by crazing that causes earlier failure, truncating the formation and growth of macroscopic shear bands. This reduction in glassy state free volume leads to an 85% reduction in failure strain, a 23% increase in tensile modulus, and a 10% increase in ultimate strength.

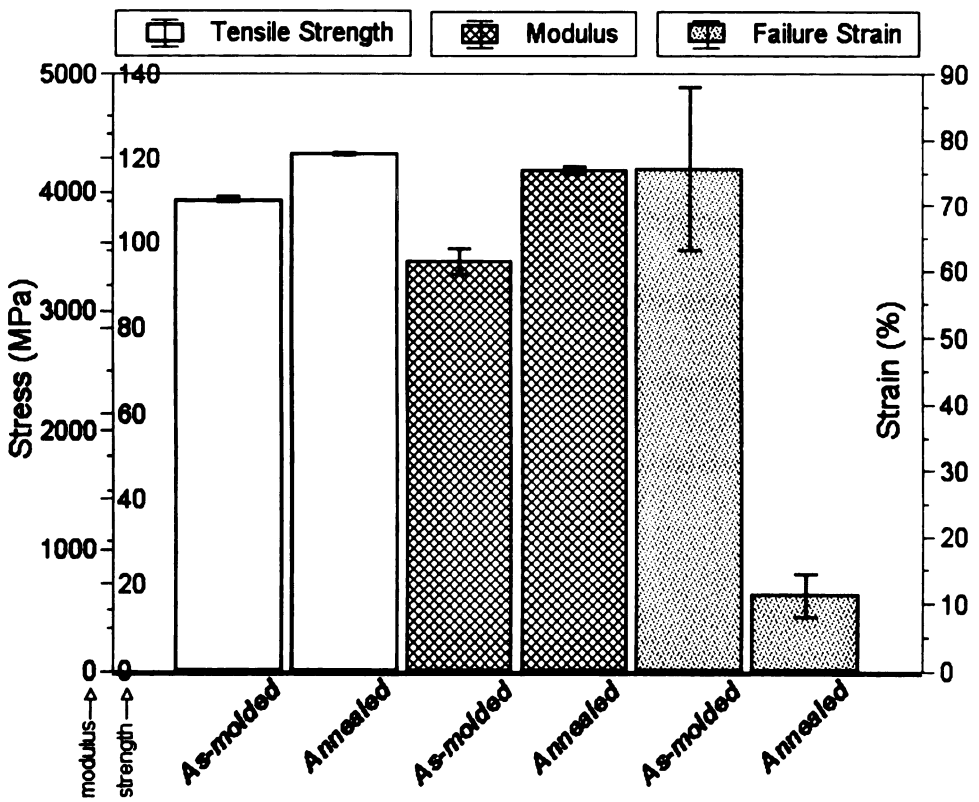

Figure 5.10: Tensile properties of PEI at 23°C.

Typica

polymer are

in Figure 5.

annealing are

annealing, po

region, a decr

A scr

obtained by r

more free vol

hydrogen bo

water up-take

both cases bu

the control,

material for v

experimental

was 0.044 g

1.278 g/cm

Typical stress versus strain curves for PEI control and as-molded polymer are shown in Figure 5.11 and their tensile fracture surfaces are shown in Figure 5.12. Differences in the deformation and failure behavior after annealing are evident upon observation of the fracture topography. After annealing, possible multiple craze formation is observed as are a smaller mirror region, a decrease in cavity development, and increased surface roughness.

A semi-quantitative measure of the free volume reduction can be obtained by moisture absorption experiments. Theoretically, the polymer with more free volume should absorb more moisture, since there are more polymer hydrogen bond sites accessible to the water molecules. Figure 5.13 displays the water up-take curves for both PEI specimens. The absorption is Fickian, in both cases but the annealed value of M_∞ is approximately 12% lower than for the control, meaning there are less accessible hydrogen bond sites in the material for water molecules. The diffusion coefficients are equivalent within experimental error. Similarly, the mass density of the annealed polyetherimide was 0.04% higher than the control material, with values of 1.2784 g/cm^3 and 1.2778 g/cm^3, respectively.

Figure

Figu

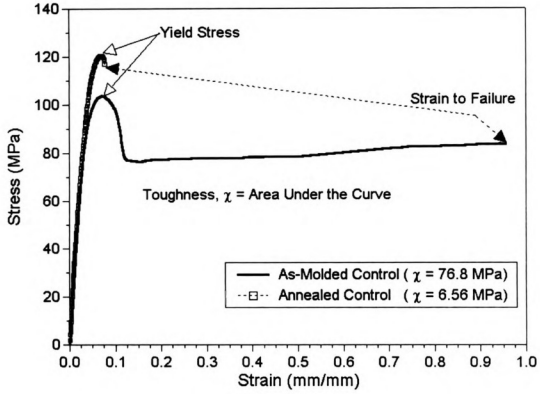

Figure 5.11: Tensile stress-strain curves for annealed and as-molded PEI.

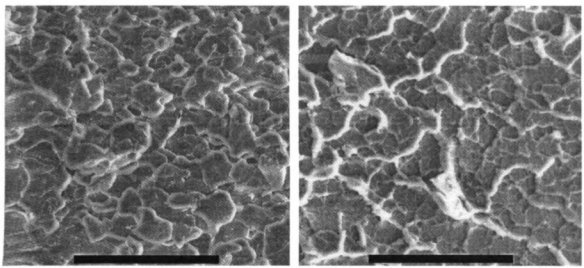

Figure 5.12: Comparative micrographs (same magnification; marker bar is 150μm) of as-molded (left) and annealed (right) PEI fracture surfaces.

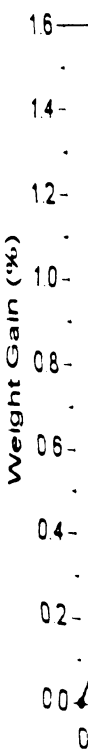

Figure 5.
annealed

5.3.4 Ph

Analysis

many st

additona

and Rad

volume

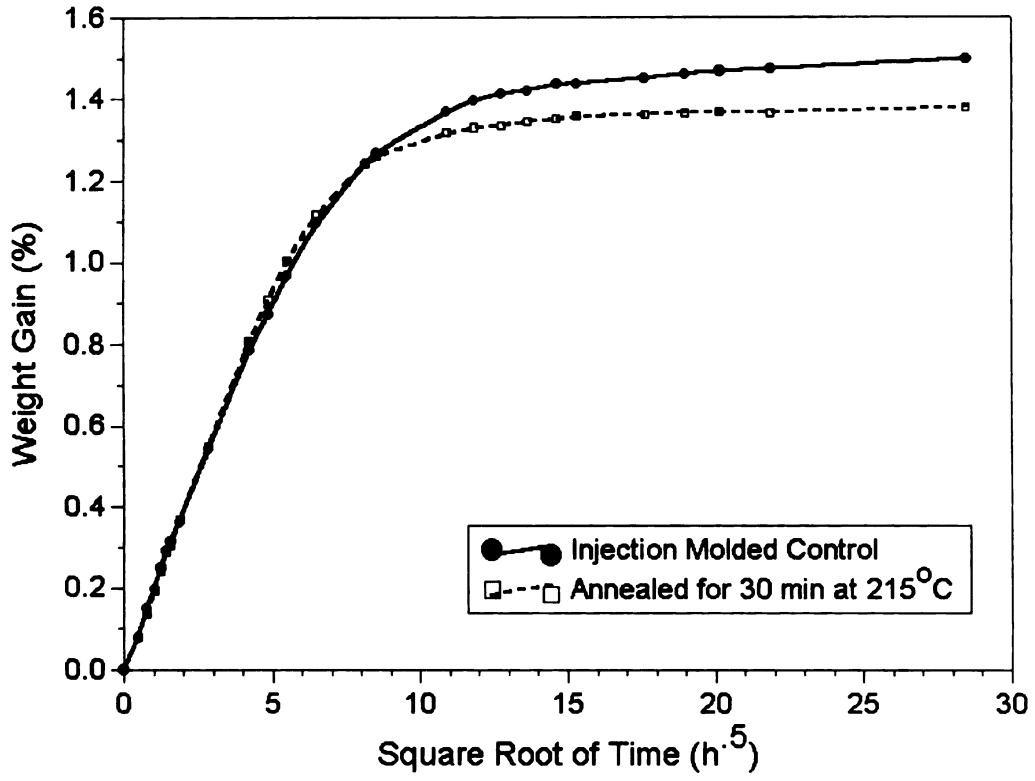

Figure 5.13: Moisture absorption curves (95°C/100%RH) of as-molded and annealed polyetherimide specimens.

5.3.4 Phenylethynyl Terminated Imide (PETI-5)

Analysis of PETI-5 is presented last since the deformation mechanisms have many similarities and parallels to all polymers discussed previously, plus additional attributes that are influential in controlling the mechanical response and failure modes of this material. That is, this polymer exhibits both free volume dependence and network structure dependence.

As r

morpholo

sum of a

The amor

presumab

this study

are the

exhibit

fabrica

Fi

As mentioned earlier, different cure cycles result in different polymer morphologies for this PETI-5 resin system. Figure 5.14 is a 20°C/min DSC scan of amorphous (371°C cure) and semicrystalline (350°C + 360°C cure). The amorphous material exhibits a 3°C higher T_g than the semicrystalline form, presumably a result of the higher degree of crosslinking of the former. From this study it is clear that the T_g is not as sensitive to the degree of crystallinity as are the mechanical properties. For semicrystalline PETI-5, the melting enthalpy is 11 J/g and melting point 392°C, both of which are independent of fabrication cooling rate within experimental error.

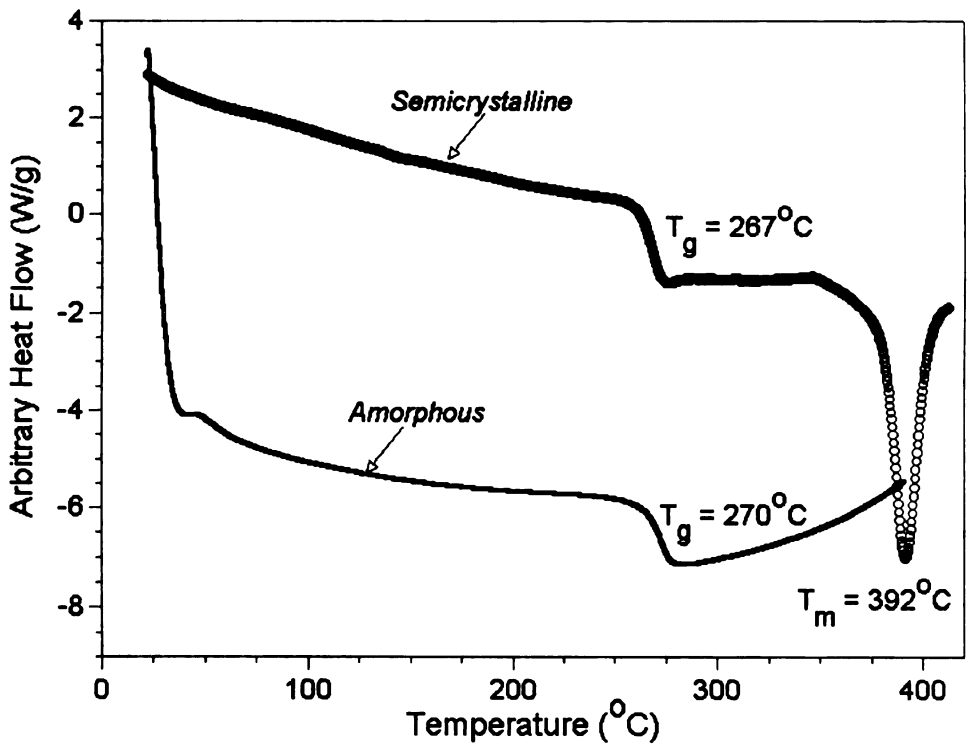

Figure 5.14: DSC scans (20°C/min) of amorphous and semicrystalline PETI-5.

Althou

nknown, th

property mo

competing w

system. Su

influence has

with differen

during the

between cro

In a

and crystal

crosslinking

slack' is ava

n the nee

significant

rate that

concentra

thickness

La

between

f the cr

Although the exact mechanism for the observed crystallization is unknown, the effects on resin mechanical response are substantial. These property modifications are manifested through crystallization prior to and/or competing with crosslinking. Crystallization inhibits crosslinking in this system. Similar crystallization behavior and corresponding deformation influence has been observed for other phenylethynyl terminated polyimides with different backbone structures [194]. It is evident from this research that during the 350-360°C isothermal holds, there are competing mechanisms between crosslinking and crystallization.

In a fundamental study, Lambert *et al.* [195] suggested that crosslinking and crystallization are interrelated in three different ways. These are: (i) crosslinking eliminates reptation in its conventional sense, and only 'reptation slack' is available for movements of the polymer chains exceeding nanometers, (ii) the need for exclusion of the bulky crosslinks for crystallization to occur significantly reduces the rate of secondary nucleation which results in a growth rate that decreases exponentially with crosslink density, and (iii) the concentration of crosslinks controls the upper limit possible for lamellar thickness.

Lambert *et al.* [195] demonstrated that when the molecular weight between crosslinks is high, crosslinks can be incorporated into the crystals, but if the crosslink density is high, the ability to crystallize decreases significantly.

Therefore, a s

cure tempera

exceed cons

amorphous p

lead to high

350C the i

reactions and

One o

crystallinity

PETI-5 neat

contain ther

mechanism

materials is

Brown [19]

is more com

required to

behavior of

Diffe

semicrystall

Table 5.3

lower mod

Therefore, a solubility limit exists for crosslinks in a crystal. At an isothermal cure temperature of 371°C for the PETI-5 system, the crosslinking kinetics exceed considerably the nucleation rate of crystal growth, and thus an amorphous polymer is obtained. Lower crystallization temperatures generally lead to higher crystallization rates [196-197], and therefore when curing at 350°C the isothermal crystallization rate competes with the crosslinking reactions and a partially crosslinked, semicrystalline morphology is obtained.

One of the goals of the present research was to determine the effects of crystallinity on the deformation processes and mechanical properties of the PETI-5 neat resin, since the fabrication of thick composite components will contain thermal gradients throughout the thickness of the mold. The actual mechanism of deformation on the molecular level for partially ordered materials is not completely understood, but has been described by Russell and Brown [198] for an aromatic polyimide using x-ray studies. Here, the situation is more complex for particles crystallized and crosslinked, and future research is required to achieve a better understanding of crystallization and crosslinking behavior of phenylethynyl terminated systems in general.

Differences between the physical and mechanical properties of semicrystalline and amorphous PETI-5 are displayed in the first two rows of Table 5.3. The amorphous polymer has a 170% higher strain to failure, a 12% lower modulus, and a 0.7% lower mass density than the semicrystalline

material. I

concentrati

Table 5.3:
morpholog

Thermal History
3 h @ 350 C
1 h @ 360 C
1.5 h @ 37
3 h @ 350 C
1 h @ 360 C
3 h @ 350 C
1 h @ 360 C
3 h @ 350 C
1 h @ 360 C

1 - Ser

Clea

failure of

beneficial

Hergentro

strength a

amorphou

interphase

transien

material. Fracture surfaces of the semicrystalline material displayed a higher concentration of defect sites than the amorphous morphology (Figure 5.15).

Table 5.3: Mechanical and physical properties of PETI-5 as a function of morphology and thermal history.

Thermal History	Cooling Rate	Mass Density (g/cm^3)	Yield Strength (MPa)	Tensile Modulus (MPa)	Failure Strain (%)
3 h @ 350°C + 1 h @ 360°C	1.1°C/min	1.354	117.5 ± 7.65	3424 ± 258	9.50 ± 2.7
1.5 h @ 371°C	1.1°C/min	1.345	120.9 ± 1.21	3024 ± 88.4	25.7 ± 4.6
3 h @ 350°C + 1 h @ 360°C	8.7°C/min	1.354	119.1 ± 4.66	3253 ± 90.7	11.6 ± 2.0
3 h @ 350°C + 1 h @ 360°C	Ice Quench	1.347	107.3 ± 4.23	3136 ± 106	20.6 ± 1.7
3 h @ 350°C + 1 h @ 360°C	1.1°C/min	1.354	119.8 ± 2.05	3091 ± 297	11.2 ± 4.7

- Semicrystalline morphology - Amorphous morphology

Clearly the morphology plays a critical role in the deformation and failure of PETI-5 neat resin, but tailoring the matrix morphology may be beneficial in specific composite structural applications. For example, Hergenrother *et al.* [199] reported a higher value for the short beam shear strength at 177°C of semicrystalline PETI-5 as opposed to the completely amorphous material, and other researchers have attributed an improved interphase in polyetheretherketone (PEEK) [200-201] and polyetherimide [202] to transient crystallinity. PETI-5 liquid crystalline precursor may lead to a more

uniformly crosslinked network because of aggregation of the liquid crystal states of phenylethynyl end-groups.

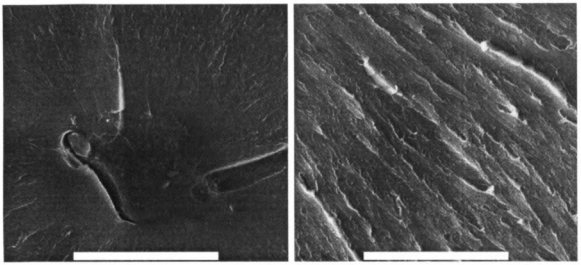

Figure 5.15: Fracture surface topography of PETI-5 showing a crack initiation site/defect and slow fracture region (left) and typical surface topography of medium/fast fracture region (same magnification; marker bar is 45μm).

In order to determine the role of free volume in the deformation mechanisms of PETI-5, various cooling rates and annealing temperatures were examined. Figure 5.16 displays the effect of cooling rate on elongation to break, modulus, tensile yield strength, and mass density of semicrystalline PETI-5. The observed increase in strain to failure, decrease in modulus, slight decrease in strength, and decrease in density with increasing cooling rate are representative of primarily a free volume-controlled deformation mechanism. With higher cooling rates from the cure temperature, additional amounts of

free volume a

dependence

crosslinked th

These chang

hypothesis of

are highly ch...

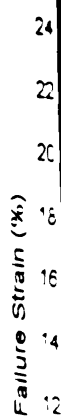

Figure 5.16(

free volume are locked into the overall structure. This significant free volume dependence is more indicative of a glassy thermoplastic than a highly crosslinked thermoset network, such as the BMI system discussed previously. These changes in toughness as a function of thermal history support the hypothesis of other researchers [185] that the phenylethynyl terminated systems are highly chain extended.

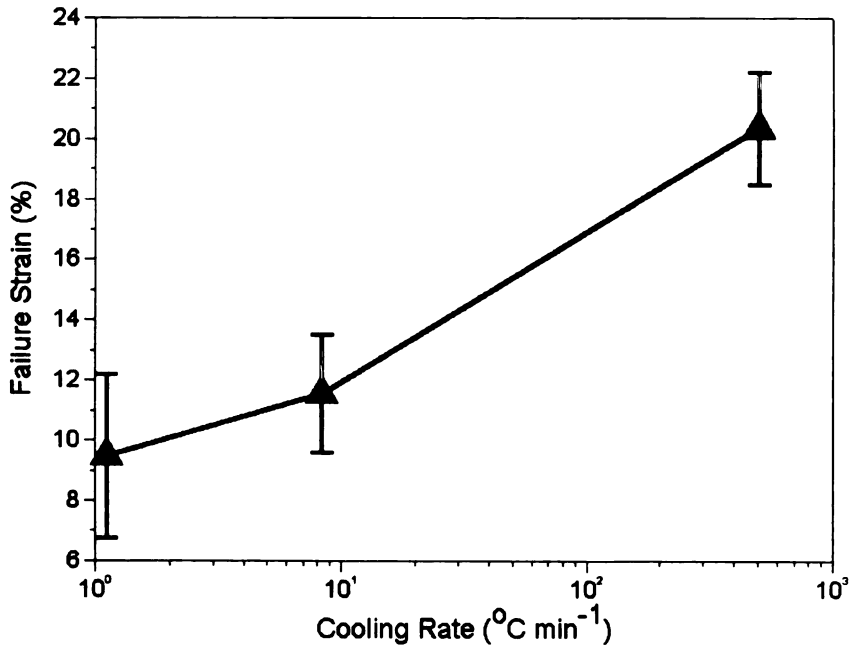

Figure 5.16(a): Effect of cooling rate on failure strain of PETI-5.

Figure 5.1

Figure

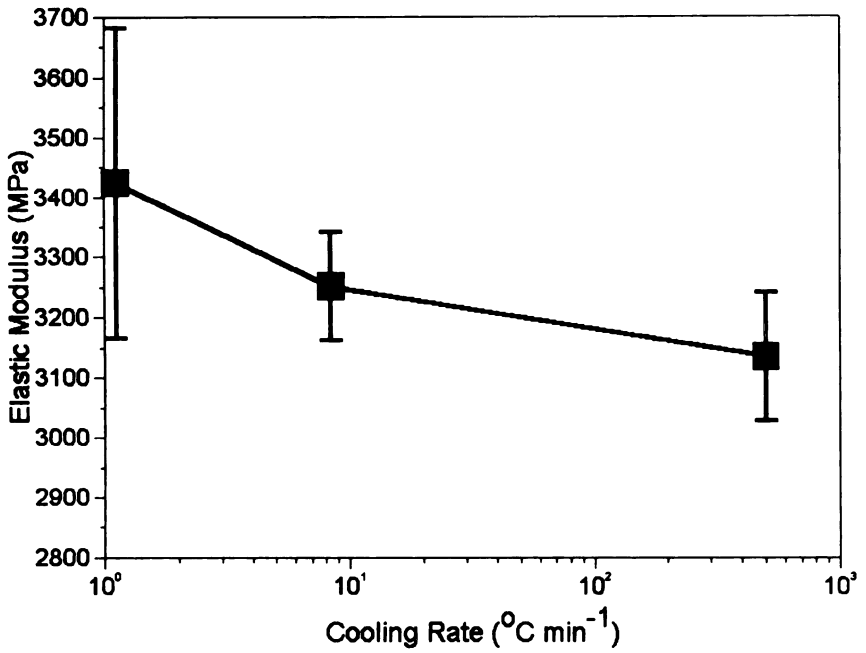

Figure 5.16(b): Effect of cooling rate on elastic modulus of PETI-5.

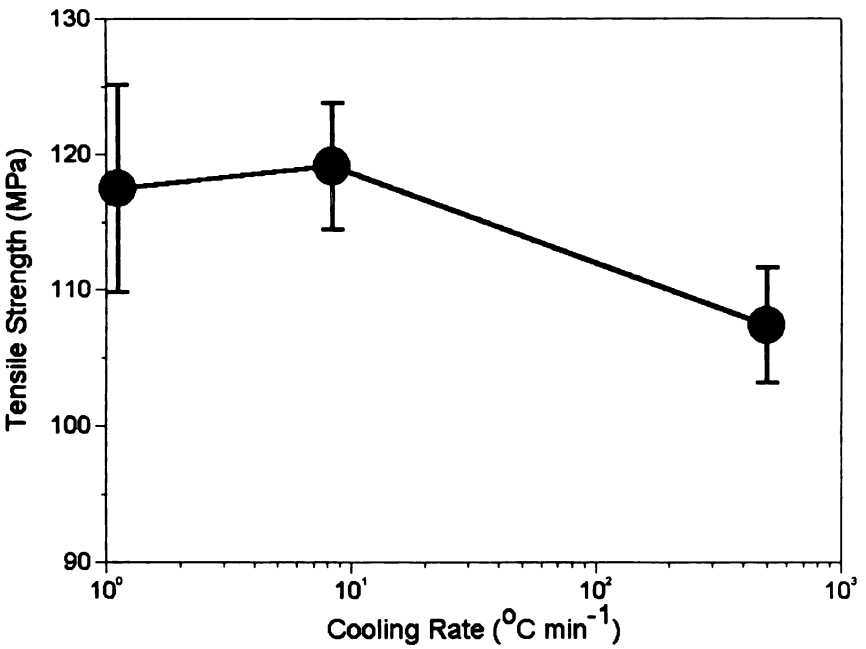

Figure 5.16(c): Effect of cooling rate on failure tensile strength of PETI-5.

Figure 5.1

In a

middle,

respectivel

semicrysta

after fabri

observed

strain to f

In

Amorphic

deformat

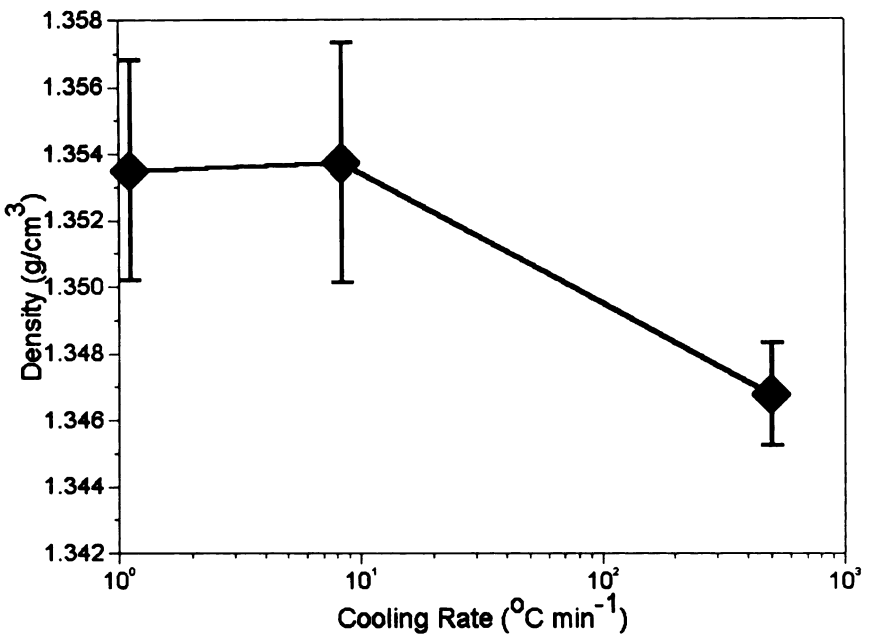

Figure 5.16(d): Effect of cooling rate on mass density of PETI-5.

In addition to cooling rate, the effects of annealing on strain to failure, modulus, yield strength, and mass density are displayed in Figures 5.17-5.20, respectively, for both slow cooled (1.1°C/min) and ice quenched semicrystalline PETI-5. For the latter case, significant free volume is present after fabrication, so upon annealing a reduction in glassy state free volume is observed by an increase in density, yield strength, modulus, and a decrease in strain to failure as a function of annealing temperature.

In contrast, annealing of the slow cooled resin results in some apparent anomalies in the mechanical response (if free volume is assumed the primary deformation controlling parameter), especially at the highest annealing

emperature of

emoved by an

hus observable

he apparent an

due to breaking

rearrangement

espective hig

For ex

olycarbonate

recrystalline

defects which

he bulk imm

an initial decr

from the gro

n melting en

so the precis

pon anneal

rystalline p

temperature of T_g – 10°C. Since there is less free volume initially to be removed by annealing, other mechanisms may become more dominant and thus observable in the deformation behavior. A possible partial explanation for the apparent anomalies upon annealing at temperatures very near T_g could be due to breaking some of the crosslinks near T_g and/or a possible modification (rearrangement, partial unfolding, growth, etc.) of the ordered phase under the respective high molecular mobility conditions.

For example, Morgan *et al.* [203-204] observed similar behavior in polycarbonate; at annealing temperatures below the glass transition temperature precrystalline and crystalline entities were able to grow on surfaces and cause defects which truncated the flow process. Crystalline growth was possible in the bulk immediately above T_g due to increased mobility. The authors reported an initial decrease upon annealing at 145°C, then a nearly 5% increase in density from the growth of ordered regions. For PETI-5 investigated here, no change in melting enthalpy or shift in T_g after any annealing condition was observed, so the precise mechanisms responsible for the trends in deformation behavior upon annealing are not conclusive, but speculated to be due in part to the crystalline phase.

Figure 5.17:
semicrystalline

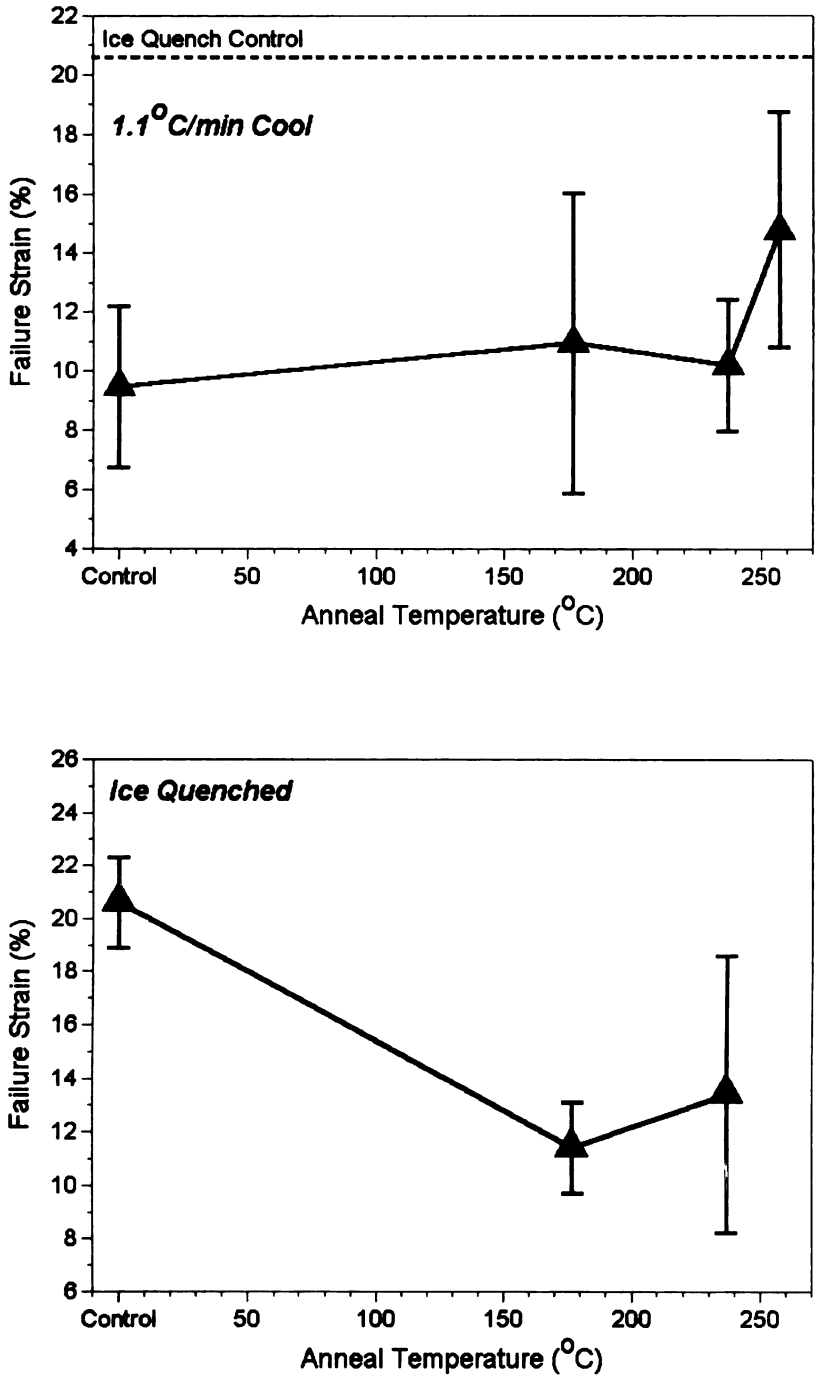

Figure 5.17: Effects of annealing temperature on the tensile strain to failure of semicrystalline PETI-5 resin for slow cooled (top) and ice quenched (bottom).

Figure

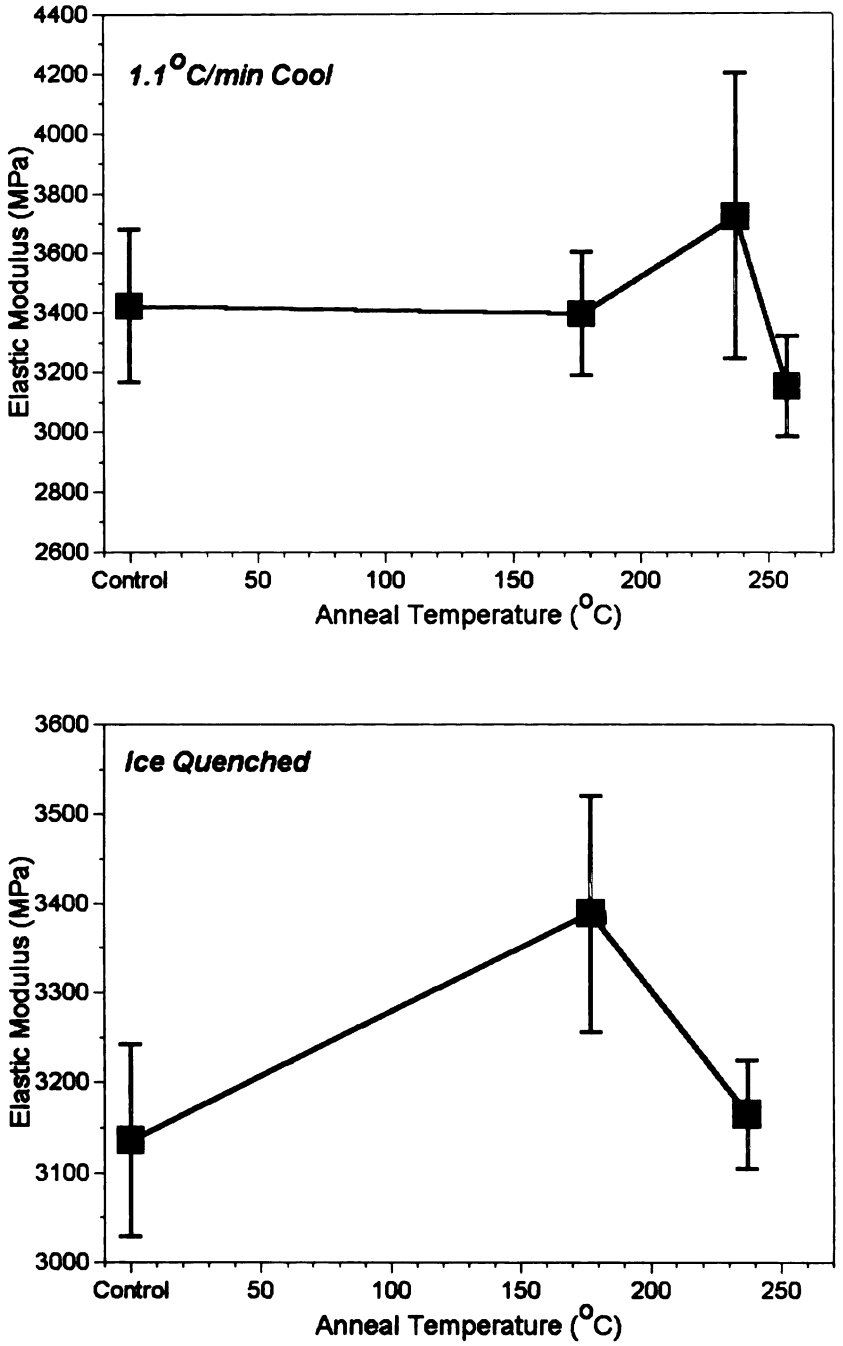

Figure 5.18: Effects of annealing temperature on elastic modulus of semicrystalline PETI-5 resin for slow cooled (top) and ice quenched (bottom).

Figure

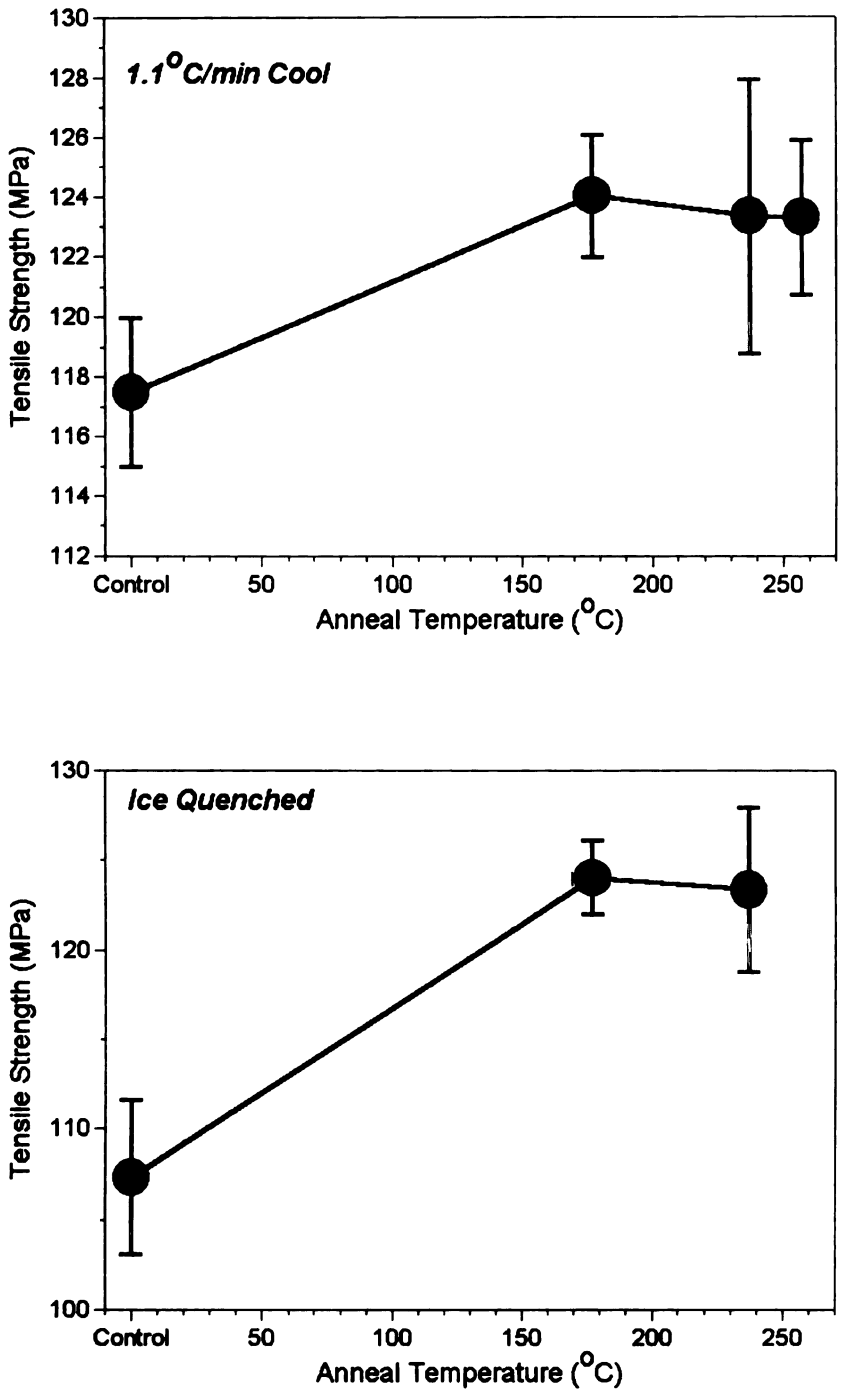

Figure 5.19: Effects of annealing temperature on tensile strength of semicrystalline PETI-5 resin for slow cooled (top) and ice quenched (bottom).

1.357
1.356
1.355
1.354
1.353
1.352
1.351
1.350
1.349
1.348
1.347
1.346
Density (g/cm3)
1.36
1.35
1.34
1.33
1.32
1.31
1.30
1.29
1.28
1.27
Density (g/cm3)

Figure 5

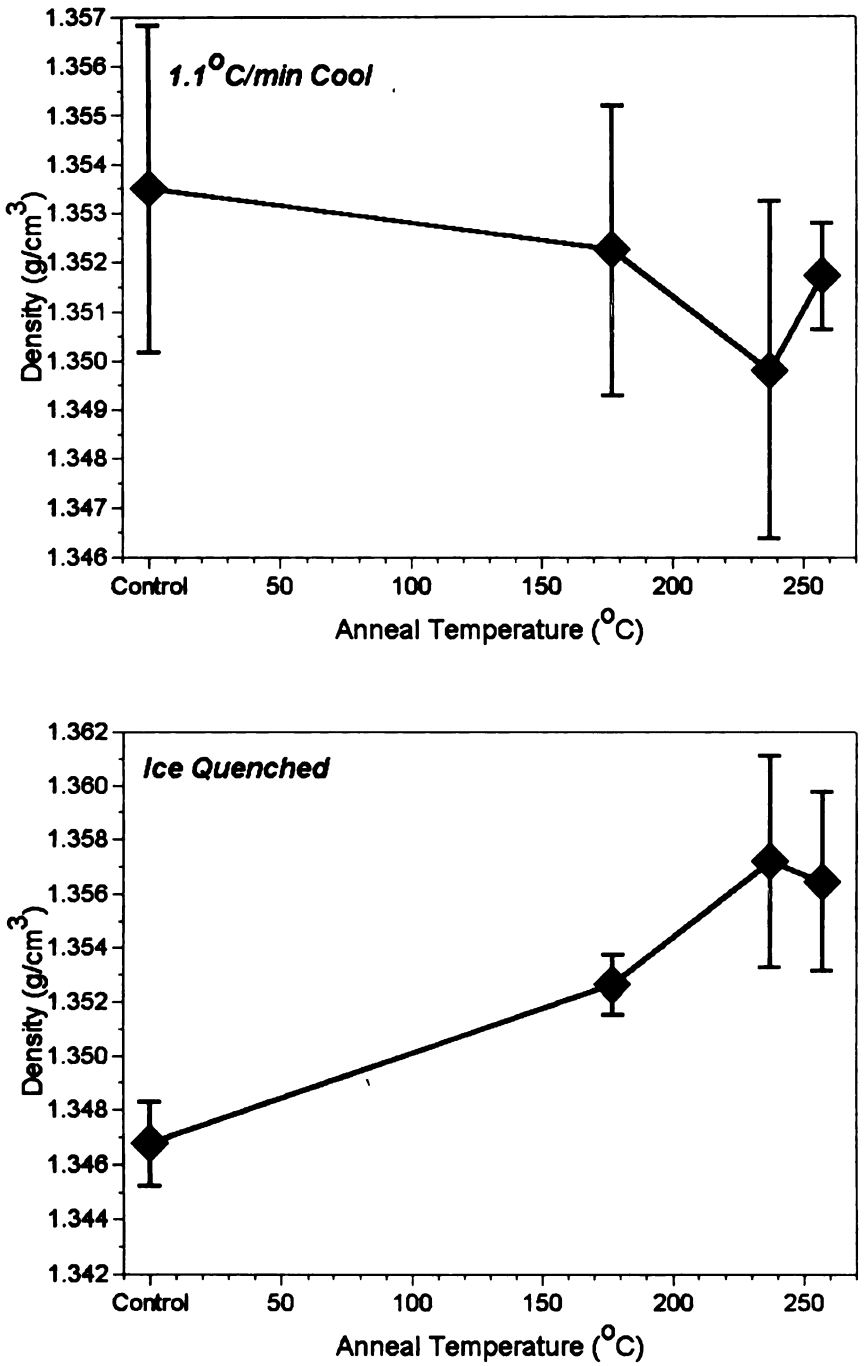

Figure 5.20: Effects of annealing temperature the mass density of semicrystalline PETI-5 resin for slow cooled (top) and ice quenched (bottom).

In gene

properties of P

temperature, an

dependent. At

deformation m

compared to the

5.4 Conclusi

The effects o

mechanisms.

crosslinked P

PETI-5 were

Defo

of thermal

induced gl

microvoid

The

amount o

strain, a 2

a 12% d

reduction

In general, the cumulative data demonstrate that the mechanical properties of PETI-5 are reversible upon annealing below the glass transition temperature, and thus the deformation mechanisms are strongly free volume dependent. Also, the presence of a crystalline phase plays a critical role in the deformation mechanism, leading to a 170% decrease in ductility when compared to the completely amorphous system.

5.4 Conclusions

The effects of processing conditions on the physical structure, deformation mechanisms, and mechanical response of thermoplastic POPPI, highly crosslinked BMI, thermoplastic PEI, and partially crosslinked, semicrystalline PETI-5 were reported.

Deformation of POPPI can be divided into three regimes as a function of thermal history and annealing conditions: (i) 300-323°C; physical aging-induced glassy state free volume decreases, (ii) 323-375°C; thermally activated microvoid collapse, and (iii) >375°C; thermooxidative chemical degradation.

The mechanical response of PEI was shown to be controlled by the amount of free volume present in the polymer. An 85% reduction in failure strain, a 23% increase in tensile modulus, a 10% increase in yield strength, and a 12% decrease in equilibrium moisture content after annealing at the glass transition temperature for 30 min were observed.

PETI-5

volume and th

170°s reducti

concentration

In general, th

temperatures

BMPY

imal mono

physical, th

proceeds, th

packing effi

segments a

crosslink fo

crosslinks

and mech

mechanica

to stiffer

network

PETI-5 displayed a deformation behavior dependent on both free volume and the presence of a crystalline phase, the latter of which resulted in a 170% reduction in ductility and fracture topography consisting of a higher concentration of defects compared to the completely amorphous morphology. In general, the toughness could be removed upon annealing below T_g, even at temperatures as low as 177°C.

BMPM/DABPA BMI network structure was shown to be a function of initial monomer stoichiometry and the network formation monitored by physical, thermal, and mechanical property changes during cure. As cure proceeds, the network becomes increasingly more three-dimensional and the packing efficiency decreases. Excess BMPM segments are stiffer than DABPA segments and do not pack as efficiently on the molecular level. Also, the ether crosslink formation, dissociation, and subsequent rearrangement to less flexible crosslinks was shown to play a critical role in the overall resin physical, thermal, and mechanical response. The primary factors controlling BMI resin mechanical response are (i) the instability and rearrangement of ether crosslinks to stiffer crosslinked segments, (ii) the presence of unreacted groups and other network defects, and (iii) network packing efficiency.

Chapter 6

Fundamental Investigation of Polyimide Deformation after Degradation and Plasticization

6.1 Introduction

Before continuing with an analysis of the hygrothermal degradation mechanisms, thresholds, and kinetics, it is first necessary to evaluate the fundamental effects of (i) matrix plasticization by moisture and (ii) thermooxidative induced chemical degradation on the mechanical properties of polyimides.

Most models that predict matrix and/or composite lifetimes in high temperature environments base their analysis primarily on mass loss, either isothermally or via techniques which employ various heating rates [147, 209-212]. Here, the correlation between weight loss and mechanical properties will be investigated for Avimid® K3B thermoplastic polyimide.

The fundamental effects of matrix plasticization by moisture, exclusive of chemical degradation, will also be correlated to mechanical and thermal properties. Although the magnitude and mechanisms of mass loss via chemical degradation and moisture plasticization effects are material dependent (chemical structure, physical structure, thermoplastic, thermoset, etc.), the

general princip

a basic unders

and the charac

and correctly

6.2 Experin

6.2.1 Mater

Around 3 K

simultaneou

approximat

and the so

was then c

into a fine

The

KSB pow

release. I

according

Bedding

the mas

supplied

general principles involved are similar for polyimide matrices (Chapter 2). Such a basic understanding is important so that correlations between lifetime models and the characterization of degradation mechanisms can be properly applied and correctly interpreted, respectively.

6.2 Experimental Techniques

6.2.1 Material Preparation

Avimid® K3B polyamic acid/*N*-methyl pyrrolidone (NMP) solution was simultaneously dried and imidized (cyclodehydration reaction) at 177°C for approximately 10 min under atmospheric pressure, then vacuum was applied and the solution heated to 210°C and held isothermally for 2 h. The material was then cooled slowly to room temperature and the imidized material ground into a fine powder by a cryogenic mill.

Thermoplastic plaques, 2 mm thick, were prepared by placing 110 g of K3B powder in a 400 cm^2 stainless steel mold coated with Frekote® 44 mold release. Pressure and heat were applied using a Tetrahedron® hydraulic press according to the processing conditions depicted in Figure 6.1 (compression molding). Using the hydrostatic weighing technique described in Chapter 3, the mass density of K3B was found to be 1.336 g/cm^3, which is the value supplied by the manufacturer, indicating no significant voids were present in

the panels.

rea of the

points along

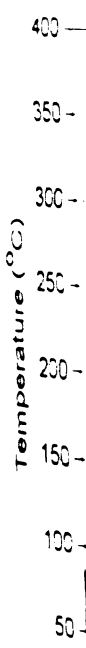

Figure 6
compres

6.2.2 S

The K3

into rec

rectang

the panels. The thickness was found to vary by less than 0.1% throughout the area of the 400 cm^2 panel, based on caliper measurements taken at various points along the plaque.

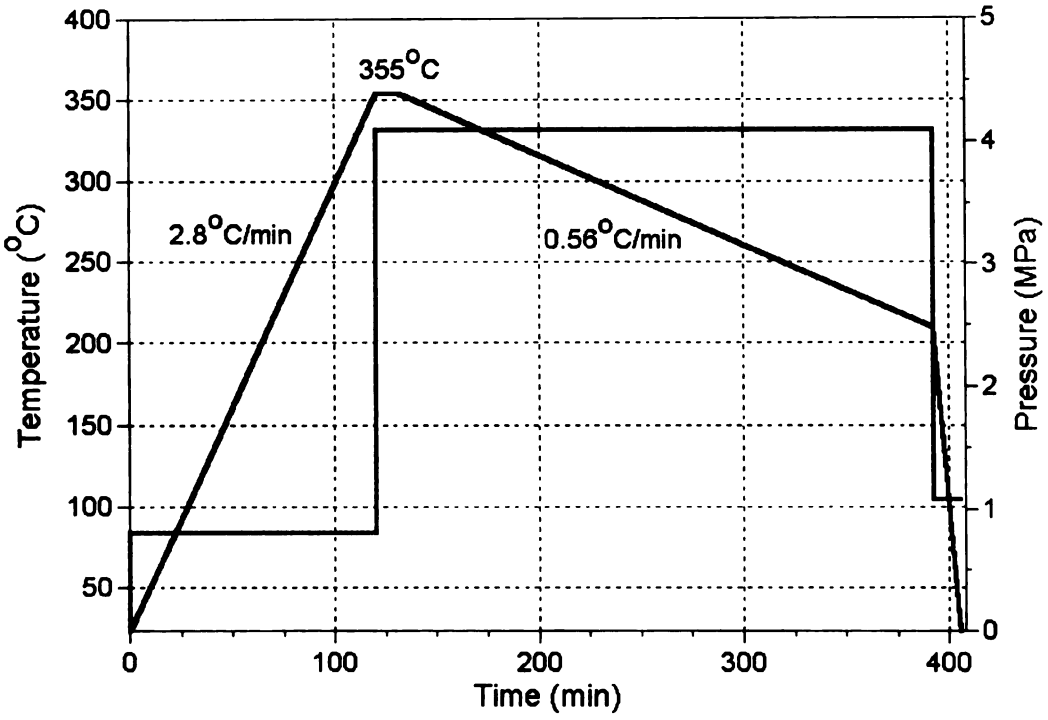

Figure 6.1: Processing conditions for the manufacture of thermoplastic K3B compression molded panels.

6.2.2 Specimen Preparation

The K3B panels were sectioned using a diamond blade saw and running water into rectangular bars with dimensions 100 mm x 15 mm x 2 mm. Some of the rectangular bars (those used for the moisture absorption experiments) were cut

into dogbon

and the edge

6.2.3 Spe

For the pla

ionized wa

completely

15% d

maximum

Upon ren

ionized w

days. T

tensile te

T

tensile s

were ex

Additio

rates w

both be

into dogbone samples with a 2.54 cm gage length using a Tensile-Cut® mill, and the edges of the milled coupons lightly polished.

6.2.3 Specimen Conditioning

For the plasticization experiment, five dogbone specimens were placed in a de-ionized water bath at 80°C, and held isothermally for 16 days (384 h) until completely saturated with moisture. The samples were found to have absorbed 1.37% (deviation $\pm$0.06%) moisture, which corresponds closely to the maximum moisture content for this material reported in the literature [159]. Upon removal from the moisture bath, the samples were maintained in de-ionized water at room temperature in a sealed container until tested (~1.5 days). The weight was recorded on a balance immediately prior to mechanical tensile testing.

Thermooxidative degradation was carried out by placing the rectangular tensile specimens on a glass plate in an air-circulating furnace. The samples were exposed to temperatures of 275, 300, 325, 350, and 375°C for 1000 min. Additional samples were exposed for 5000 min at 325°C. Heating and cooling rates were 2.5°C/min and 1°C/min, respectively. Sample mass was recorded both before and after thermal exposure.

6.3 Results a

6.3.1 Matrix P

The T_g depres

polyimide. Thi

that the T_g is d

reduction in T

35°C lower if s

Table 6.1: T

Moisture Con
1.37 ± 0.0

The r

change due

strength, a

modulus w

decrease in

Young's m

absorbed

for this po

depend on

6.3 Results and Discussion

6.3.1 Matrix Plasticization

The T_g depression by matrix plasticization is shown in Table 6.1 for K3B polyimide. This value corresponds closely to the rule of thumb for polyimides that the T_g is decreased 25°C / weight % absorbed moisture. This significant reduction in T_g indicates that the maximum use temperature for K3B will be 35°C lower if saturated with moisture.

Table 6.1: T_g knockdown of K3B after moisture saturation.

Moisture Content	Wet T_g	Dry T_g	%Δ
1.37 ± 0.06	212	247	14

The mechanical properties, on the other hand, show only a minor change due to matrix plasticization, as shown in Figure 6.2. A 2% decrease in strength, a 4% increase in strain to failure, and a 6.5% decrease in Young's modulus were observed. Extrapolated, these changes correlate to a 1.5% decrease in strength, 2.9% increase in failure strain, and a 4.7% reduction in Young's modulus per weight percent moisture. Clearly plasticization due to absorbed moisture is more influential to the T_g than the mechanical properties for this polyimide, but it should be noted that the effects of plasticization also depend on the physical structure of the polymer.

Figure 6.2:
plasticizatio

6.3.2 Ther

Mass loss

highest ma

condition.

composite

In o

properties,

temperatu

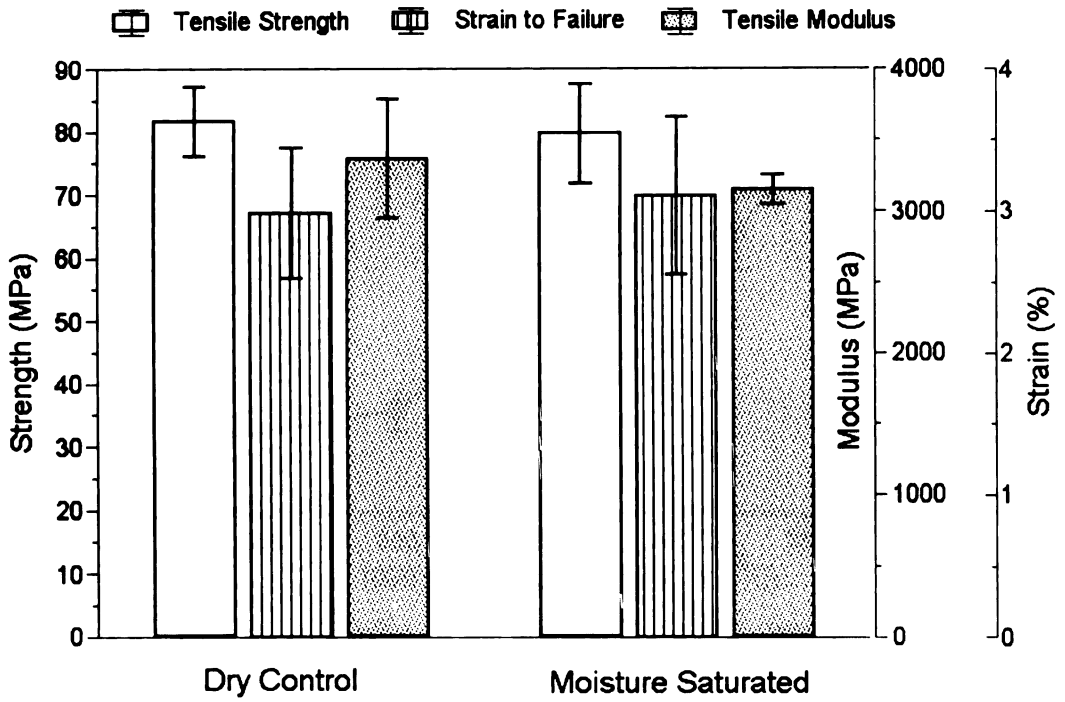

Figure 6.2: Mechanical property changes of K3B polyimide after matrix plasticization due to absorbed moisture (1.37 weight %).

6.3.2 Thermooxidative Degradation

Mass loss as a function of aging temperature is plotted in Figure 6.3. The highest mass loss of 2.97% was observed after the 375°C/1000 min aging condition. Usually, a mass loss of 2% for a 60% fiber volume fraction composite is considered adequate thermooxidative stability.

In order to examine the relationships between mass loss and mechanical properties, plots were constructed as a function of weight loss and aging temperature, shown in Figures 6.4 and 6.5, respectively.

Figure
function

Young's Modulus (MPa)

Figure 6.1

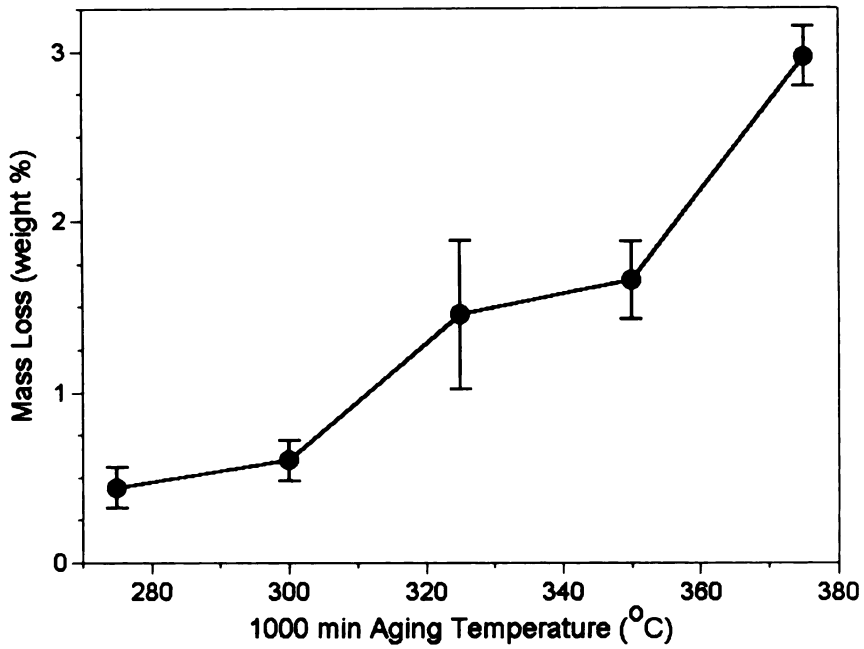

Figure 6.3: Mass loss due to thermooxidative degradation of K3B as a function of aging temperature.

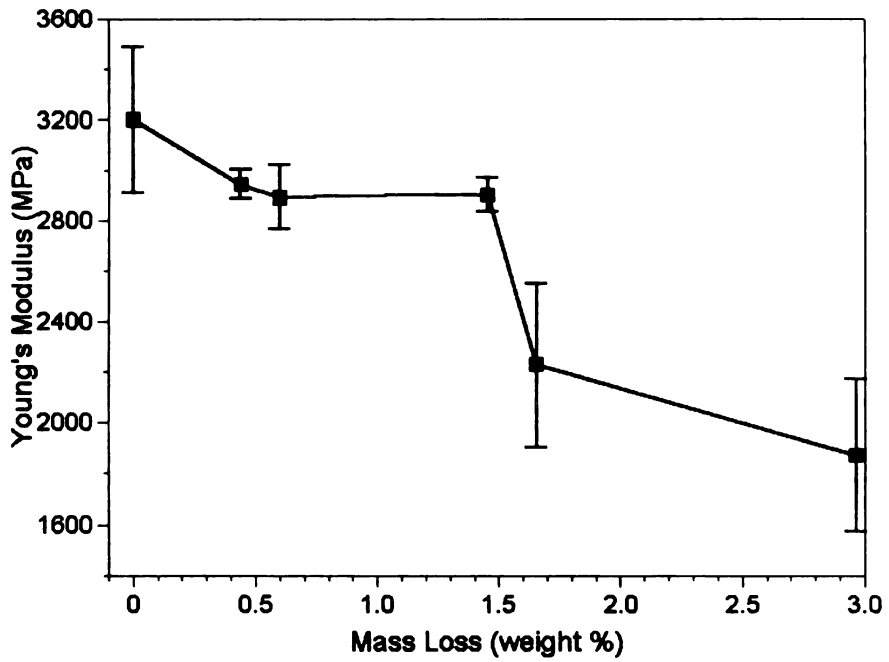

Figure 6.4(a): Young's modulus as a function of thermooxidative mass loss.

Figu

Figure

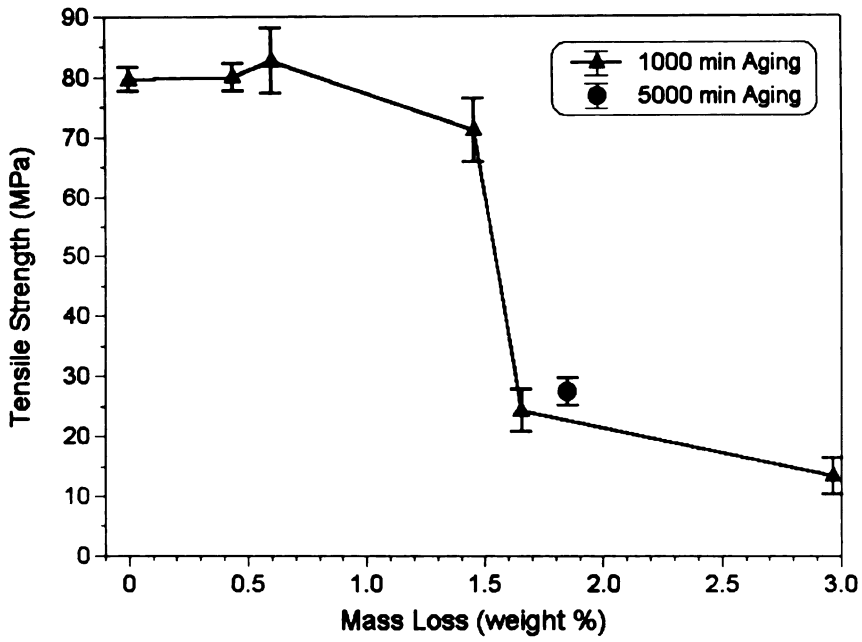

Figure 6.4(b): Tensile strength as a function of thermooxidative mass loss.

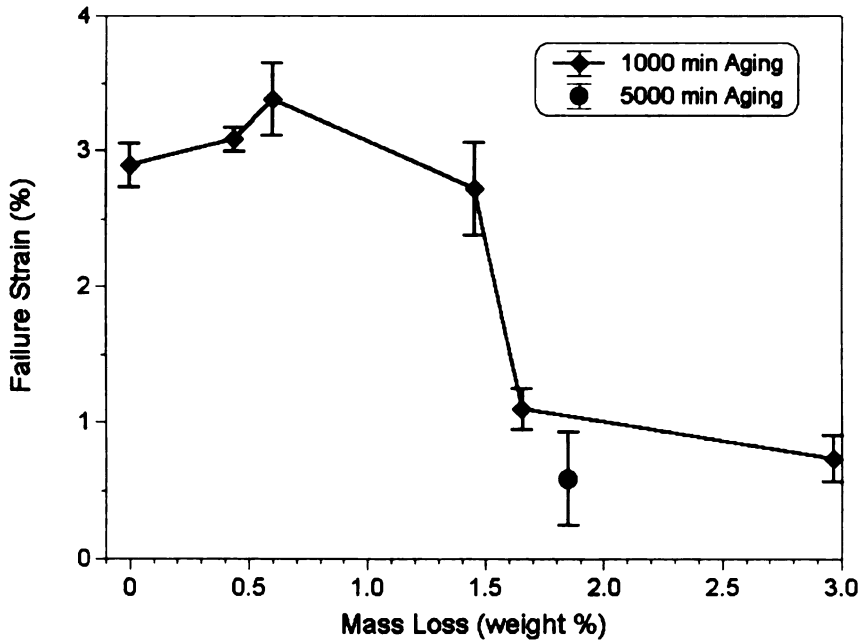

Figure 6.4(c): Failure strain as a function of thermooxidative mass loss.

Young's Modulus (MPa)

ure 6

Tensile Strength (MPa)

re 6.

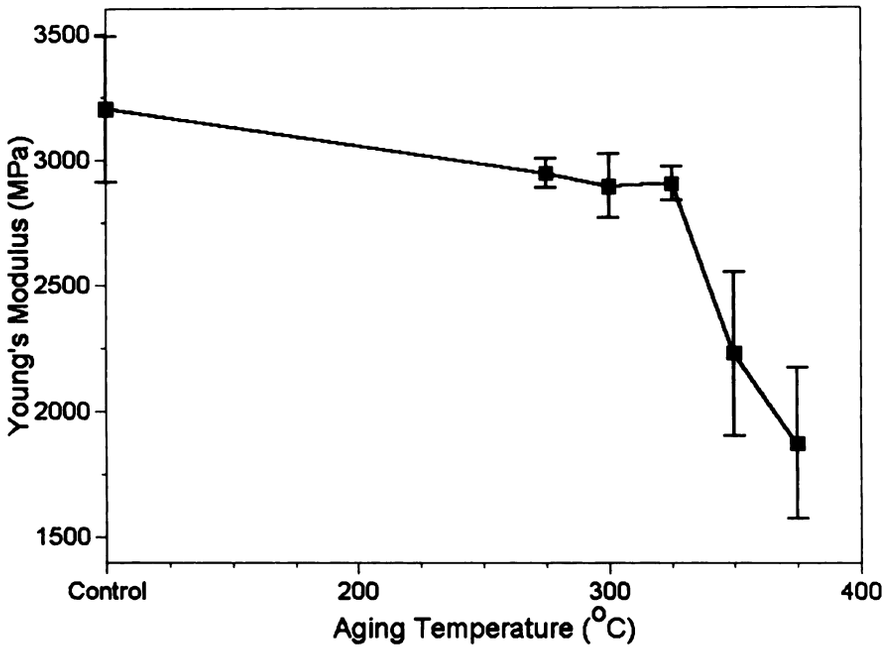

Figure 6.5(a): Young's modulus as a function of 1000 min aging temperature.

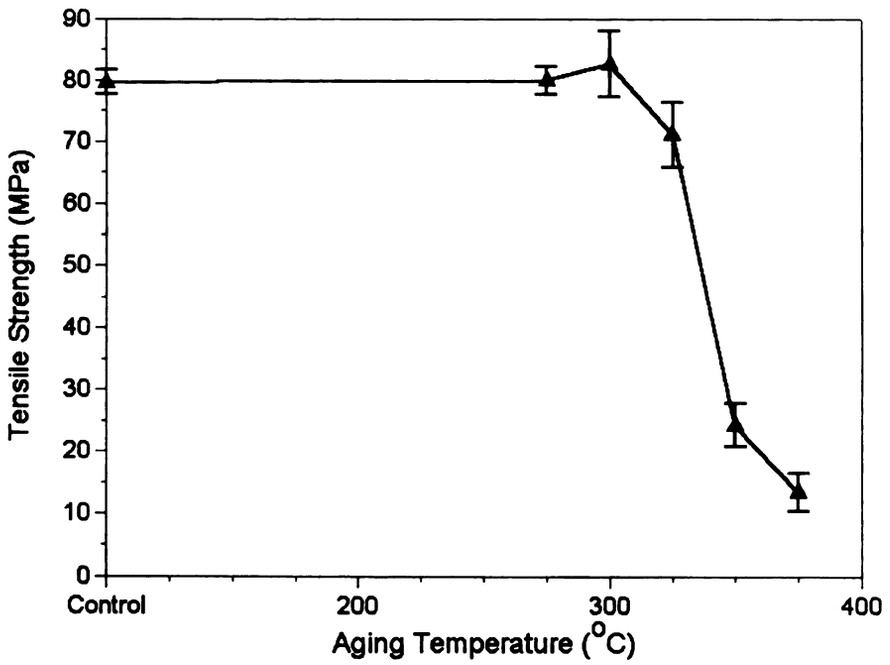

Figure 6.5(b): Tensile strength as a function of 1000 min aging temperature.

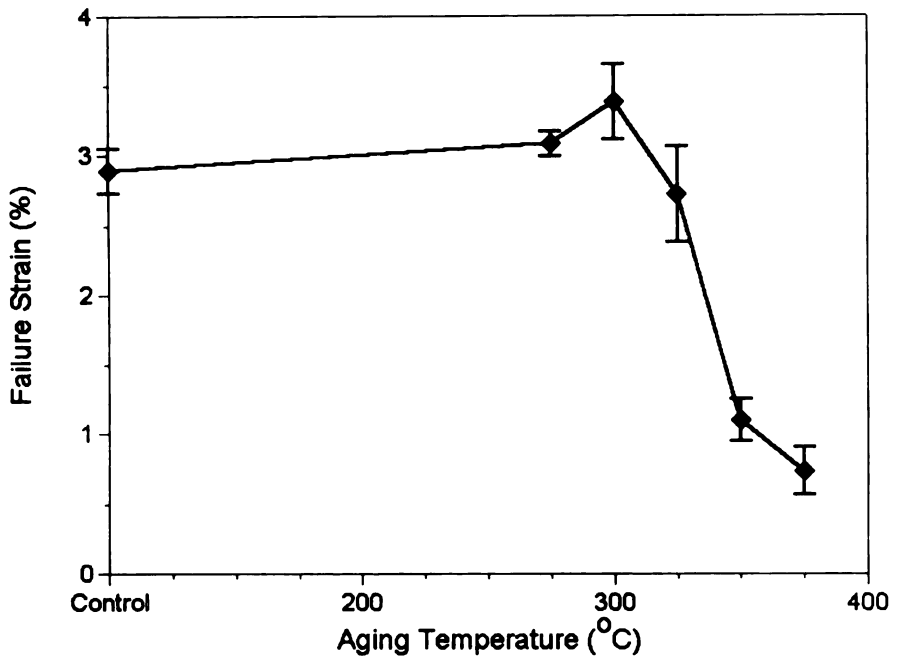

Figure 6.5(c): Failure strain as a function of 1000 min aging temperature.

From the above curves, it is clear that the mechanical properties decrease as a function of mass loss due to thermooxidation, with the most dramatic decrease occurring at aging temperatures >350°C, which corresponds to a mass loss of ~1.5%. The initial increase in mechanical toughness for lower aging temperatures is most likely a result of microvoid collapse, as discussed for POPPI in Chapter 5.

Based on the 5000 min aging conditions at 325°C, the mechanical property reduction appears to be controlled primarily by mass loss and is fairly temperature independent. Therefore, there is a correlation between mass loss and mechanical properties, but a sharp decrease in mechanical properties is

observed

correspo

and a 6

respect t

In

temperat

discussed

care sho

primarily

additiona

thermoo

6.4 Con

Two para

have beer

Polyamide

Fro

% decreas

increases i

plasticizat

mechanical

observed above ~1.5% mass loss. Interestingly, a mass loss of only 1.65% corresponds to a 30% reduction in Young's modulus, a 70% loss of strength, and a 67% decrease in ductility. The observed sharp decline in properties with respect to a small increment in mass loss is critical.

In addition, the degradation mechanisms generally differ with temperature, are diffusion controlled, and are structurally dependent, as discussed in Chapter 2. These factors and the data presented here indicate that care should be taken when attempting thermal stability predictions based primarily on mass loss. Due to the complexity of thermooxidative degradation, additional mechanical screening is necessary to compliment weight loss data for thermooxidative stability predictions and lifetime models therefrom.

6.4 Conclusions

Two parameters that effect the deformation and failure processes of polyimides have been investigated from a fundamental perspective for thermoplastic K3B polyimide: (i) matrix plasticization and (ii) thermooxidative degradation.

From the results presented, moisture induced matrix plasticization leads to decreases in the glass transition temperature, modulus, and strength, with increases in the failure strain as a result of increased free volume. For K3B, the plasticization effect was more significant with respect to the T_g than the mechanical properties.

Th

mechanica

nature of

complexit

prediction

loss is a s

properties

Thermooxidative aging of K3B demonstrated that a severe loss in mechanical properties was obtained after only 1.65% weight loss. Also, the nature of the mechanical property curves as a function of weight loss and complexity of thermooxidative degradation indicates that thermal stability predictions should not be based solely on weight loss alone, even though mass loss is a satisfactory initial screening technique. Sharp decreases in mechanical properties were observed over only a small increment in weight loss.

Chapter 7

Hydrolytic Degradation Mechanisms and Service Environment Durability of Thermoplastic Polyetherimide

7.1 Introduction

In addition to composite matrices, thermoplastic polyetherimide is used in a variety of structural consumer applications as a neat polymer. The focus of the present investigation was to study the service environment durability of polyetherimide in the following three categories: (i) thermal-chemical cycle induced degradation, (ii) T_g depression by absorbed moisture, and (iii) molecular weight characterization as a function of thermal-chemical exposure conditions.

Unfortunately, specific service environment parameters, applications, and other specific experimental results cannot be discussed here due to pending proprietary and legal matters. Instead, the following characterization is approached only from a fundamental perspective of the hydrolytic degradation of polyimides and its relationship to the present dissertation.

7.2 Exp

7.2.1 M

Ultem 1

coupons

7.2.2 Cl

Tensile te

with a ter

experimer

occurred

represent

generally

failure an

are reprod

investigati

In a

to the hyd

weight wa

analysis wa

7.2 Experimental Techniques

7.2.1 Material and Specimen Preparation

Ultem 1000® polyetherimide amorphous thermoplastic (Figure 2.25) tensile coupons (5.08 cm gage lengths) were prepared by injection molding.

7.2.2 Characterization Methods

Tensile tests were performed on an MTS® servo-hydraulic mechanical test unit with a tensile test speed of 20 mm/min. No extensometer was used during the experiment, so the strain was determined assuming (i) the deformation occurred entirely in the gage region and (ii) the instrument displacement represented the actual change in length of the gage region. These assumptions generally lead to two primary inaccuracies: (i) a higher than actual strain to failure and (ii) a lower than actual Young's modulus. Still, these experiments are reproducible for comparative purposes, which was required for the present investigation. Five tests per condition were conducted.

In addition to tensile properties, mass density was determined according to the hydrostatic weighing technique discussed in Chapter 3 and molecular weight was determined by gel permeation chromatography (GPC). Surface analysis was performed by optical microscopy.

7.2.3

Inject

heat

H_2O

The e

mecha

techni

7.2.4

Both a

for 17

obtain

describ

measur

thermo

extrapo

7.2.4 M

PEI was

injection

7.2.3 Thermal-Chemical Cycling

Injection-molded tensile bars, as-molded and annealed for 30 min at 215°C (heating and cooling rates of 2.5°C/min), were exposed to 20 cycles of pH 1 H_2O/SO_2 acid fog at 30°C for 2 h followed by 150°C in air for 10–15 min. The effects of annealing and thermal cycling upon surface damage, residual mechanical properties, and associated surfaces were monitored using the techniques described in Section 7.2.2.

7.2.4 T_g Depression by Absorbed Moisture

Both annealed and as-molded specimens were dried in a vacuum oven at 80°C for 175 h and then exposed to 80°C/100% RH conditions until saturation was obtained. Moisture uptake curves were generated using the same techniques described previously in Chapters 3 and 5. The glass transition temperature was measured at heating rates of 2, 5, 10, and 20°C/min using a TA Instruments® thermomechanical analyzer (TMA). Plots of T_g versus heating rate allowed for extrapolation to zero heating rate. Three experiments per condition were run.

7.2.4 Molecular Weight Characterization

PEI was cryogenically ground into powder of less than 100μm diameter. Both injection molding pellets and powder were exposed to various acidities, ranging

from 1 t

aqueous

refluxing

simultan

was m

aforemer

were re

chromat

7.3 Res

7.3.1 Th

Figure 7

fraction

materials

with diffe

loss by hy

Tab

both cont

stress-stra

molded co

from 1 to 7 (H_2O), by suspension in a 50 weight % mixture of solid PEI and aqueous H_2SO_4. The mixtures were continuously boiled in borosilicate glass refluxing units. Suspensions of pure liquids with the same pH values were simultaneously, separately refluxed. Two times per week the pH of each liquid was monitored using a calibrated pH meter. After 368 days of the aforementioned continuos boiling experiments, the powder and pellet samples were removed, thoroughly washed with distilled water, dried, and then chromatographed as discussed above.

7.3 Results and Discussion

7.3.1 Thermal-Chemical Cycling Characterization

Figure 7.1 displays the chemical degradation in terms of weight loss curves as a function of acid fog cycling for both the annealed and as-molded PEI materials. No significant difference between the behavior of the two materials with different thermal histories could be determined, and the rate of weight loss by linear regression was calculated to be 0.013 weight %/min.

Table 7.1 represents the corresponding tensile and density properties of both control and thermal-chemical cycled systems. Representative plots of the stress-strain curves are shown in Figure 7.2 for as-molded cycled and as-molded control.

Figure 7

Table 7.

Therm Histo
As-Mo Cont
As-Mo 20 Cy
Annea Cont
Annea 20 Cy

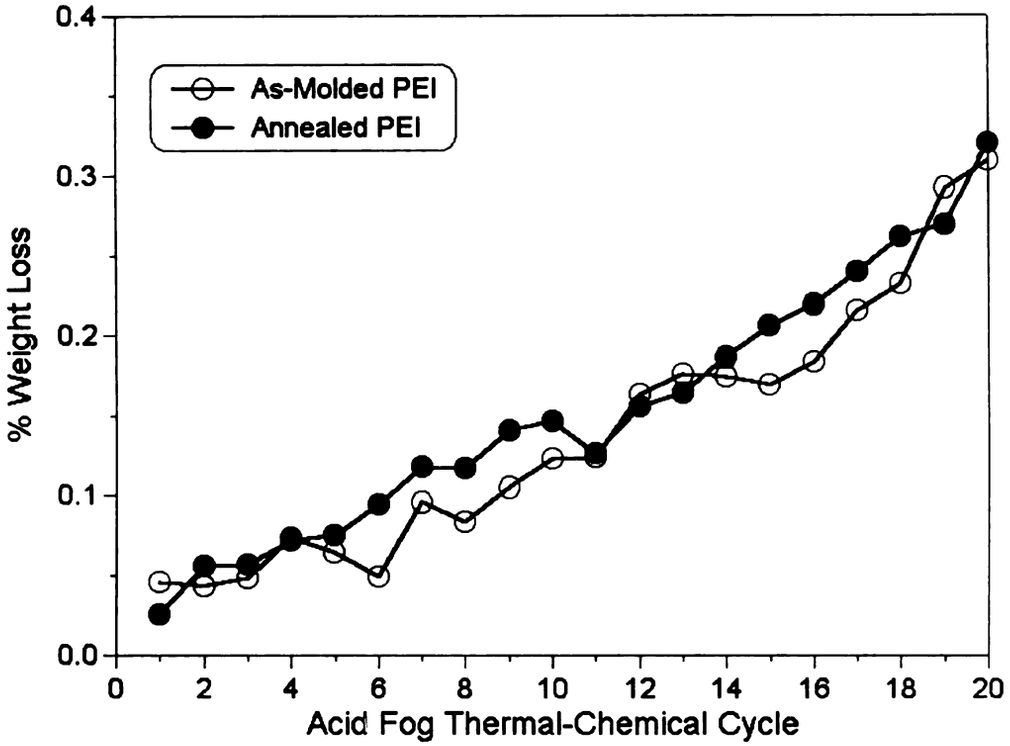

Figure 7.1: Weight loss during acid-fog thermal cycling of PEI.

Table 7.1: Tensile results of thermal-chemical cycling.

Thermal History	Yield Stress (MPa)	Failure Strength (MPa)	Elastic Modulus (MPa)	Failure Strain (%)
As-Molded Control	114 ± 1.4	88.3 ± 0.2	1360 ± 120	75.5 ± 12
As-Molded 20 Cycles	90.0 ± 8.1	90.0 ± 8.1	1473 ± 23	7.2 ± 0.8
Annealed Control	124 ± 4	87.5 ± 5.1	1670 ± 33	15.0 ± 1.2
Annealed 20 Cycles	124 ± 1	90.0 ± 2.4	1691 ± 62	23.5 ± 7.6

Figure

Figure 7
cycles.

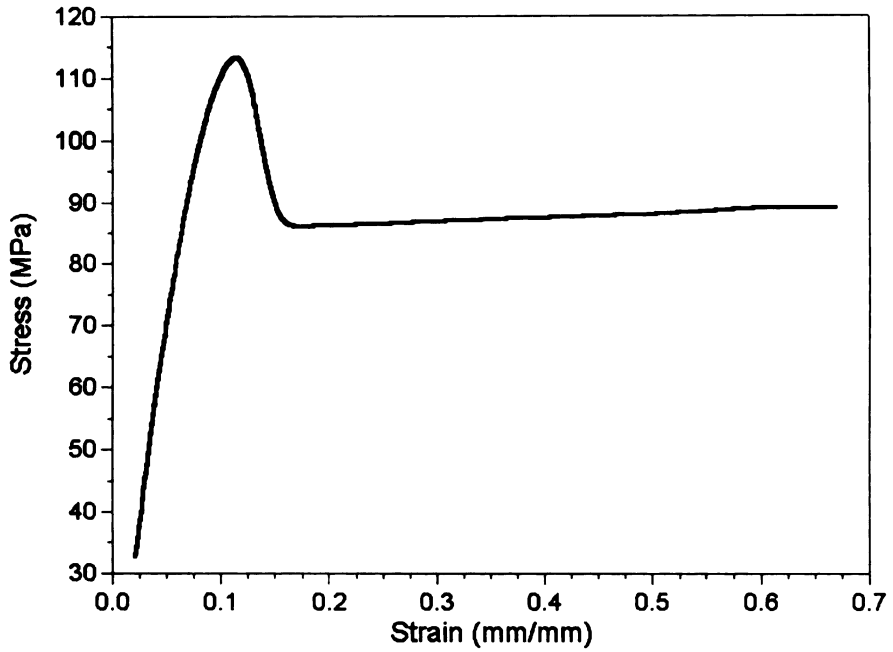

Figure 7.2 (a): Representative stress-strain curves for as-molded control PEI.

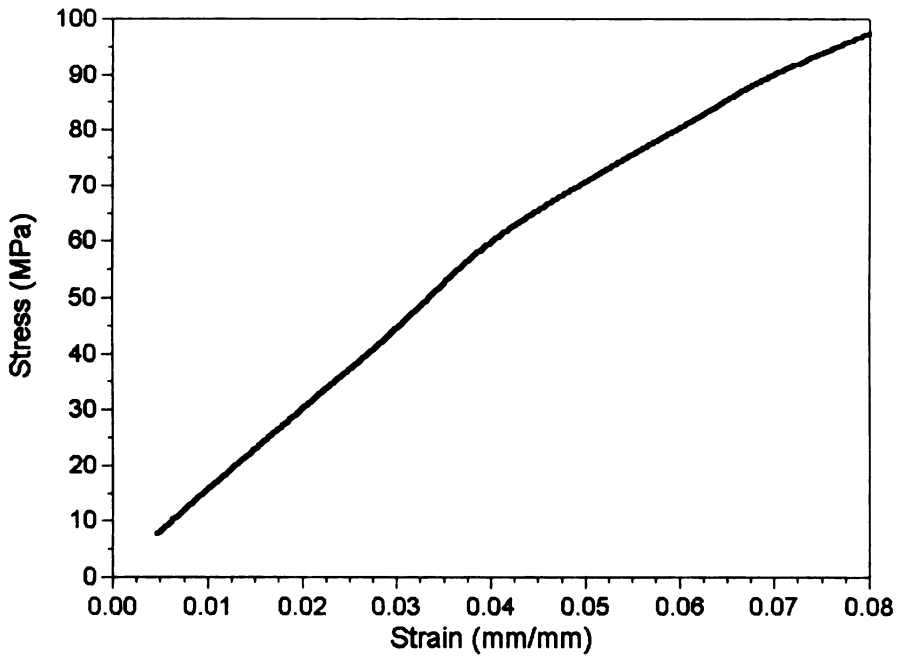

Figure 7.2(b): Representative stress-strain curve for PEI after 20 acid fog cycles.

bcm

glass

sgm

mcre

decre

neach

an ind

results

subsu

of ann

sub-su

fabric

obvious

degrad

reduc

some re

As discussed in Chapter 5, there is a significant reduction in ductility between the as-molded and annealed control PEI specimens as a result of glassy state free volume decreases associated with annealing.

In terms of chemical degradation, the as-molded polymer experiences significant embrittlement after thermal-chemical cycling and a corresponding increase in modulus (8%), decrease in ultimate tensile strength (21%), and decrease in failure strain (90%). On the contrary, the annealed material displays nearly indistinguishable evidence of mechanical property deterioration and even an increase (57%) in strain to failure.

The reason for this improvement in hydrolytic stability most likely results from alleviation of injection-molding induced polymer surface and subsurface orientations. Figure 7.3 is a polarized light microscopy micrograph of annealed and as-molded PEI materials. Note that even though surface and sub-surface orientations have been removed, central polymer orientations and elastic stresses are still observable. From the mechanical property data, it is obvious that the surface orientations significantly reduce the rate of hydrolytic degradation of polyetherimide. Also, glassy state free volume decreases lead to a reduction in the maximum moisture content (Chapter 5) which may also play some role in the observed higher durability upon annealing.

Figure
elastic str
dissertati

Th

make tho

displayed

Annealed

Optical m

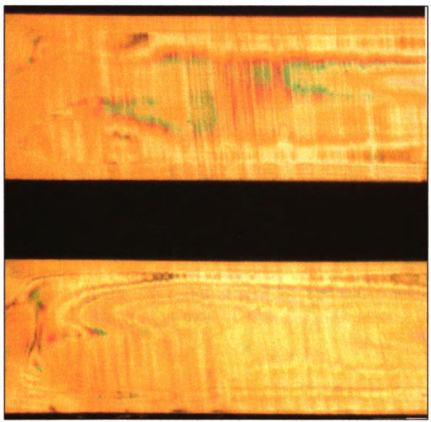

Figure 7.3: Polarized light micrograph displaying polymer orientation and elastic stresses for annealed (top) and as-molded (bottom) PEI. Images in this dissertatin are presented in color.

The high orientation and elastic stresses near the surface of the PEI make those sites susceptible to hydrolytic attack. Cycled as-molded specimens displayed surface etching and cracking, especially near the coupon edges. Annealed samples, however, demonstrated little or no surface cracking. Optical micrographs are shown in Figure 7.4 which demonstrate this behavior.

Figu
surfa
view
right

mecha

mecha

initia

solven

orienta

tensile

observ

specim

volume

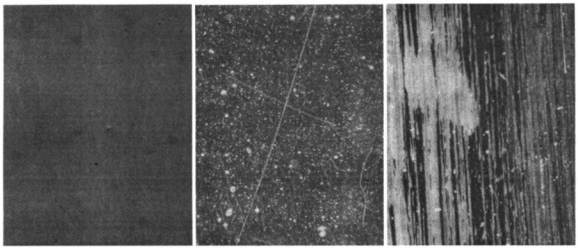

Figure 7.4: Optical micrographs of as-molded control top surface (left), top surface for as-molded after 20 cycles of acid fog exposure (middle), and side view of cracks and etching of as-molded after 20 cycles of acid fog exposure (right).

From the optical microscopy characterization of the surface and mechanical testing of both annealed and as-molded PEI, the degradation mechanism can be deduced as follows. Surface etching and microcrack initiation lead to larger, sub-surface cracks as a result of $H_2SO_{4\,(aq)}$ acting as a solvent and causing relaxation of local injection-molding induced polymeric orientations. These cracks, when stressed, cause rapid crack propagation in the tensile specimens that occurs prior to macroscopic shear yielding, leading to the observed failure strain and strength decreases. During mechanical testing, the specimens shatter violently at failure. The increased modulus results from free volume decreases induced by the 150°C drying exposure in the acid fog cycle.

Recall that the annealed materials exhibited a 57% increase in elongation to break after thermal-chemical cycling. Microscopy relvealed ductile crack inititation and propagation along the fracture specimen edges, which can be attributed to the $H_2SO_{4\,(aq)}$ serving as a solvent and plasticizer near the tensile coupon surfaces that results in the residual increase in polymer ductility. Note that this mechanism contrasts the solvent stress cracking role of the aqueous sulfuric acid in unannealed PEI.

7.3.2 T_g Depression by Matrix Plasticization

The results of moisture absorption for PEI were discussed in Chapter 5, where it was observed that annealing at 215°C for 30 minutes resulted in a 12% reduction in equilibrium moisture content. Here, the goal was to determine the magnitude of the effects of matrix plasticization by absorbed moisture on the glass transition temperature. Figure 7.5 displays the technique used to determine the zero-heating rate T_g of PEI from TMA experiments. The calculated values for the various thermal history conditions are listed in Table 7.2. Combining the moisture absorption data presented in Chapter 5 with the T_g data reported here, it can be stated that the T_g decreases by 21°C / weight % of absorbed moisture. This plasticization-T_g knockdown relationship is consistent with reports from Morgan *et al.* [7] of a 'rule of thumb' for polyimides that the T_g decreases ~25°C per 1 weight % of absorbed moisture.

Glass Transition Temperature (^{o}C)

Figu
for d

Tabl

Appe

bot

Servic

Gas E

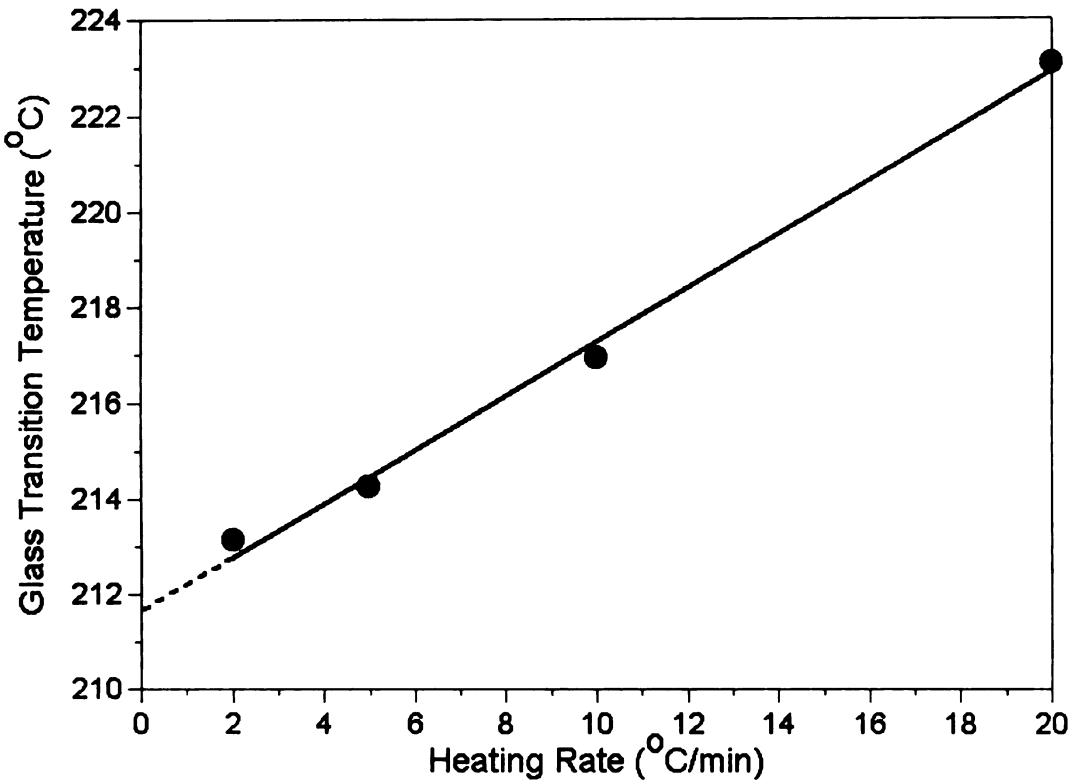

Figure 7.5: Determination of the zero heating rate T_g from TMA experiments for dry as-molded control PEI. The extrapolated value is 212°C.

Table 7.2: Dry and wet T_g (zero heating rate) of PEI.

Thermal History	Dry T_g (°C)	Wet T_g (°C)
As-Molded	212	178
Annealed	212	175

The significance of the observed T_g knockdown effects indicate that the upper use temperature of this polyimide is less than 178°C if it is used in a hot/wet environment as would be observed in many aerospace applications. Service use of this material as a composite matrix or as a structural plastic are thus limited in moist environments, since microcrack initiation is possible at

temper

water.

7.3.3 I

Chrom

exposed

chroma

higher

exposed

were ob

effect o

V

molecul

a functio

temperatures well below the dry glass transition temperature in the presence of water.

7.3.3 Hydrolytic Degradation Kinetics

Chromatogram plots of concentration versus retention volume for each exposed PEI material (pellets and powder) were overlaid against the chromatogram plot for the control powder (no exposure). A significant shift to higher retention volume (lower molecular weight) was observed for each exposed powder relative to the control powder, and no significant differences were observed between pellets and powder, ruling out a significant particle size effect on the degradation rates.

Values of number average molecular weight (M_n), weight average molecular weight (M_w), and polydispersity index, P, are tabulated in Table 7.3 as a function of pH. The above variables are defined as follows:

$$M_n = \frac{\sum N_x M_x}{\sum N_x} \tag{7.1}$$

$$M_w = \frac{\sum N_x M_x^2}{\sum N_x M_x} \tag{7.2}$$

$$P = \frac{M_w}{M_n} \tag{7.3}$$

Above

weigh

indica

since t

longer

Table

E
Con
pH

of pH

for one

If the s

(45 g/ye

strength

polymic

temperat

Above, N_x is the number of moles of polymer molecules whose molecular weight is M_x. Changes in the weight average molecular weight are more indicative of the changes in mechanical properties of a thermoplastic polymer, since the longer chains are weighted more heavily, and during deformation the longer chains dominate the polymer properties.

Table 7.3: GPC data of PEI after exposure in boiling solutions of various pH.

Exposure	M_n	M_w	P
Control Powder	18,170	47,263	2.61
pH 7 (water)	12,459	38,030	3.06
pH 4	8,998	35,431	3.83
pH 3	10,448	38,171	3.66
pH 2	6,908	31,190	4.52
pH 1	6,628	32,061	4.84

Figure 7.6 is a plot of the weight average molecular weight as a function of pH for exposed PEI. The data indicates that under boiling water exposure for one year, PEI experiences a 21% decrease in M_w and a 32% decrease in M_n. If the solution is acidic (pH = 1) the rates of degradation increase to 33 and 64%/year, respectively.

Molecular weight decreases are proportional to losses in mechanical strength, indicating that significant hydrolytic degradation can occur in this polyimide under synergistic service environments of moisture and high temperature, with significant increases in the degradation rates as a function of

inc

init

diff

cha

poly

% Decrease in M_w per year

Figure
a func

increased acidity. In the case of thermosetting polymers, which consist of infinite molecular weight, or thermoplastic polymers whose molecular weight is difficult to measure, degradation kinetics are not as easily obtainable and other characterization techniques must be employed. This aspect for other polyimides will be explored in Chapter 9.

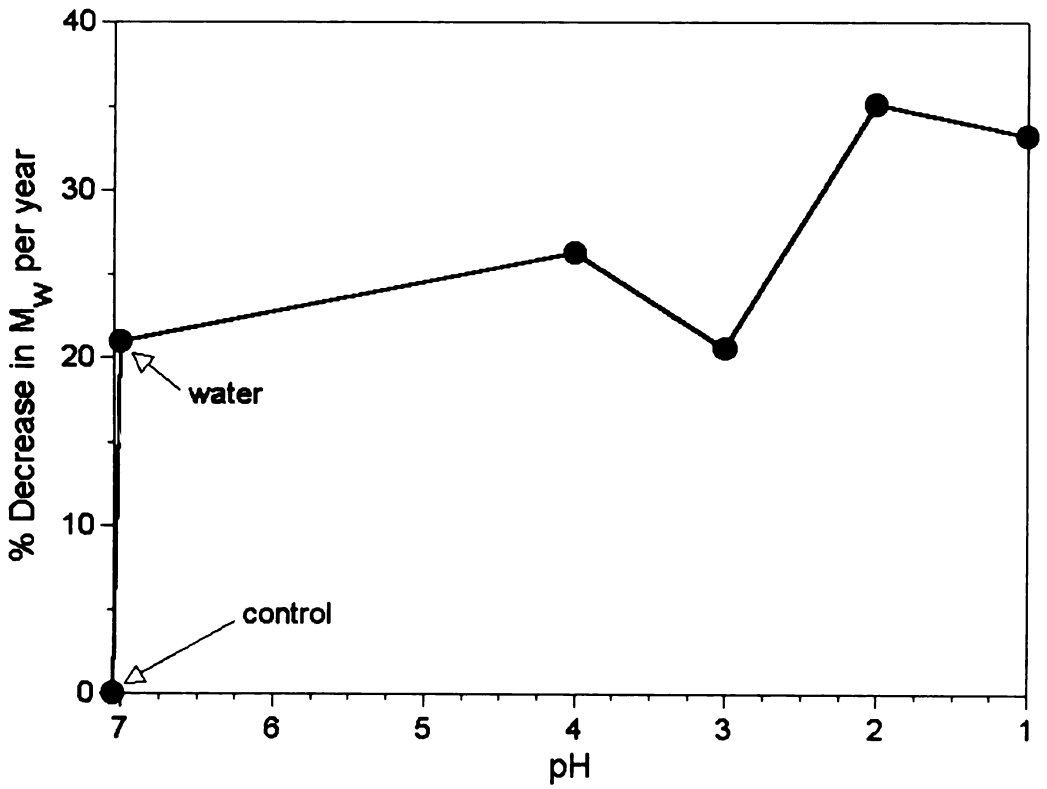

Figure 7.6: Decrease in the weight average molecular weight of PEI per year as a function of pH in boiling (100°C) solution.

7.4 Co

The se

and hy

investi

resistar

as-mol

an app

injecti

H_2SO_4

in duc

mech

sub-s

relax

crack

mac

dee

ma

ter

7.4 Conclusions

The service environment durability, degradation mechanisms, T_g depression, and hydrolytic degradation kinetics of Ultem 1000® polyetherimide have been investigated. Annealing PEI for 30 min at 215°C demonstrates improved resistance to surface etching and microcracking under acid fog exposure over as-molded PEI. Annealing reduces the likelihood of premature failure under an applied stress as a result of the relaxation of surface and near-surface injection molding induced elastic stresses and molecular orientation. The $H_2SO_{4\,(aq)}$ acts as a plasticizer in the annealed polyimide, leading to an increase in ductility.

If the polymer is not annealed prior to exposure, however, the mechanism changes and surface etching and microcrack initiation lead to larger, sub-surface cracks as a result of $H_2SO_{4\,(aq)}$ acting as a solvent and causing relaxation of local injection-molding induced polymeric orientations. These cracks, when stressed, cause rapid crack propagation that occurs prior to macroscopic shear yielding, leading to dramatic failure strain and strength decreases.

In addition to acid fog exposure, the presence of moisture plasticizes the matrix, leading to a 21°C/1 weight % water decrease in the glass transition temperature. This is consistent with the plasticization effect of other

polyimides and demonstrates that in hot/wet environments experienced in numerous aerospace and consumer applications, the upper use temperature of PEI is significantly reduced.

Finally, further quantification of the hydrolytic susceptibility of PEI was demonstrated from molecular weight measurements upon exposure to boiling PEI powder in solutions of water/sulfuric acid mixtures. The weight average molecular weight was found to degrade at a rate of 33%/year in boiling water and 64%/year in a pH 1 solution, which is significant in that M_w is proportional to mechanical strength.

Chapter 8

Damage Threshold Determination of High Temperature Polyimide Composite Matrices

8.1 Introduction

Chapters 8 and 9 represent specific segments of the overall AFOSR programs discussed in Chapter 1 concerning the hygrothermal durability of polyimide and bismaleimide matrices and their carbon fiber composites. As mentioned in Chapters 1 and 2, present and future high temperature polymer matrix – carbon fiber composites are exposed to service environments that involve combined stress, time, temperature, moisture, chemical, and atmospheric exposure conditions. These environments can lead to complex synergistic environmental induced degradation of composite performance, so a thorough understanding of potential physical, chemical, and mechanical induced composite degradation mechanisms, and their synergistic effects that lead to the most probable critical failure path is crucial.

The contribution of this chapter to the overall durability program plan involves a series of core test programs that separate distinct service environment conditions and their effect on composite performance. Here, the goals are to (i) identify the synergistic critical failure path and its associated

perfor

and te

on the

temper

aircraf

and bi

of i

hygro

were

8.2 I

8.2.

The

Aver

Mi

Syst

was

Re

In

performance deterioration mechanisms, (ii) conduct synergistic (moisture, time, and temperature) service environment accelerated performance testing based on the physics, chemistry, and/or mechanics of the aging mechanisms of high temperature polymer matrix composites for potential utilization in high speed aircraft, and (iii) determine the damage threshold characteristics for polyimides and bismaleimides.

These exposure conditions and characterizations were performed by way of (i) accelerated hygrothermal exposure using a sealed pressure vessel and (ii) hygrothermal spiking. Physical, thermal, and mechanical property evaluation were conducted for mechanism identification.

8.2 Experimental Techniques

8.2.1 Material Preparation

The materials investigated include the Matrimid 5292® BMI resin system, Avimid® K3B thermoplastic polyimide, AFR700B thermoset polyimide, IM7/BMI $[0°/90°]_{4S}$ laminates, and IM7/K3B $[0°/90°]_{4S}$ laminates. The BMI systems were prepared using the same techniques outlined in Chapters 3 and 4, with a composite cure cycle of 177°C / 1h + 200°C / 2h + 250°C / 6h. K3B neat plaques, 2 mm thick, were prepared using the same procedures discussed in Chapter 6. IM7/K3B laminates were fabricated using a PMR-like approach

(Chapter 2) with *N*-methyl-pyrrolidone (NMP) as the solvent. Consolidation was performed at 360°C. AFR700B (Chapter 2) resin plaques were obtained form Air Force Research Laboratory, Wright-Patterson Air Force Base.

8.2.2 Specimen Preparation and Pre-Conditioning

8.2.2.1 Hygrothermal Spiking Specimens

Rectangular flexural specimens (all materials) of dimensions 50 mm x 10 mm x 2 mm were sectioned using a diamond blade saw and running water. All samples were initially dried at 80°C under vacuum for 400 h.

Both a neat BMI resin sample with a thermocouple in its center and a $[0°]_{16}$ IM7/BMI laminate with thermocouples embedded between each ply were fabricated to determine the amount of time necessary to achieve thermal equilibrium during a thermal spike. It was determined that equilibrium was maintained (about 95% of final temperature) after ~5 min at a thermal spike temperature of 250°C (Figure 8.1). From this experiment, 15 min was used for the hygrothermal spiking time.

Figu
ther

8.2

Sma

8.2

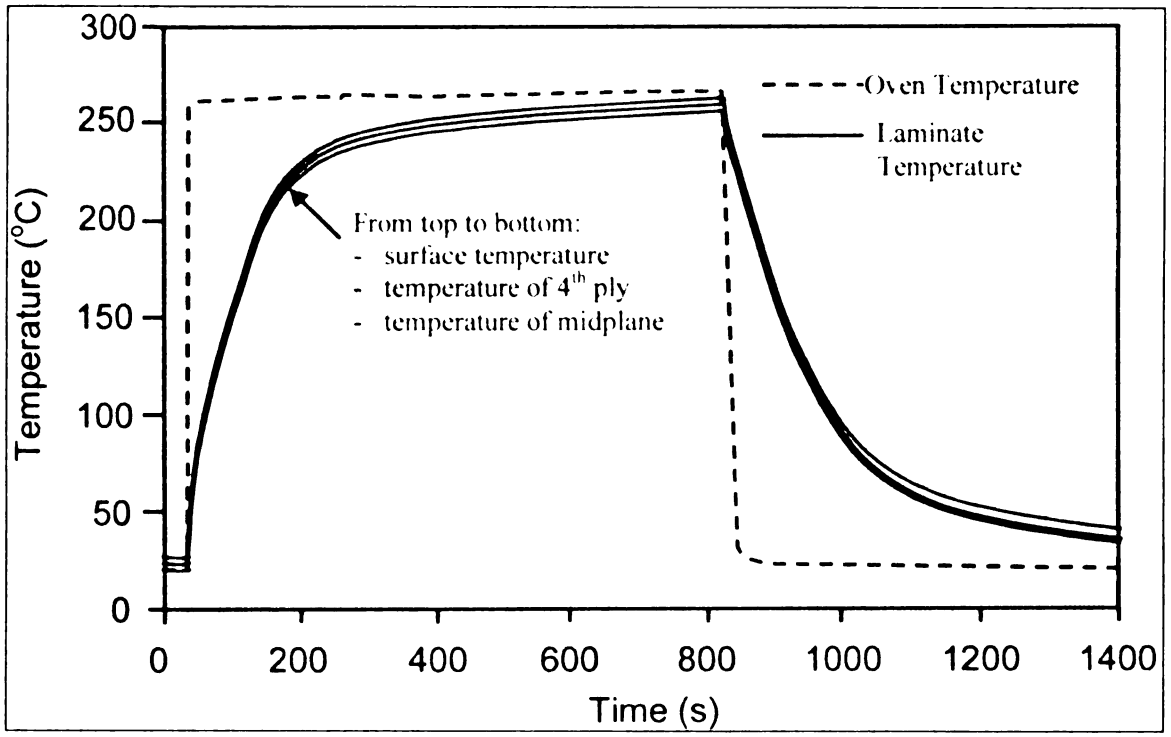

Figure 8.1: Temperature profile of a $[0^{\circ}]_{16}$ IM7/BMI laminate exposed to a thermal spike of 250°C.

8.2.2.2 Pressure Bomb Specimens

Small specimens of K3B and AFR700B (2 mm thickness) were initially dried in 30 mm Hg vacuum according to the following schedule: 100°C / 48 h + 180°C / 48 h + 230°C / until no weight change was observed.

8.2.3 Hygrothermal Spiking Exposure

All samples were exposed to 30°C / 80% relative humidity for ~2400 h in an environmental chamber, and the moisture uptake monitored as a function of exposure time using the procedures outlined in Chapter 3 (three specimens per

data point). The samples were placed in specially designed glass trays to prevent possible galvanic corrosion.

Upon saturation, the samples were removed from the humidity chamber, exposed to a thermal spike of 250°C for 15 min, the weight was again monitored, and the samples were returned to the humidity chamber. A total of 10 thermal spike cycles were conducted. Dry samples were also exposed to the same thermal spikes and stored under vacuum between spikes. All samples were dried at 80°C under 30 mm Hg vacuum.

The mechanical properties of IM7/BMI and IM7/K3B laminates were monitored by flexural (4-point loading) deformation using a span-to-depth ratio of 16 and a 1 mm/min crosshead speed on an MTS® mechanical testing instrument. BMI neat resin flexural properties were monitored using the same parameters as discussed in Chapter 3. All samples were dried for 340 h at 80°C prior to testing. Five specimens per condition were tested.

8.2.4 Pressure Bomb Exposure

The dried samples were suspended in a Teflon® basket in a sealed stainless steel pressure bomb and exposed to pressurized steam (deuterated water was used, ^2H_2O, since some samples were sent to Air Force Research Laboratory for Nuclear Magnetic Resonance (NMR) analysis) (160°C / 760 kPa) for a total

of ~1000 h. Uniform moisture absorption can be obtained in a relatively short time period using this procedure. The samples were then removed and dried according to the procedures in Figure 8.2.

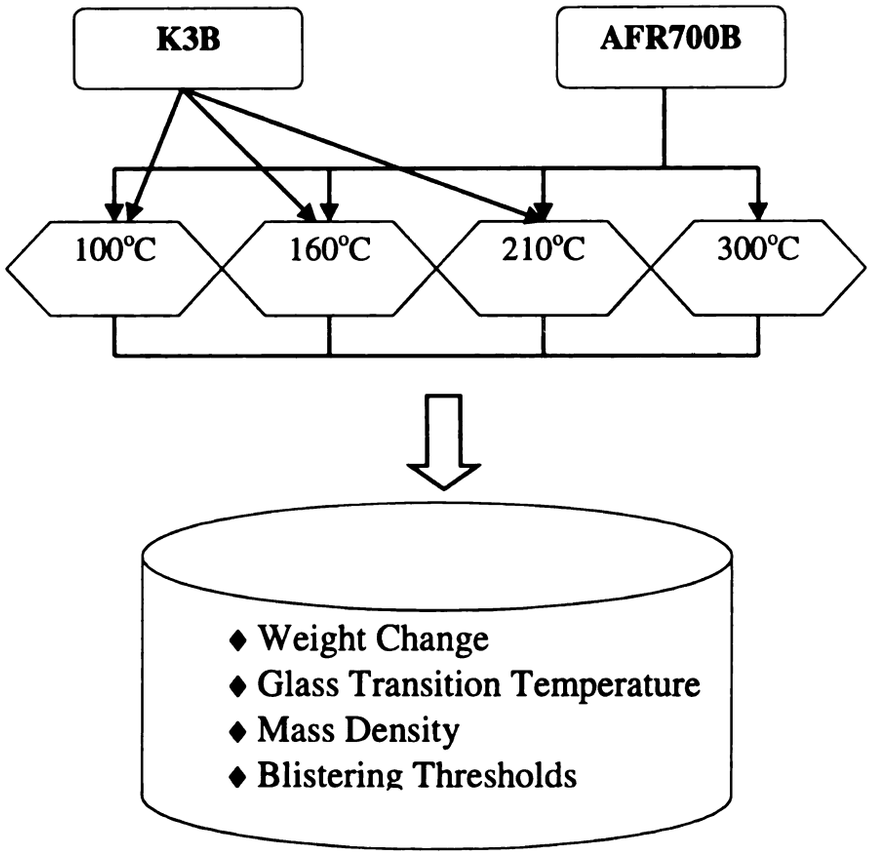

Figure 8.2: Drying conditions and experimental design used after pressure bomb exposure of K3B and AFR700B neat matrix materials.

Weight loss, glass transition temperature, and mass density were monitored using a mass balance, thermomechanical analysis (heating rates of 10°C/min), and hydrostatic weighing (Chapter 3). Blistering temperatures were also monitored by TMA. Moisture absorption (80°C/100% RH) was

condu

expos

8.3 F

8.3.1

The r

show

track

Fig
ma

conducted to compare diffusivity parameters before and after pressure bomb exposure and to compare ^2H_2O and H_2O diffusion behavior.

8.3 Results and Discussion

8.3.1 Hygrothermal Spiking

The moisture content as a function of exposure time and spiking conditions is shown in Figure 8.3. Note that the plot is normalized to the specimen thickness, since each of the materials varied slightly in thickness.

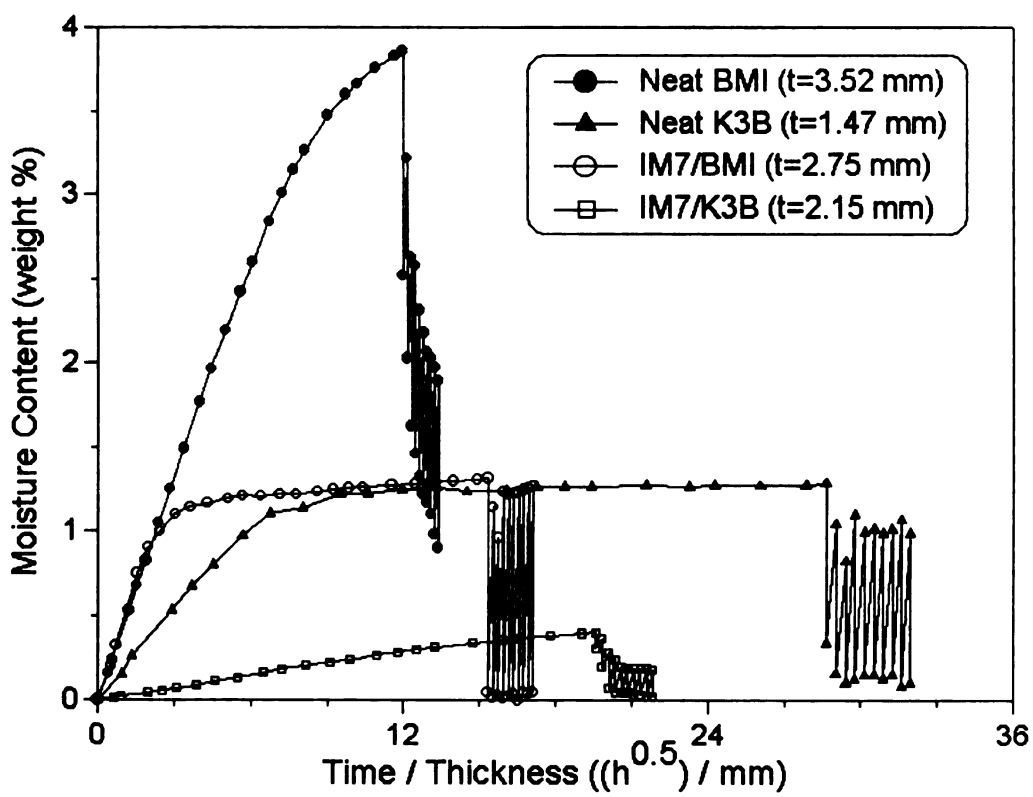

Figure 8.3: Overall moisture absorption-desorption behavior for polyimide matrices and composites after 250°C thermal spiking.

Significant physical changes were observed after thermal spiking. Most notably, the K3B neat and composite specimens displayed significant macroscopic blistering after only one thermal spike (Figures 8.4 and 8.5). No blistering was observed in the BMI resins or laminates, or in any of the dry-spiked materials, the latter indicating that the moisture present in the specimens was responsible for the observed blistering and subsequent delamination.

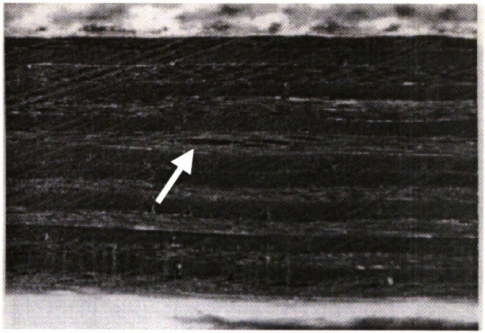

Figure 8.4: Optical micrograph showing edge delamination of an IM7/K3B composite laminate due to blistering after one hygrothermal spike of 250°C.

When the trapped vapor pressure exceeds the local yield stress of the matrix, plastic deformation (matrix cavitation) and subsequent macroscopic blistering failure will occur. This was clearly evident in the case of the K3B

materials, but no blistering was observed for the IM7/BMI or neat BMI systems. The latter phenomenon can most likely be attributed to (i) the presence of processing-induced microcracks in the IM7/BMI laminates that allow for faster diffusion of water molecules out of the composite during a dynamic thermal excursion and (ii) the lesser susceptibility of thermoset matrices to blister, since blistering in thermosets requires rupture of covalent crosslinked molecular segments (Chapter 2).

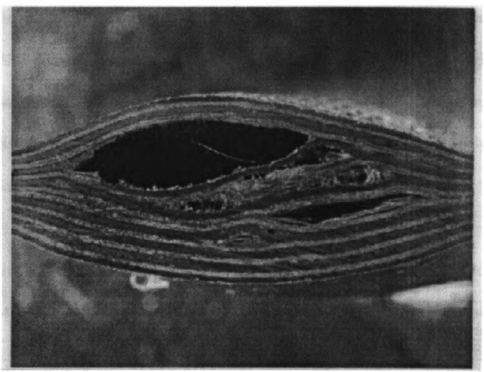

Figure 8.5: Optical micrograph of the center cross-section showing a macroscopic blister and subsequent delamination of an IM7/K3B composite laminate after one hygrothermal spike of 250°C.

In addition, blistering is a multivariable degradation mechanism, dependent on (i) previous time-temperature-humidity exposure and associated moisture concentration profiles, (ii) component thickness and geometry, and (iii) rapid heat-time service environment exposures, such as the thermal spike investigated here. Blistering is examined in detail in Section 8.3.2.

During the initial moisture absorption cycle, the BMI laminate and K3B neat polymer reached equilibrium moisture conditions in a relatively short exposure time/thickness as opposed to the BMI neat resins and K3B laminates. Upon thermal spike exposure, both K3B neat polymer and IM7/BMI always maintained a high moisture content and 80-90% weight gain and loss during spiking, which implies a high diffusion rate of these systems. The diffusivity parameters, calculated by non-linear regression analysis of Equation 2.10, are shown in Table 8.1.

Table 8.1: Moisture absorption parameters for thermally spiked neat matrix polymers and composites at 30°C/80% RH absorption conditions. Absorption data was fit to Equation 2.10.

Material	**D** (cm^2/s)	**M_∞** (wt%)	**Regression Coefficient**
BMI Neat Resin	3.60×10^{-7}	4.02	0.998
IM7/BMI Composite	3.98×10^{-6}	1.29	0.988
K3B Neat Resin	6.06×10^{-7}	1.26	0.998
IM7/K3B Composite	1.77×10^{-7}	0.39	0.971

For the IM7/BMI cross-ply laminates, the processing induced microcracks are primarily responsible for this observed moisture diffusion behavior. In the case of K3B matrix material, which was fabricated by compression molding of completely imidized K3B powder, intergranular boundary effects [205-207] are most likely responsible. Microstructural granular boundaries can serve as fast diffusion paths for water molecules.

The results of physical and chemical damage mechanisms incurred during hygrothermal spiking are shown in Tables 8.2 and 8.3 for the composite laminates and BMI neat resins, respectively. IM7/K3B laminates obviously displayed the most significant property degradation as a result of microcavitation, macroscopic blistering, and subsequent delamination.

Table 8.2: Residual flexural properties of IM7-reinforced composite laminates before and after seven hygrothermal spikes of 250°C.

Material/Exposure		**Modulus (GPa)**		**Strength (MPa)**		**Failure Strain (%)**	
		Average	**%Δ**	**Average**	**%Δ**	**Average**	**%Δ**
IM7/ BMI	Dry Control	100	0	1054	0	1.06	0
	Wet Control	101	1	1069	1.4	1.09	2.8
	Dry Spiked	99	-1	1064	1	1.31	24
	Wet Spiked	96	-4	1058	0.4	1.32	25
IM7/ K3B	Dry Control	100	0	1130	0	1.21	0
	Wet Control	102	2	1161	5.3	1.28	6
	Dry Spiked	100	0	1113	1	1.19	-2
	Wet Spiked	92	-8	571	-48	0.71	-41

In contrast to IM7/K3B, the IM7/BMI laminates displayed small improvements in ductility and strength after hygrothermal spiking. This may be due in part to molecularly 'locked-in' water molecules. In a hygrothermal environment, high temperatures allow for increased availability for hydrogen boding sites to be susceptible to moisture, as the molecular structure expands with temperature. During a relatively rapid cool-down, water molecules become trapped or 'locked-in' to molecular 'cages', and may only diffuse out upon subsequent exposure to high temperatures. The molecularly 'locked-in' water molecules cannot escape under low temperature conditions and will thus lead to matrix plasticization.

Table 8.3: Residual flexural properties of BMI neat resins before and after seven hygrothermal spikes of 250°C.

Material	**Modulus (MPa)**		**Strength (MPa)**		**Failure Strain (%)**	
	Average	**%Δ**	***Average***	**%Δ**	***Average***	**%Δ**
Dry Control	3244 ± 59	0	162 ± 10	0	5.19 ± 0.46	0
Wet Control	3270 ± 86	0.8	153 ± 22	-6	4.87 ± 0.95	-6
Dry Spiked	3255 ± 35	0.3	141 ± 11	-13	4.41 ± 0.45	-15
Wet Spiked	3312 ± 23	2.1	125 ± 14	-23	3.75 ± 0.42	-28

Drying all exposed samples at 80°C under vacuum until no weight change was observed provides additional evidence to this theory for the BMI composites. The IM7/BMI laminates always contained some residual moisture

(~0.2 wt%) after drying, whereas the IM7/K3B, neat K3B, and neat BMI resins returned to their original dry weight.

Despite the apparent degradation resistance of IM7/BMI laminates, significant embrittlement was observed after both hygrothermal and thermal spiking of BMI neat resins (Table 8.3). This demonstrates that the degradation mechanisms in the composite and neat resin matrices are different, possibly due in part to the ability of moisture to diffuse out of the microcracked composites rapidly compared to the neat resin or the role played by the fiber/matrix interphase [26]. Also, the properties of the composite are fiber dominated, so changes in the matrix mechanical properties may be difficult to detect in specific lay-up/loading condition configurations.

In summary, the IM7/BMI laminates are more resistant to hygrothermal spiking than IM7/K3B laminates. After only one hygrothermal spike of 250°C, the K3B laminates were severely blistered and delaminated, which resulted in a 48% reduction in composite strength. Relative to IM7/K3B, the higher hygrothermal durability demonstrated by the $[0°/90°]_{4S}$ BMI composites was most likely from a contribution of a number of factors, including (i) higher T_g of the BMI resin, (ii) lesser susceptibility of thermosets to blister, since blistering would required rupture of covalent crosslinked segments, and (iii) the presence of processing induced microcracks that allow for the fast diffusion of moisture in and out of the composite.

8.3.2 Pressure Bomb

8.3.2.1 Moisture Absorption/Desorption Results

Figure 8.6 displays the moisture absorption curves at 80°C saturated steam for K3B and AFR700B for unexposed and ~1000 h pressure bomb exposed neat resins, respectively. The diffusivity parameters are summarized in Table 8.4. For both materials, the rate of moisture absorption (measured by D) was slightly lower (10-30%) after pressure bomb exposure. K3B displayed a higher value for M_∞ after exposure, whereas the equilibrium moisture content was slightly lower for AFR700B after pressure bomb exposure.

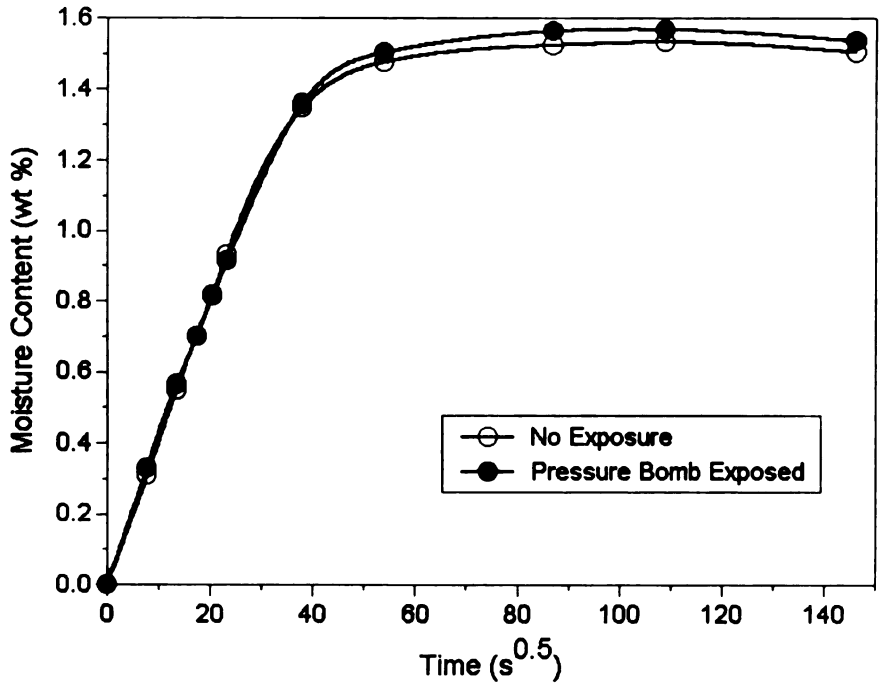

Figure 8.6(a): Moisture absorption (H_2O) (80°C/100% RH) of K3B neat polymer before and after pressure bomb exposure.

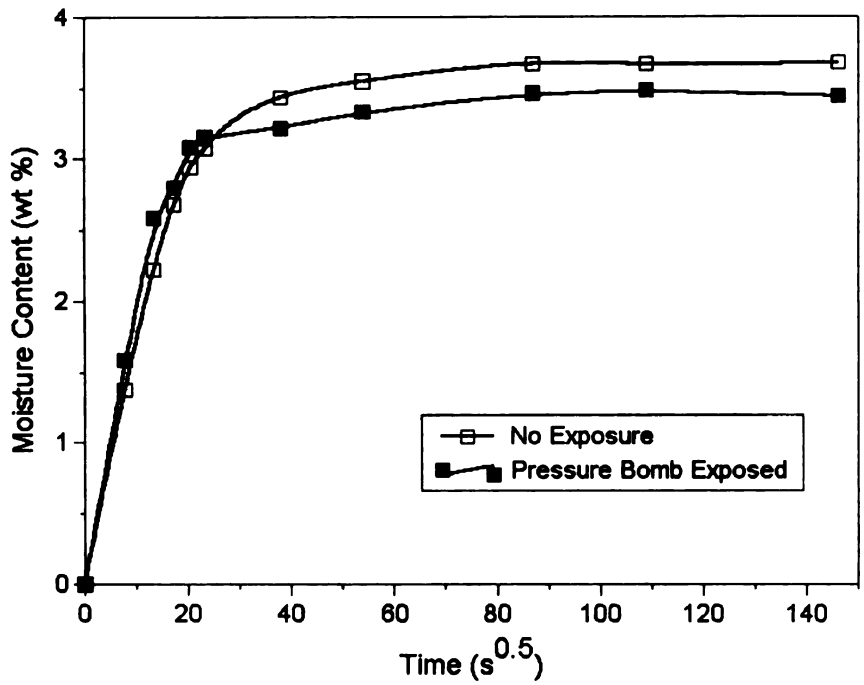

Figure 8.6(b): Moisture absorption (H_2O) (80°C/100% RH) of AFR700B neat resin before and after pressure bomb exposure.

Table 8.4: Moisture absorption parameters (H_2O) for K3B and AFR700B before and after pressure bomb exposure.

Material / Exposure	D (cm^2/s)	% Δ	M_∞ (wt%)	% Δ	Regression Coefficient
K3B / Control	4.41×10^{-6}	-11	1.53	+2.6	0.998
K3B / Exposed	3.92×10^{-6}		1.57		0.997
AFR700B / Control	8.16×10^{-6}	-27	3.67	-5.2	0.984
AFR700B / Exposed	5.94×10^{-6}		3.48		0.981

It should be noted that moisture absorption was also conducted for ^2H_2O under the same conditions to compare the moisture absorption behavior for ^2H_2O and H_2O. The data showed that the diffusivities were identical within experimental error, but the value for M_∞ was slightly higher (~0.2 wt%) for the

case of deuterium. The latter phenomenon was expected, since the molecular mass of the ^{2}H (deuterium) isotope is larger than for hydrogen.

From the results above, it is clear that some chemical and/or physical modification of the two polymer structures has taken place. It is unlikely, however, that all mechanisms responsible for the observed moisture absorption characteristic modifications are identical, since K3B is a thermoplastic and AFR700B a thermoset.

Also, the moisture desorption behavior was monitored as a function of time at 80°C / vacuum conditions for all absorbed materials. The comparative plots between the diffusivity into and out of K3B and AFR700B are shown in Figure 8.7.

In addition to the above experiments, the moisture desorption was monitored as a function of the drying time-temperature conditions shown in Figure 8.8. The moisture desorption parameters at the different drying temperatures were determined using Equations 2.10 and 2.11 (Table 8.5).

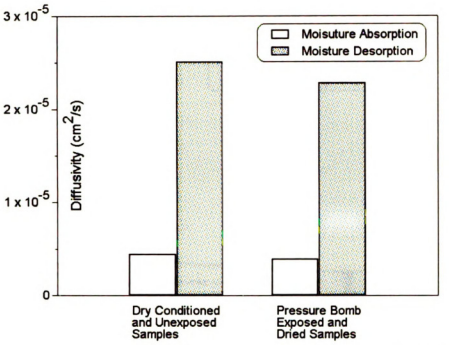

Figure 8.7(a): Comparative diffusivities for absorption (80°C/100% RH) and desorption (80°C / vacuum) after pressure bomb exposure for K3B.

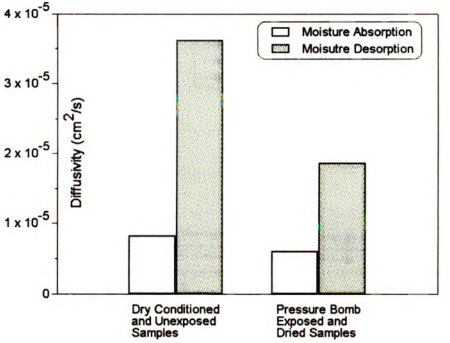

Figure 8.7(b): Comparative diffusivities for absorption (80°C/100% RH) and desorption (80°C / vacuum) after pressure bomb exposure for AFR700B.

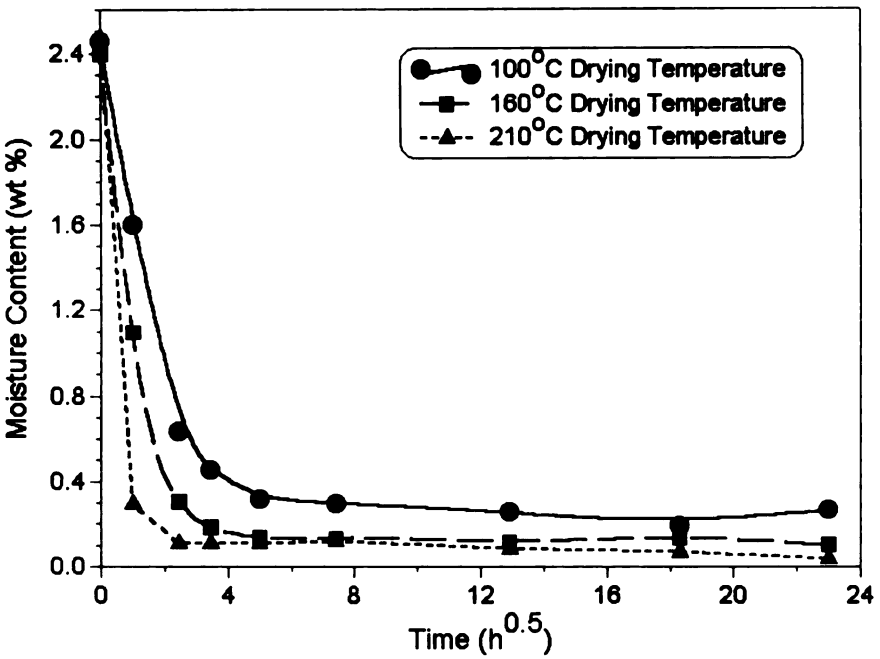

Figure 8.8(a): Drying of pressure bomb exposed K3B as a function of time-temperature conditions under vacuum.

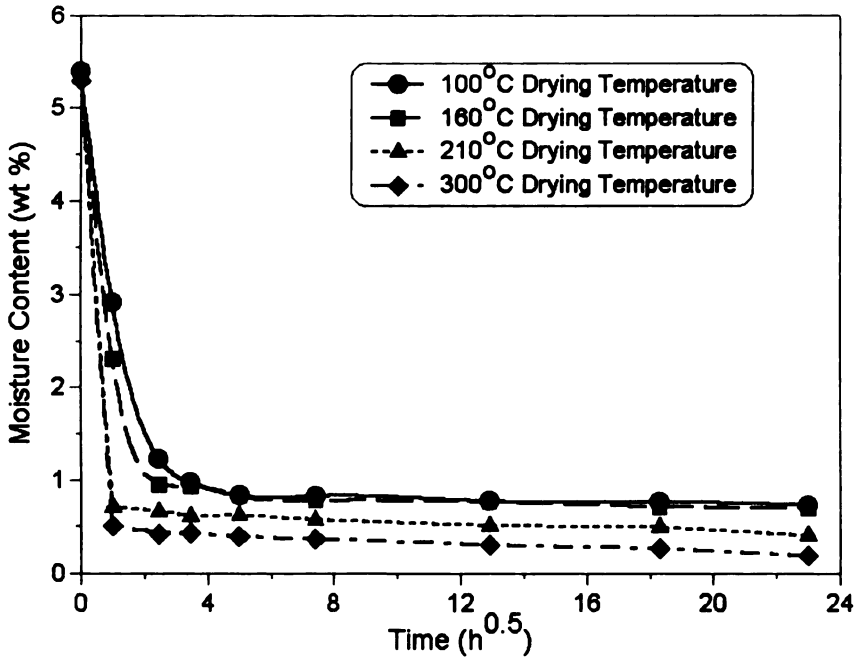

Figure 8.8(b): Drying of pressure bomb exposed AFR700B as a function of time-temperature conditions under vacuum.

Table 8.5: Moisture desorption properties for pressure bomb exposed K3B and AFR700B polyimides as a function of temperature.

Material	Drying Temperature (°C)	D (cm^2/s)	Residual Moisture (wt%)
AFR700B	100	1.66×10^{-5}	0.72
	160	5.66×10^{-5}	0.69
	210	1.15×10^{-4}	0.40
	300	3.32×10^{-4}	0.19
Activation Energy = 26.5 kJ/mol		$D_o = 0.08641\ cm^2/s$	
K3B	100	1.49×10^{-5}	0.27
	160	3.40×10^{-5}	0.10
	210	6.89×10^{-5}	0.04
Activation Energy = 24.6 kJ/mol		$D_o = 0.03147\ cm^2/s$	

From the above results, some interesting phenomena are observed. The moisture absorption, desorption, and re-absorption data demonstrate that (i) the re-absorption diffusivity parameters for the pressure bomb aged samples are different than the non-exposed materials, (ii) the water diffuses out of the material after hygrothermal exposure faster than it diffuses into the materials at 80°C, and (iii) even after drying for 1000 h up to 300°C, some residual moisture remains in the polymers. These results clearly indicate that chemical and/or physical structure of the polymer matrices has been compromised. Such chemical and physical structural modifications are likely manifested through a combination of physical densification of the structure, physically trapped (molecularly 'locked-in') water molecules, and/or chemically bound water as a result of hydrolysis of the polyimide.

In addition, the above results are consistent with permanent dry T_g decreases reported in the literature [119, 259-261] for polyimides after hygrothermal exposure and subsequent drying. These T_g decreases have been shown to be severe (25 ~ 200°C), and attributed to possible imide ring hydrolysis at high temperatures leading to a reversal of the polymerization reaction and a resulting polyamic acid. The polyamic acid species is then more susceptible to hydrolysis, and further degradation may occur at even faster rates, ultimately resulting in regeneration of the monomers by such mechanisms as decarboxylation. For example, Nechaev *et al.* [265] studied the hydrolytic degradation of polyimides using model compounds (phthalanilic acid and phthalanil) in concentrated sulfuric acid, and reported amide hydrolysis occurred 550 times faster than imide ring hydrolysis.

The aforementioned decreases in T_g would require roughly 30-40% depolymerization to polyamic acid linkages, indicating that the molecular 'lock-in' mechanism (leading to plasticization) may be a contributor to these reported T_g decreases. Here, the results are supportive of this theory (residual moisture is present even after drying at 300°C), and further insight on the molecular level to the nature of water in the polyimides after exposure has been conducted at Air Force Research Laboratory using NMR studies [223], the results of which are discussed below.

8.3.2.2 Mass Density Results

The mass density curves of K3B and AFR700B polyimides are presented in Figure 8.9 as a function of drying time-temperature conditions after pressure bomb exposure.

From the K3B curve, three physical transitions are observed which are related to the physical/chemical structural state of the polyimide. These are (i) an initial decrease in density at all temperatures resulting from the loss of moisture, (ii) a rapid and significant density decrease (~4.5% below the unexposed control density) under the 210°C drying conditions due to hygrothermal induced microcavitation damage, which was discussed previously in the hygrothermal spiking exposure program, and (iii) an increase in density after long drying times for the 160°C and 210°C temperatures due to physical aging induced molecular densification, which is common in thermoplastic polyimides, as discussed in Chapter 5.

For the case of the highly crosslinked AFR700B, the final mass density of the original dry control material was never regained. Instead, the density remained on the order of 1.5% higher than the original density. This most certainly results from a combination of residual moisture still present in the resin and a modification of the polyimide physical and chemical structural state.

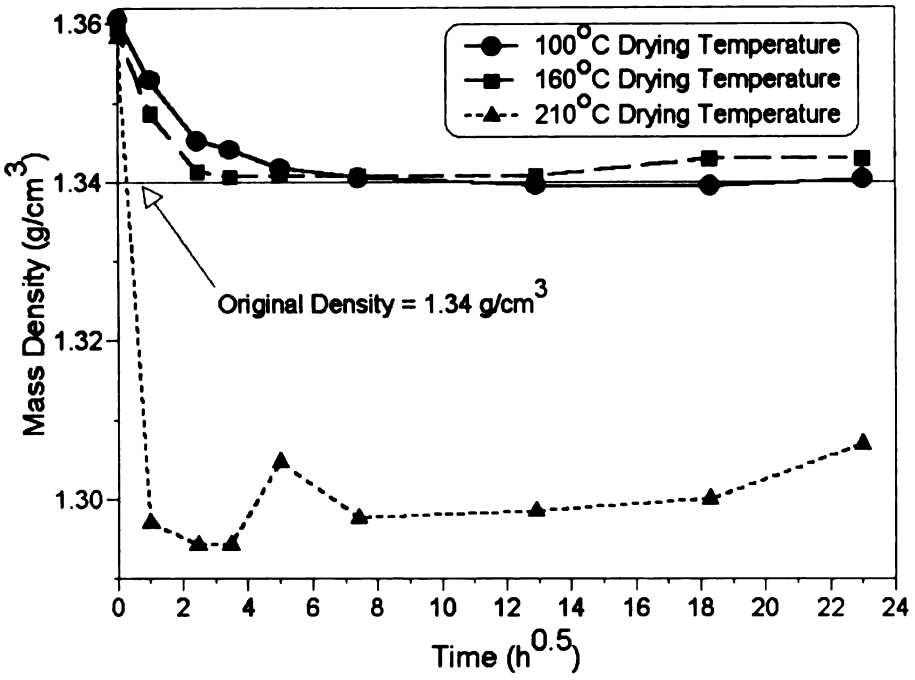

Figure 8.9(a): Mass density of hygrothermally aged (pressure bomb exposed) K3B polyimide under various isothermal vacuum drying temperatures.

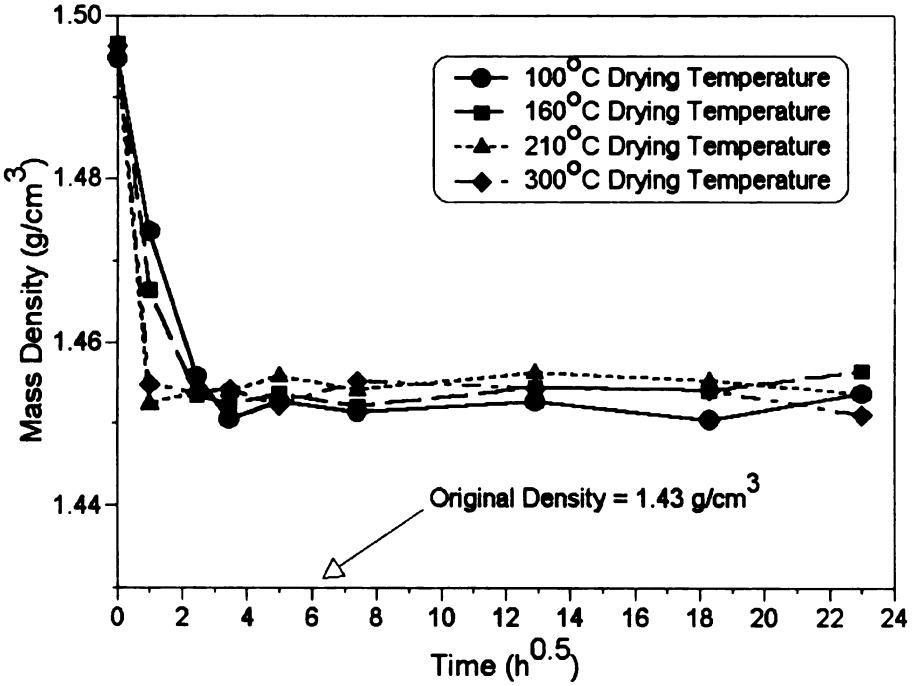

Figure 8.9(b): Mass density of hygrothermally aged (pressure bomb exposed) AFR700B polyimide under various isothermal vacuum drying temperatures.

Curliss *et al.* [263] conducted ^{2}H NMR studies on the K3B and AFR700B pressure bomb exposed resins at Air Force Research Laboratory and demonstrated that chemically bound water (due to hydrolysis) remains in the polyimides after drying. Therefore, the observed residual moisture present in the polymers and observed mass density phenomena are a result of chemical hydrolytic degradation of the polyimides possibly coupled with molecularly 'locked-in' water molecules and physical densification.

8.3.2.3 Permanent Glass Transition Temperature Decreases

From the aforementioned results and work conducted by Air Force Research Laboratory, it is clear that the reported permanent dry T_g decreases for these polyimides is definitely a result of hydrolytic degradation of the polyimides, with additional contributions from possible molecularly 'locked-in' water molecules. Chapter 9 investigates the actual mechanisms responsible for the hydrolytic degradation by examining the degradation kinetics of a variety of polyimides of different chemical structures.

In this study, TMA was used to determine the glass transition temperatures for K3B and AFR700B since this technique allowed for simultaneous determination of both blistering temperatures and T_g. A typical TMA curve is shown in Figure 8.10 for an AFR700B specimen saturated with water (wet control; no pressure bomb exposure).

Control properties of wet and dry K3B and AFR700B are shown in Table 8.6, and the glass transition temperature as a function of time-temperature drying conditions and moisture content are plotted in Figures 8.11 and 8.12, respectively.

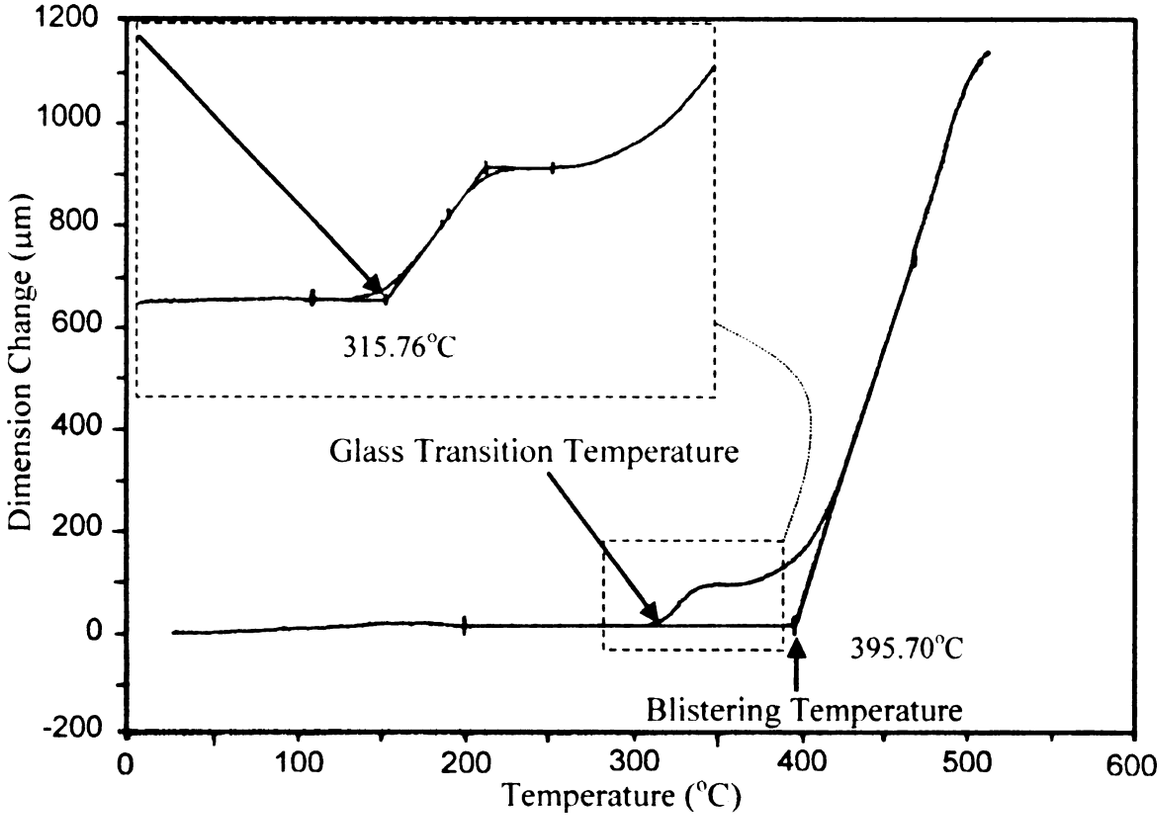

Figure 8.10: Typical TMA curve (shown is AFR700B wet control) used to measure the blistering and glass transition temperatures of pressure bomb exposed polyimides.

Table 8.6: Control values of T_g (via TMA) for K3B and AFR700B. Dry T_g is the initial T_g after step drying and wet T_g was measured on completely saturated (80°C/100% RH) polyimides.

Material	Dry T_g (°C)	Wet T_g (°C)	T_g Decrease per wt% Moisture
K3B	241	204	24
AFR700B	384	315	20

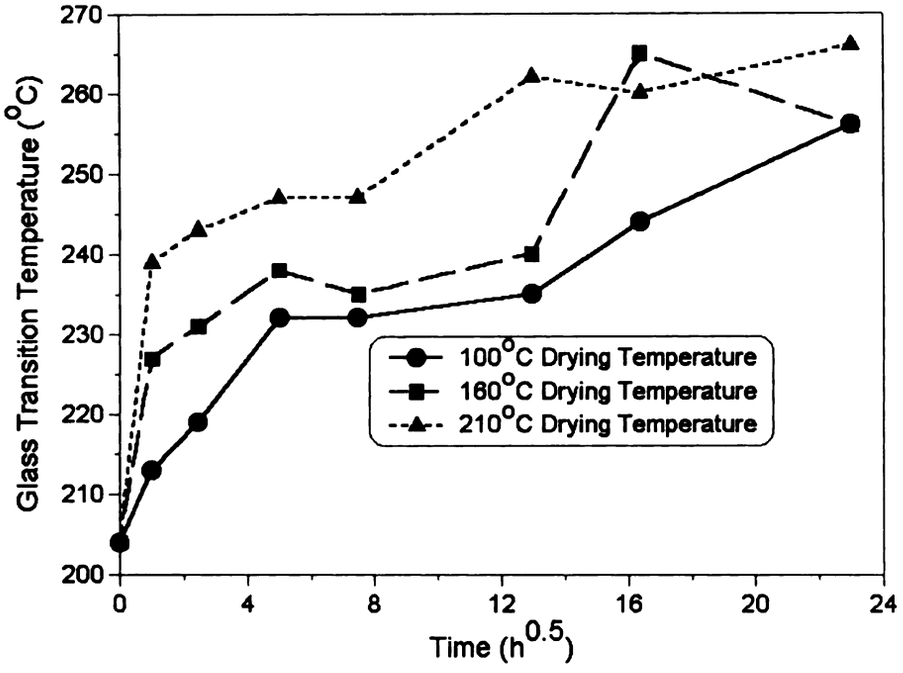

Figure 8.11(a): Glass transition temperature of K3B after hygrothermal aging as a function of drying time-temperature conditions.

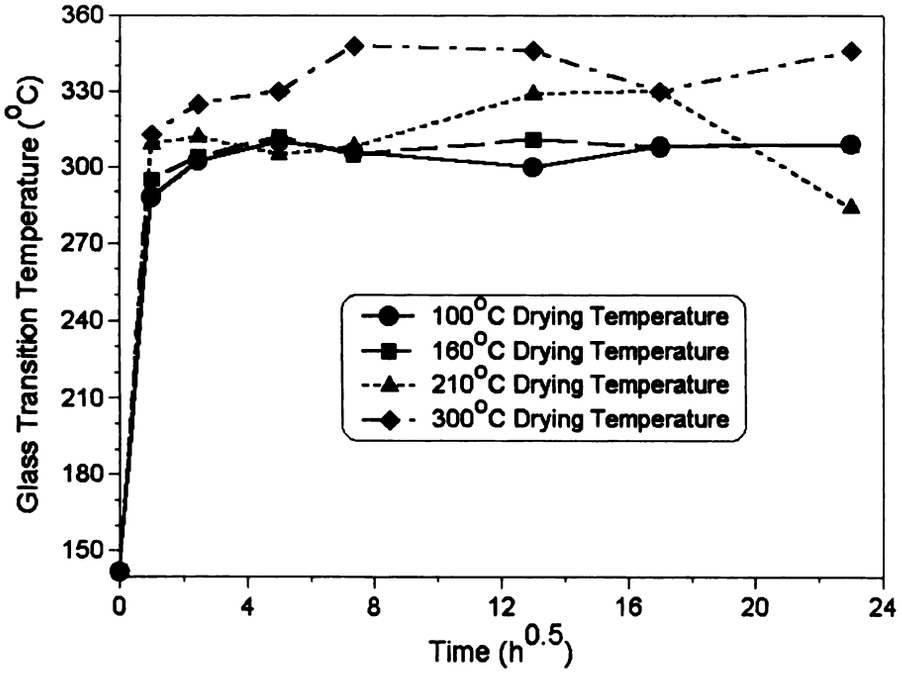

Figure 8.11(b): Glass transition temperature of AFR700B after hygrothermal aging as a function of drying time-temperature conditions.

It should be mentioned that the dry and wet T_g values reported for K3B are slightly different than those reported in Chapter 6. This is because the techniques used to measure T_g differed, as did the specimen geometries, heating rates, and exposure conditions. The reductions in T_g, however were both on the order of ~40°C. Also, the wet T_g values are assumed to be primarily a result of matrix plasticization with no hydrolysis.

Figure 8.12 are plots of moisture content as a function of T_g for K3B and AFR700B, irrespective of drying temperature. As shown, the T_g follows a linear relationship for both polyimides. Both of these curves can be fitted to the linear Equation 8.1, where T_g^M is the glass transition temperature (°C) as a function of moisture concentration after hygrothermal aging, T_g^{exp} represents the dry glass transition temperature of the polyimide after hygrothermal aging, M is the moisture concentration (in wt%), and χ provides rate of T_g knockdown as a function of residual moisture (in °C/wt%).

$$T_g^M = T_g^{exp} - \chi M \tag{8.1}$$

The data for K3B and AFR700B are listed in Table 8.7. From Figure 8.11, the original dry T_g is regained upon drying for K3B at all drying temperatures, but for AFR700B the initial T_g was never obtained for any of the drying conditions, indicating permanent hydrolytic degradation.

As discussed in Chapters 6 and 7 and reinforced from the data in Table 8.7, if matrix plasticization were the only factor influencing a lower measured value for T_g, the decrease should be on the order of ~25°C/wt% moisture. For K3B, the measured values as a function of drying conditions correspond roughly to this value, but the measured value for AFR700B was ~75°C/wt% moisture. This enforces the data generated by Curliss *et al.* [263] that hydrolytic degradation has taken place, in addition to any molecularly trapped water molecules. Also, the data suggests that the extent of hydrolytic degradation in AFR700B is more severe than for K3B.

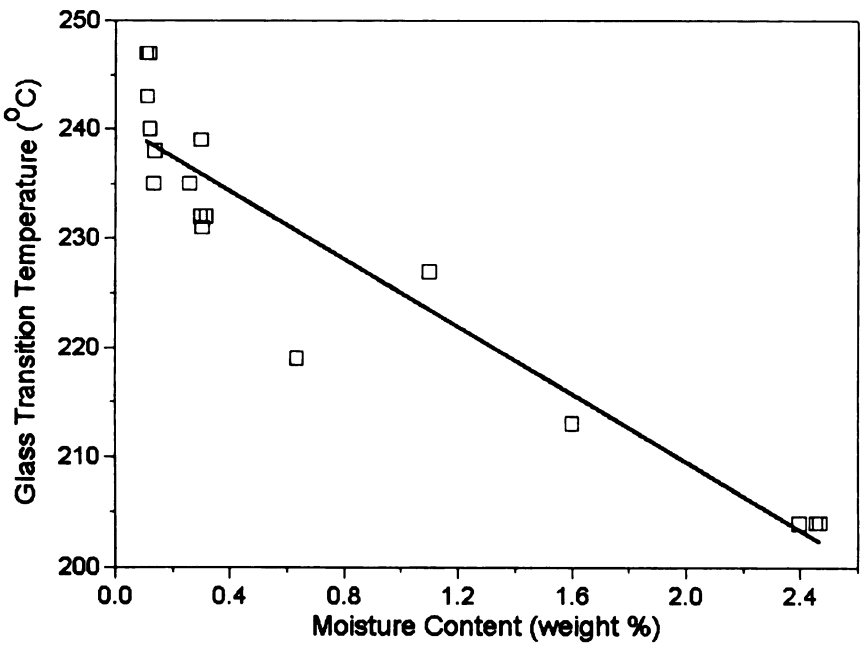

Figure 8.12(a): Glass transition temperature of K3B after hygrothermal aging as a function of moisture content.

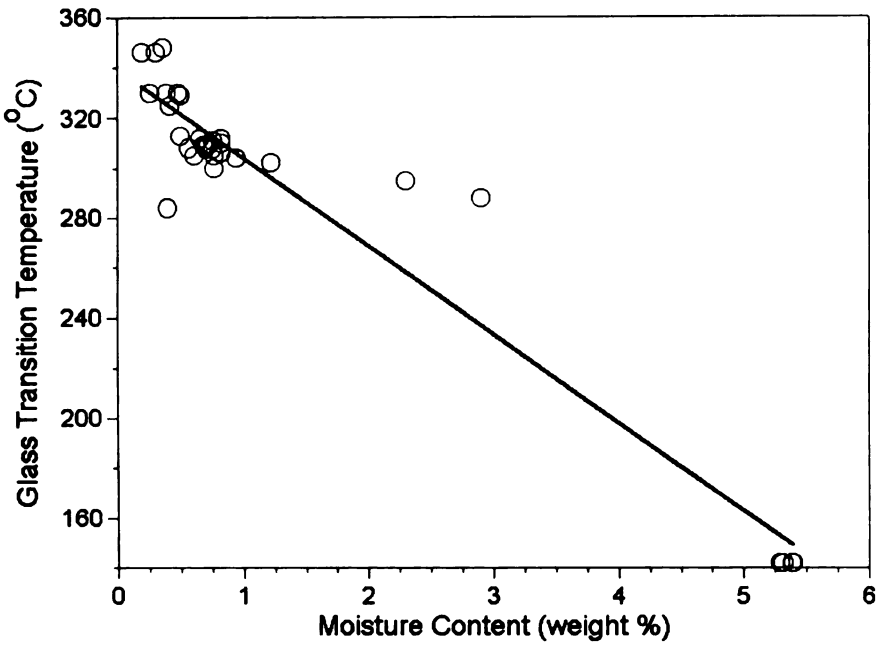

Figure 8.12(b): Glass transition temperature of AFR700B after hygrothermal aging as a function of moisture content.

In addition, the aforementioned phenomena are also supported by the actual values of T_g after hygrothermal exposure. The wet T_gs (moisture saturated at 80°C) for K3B and AFR700B are 204°C and 315°C, respectively, which corresponds to the T_g of K3B immediately after hygrothermal exposure. In contrast, the T_g of AFR700B immediately after exposure was only 142°C; 173°C lower than the wet T_g. This also indicates that hydrolytic chemical degradation has taken place in addition to any plasticization for AFR700B, but much less severe (if at all) for K3B polyimide.

Table 8.7: Curve fit values to Equation 8.1 for K3B and AFR700B (Figure 8.12) after hygrothermal aging.

Material	Dry T_g (°C)	Wet T_g (°C)	T_g^{exp} (°C)	χ (°C/wt%)	Regression Coefficient
K3B	241	204	240	16	0.929
AFR700B	384	315	339	35	0.887

As expected, the observed permanent dry T_g decreases also correspond to reductions in dry mechanical properties after hygrothermal exposure. Morgan *et al.* [20] reported a 70% loss of strength and 85% loss of strain to failure for AFR700B and a 5% loss of strength and 20% decrease in ductility for K3B after the pressure bomb exposure and subsequent drying conditions used in this study.

An important additional comment regarding the above results concerns the polymerization reactions for polyimides. Under high temperature drying conditions, the degraded polymer (polyamic acid species) can undergo re-imidization, so part of the degradation may be reversible. The 300°C drying temperature for AFR700B is evidence of re-imidization, for example, since much higher T_g values are obtainable at this drying temperature compared to the others, even at equivalent moisture concentrations. Lee [264] has demonstrated, using dynamic mechanical analysis, that isothermal heating at 400°C of hydrolytically degraded AFR700B can lead to complete or nearly complete regeneration of the dry T_g. This reversibility will be examined in Chapter 9 for polyimides of varying chemical structures.

8.3.2.4 Blistering Thresholds

In the hygrothermal spiking program discussed earlier, severe blistering and delamination were observed for K3B polymers and composites. Here, the critical thresholds in terms of moisture content-time-temperature conditions are investigated for both K3B and AFR700B neat resins.

Blistering was monitored using TMA, where a dramatic increase in the thickness dimension of the polymer samples was observed. A typical severe blistering phenomenon is displayed in Figure 8.13 for an AFR700B polyimide hygrothermally aged in the pressure bomb and subsequently dried at 100°C for 6 h. After exposure, severe blisters and cracks were observed in the AFR700B polyimide samples, but the more ductile K3B matrix displayed closed blisters.

Figure 8.14 displays the blistering thresholds as a function of the moisture content for the various drying temperatures for K3B and AFR700B. Interestingly, only very small moisture contents (0.3~0.4 wt%) are required to initiate blistering in these materials, with the blistering temperature being a function of the moisture content. Interestingly, for AFR700B, the 0.4 wt% moisture required to induce blistering corresponds to scission of one hydrolyzed imide linkage per chain [125]. These findings are significant because during real aerospace service exposure conditions, cavitation, blistering and subsequent composite delamination can occur in these polyimides.

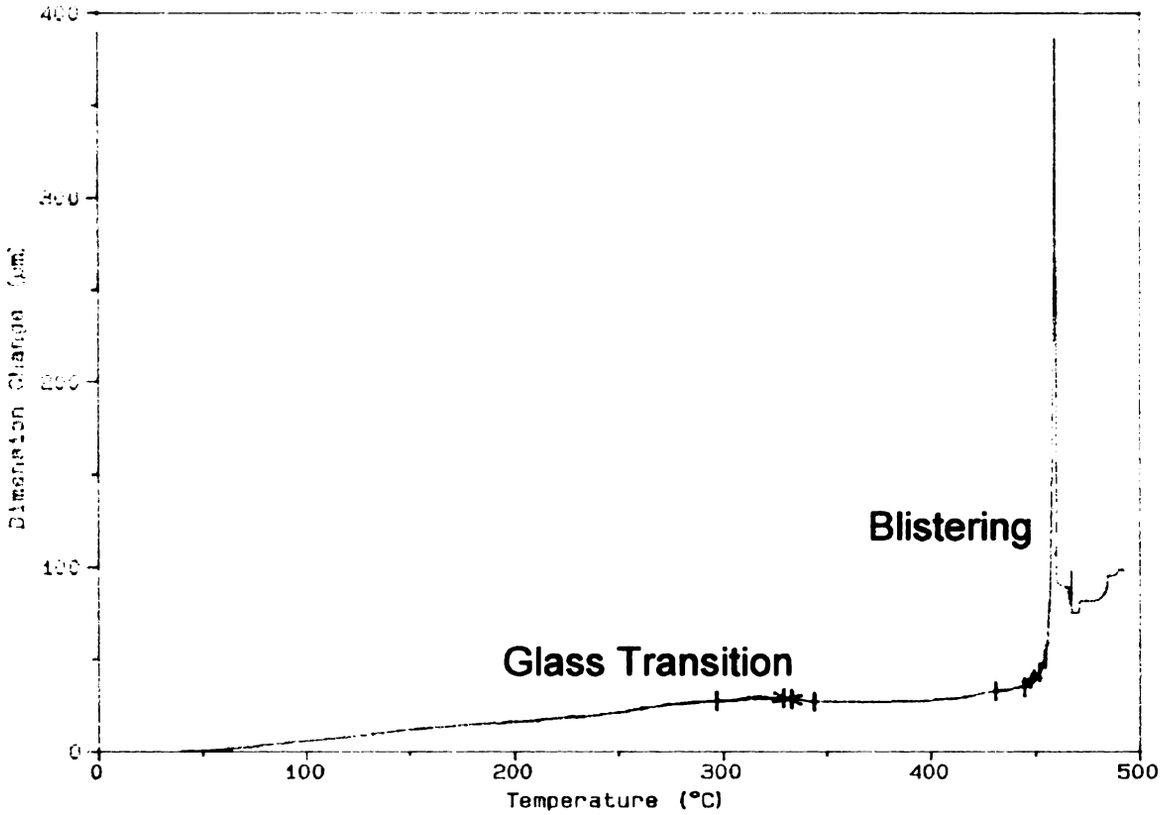

Figure 8.13: Blistering characterization in a TMA experiment for an AFR700B polyimide hygrothermally aged then dried at 100°C for 6 h.

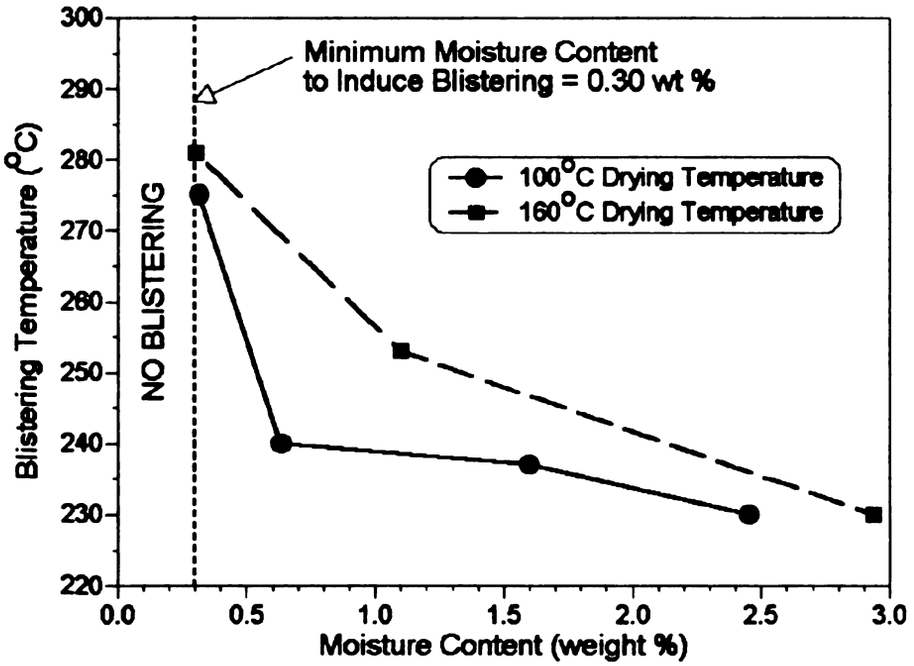

Figure 8.14(a): Blistering threshold characterization for K3B polyimide.

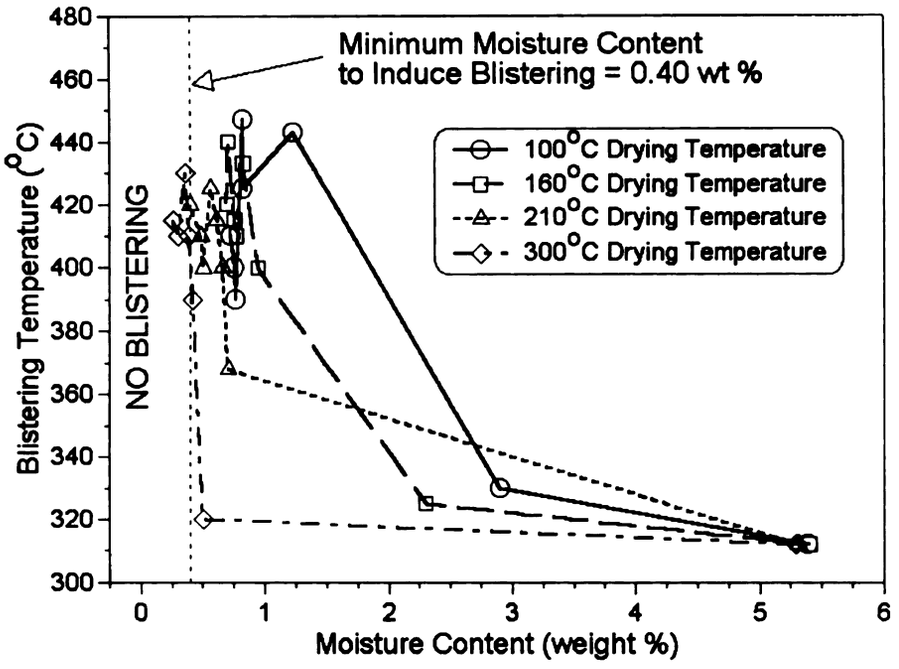

Figure 8.14(b): Blistering threshold characterization for AFR700B polyimide.

Finally, it should be reiterated that in addition to the time-temperature-moisture conditions discussed above, component geometry, processing conditions (thermal history; see Chapters 3 and 5), moisture concentration profiles, heating rate, and fiber volume fraction also play a role in blistering in composite laminates. Rice *et al.* [263], for example, conducted fundamental studies to predict steam induced delamination in AFR700B composite laminates based on the pressure inside of microcavities (taking into account the cavity geometry), component thickness, moisture concentration profile, and drying time-temperature conditions. From their studies, the researchers were able to construct damage threshold envelopes of safe operation as a function of

moisture concentration and temperature for the respective composite materials. Their results can be used by component designers to determine if or when a part of a given thickness and initial moisture content is likely to blister while undergoing a particular thermal cycle.

8.4 Conclusions

The physical structural states of polyimide neat resins and composites were investigated as a function of (i) hygrothermal spiking and (ii) accelerated hygrothermal aging, and related to physical, thermal, and mechanical properties.

From the hygrothermal spiking program, thermoplastic K3B polyimide was shown to be susceptible to vapor pressure induced matrix cavitation, blistering and subsequent laminate delamination. Significant decreases in mechanical integrity were observed after hygrothermal aging. IM7/BMI laminates were not susceptible to the respective unacceptable damage, due to (i) transverse cure induced microcracks which allowed for rapid diffusion of moisture out of the composite during high temperature thermal excursions, (ii) the lesser susceptibility of thermosets to blister, which would require rupture and/or hydrolysis of covalent crosslinked segments, and (iii) the higher T_g of the BMI resin compared to K3B.

In the hygrothermal aging study, both K3B and AFR700B polyimides were susceptible to blistering, mass density changes, modifications of the

moisture absorption/desorption characteristics, and permanent dry T_g decreases. These reported physical, thermal, and mechanical material property changes are a result of hydrolytic degradation of the polyimides and matrix plasticization via molecularly trapped water molecules.

Permanent glass transition temperatures were observed for both polyimides, but the original dry T_g of K3B could be regained upon drying whereas the final T_g of hygrothermally aged AFR700B after drying was ~50°C lower than the initial value. This coupled with moisture absorption/desorption results, density changes, and literature data generated in conjunction with this research (regarding mechanical properties and ^2H NMR studies) indicate that the hydrolysis of AFR700B is more severe than for K3B.

Characterization of the blistering thresholds as a function of moisture content and time-temperature drying profiles also revealed that very low moisture contents (0.3 – 0.4 wt%) are required to initiate blisters in these polyimides. For AFR700B, the 0.4 wt% blistering threshold corresponds roughly to one hydrolyzed imide linkage per chain, indicating a possible connection between molecular structure and unacceptable hygrothermal induced physical degradation.

In Chapter 9, accelerated hygrothermal aging is presented to further ascertain the relationships between physical/chemical structure and hygrothermal durability so that future material improvements may be achieved.

Chapter 9

Accelerated Hygrothermal Aging and Degradation Kinetics of Polyimides

9.1 Introduction

In previous chapters, the relationships between polyimide structure, properties, processing conditions, and hygrothermal durability were investigated. Specifically, in Chapter 8, AFR700B thermosetting polyimide was shown to be highly susceptible to hydrolysis under hygrothermal exposure conditions. This hydrolytic degradation lead to permanent reductions in the dry T_g and blistering damage after aging during thermal excursions.

Here, further insight into the mechanisms of hydrolytic degradation is presented by accelerated hygrothermal aging of three high temperature polyimides: AFR700B, K3B, and PETI-5 (Figure 9.1). Through a comparative analysis of degradation (based on T_g), the permanent and reversible components will be separated out to determine the hydrolytic stability as a function of molecular structure. Using the results presented previously in this dissertation, the data generated in the program below, and results from the literature, characterization of the fundamental degradation mechanisms for AFR700B, K3B, and PETI-5 high temperature polyimides will be presented.

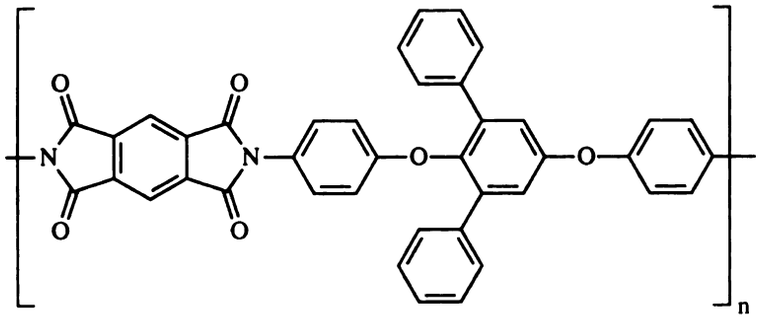

K3B

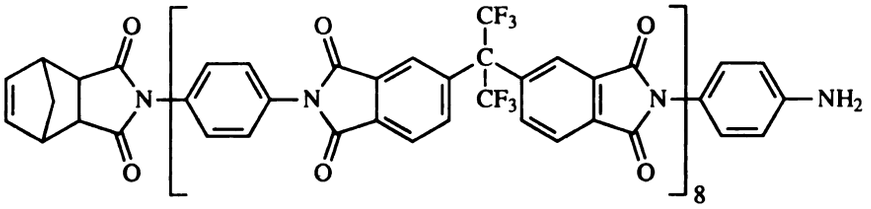

AFR700B

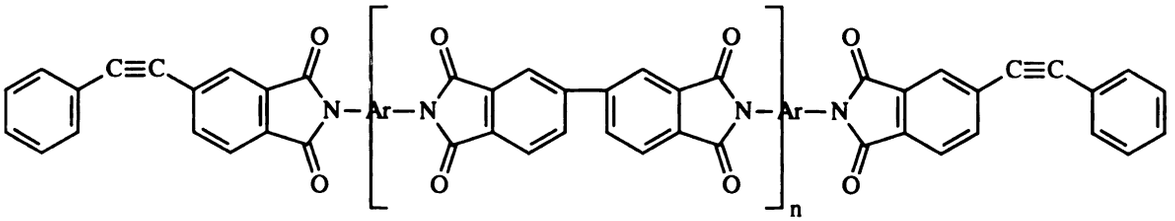

Where Ar = 85% 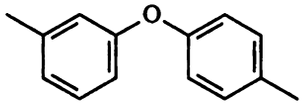 & 15% 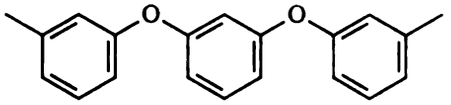

PETI-5

Figure 9.1: Comparative depiction of the chemical structures for K3B, AFR700B, and PETI-5 polyimides analyzed in the hygrothermal aging study.

The AFR700B polyimide is of particular interest for Air Force applications due to the combined thermal stability and toughness relative to other high temperature polyimides. As discussed in Chapter 2, AFR700B can be used for 150°C higher temperature applications than PMR-15. Studies indicate that the respective combination of the fluorinated backbone and choice of diamine for this polyimide lead to these observed properties [97, 208-211, 214, 216, 220, 221, 230]. In the current AFOSR group program, the ultimate goal was to characterize the weak link in AFR700B so that possible chemical modifications could be made to improve the material properties and environmental durability (Chapter 10).

9.1.1 AFR700B Crosslinking Reactions

In order to characterize the degradation of AFR700B, it is necessary to comprehend the crosslinking reactions so that suggestions regarding hydrolytic degradation sites can be made and subsequently investigated using model compound studies. As such, the primary crosslinking reactions for AFR700B will be briefly reviewed.

For the other two polyimides these details are not necessary for this study, as will be shown in the results discussed below. K3B is a thermoplastic, so hydrolytic degradation induced chain scission occurs either at the ends of the molecules or randomly along the chain (Chapter 2). For PETI-5, the

crosslinking reactions through the C≡C triple bond are not well understood, as discussed in Chapter 5. Regardless of the structure, if reversion to polyamic acid and hydrolysis of crosslinks can be minimized, the hygrothermal durability will be subsequently improved. Recall from Chapter 8 that the hydrolysis of the amide acid occurs at rates 550 times faster than imide ring hydrolysis.

A detailed analysis of the crosslinking reactions in AFR700B has been published by Russell *et al.* [114]. The main crosslinking reactions consist primarily of norbornene and maleimide reactions, but thermooxidative crosslinking can also occur via scission of trifluoromethyl ($-CF_3$) groups from the polymer backbone, forming a carbonyl group that is capable of forming ether crosslinks between chains. In terms of the norbornene reactions, these include (i) biradical homopolymerization and (ii) retro Diels-Alder reactions. For the maleimide groups, the reactions consist of (i) the BMI homocrosslink reaction, (ii) Michael addition reaction, and (iii) an aminolysis reaction. These are shown in Figure 9.2.

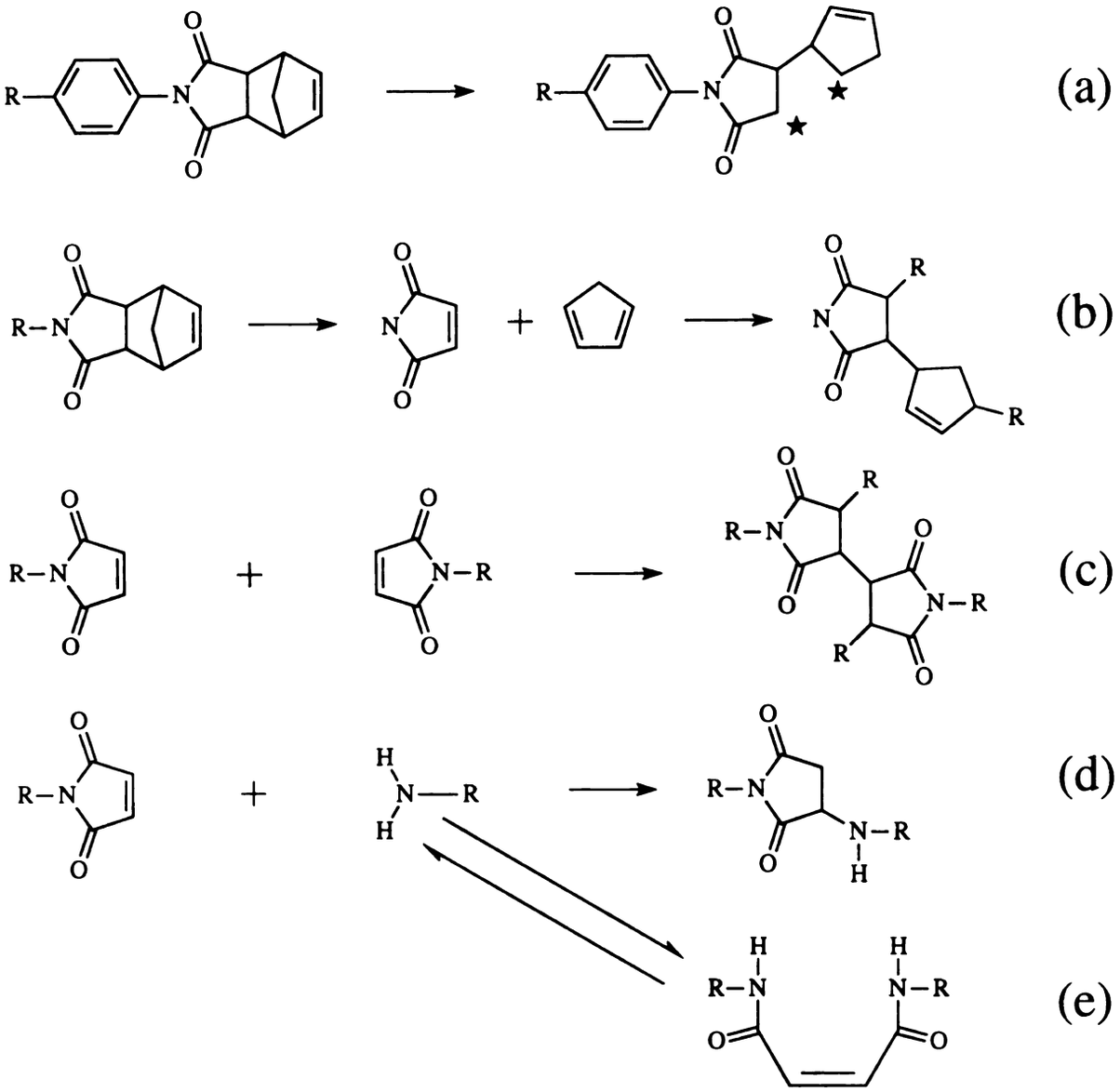

Figure 9.2: Norbornene and maleimide crosslinking reactions for AFR700B: (a) biradical homopolymerization, (b) retro Diels-Alder reaction, (c) BMI homocrosslink reaction, (d) Michael addition reaction, and (e) aminolysis reaction [114, 223]. R represents a continuation of the polymer network.

From the reactions it is important from a structural standpoint to note the retro Diels-Alder reaction, which releases cyclopentadiene at high temperatures (>200°C) during cure. Thorp *et al.* [223], used model compounds to compare the effects of pressure on network structure. In an open vial cure

environment (as opposed to a compression mold environment), a higher concentration of Michael addition and/or aminolysis reaction products were observed, as shown schematically in Figure 9.3. The retro Diels-Alder reaction occurred for both pressure cured and vial cured model compounds, but in the absence of pressure the volatile cyclopentadiene was in lower concentration in solution. As a result, the maleimide double bond could react with the free amine to form a higher concentration of Michael addition and/or aminolysis crosslinks. Therefore, heating in the absence of a closed mold increases the total amount of Michael addition and/or aminolysis crosslinks in the network.

With respect to a hygrothermal durability standpoint, these reaction pathways and structural state of the crosslinks are important in terms of identifying the hydrolytically unstable (weak link) in the AFR700B structure. In the same paper, Thorp *et al.* used model compound studies to identify the most likely critical failure path of the resin in terms of chemical structure. The aforementioned model compound studies will be discussed below with respect to the results obtained from the present investigation.

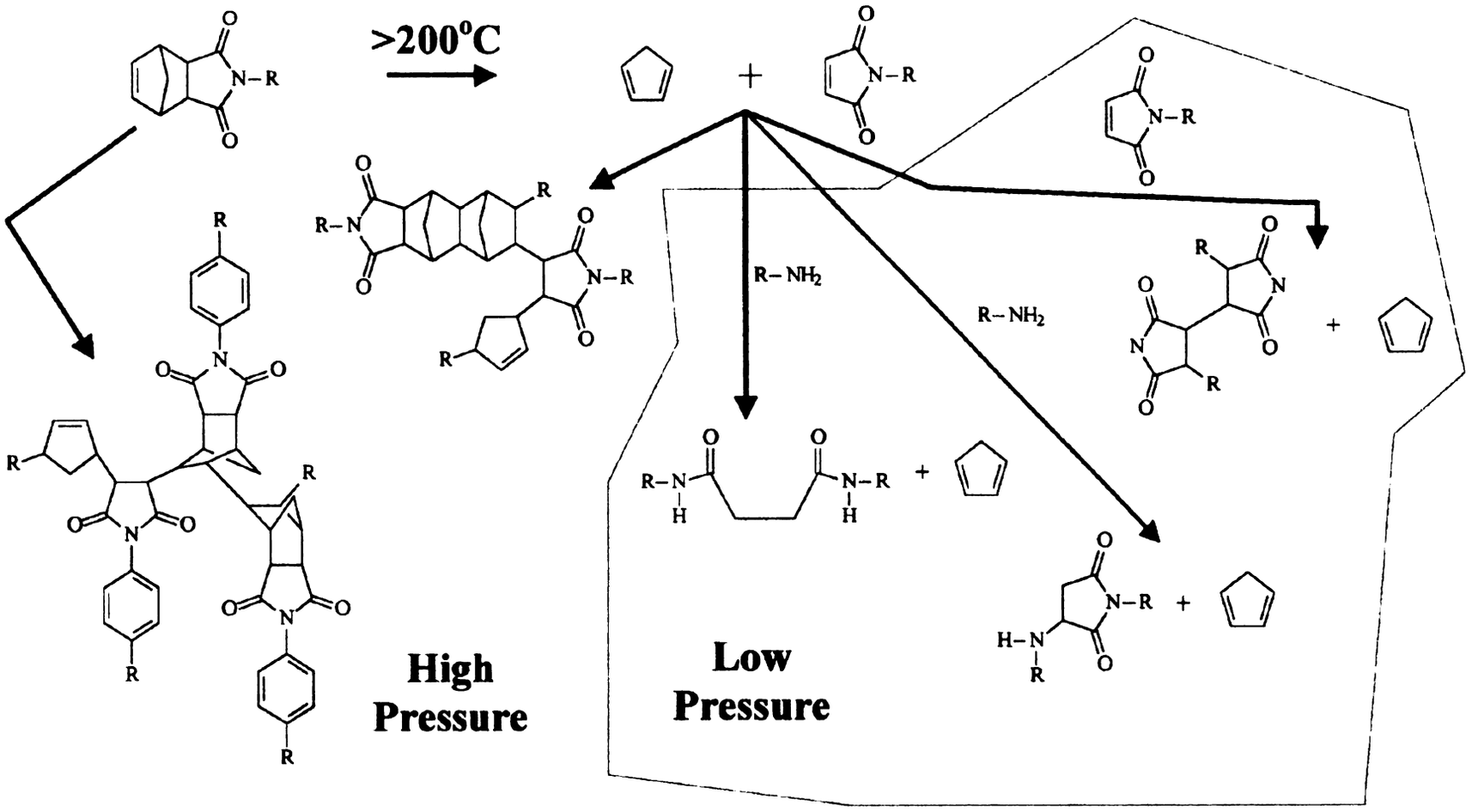

Figure 9.3: Effects of processing pressure on the norbornene crosslinking reactions in AFR700B [223].

9.2 Experimental Techniques

9.2.1 Materials

The polyimide resins utilized were K3B, PETI-5 (5000 g/mol), and AFR700B. K3B raw material (consisting of aromatic diethyl ester diacid and aromatic diamine in NMP) was dried at 200°C under vacuum for 1 h, then fully imidized by heating at 360°C for 2 h. Imidized PETI-5 powder was cured at 260°C/2 h + 371°C/1.5 h in air to simulate standard cure conditions for PETI-5 composites. Imidized AFR700B oligomer, obtained from Air Force Research Laboratory, Wright-Patterson Air Force Base, was cured at 382°C for 1 h. The K3B, PETI-5, and AFR700B materials were then cryogenically pulverized using a cryogenic mill (SPEX CertiPrep 6750). Consistent milling procedures were used to produce powders with particle sizes ranging from 80 – 100μm so that comparative analysis could be made in the hygrothermal aging experiments.

9.2.2 Hygrothermal Aging

The conventional pressure bomb method was used to simulate a high temperature steam environment at temperatures ranging from 177 - 250°C and times from 0.5 - 1536 h. In order to avoid possible galvanic degradation, the sample powders were contained in quartz test tubes and then placed in a pressure bomb containing de-ionized water. The pressure bomb was heated to

the temperature selected at a rate of 1.5°C/min. At the end of each time-temperature hygrothermal aging treatment, the bomb was opened around 130°C, to prevent any possible condensation of liquid water into the sample tube. After the exposure, the powder was dried at room temperature and full vacuum for 48 hours, then re-powdered cryogenically prior to various analytical tests. Table 9.1 displays the overall pressure bomb test matrix for various polyimide systems and exposure time-temperature conditions.

Table 9.1: Time-temperature pressure bomb accelerated exposure conditions for K3B, PETI-5, and AFR700B DSC characterizations.

Polyimide	**Exposure Temperature (°C)**	**Measurement Exposure Times (h)**
K3B	177	192, 768, 1536
	185	96, 192, 384
	200	0.5, 3, 12, 18, 24, 96, 384, 768
	225	0.5, 3, 12, 24, 96, 192
	250	0.5, 3, 12, 24, 96, 192
PETI-5	177	384, 768, 1536
	200	96, 192, 768
	225	24, 96, 192
	250	24, 96, 192
AFR700B	177	96, 192, 384
	200	24, 96, 192
	250	24, 96, 192

9.2.3 Characterization Techniques

DSC measurements were conducted using the same instrument and techniques discussed previously. All scans were performed from 23 – 400°C at 10°C/min under nitrogen gas. Fourier transform infrared spectroscopy (FTIR) spectra were obtained using a Nicolet® 20DXB spectrometer. FTIR specimens were prepared by compressing the mixture of polyimide powder (about 1 wt%) and KBr powder into thin discs. Quantification of degradation was found to be difficult, so DSC was used as the primary characterization method in the studies (four specimens per condition were tested). Thorp *et al.* [262] have shown by comparative NMR, DSC, and TGA analysis that decreases in the glass transition temperature and weight changes directly correspond to hydrolytic induced molecular structure modifications of polyimides.

It must be noted that many of the aforementioned experiments in this chapter were performed by Jiang Zhou, a visiting scientist at the Advanced Materials Engineering Experiment Station (AMEES-MSU), as portion of the overall joint AFOSR program. The author, however, performed analysis of the data and interrelationships with the corresponding studies of this dissertation.

9.2.4 Kinetics Relationships

The extent of reversible and irreversible degradation can be separated out from two DSC scans of a hydrolytically degraded polymer. In the first scan, the glass transition temperature is measured and recorded as T_g^1. The same specimen is cooled to room temperature and subsequently rescanned to obtain T_g^2. From the common Fox relationship, the change in T_g is assumed to be proportional to the inverse of the molecular weight (thermoplastics) by Equation 9.1.

$$\Delta T_g \alpha \frac{1}{M_n} \tag{9.1}$$

Therefore, the extent of reversible (Ψ_I), irreversible (Ψ_R), and total degradation (Ψ) can be written according to the following three equations:

$$\Psi_I = \frac{T_g^{dry} - T_g^2}{T_g^{dry}} \tag{9.2}$$

$$\Psi_R = \frac{T_g^2 - T_g^1}{T_g^{dry}} \tag{9.3}$$

$$\Psi = \Psi_I + \Psi_R \tag{9.4}$$

In the above equations, T_g^{dry} is the glass transition temperature of the dry control polymer prior to any hygrothermal exposure.

In order to obtain kinetics of degradation and corresponding activation energies, the phenomenological rate equations can be applied [223]:

$$\frac{d\Psi}{dt} = -k\Psi C \tag{9.5}$$

$$k' = kC_{sat} \tag{9.6}$$

$$\frac{d\Psi}{dt} = -k'\Psi \tag{9.7}$$

$$\Psi(t) = \exp(-k't) \tag{9.8}$$

$$k' = A\exp\left(-\frac{E}{RT}\right) \tag{9.9}$$

$$\Psi(t) = \frac{T_g^f - T_g(t)}{T_g^f - T_g^{dry}} \tag{9.10}$$

Above, t represents the time of exposure, T is the absolute temperature, k is the rate constant, k' is the apparent rate constant which takes into account contributions from absorbed moisture, C is the concentration of moisture and C_{sat} represents the saturated moisture concentration. A is a pre-exponential parameter and E is the activation energy of hydrolytic degradation. The term T_g^f is the final T_g after complete degradation and $T_g(t)$ is the glass transition temperature after time t at temperature T.

9.3 Results and Discussion

9.3.1 DSC and FTIR Results

Information obtained from the DSC scans may be directly related to the chemistry of the polyimides. Figure 9.4, for example, shows the first and second scans of a K3B polyimide exposed in the pressure bomb at 250°C. Three endothermic peaks are present immediately after hygrothermal exposure and subsequent drying, which may possibly correspond to the following hydrolysis reaction products: (i) phthalic acid; melting temperature of 205°C (ii) pyromellitic acid; melting temperature of 283-286°C, and (iii) terephthalic acid; sublimation at temperatures >300°C.

In the case of the three polyimides, a variety of characteristic DSC traces were observed after hydrolytic degradation, as shown in Figures 9.5 and 9.6 for first and second scan DSC runs, respectively. These characteristic extents of degradation were then characterized according to the color codes in Table 9.2 and applied to K3B, PETI-5, and AFR700B, shown in Table 9.3 as a function of time-temperature exposure conditions.

Determination of the values for T_g^1 in the case of K3B and PETI-5 were often cumbersome due to the physical aging effect (PAE) resulting from the endothermic residual enthalpy peak. Based on the assumption that the degree of the PAE is linearly proportional to the endothermic peak area, and thus the peak temperature, a conversion factor to calculate the actual T_g could be

determined. This was carried out by regression analysis of the endothermic peak temperature versus endothermic peak area correlation, as shown in Figure 9.7. It is also of interest to note that K3B showed a linear correlation between the endothermic peak temperature and exposure time, and the physical aging was strongly dependent on exposure time-temperature conditions. In the case of thermoset PETI-5, the relation was temperature independent and the effects of physical aging were significantly lower as a result of the crosslinked structure. In the case of AFR700B, which is a highly crosslinked system, the physical aging effect was not observed.

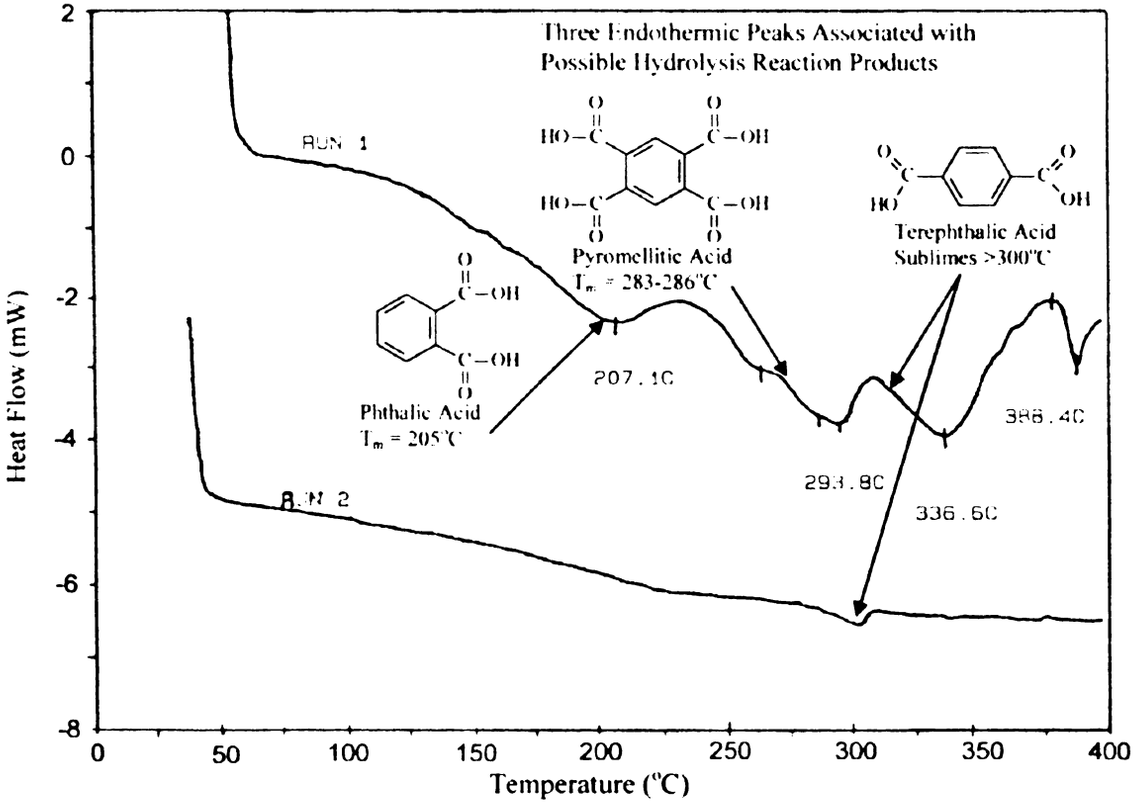

Figure 9.4: DSC trace of hydrolytically degraded K3B showing possible hydrolysis reaction products from endothermic melting peaks.

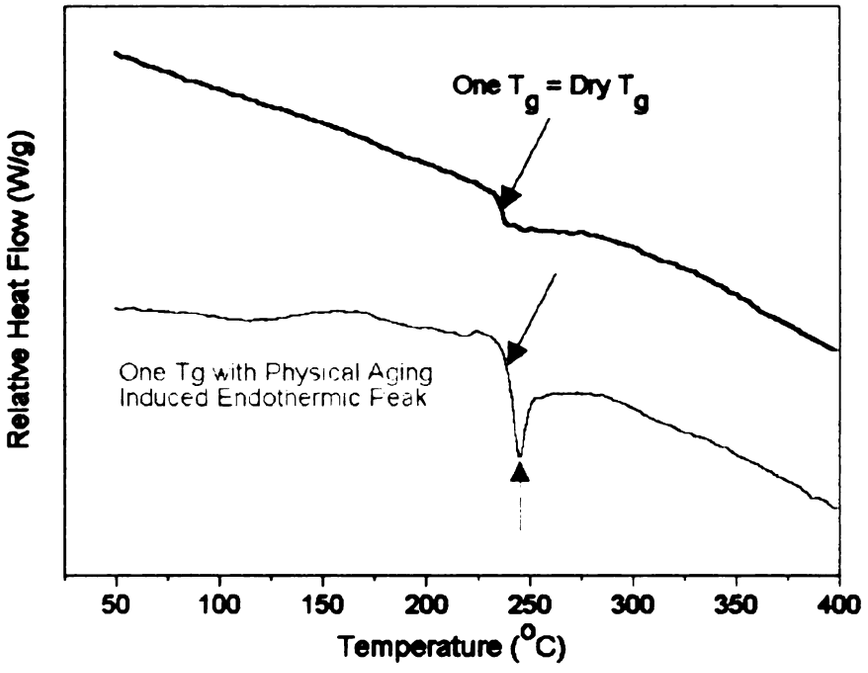

Figure 9.5(a): Common first scan DSC traces of polyimides showing the control and the case where a physical aging induced endothermic peak appears.

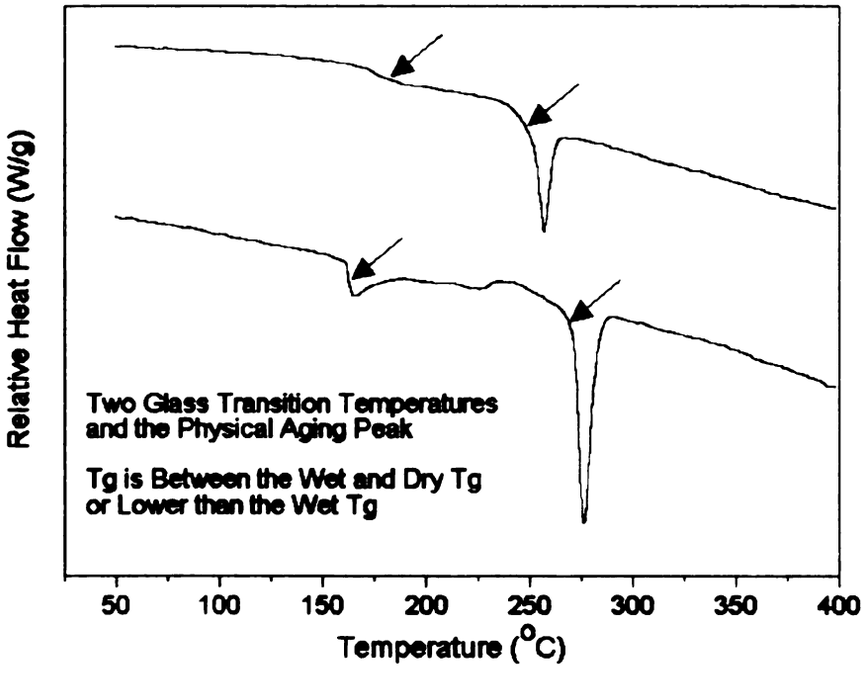

***Figure* 9.5(b):** Common first scan DSC traces of polyimides showing the instance where two glass transition temperatures exist.

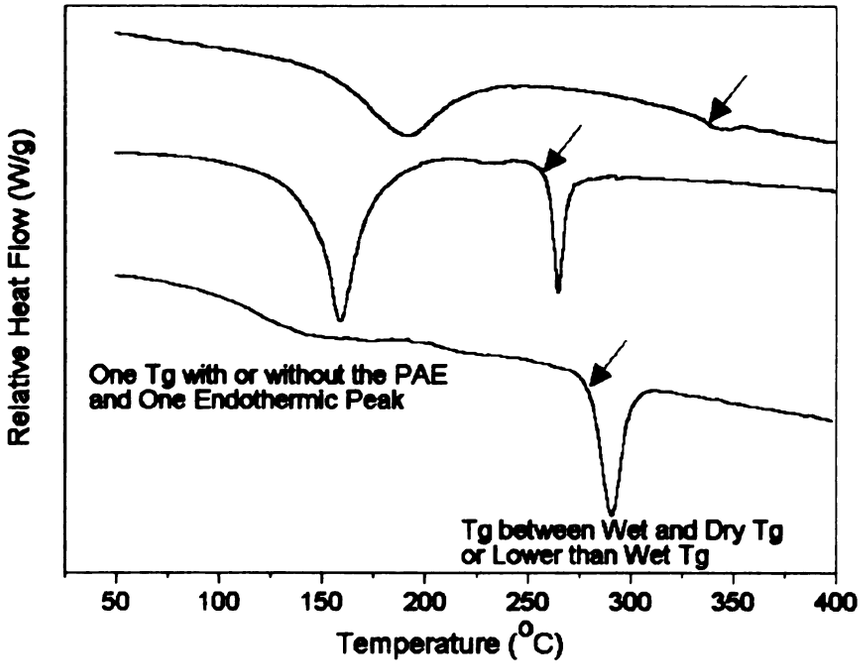

Figure 9.5(c): Common first scan DSC traces of polyimides showing multiple endothermic peaks, physical aging effect, and T_g.

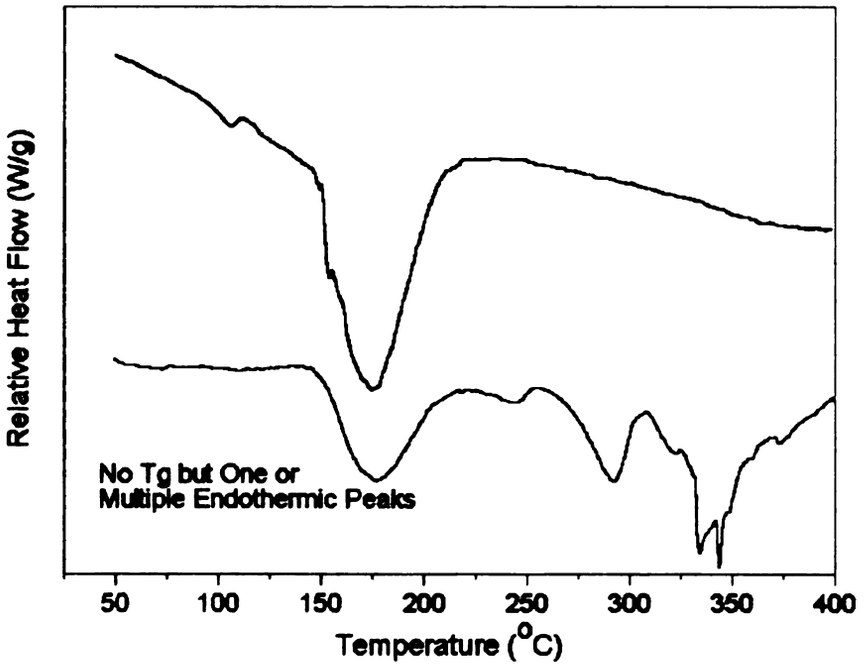

Figure 9.5(d): Common first scan DSC traces of polyimides showing multiple endothermic peaks and no observable T_g.

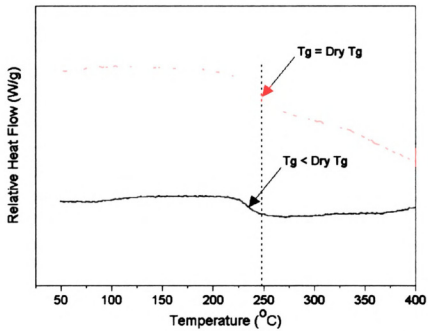

Figure 9.6(a): Typical second scan DSC traces of polyimides showing no reduction and permanent reduction of T_g after hygrothermal exposure.

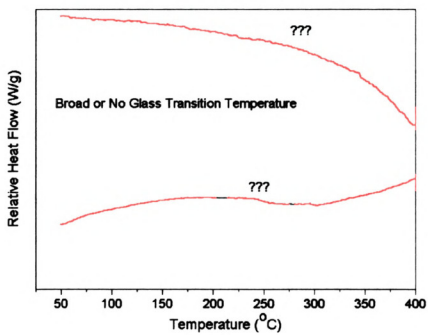

Figure 9.6(b): Typical second scan DSC traces of polyimides showing no observable T_g after hygrothermal exposure.

Table 9.2: Color code characterization of hydrolytic degradation for polyimides as obtained from the DSC and FTIR curves. PAE is the physical aging effect (endothermic peak). Images in this dissertation are presented in color throughout this chapter.

COLOR CODE	DESCRIPTION	MOLECULAR MECHANISM
FIRST SCAN DSC		
	One T_g w/PAE, but lower than the Dry T_g	*Minor Chain Scission and/or Residual Plasticization*
	Two T_gs; high temperature T_g w/PAE but lower than dry T_g	*Depolymerization to Polyamic Acid and Possible Chain Scission*
	One T_g w/PAE, and one lower temperature endothermic peak	*Partial Depolymerization to Monomers and/or Chain Scission*
	One T_g, no PAE, and one lower temperature endothermic peak	*Partial Depolymerization to Monomers and/or Chain Scission*
	One T_g w / PAE and multiple endothermic peaks	*Partial Demonomerization*
	No observed T_g, but one endothermic peak	*Complete Depolymerization and Partial Demonomerization*
	Multiple endothermic peaks without observable T_g	*Complete Demonomerization*
SECOND SCAN DSC		
	One $T_g \approx$ Dry T_g	*Reversible Degradation*
	One T_g or Two T_gs < Dry T_g	*Partially Irreversible Degradation*
	No T_g	*Complete Permanent Degradation*

Table 9.3: Extent of degradation of hygrothermally aged polyimides. Color code based on Table 9.2.

K3B	First Scan T_g (°C)					Second Scan T_g (°C)				
Exposure	177°C	185°C	200°C	225°C	250°C	177°C	185°C	200°C	225°C	250°C
0.5 h	⊗	⊗	229	225	???	⊗	⊗	240	239	236
3 h	⊗	⊗	218	226	???	⊗	⊗	240	239	229
12 h	⊗	⊗	229	227	???	⊗	⊗	239	237	219
18 h	⊗	⊗	222	⊗	⊗	⊗	⊗	238	238	⊗
24 h	⊗	⊗	231	226	???	⊗	⊗	237	237	209
4 days	⊗	225	239	223	???	⊗	240	233	231	187
8 days	224	222	⊗	???	???	238	239	⊗	211	???
16 days	⊗	230	235	⊗	⊗	⊗	243	235	⊗	⊗
32 days	224	⊗	235	⊗	⊗	239	⊗	237	⊗	⊗
64 days	221	⊗	⊗	⊗	⊗	240	⊗	⊗	⊗	⊗
Dry T_g = 247°C (DSC, 10°C/min); Wet T_g = 212°C (M_∞ = 1.5 wt% at 80°C/100% RH)										

PETI-5	First Scan T_g (°C)				Second Scan T_g (°C)			
Exposure	177°C	200°C	225°C	250°C	177°C	200°C	225°C	250°C
24 h	⊗		262	257	⊗	⊗	272	272
4 days	⊗	266	263	240	⊗	276	279	265
8 days	⊗	262	253	230	⊗	272	270	255
16 days	265	⊗	⊗	⊗	274	⊗	⊗	⊗
32 days	268	267	⊗	⊗	278	278	⊗	⊗
64 days	269	⊗	⊗	⊗	278	⊗	⊗	⊗
Dry T_g = 271°C (DSC, 10°C/min); Wet T_g = 220°C (TMA) (M_∞ = 1.0 wt% at 95°C/100% RH)								

AFR-700B	First Scan T_g (°C)			Second Scan T_g (°C)		
Exposure	177°C	200°C	250°C	177°C	200°C	250°C
24 h	⊗	337	292	⊗	374	328
4 days	309	???	242	289	302	318
8 days	322	???	???	375	296	???
16 days	336	⊗	⊗	333	⊗	⊗
Dry T_g = 388°C(DSC, 10°C/min) ; Wet T_g = 305°C (M_∞ = 3.7 wt% at 80°C/100% RH)						

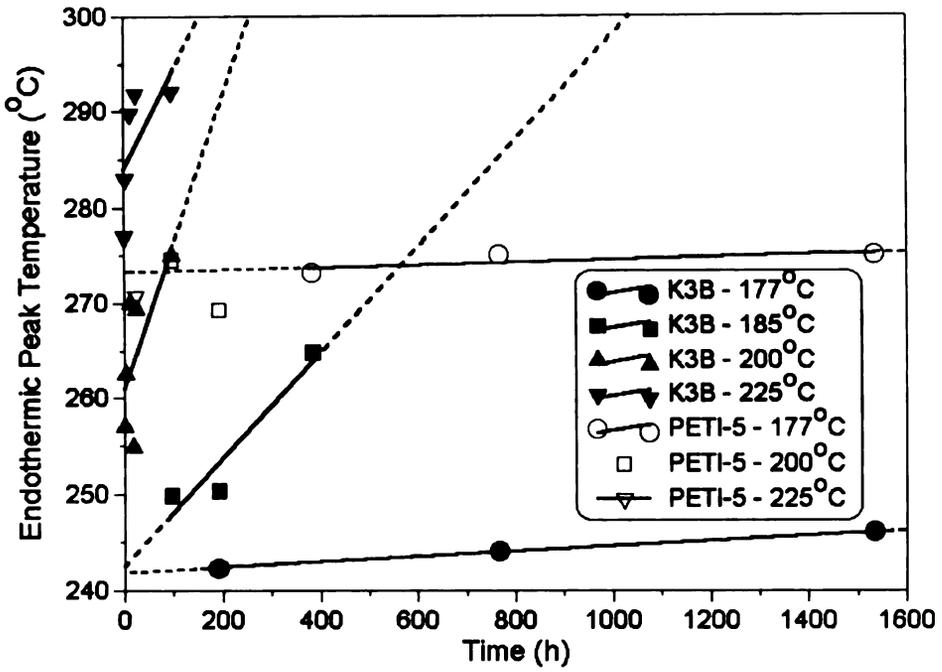

Figure 9.7(a): Plot of endothermic peak temperature as a function of aging time at various temperatures. Regression analysis used for peak correlation.

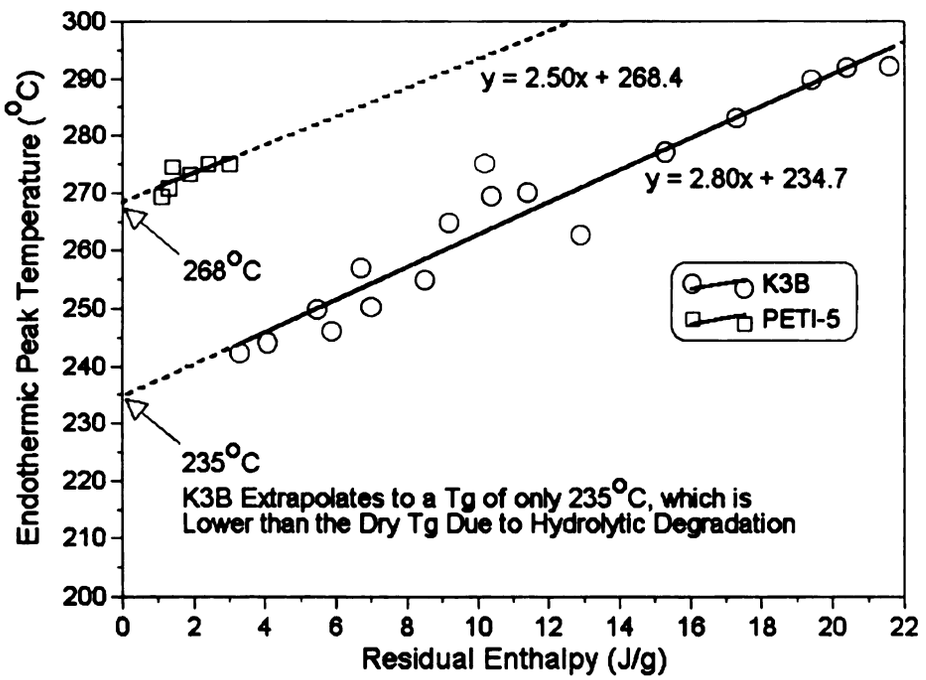

Figure 9.7(b): Plot of endothermic peak temperature as a function of the residual enthalpy used in determination of T_g masked by physical aging.

In addition to the aforementioned experiments, multiple DSC scans (up to 4) were conducted to verify the assumption that the value for T_g^2 corresponded to the actual degraded (irreversible) glass transition temperature. As shown in Figure 9.8, multiple scans produced roughly the same value of T_g for K3B and PETI-5, and only a slight increase was observed after 4 scans of AFR700B. This indicates that the aforementioned assumption was valid.

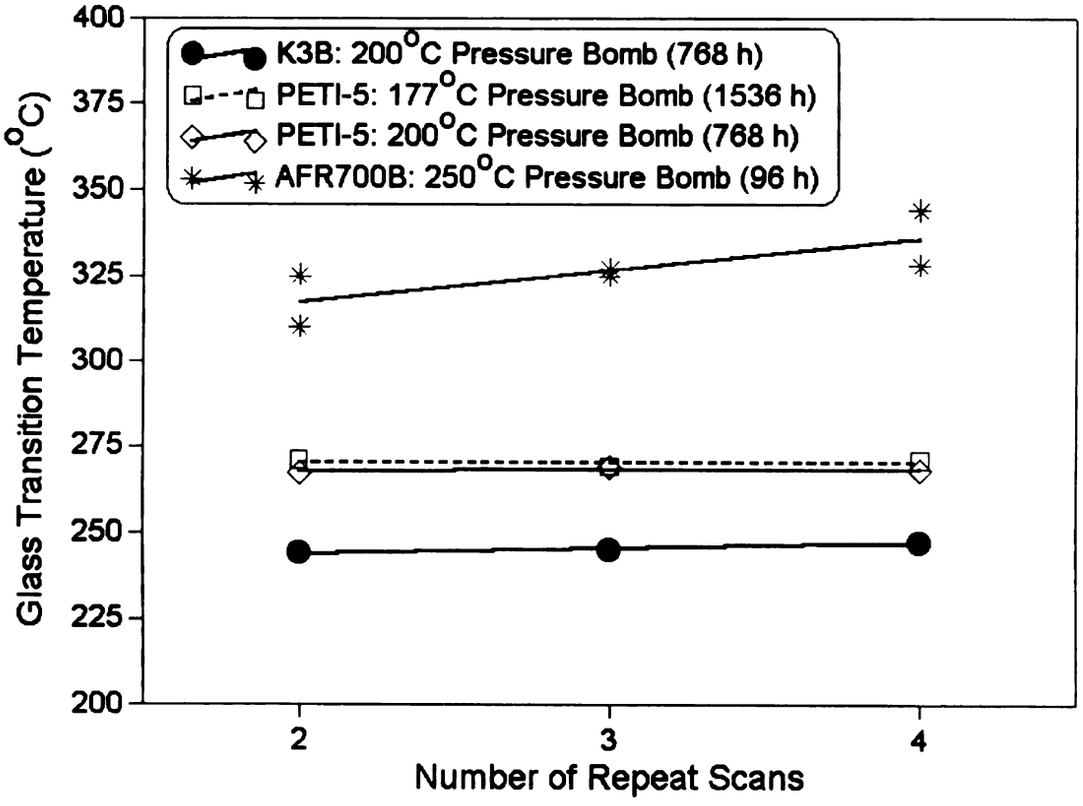

Figure 9.8: Multiple DSC repeat scans to measure T_g for various exposure conditions of polyimides.

Additional evidence to support the separation of reversible and irreversible degradation was obtained from FTIR experiments. Although there was significant scatter when attempting to quantify the results, both AFR700B and K3B displayed a reduction and/or loss in peak intensities related to the imide ring (such as the imide carbonyl stretching band at ~1780 cm^{-1}).

These decreases were coupled with increases and/or appearances of new peaks associated with polyamic acid and starting monomers (bands that appeared initially only in the oligomers or starting monomers again appeared in the degraded polyimides), indicating hydrolytic chain scission and likely dissociation of the monomers under the most severe exposure conditions.

Infrared spectra for K3B and AFR700B are shown in Figure 9.9 for 250°C hygrothermal aging conditions. Table 9.4 depicts some of the important polyimide and polyamic acid peak assignments for both spectra in Figure 9.9 [97, 113].

No peaks were lost or gained for the PETI-5 material, only moderate decreases in the imide peak intensities were observed, indicating that hydrolysis most likely occurs through attack of the imide ring and reversion to polyamic acid. No demonomerization was observed from the infrared spectra for the hygrothermal exposure conditions examined.

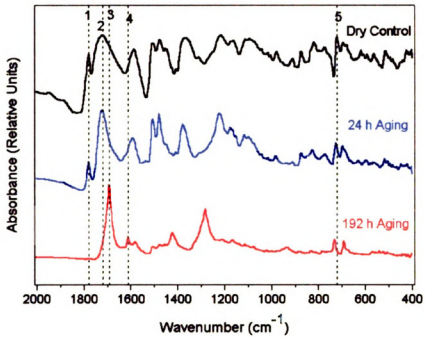

Figure 9.9(a): FTIR spectra of K3B hygrothermally aged in a pressure bomb for various times at 250°C. Shown is characteristic region.

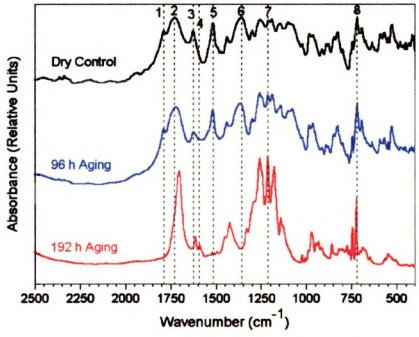

Figure 9.9(b): FTIR spectra of AFR700B hygrothermally aged in a pressure bomb for various times at 250°C. Shown is characteristic region.

Table 9.4: Some characteristic peak assignments for Figure 9.9 [97, 113].

Material	Peak Number	Wavenumber (cm^{-1})	Description
K3B	1	1779	Imide C=O Stretching
	2	1720	Imide C=O Symmetric Stretching
	3	1691	C=O Stretching of Amide
	4	1610	C=O Vibrations of Amide
	5	720	Imide/Anhydride Ring Bending
AFR700B	1	1788	Imide/Anhydride C=O Stretching
	2	1729	Imide C=O Symmetric Stretching
	3	1626	Amine N-H Bending
	4	1592	Amine N-H Bending (Amide)
	5	1515	Aromatic Carbon Ring Vibrations
	6	1360	Imide C-N Stretching
	7	1212	C-F Vibrations
	8	722	Imide/Anhydride Ring Bending

9.3.2 Extent of Degradation Diagram for K3B

Using Equations 9.1 – 9.4, a series of extent of degradation diagrams (EOD diagrams) were developed for thermoplastic K3B polyimide. Using the data in Table 9.3, the EOD diagrams were generated as shown in Figure 9.10 for exposure temperatures of 177°C, 200°C, and 250°C. These individual curves were then compiled to generate the master diagram, shown in Figure 9.11. Depicted in the diagram are the extents of degradation after various hygrothermal exposure conditions based on the physical and chemical structural state of the polymer matrix. The results of this diagram yield thresholds for reversible (depolymerization to polyamic acid) and irreversible (permanent degradation, including hydrolytic attack of the polyamic acid and/or demonomerization).

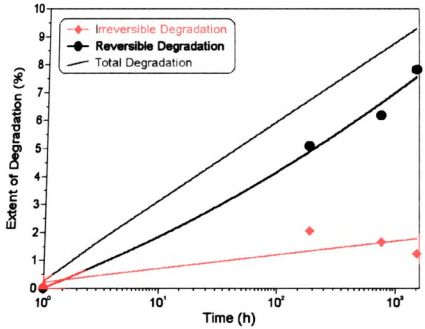

Figure 9.10(a): Extent of degradation (EOD) diagram for K3B polyimide after 177°C hygrothermal aging for various times in a pressure bomb.

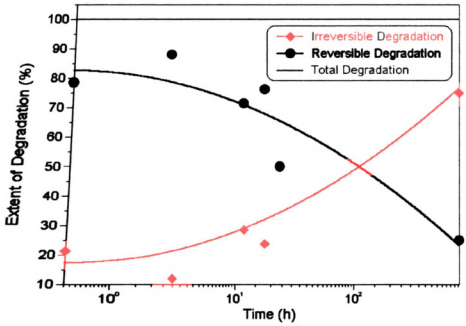

Figure 9.10(b): Extent of degradation (EOD) diagram for K3B polyimide after 200°C hygrothermal aging for various times in a pressure bomb.

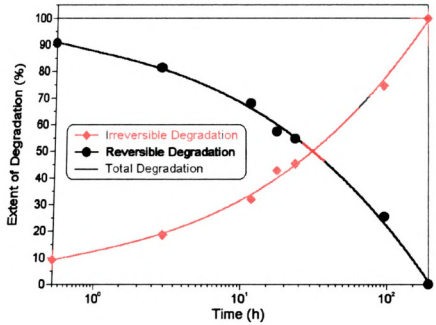

Figure 9.10(c): Extent of degradation (EOD) diagram for K3B polyimide after 250°C hygrothermal aging for various times in a pressure bomb.

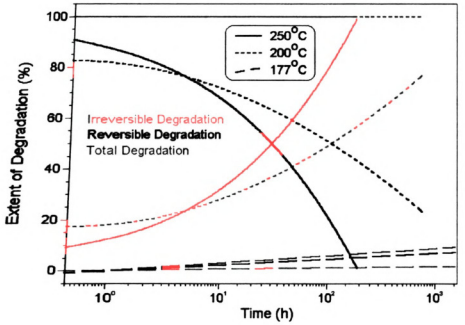

Figure 9.11: Extent of degradation (EOD) master diagram for K3B polyimide for 177 – 250°C hygrothermal aging temperatures.

9.3.3 Hygrothermal Durability Comparison – Phase Diagrams

One of the goals of the current study was to compare the hygrothermal durability of the three polyimides based on molecular structure. This was performed by generation of a structural state phase diagram, which depicts the onset of reversible and irreversible degradation of polyimides. The criterion for the specific states of degradation are based on the FTIR and DSC data generated above, and the phase diagram generated from the respective research is displayed in Figure 9.12.

In the figure, the curves higher on the plot have a higher hygrothermal damage threshold than those towards the bottom of the plot do. Solid lines indicate irreversible degradation whereas dashed lines represent degradation that is reversible upon heating (re-imidization). Therefore, with respect to hygrothermal durability, PETI-5 > K3B > AFR700B.

The reasons for the observed differences in hygrothermal durability stem from the chemical structures of the polyimides. In the case of K3B, which is a thermoplastic, one random scission per macromolecule would statistically result in a 50% reduction in strength [10]. If hydrolytic degradation were to occur at the ends of the chains, significant reductions in the T_g and corresponding mechanical properties would not be observed. Since the chemical structure of K3B is similar to POPPI discussed previously, one would expect the degradation mechanisms and associated kinetics to be similar.

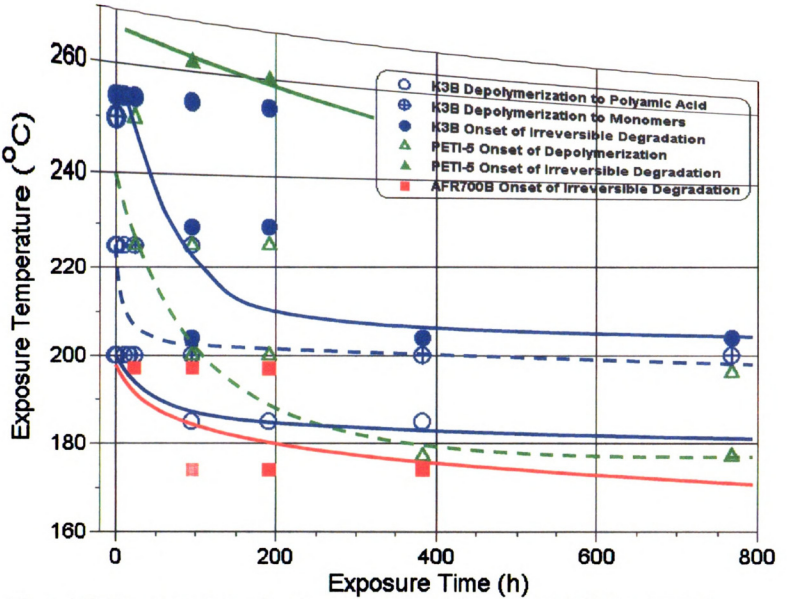

Figure 9.12: Hygrothermal phase diagram comparing the stability of K3B, AFR700B, and PETI-5.

Conversely, PETI-5 and AFR700B are crosslinked systems, but the geometric location of hydrolytic attack also plays a major role in the hydrolytic stability of these polyimides. From the data generated above, it is clear that there is a significant hydrolytic weak link in the AFR700B structure, which is most likely associated with the norbornene crosslinks in this system. The hydrolytic satiability of PETI-5 is far superior to either of the other two polyimides, suggesting that the phenylethynyl terminal groups and their corresponding crosslinks are more hydrolytically stable.

9.3.4 Degradation Kinetics Calculations

Equations 9.5 through 9.10 were applied in order to obtain kinetic parameters. The results listed in Table 9.5 are consistent with the degradation characterization completed above. In terms of degradation kinetics, the rate of *hydrolytic* degradation was found to be AFR700B > K3B >> PETI-5. The activation energy for AFR700B is slightly lower than the value reported in the literature (67 kJ/mol from [223]), but the exposure conditions used here were more severe. Also, the initial dry T_g of the resin used in this study was ~40°C lower than the AFR700B system used in the literature reference (due to different cure time-temperature conditions). Both of these variables have been shown to influence the degradation kinetics [223].

Table 9.5: Degradation kinetics constants of hygrothermally aged polyimides.

Polyimide	E (kJ/mol)	A (1/min)	Regression Coefficient
AFR700B	47.0	2.24	0.58
K3B	93.9	12.5	0.99
PETI-5	212	41.2	0.87

For the sake of comparison, the temperature dependence of the rate constant, k' is plotted for the three polyimides in Figure 9.13. Although there was significant scatter in the data, these results reinforce those obtained previously using DSC and FTIR studies. For example, the rate constant of PETI-5 under 177°C hygrothermal exposure conditions was found to be on the order of 10^{13} times smaller than AFR700B. Certainly the structure of PETI-5 offers a dramatic improvement over the other polyimides, most likely as a result of the phenylethynyl crosslink stability.

As mentioned above, K3B has a similar structure as POPPI, indicating that the degradation mechanisms and kinetics should be similar to those of POPPI. In the literature, an activation of ~70 kJ/mol has been reported for Kapton® film [174], indicating that the mechanisms of degradation are similar (under low temperature exposure conditions) to those of K3B, although these parameters are a function of molecular weight and end group chemistry. This is also consistent with decreases in mechanical properties of K3B after hygrothermal exposure reported by Shin *et al.* [133].

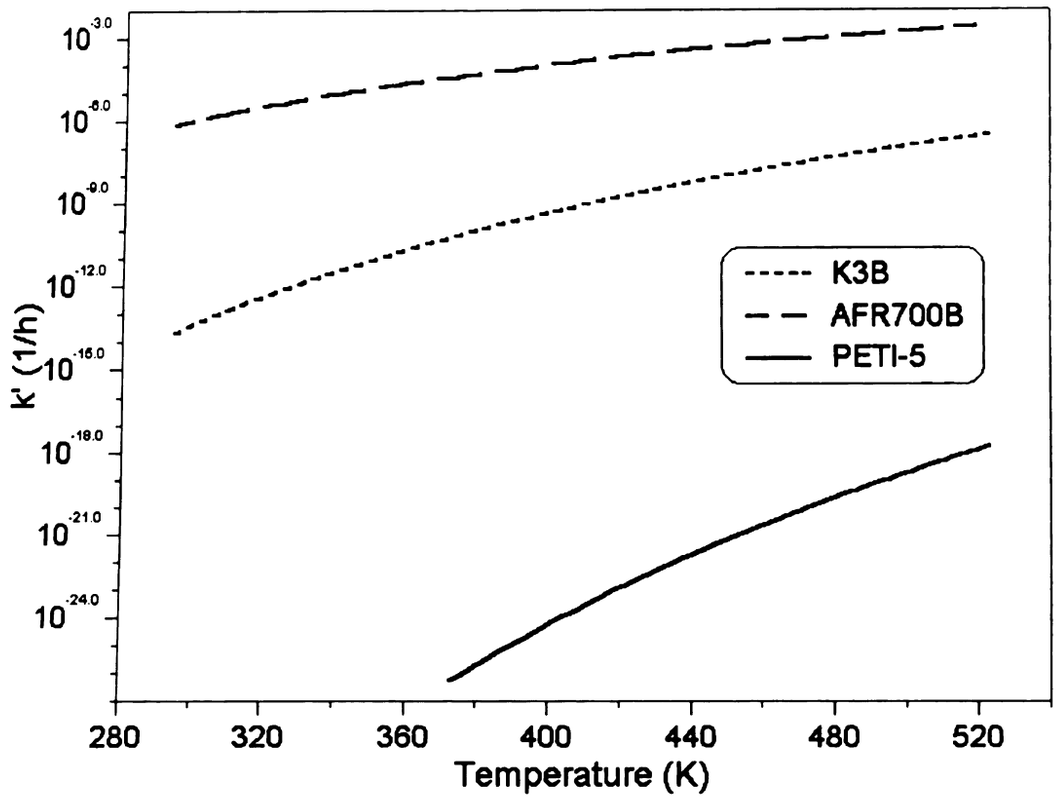

Figure 9.13: Temperature dependence of the hydrolytic degradation rate constant for AFR700B, K3B, and PETI-5 polyimides.

9.3.5 Characterization of the Weak Link in AFR700B

As a result of the findings generated above and research conducted at Air Force Research Laboratory, model compound studies of AFR700B polyimides were performed by Thorp *et al.* [223] to verify that the weak link in AFR700B was associated with the nadic end caps, as postulated, and not with the fluorinated backbone. Specifically, Thorp *et al.* examined the hydrolytic degradation of a variety of model compounds and found that the Michael

addition model compound, shown in Figure 9.14, was hydrolytically unstable. Hygrothermally aged model compounds containing (i) nadimide crosslinks, (ii) maleimide homocrosslinks, and (iii) fluorinated backbone model compounds, were found to be hydrolytically stable.

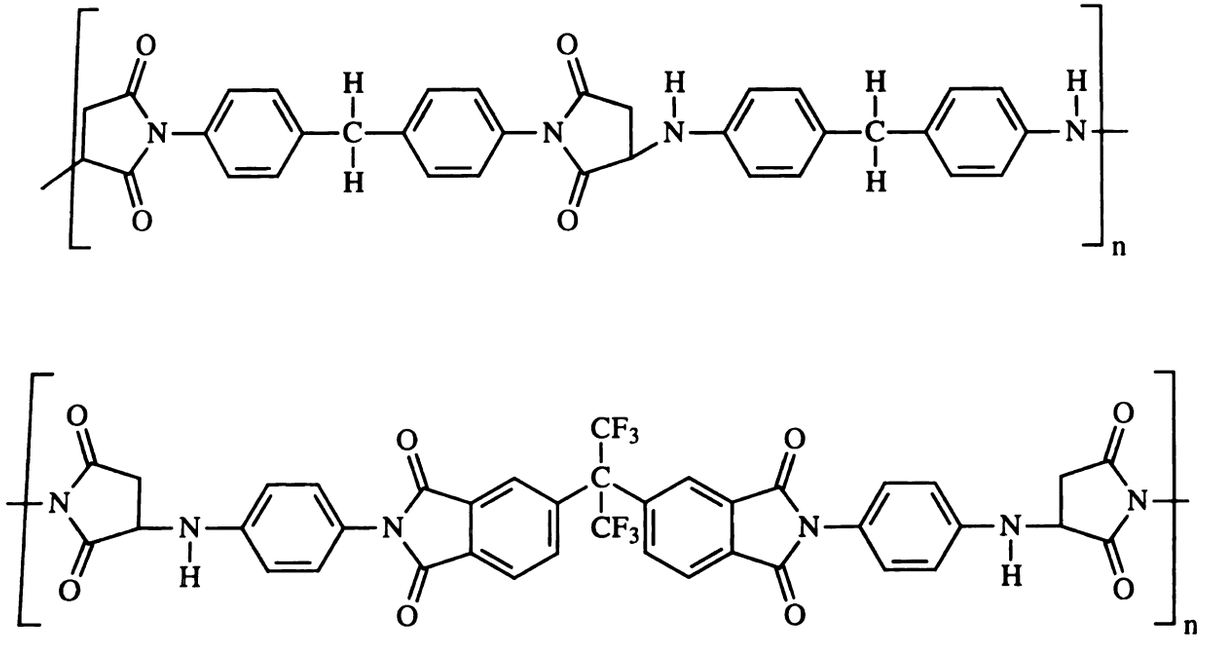

Figure 9.14: Michael addition model compounds used by Thorp *et al.* [223] which was found to be hydrolytically unstable; the weak link in AFR700B.

Therefore, after compilation of the results obtained from this dissertation and model compound studies from Thorp *et al.*, it is clear that the weaknesses of the AFR700B polyimide are the norbornene crosslinks associated with the Michael addition reaction. As a result, nadic end caps should not be used to achieve a hydrolytically stable polyimide.

In addition, based on the hydrolytic degradation studies conducted here, a solution to the durability problem would be to end cap the AFR700B backbone with phenylethynyl functional groups. This is suggested based on the enormous hygrothermal durability of PETI-5 relative to AFR700B and K3B. Also, as discussed in Chapter 5, phenylethynyl terminal groups have other desired properties, including enhancement of polyimide toughness and processability. These structural modifications to the AFR700B oligomer will be investigated in Chapter 10.

9.4 Conclusions

A comparative hygrothermal durability study for AFR700B, PETI-5, and K3B polyimides was presented. Based on the developed EOD and structural state phase diagrams and upon calculation of the degradation kinetics parameters, the hydrolytic stability follows the inequality PETI-5 > K3B > AFR700B. The rates of degradation for AFR700B were found to be on the order of 10^{13} higher than for PETI-5, although there was significant scatter in the data. Regardless, the hygrothermal durability of PETI-5 was found to be far superior to K3B or AFR700B.

The poor hydrolytic stability of AFR700B is a result of the crosslinks associated with the Michael addition reaction. Hydrolytic induced chain scission at crosslink junctions is the most severe form of hydrolytic attack,

leading to rapid decreases in T_g and mechanical integrity. As a result, norbornene terminated polyimides do not provide hydrolytically stable polymers relative to other end groups, such as phenylethynyl.

In the case of K3B, degradation occurs via depolymerization and eventual demonomerization after extreme exposure conditions. The mechanisms associated with this degradation were postulated to be similar to those for POPPI, based on literature results. Also, Morgan *et al.* [20] proposed that degradation is accelerated by initial attack at the ends of the polyimide chains which leads an acidic chemical hydrolysis product that can further autocatalyze the degradation.

Finally, with respect to PETI-5, the superior hydrolytic stability can be attributed to the phenylethynyl end caps that lead to hydrolytically stable crosslinks for completely cured PETI-5. Based on the studies presented here and in the literature, it is proposed that the norbornene end group and the free amine in AFR700B be replaced with phenylethynyl groups in order to obtain the best combination of thermal and hydrolytic stability.

Chapter 10

Synthesis and Characterization of Phenylethynyl Terminated 6FDA Imide Oligomers – Initial Studies in the Development of AFR700C Thermoset Polyimide

10.1 Introduction

As discussed in the previous chapter, although AFR700B demonstrates a combination of superior high temperature stability and toughness relative to other thermoset polyimides, this material is susceptible to hydrolytic attack at the crosslinks associated with the Michael addition reaction. End capping polyimides with phenylethynyl groups, however, has proven to provide improvements in hydrolytic stability compared to norbornene/amine terminated systems. As a result, it was postulated that end capping the fluorinated backbone in AFR700B would provide hydrolytic stability comparable to PETI-5.

In fact, research conducted at AFRL and the University of Dayton Research Institute has shown this postulation to indeed be true [164]. Rice [164, 218, 219] reported a 3-5% decrease in the dry T_g for phenylethynyl terminated AFR700B (AFR-PEPE, various molecular weights) after hygrothermal exposure compared to a 20% decrease for AFR700B. In addition, the phenylethynyl terminated systems were found to have the

following qualities: (i) extremely high T_gs (435-455°C), (ii) significantly improved mechanical properties at 300°C compared to AFR700B, (iii) could possibly be processed by resin transfer molding (RTM), and (iv) high ductility for a high temperature polyimide (elongation to break of 5%). Rice reported slightly lower values of thermooxidative stability compared to AFR700B, but no large-scale systematic characterization was completed.

The earliest synthesis of these polyimides reported in the literature was by Johnston *et al.* [220], in 1994. In their paper, the authors' primary goal was synthesis of the polyimides and possible use as an adhesive. No data with respect to hydrolytic stability or processability was presented. Researchers at NASA Glenn (Lewis) Research Center reported mechanical property data of composites with the same structures but higher molecular weights [214].

Presently, the Air Force has interest in the possible development of these polyimides, with the ultimate goal of obtaining a polyimide with the following properties: (i) RTM processable, (ii) thermooxidative stability equivalent to AFR700B, (iii) high temperature (300°C) mechanical properties equivalent to AFR700B, and (iv) hydrolytic stability comparable to PETI-5.

In this chapter, the initial systematic characterization of these materials, appellated AFR-PEPA-N, will be presented with respect to structure-property-processing relationships. Future work will be conducted at Air Force Research Laboratory if the initial findings indicate that the above requirements are

achievable. From work reported by Rice [164], these materials appear to meet criteria (iii) and (iv) above.

Here, the following will be characterized as a function of initial imide oligomer molecular weight for AFR-PEPA-N polyimides in an effort to eventually develop the next class of polyimide that meets the requirements discussed above ('AFR700C'): (i) rheological properties, (ii) mechanical properties, (iii) glass transition temperature, (iv) cure kinetics, (v) thermal stability, and (vi) possible crystallization (as observed in PETI-5).

10.2 Experimental Techniques

10.2.1 AFR-PEPA-N Monomers

4–(phenylethynyl) phthalic anhydride (PEPA, Figure 10.1) end cap was obtained from Daychem®, Dayton, OH, and the purity verified by DSC, solution NMR, GPC, and mass spectrometry at Air Force Research Laboratory. A sharp melting peak centered at 157°C was observed in the DSC trace, with the material becoming volatile around 350°C. This monomer was dried for 24 h at 60°C under vacuum prior to use.

The backbone monomer 2,2'–bis(3,4-dicarboxyphenyl) hexafluoro-propane dianhydride (6FDA, Figure 10.1) was also obtained from Daychem and found to have a sharp melting peak centered at 249°C with volatility

occurring above 320°C. 6FDA was dried at 160°C under vacuum for 24 h prior to use. Para-phenylenediamine (*p*-PDA, Figure 10.1) and the solvent NMP were obtained from Aldrich® chemical company and used as received.

10.2.2 AFR-PEPA-N Synthesis Procedures

Four imide oligomers were synthesized according to Figure 10.1 in NMP using only 10% solids by weight, where n was either 1, 2, 4, or 8. Monomer and oligomer theoretical data is listed in Table 10.1.

In a glass beaker, a solution of the desired amount of *p*-PDA was combined with NMP under a nitrogen atmosphere, then stirred until completely dissolved. This solution was then added to a 250 mL round bottom flask equipped with a Teflon® coated stirring bar and a gas adapter under a nitrogen atmosphere at room temperature.

Simultaneously, a solution of 6FDA and NMP was prepared under a nitrogen atmosphere. After complete mixing, the solution was added slowly (three portions over 3 h) to the *p*-PDA solution. The diamine-anhydride reaction is exothermic, which raised the temperature of the solution to ~60°C. Once all of the 6FDA solution was added, mixing continued for 20 h at room temperature under nitrogen to assure complete reaction of the monomers.

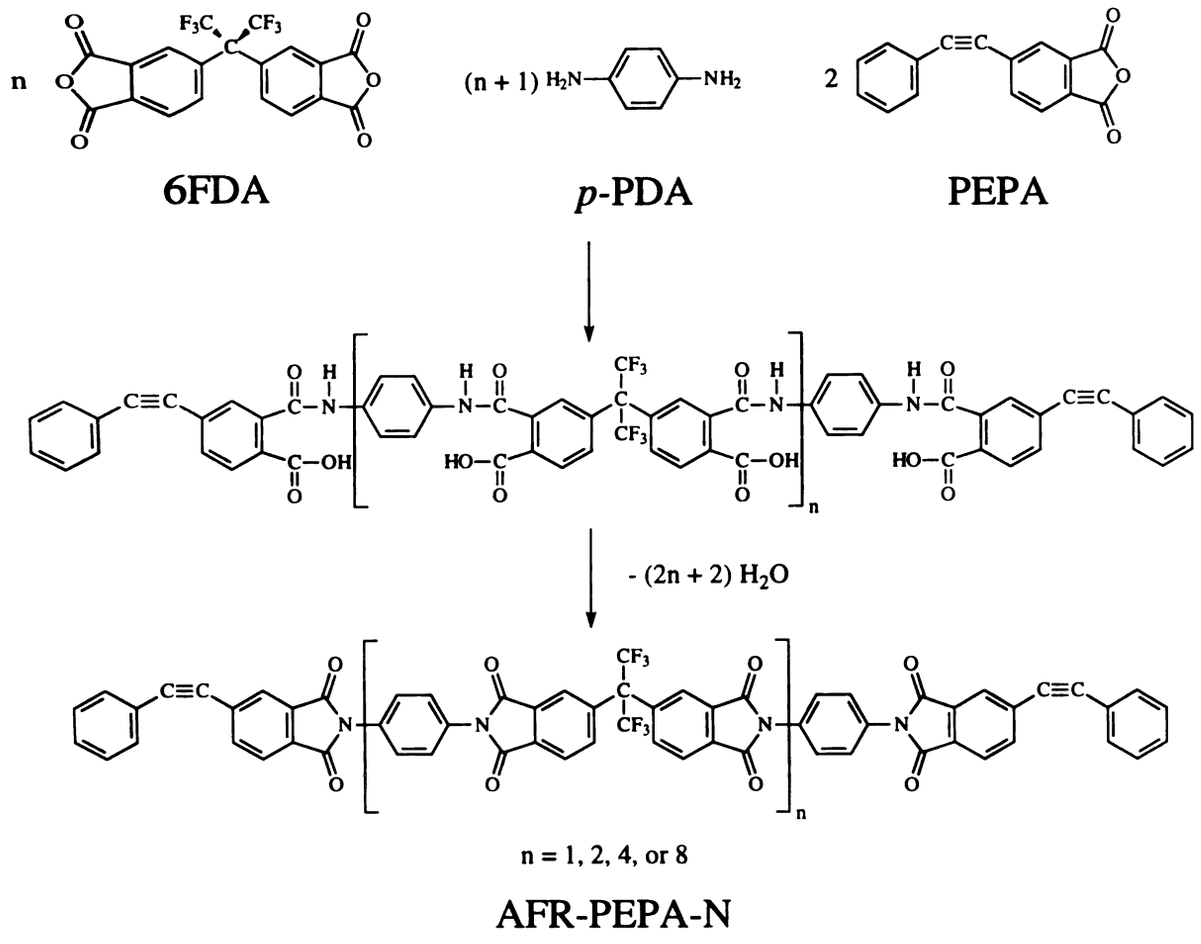

Figure 10.1: Synthesis of AFR-PEPA-N imide oligomers.

PEPA was added as a solid and stirred until completely reacted (~4 hours) under nitrogen. The resulting mixture contained a solution of polyamic acid and NMP, which was then imidized by heating to 185°C under vacuum pressure for 12 h, during which time water from the cyclodehydration reaction was removed. Toluene may also be added prior to imidization to assist in the removal of water via azeotropic distillation.

Finally, the reaction mixtures were added to distilled water, filtered, washed in boiling water and then in warm methanol to remove the NMP. This produced very fine yellow powders of oligomers that were dried under vacuum for 24 h at 200°C. Yields greater than 98% were obtained.

Table 10.1: Molecular mass data for AFR-PEPA-N synthesis.

Monomer or Oligomer	Chemical Formula	Molar Mass (g/mole)	Composition
6FDA	$C_{19}H_6F_6O_6$	444.24	C = 51.37% H = 1.360% F = 25.66% O = 21.61%
p-PDA	$C_6H_8N_2$	108.14	C = 66.64% H = 7.460% N = 25.90%
PEPA	$C_{16}H_8O_3$	248.23	C = 77.42% H = 3.250% O = 19.34%
AFR-PEPA-1	$C_{63}H_{30}F_6N_4O_8$	1084.94	C = 69.74% H = 2.790% F = 10.51% N = 5.160% O = 11.80%
AFR-PEPA-2	$C_{88}H_{40}F_{12}N_6O_{12}$	1601.29	C = 66.01% H = 2.520% F = 14.24% N = 5.250% O = 11.99%
AFR-PEPA-4	$C_{138}H_{60}F_{24}N_{10}O_{20}$	2634.01	C = 62.93% H = 2.300% F = 17.31% N = 5.320% O = 12.15%
AFR-PEPA-8	$C_{238}H_{100}F_{48}N_{18}O_{36}$	4699.43	C = 60.83% H = 2.140% F = 19.40% N = 5.360% O = 12.26%

10.2.3 Oligomer Characterization Methods

The oligomers were chromatographed by a size exclusion method to determine the molecular weight. AFR-PEPA-N powder was dissolved in NMP and filtered prior to being injected into the column. It was eluted from a 50 nm ultrastyragel column with tetrahydrofuran (THF) at a flow rate of 1 mm/min. The column effluent was monitored with a Waters Corporation Model 410 refractive index detector and a Waters Corporation Model 490 multi-wavelength programmable ultraviolet-visible detector set at 254 nm, 280 nm, and 330 nm. These experiments were conducted by scientists at Air Force Research Laboratory.

Differential scanning calorimetry was determined using heating rates of 20°C/min on the same instrument discussed in previous chapters to determine imide oligomer heat of reaction, T_g, and other phenomena (nitrogen atmosphere). Mass spectrometry was conducted by contract sources available from Air Force Research Laboratory.

10.2.4 Rheological Measurements

Imide oligomer powders were compressed into 2 mm thick cylindrical disks, 25 mm in diameter, using a hydraulic press, circular mold, and 45 MPa of pressure for 15 min. Isothermal viscosity profiles were obtained by parallel plate

rheometry on a Rheometrics Scientific ARES® 3A1:RS1 Orchestrator Rheometer, using an angular frequency of 10.0 rad/s, 10% strain, a 50.0 g sensitivity, and a 25.0 g initial static force. Isothermal hold temperatures ranged from 320-430°C, depending on the oligomer system being characterized, for a time of 1 h.

10.2.5 Analysis of the Cure Reactions and Kinetics

Cure reactions were characterized by an attenuated total reflectance-Fourier transform infrared spectroscopy technique (ATR-FTIR, See Appendix). NMP/polyamic acid solutions of AFR-PEPA-2 were cast onto NaCl disks and heated for 100°C/15 h + 170°C/1 h + 210°C/1 h + 230°C/3 h under vacuum to imidize and remove NMP which can mask the infrared peaks, then for various time-temperature conditions from 320-390°C in a nitrogen circulating furnace. All of the NaCl coated disks were surrounded by steel tooling bags to act as oxygen 'getters' during opening and closing of the furnace door. The partially cured resins were then analyzed by ATR-FTIR (Nicolet®) and DSC.

From the above experiments, there was significant scatter in the data, so isothermal DSC kinetics were also used to monitor the cure reactions. This technique was discussed in Chapter 4. Isothermal scans for 8 h at temperatures ranging from 340-410°C were conducted.

10.2.6 Mechanical and Physical Property Measurements

AFR-PEPA-2 and AFR-PEPA-4 imide oligomer powders were compression molded on a Tetrahedron® press using an aluminum mold coated with Kapton® film and Frekote® 44 mold release at temperatures of 360°C, 371°C, and 390°C for 1 h. Only contact pressure (~55 kPa) was needed to mold the AFR-PEPA-2 system, and 1.4 MPa was used for the N = 4 system.

From the ~2 mm thick, 169 cm^2 panels, five dogbone specimens (10 cm long, 2 cm gage length) and five density specimens (6.5 cm^2) were sectioned using a diamond blade saw and running water. All specimens were dried in a dessicator for ~300 h prior to testing.

Mechanical tests were performed on an UTS® mechanical testing instrument, laser extensometer, and 1 mm/min crosshead speeds. Mass density was determined using the hydrostatic weighing procedure described in Chapters 3 and 5, at room temperature. Five specimens per condition were tested.

10.2.7 Thermal Stability

Lifetime model predictions were generated using the technique developed by Toop [147], which is discussed further in the Appendix. Cured samples (390°C/1h) of AFR-PEPA oligomers of molecular weights N = 2, 4, and 8

were heated at rates of 1, 2, 5, 10, and 20°C/min under a nitrogen atmosphere from 150-800°C. From the data generated, the following equation was applied (Appendix):

$$\ln t_f = \frac{Q}{RT_f} + \ln\left[\frac{Q}{\beta R} \times p\left(\frac{Q}{RT_c}\right)\right] \tag{10.1}$$

Above, t_f is the estimated time to failure (min), T_f is the failure temperature (K), $p(Q/RT_c)$ is a value from an integral table, β is the heating rate (°C/min), T_c represents the critical temperature of interest at a specific weight loss, R is the gas constant (8.314 J/mol-K), and Q is the activation energy, which fits the Arrhenius relationship with respect to the heating rate shown in Equation 10.2, where C is a constant (0.457).

$$Q = -\frac{R}{C}\left[\frac{d\log_{10}\beta}{d(1/T)}\right] \tag{10.2}$$

In addition to lifetime model predictions, the decomposition temperature was determined from the step transition in the weight loss versus temperature curve as a function of heating rate, since there is disagreement with the variable heating rate method, as discussed in Chapter 2. However, the primary interest in this initial study was for comparative purposes and semi-quantitative predictions of mass loss as a function of service time-temperature conditions.

10.3 Results and Discussion

10.3.1 Oligomer Characterization

Chromatography and mass spectrometry experiments conducted by Air Force Research Laboratory on the imidized oligomers indicate that the molecular weights for the N = 1 and 2 systems had a broad distribution ranging from approximately N = 1 to N = 5. In the case of the N = 4 and N = 8 oligomers, the distributions were narrow, with the averages being N = 4 and 6, respectively. Typical chromatographs and mass spectra for AFR-PEPA-N oligomers are shown in Figures 10.2 and 10.3, respectively.

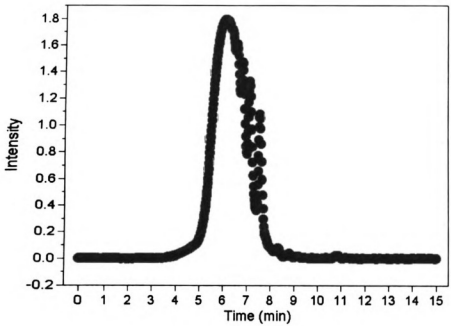

Figure 10.2: Representative time exclusion chromatograph of the imide oligomers (AFR-PEPA-4 at 254 nm wavelength).

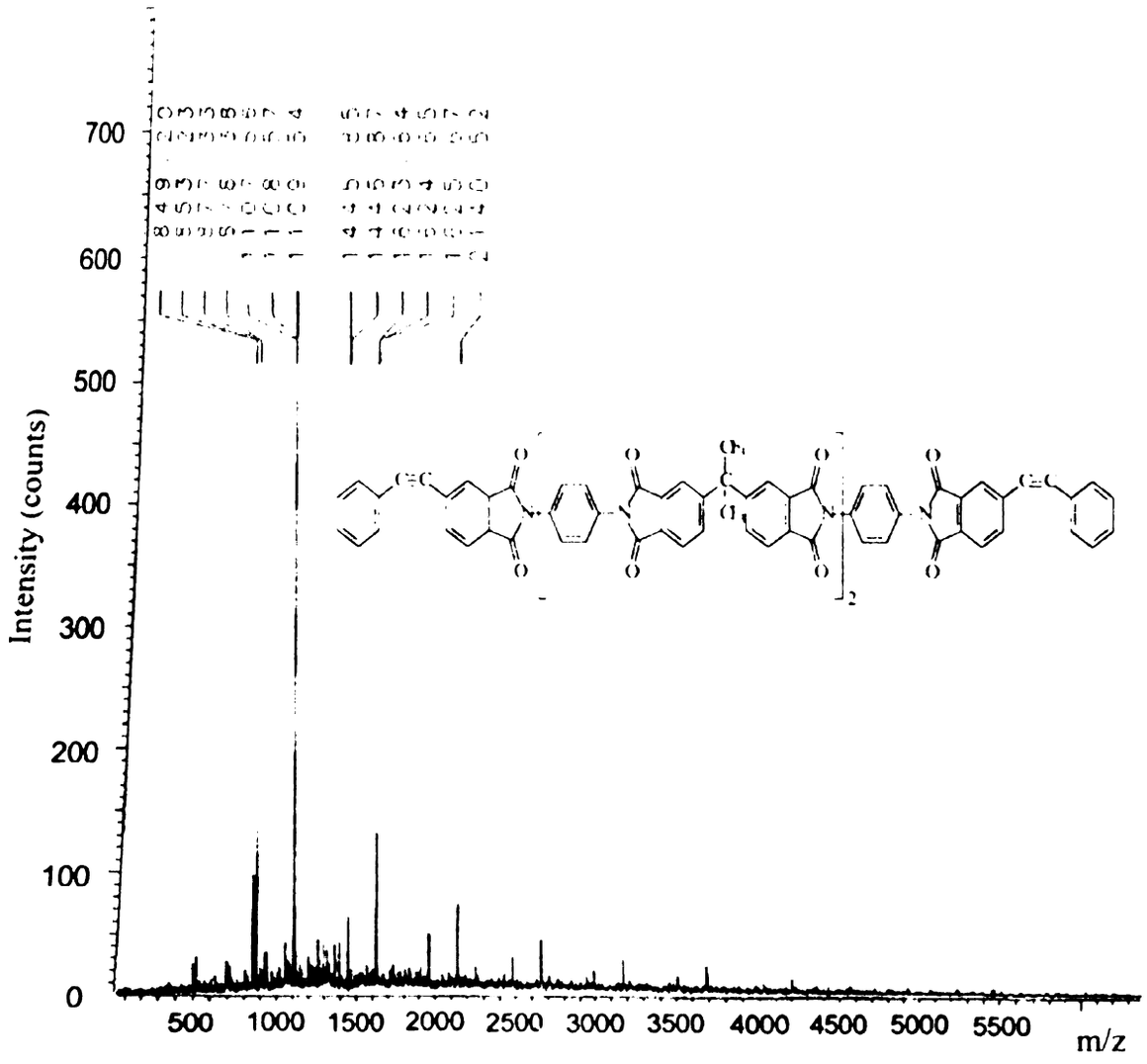

Figure 10.3: Representative mass spectrum of polyimides (AFR-PEPA-2).

Differential scanning calorimetry results on the imidized oligomers yielded the values presented in Table 10.2 and Figure 10.4. The values for the $N = 8$ system are believed to be skewed (lower value of T_g) due to the presence of residual NMP as observed from TGA analysis on the oligomer powder. A typical DSC trace of the oligomer powder is shown in Figure 10.5. In all cases,

the phenylethynyl crosslinking reaction through the C≡C bond begins to occur near ~330-360°C, which is similar to the crosslinking behavior reported for PETI-5 (Chapter 5).

Table 10.2: DSC characterization of AFR-PEPA-N imide oligomers (average of three scans at 20°C/min).

Oligomer	T_g (°C)	ΔH_{rxn} (J/g)	Reaction Peak Temperature (°C)
AFR-PEPA-1	171.35 ± 0.72	245 ± 14	392 ± 0.84
AFR-PEPA-2	193.89 ± 0.14	180 ± 1.4	403 ± 0.47
AFR-PEPA-4	198.85 ± 1.10	108 ± 9.0	406 ± 1.34
AFR-PEPA-8	181.89 ± 2.61	44.8 ± 4.6	416 ± 0.33

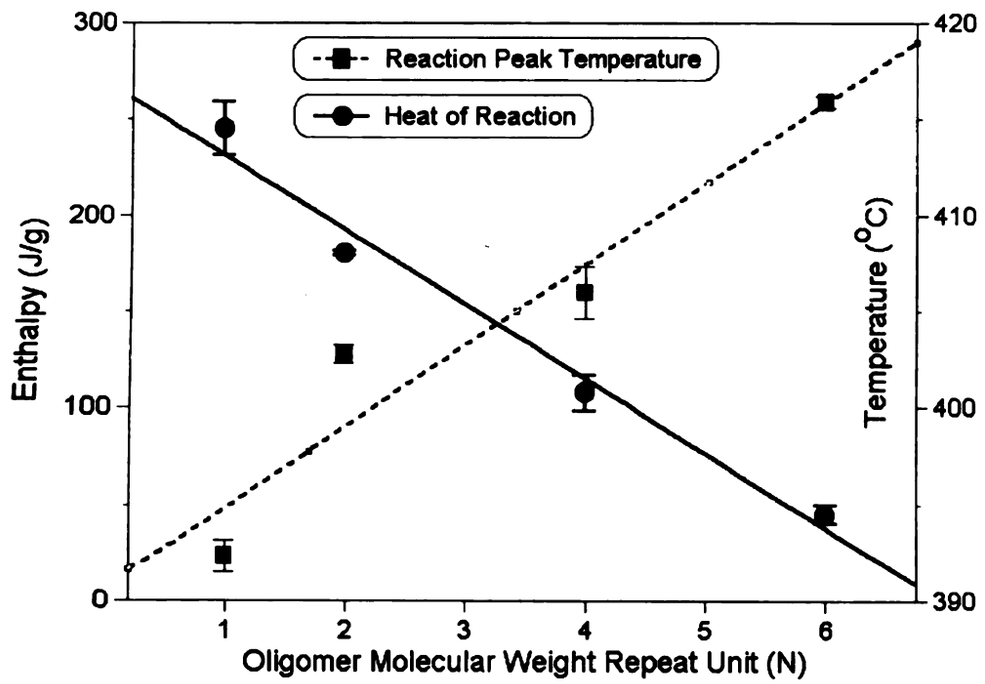

Figure 10.4: Plot of reaction peak temperature and enthalpy as a function of imide oligomer repeat unit (estimated from mass spectrometry and chromatography).

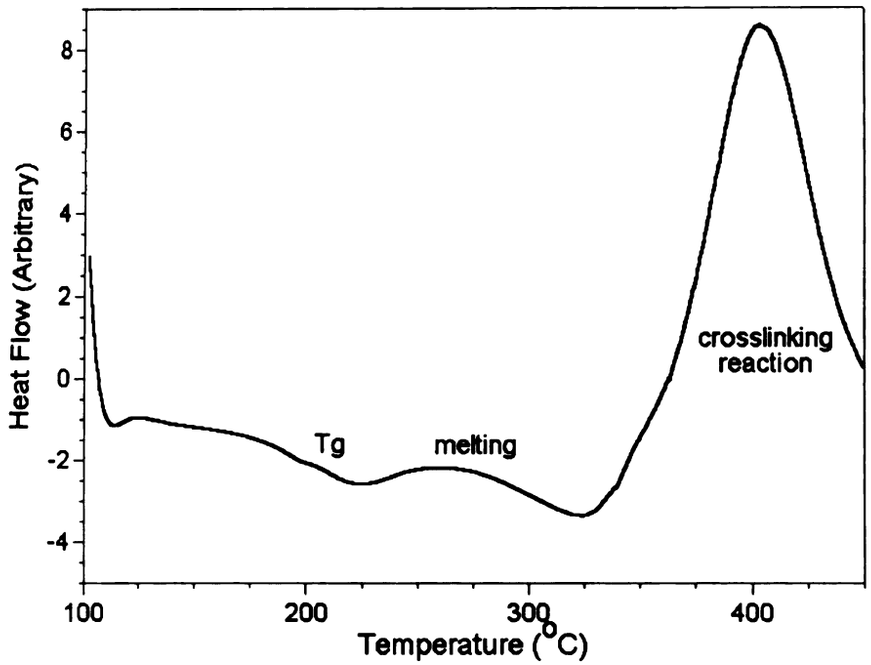

Figure 10.5: Typical DSC trace of imide oligomer at heating rates of 20°C/min (AFR-PEPA-2).

From the above data, the trends shown are as expected. The heat of reaction decreased with the concentration of phenylethynyl end groups and the reaction peak temperature increased proportionally to the concentration of end caps, since the crosslinking reaction occurs through the C≡C bond, reportedly via a free radical mechanism [161, 166, 168, 172].

10.3.2 Rheological Properties

A typical isothermal viscosity profile is shown in Figure 10.6. The time to reach gelation (t_{gel}) was calculated from the onset point where the viscosity increased rapidly. Characterization of the gel point where the tan δ reached unity also gave roughly the same values. These results and corresponding viscosities are displayed in Table 10.3.

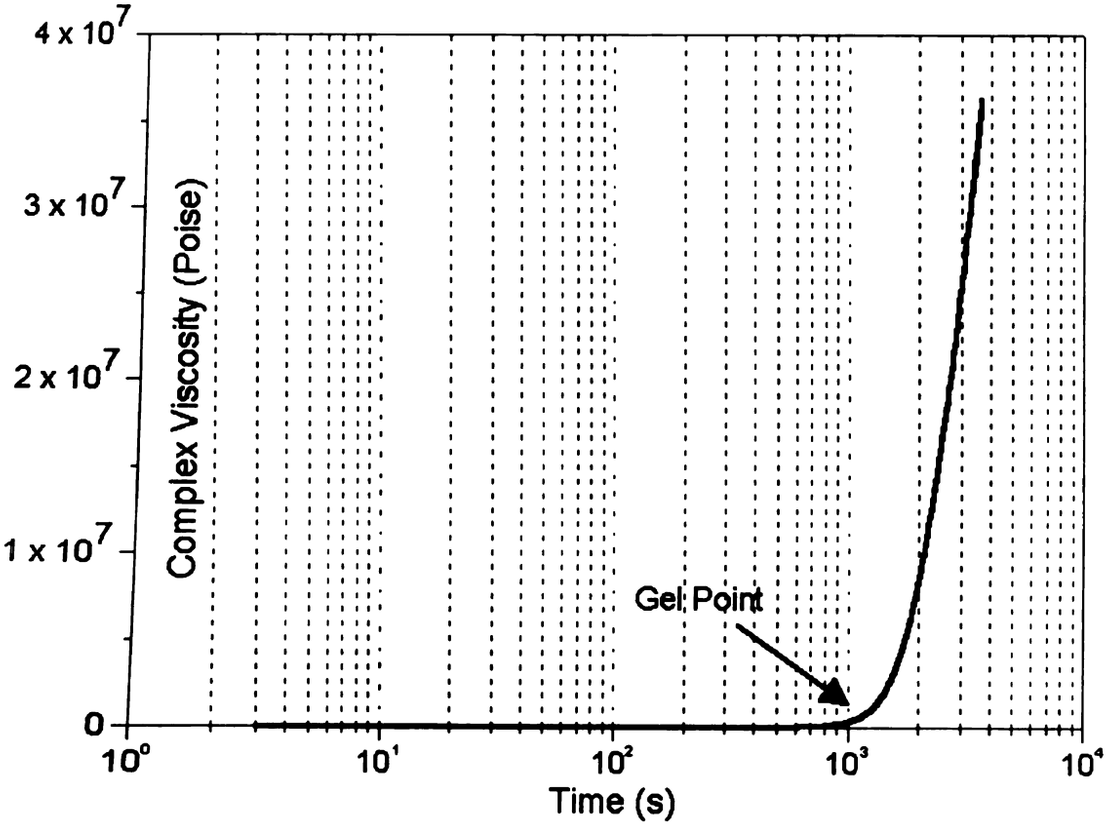

Figure 10.6: Typical isothermal viscosity profile, shown above for AFR-PEPA-*2* at 371°C.

Table 10.3: Rheological properties of AFR-PEPA-N polyimides.

Polyimide	Cure Temperature (°C)	Minimum Complex Viscosity (Poise)	Gel Time (s)
AFR-PEPA-2	320	190	4500
	340	100	3000
	360	50	2100
	371	10	1680
	390	19	1200
AFR-PEPA-8	360	4100	780
	371	2270	900
	390	840	402
	410	540	198
	430	550	102

In order to obtain a resin system that is easily processed by RTM, desired viscosities are on the order of 0.1 - 10 Poise. From the above data, the AFR-PEPA-2 system appears to be relatively borderline processable by this method. The N = 8 system does not appear to be processable by resin transfer molding, due to the high viscosity. Although not measured in this study, the trends suggest that the AFR-PEPA-1 system should have a lower viscosity than the N = 2 system, and the N = 4 system should have viscosity values somewhere in between the N = 2 and N = 8 systems.

For comparison, PETI-5 has a minimum melt viscosity of 10,000 Poise at 371°C. Therefore, the polyimide systems developed here have viscosity values ranging from 0.1–41% of this value; a significant improvement in melt viscosity.

Although the AFR-PEPA-2 system appears to be borderline processable by traditional RTM techniques, Scola *et al.* [217] have shown that (i) the addition of small weight percents (~10%) of low viscosity reactive diluents or (ii) the introduction of meta-substituted diamine linkages in place of the present para-substitution, can significantly reduce the melt viscosities of polyimides. Therefore, it is possible to further reduce the viscosity of these AFR-PEPA-N systems by minor chemical modifications.

10.3.3 Cure Reactions and Kinetics

A typical FTIR spectrum of AFR-PEPA-2 is shown in Figure 10.7. The C≡C triple bond occurs at a wavenumber of 2213 cm^{-1}, and was monitored as a function of cure time-temperature conditions to determine the degree of cure by the equation

$$\alpha = \frac{\left(I_{C\equiv C} / I_n\right)_t}{\left(I_{C\equiv C} / I_n\right)_{t=0}} \qquad (10.3)$$

where I is the peak intensity of the given subscript bond energy, n is the peak used to normalize the results, and t represents the time at a given cure temperature. Depending on which peak was used to normalize the data, slightly different values in the degree of cure were obtained, as shown in Figure 10.8. The peak assignments are tabulated in Table 10.4.

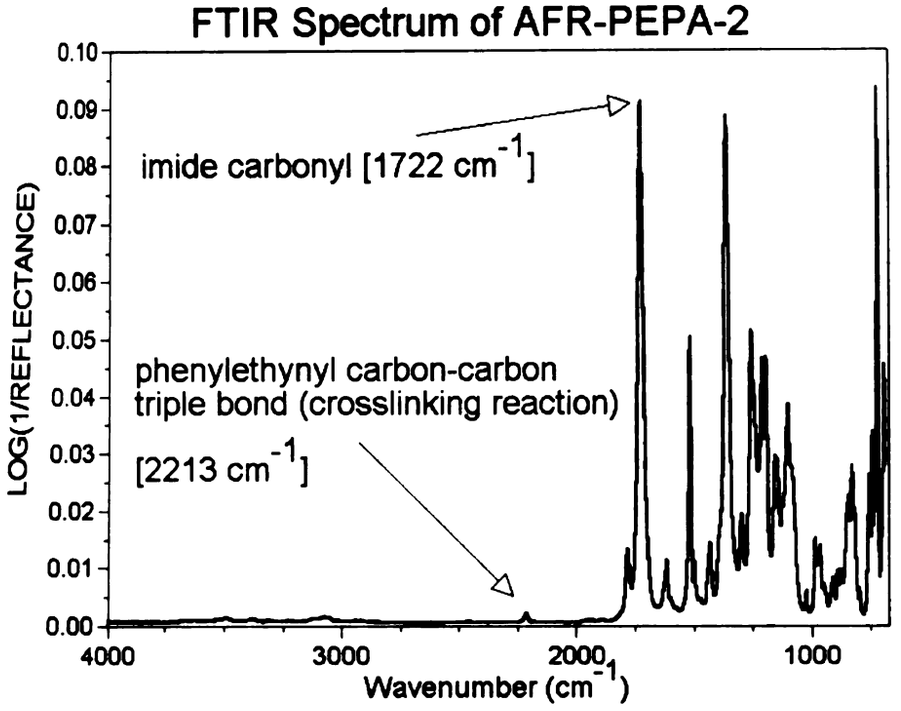

Figure 10.7(a): Typical ATR-FTIR spectrum of AFR-PEPA-2.

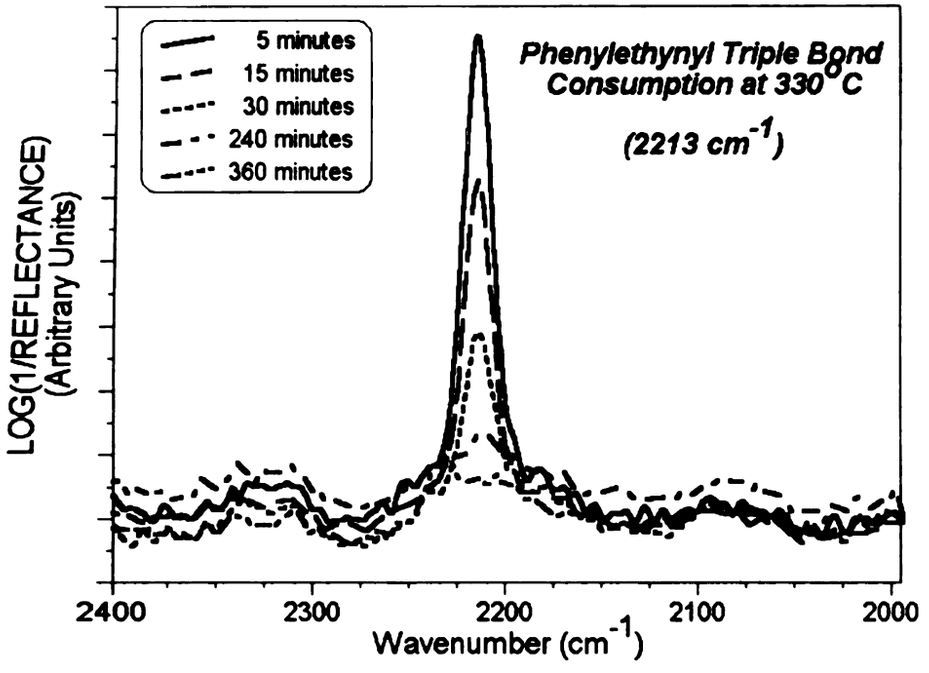

Figure 10.7(b): ATR-FTIR spectrum showing the triple bond consumption.

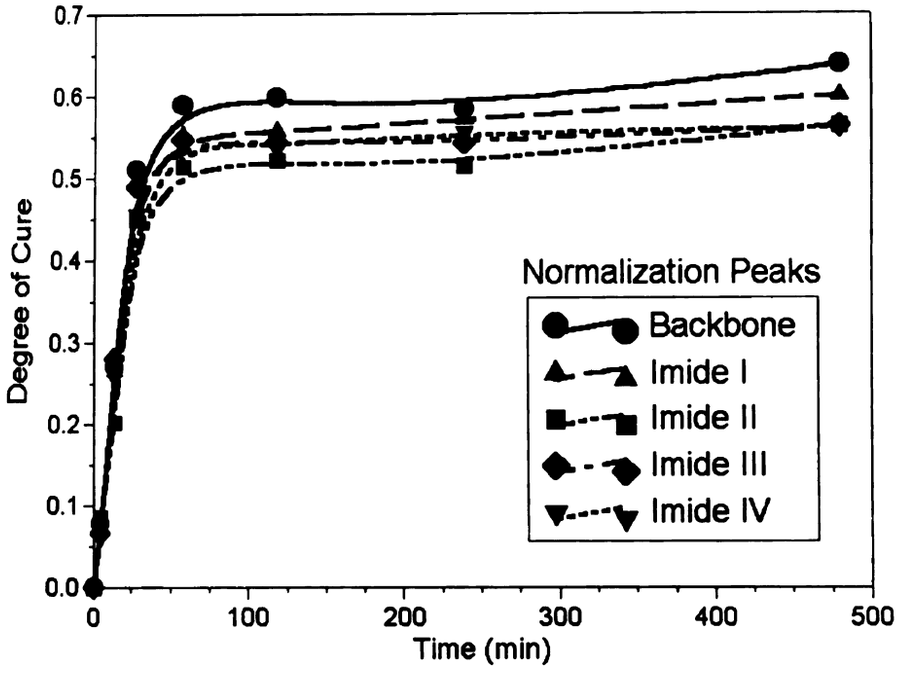

Figure 10.8: Degree of cure as a function of cure time at 330°C for AFR-PEPA-2, determined from FTIR analysis and normalized to various peaks.

Table 10.4: Peak assignments in the AFR-PEPA-N infrared spectra [97, 113].

Peak Assignment	Wavenumber (cm^{-1})	Description
Imide I	1780	Imide C=O asymmetrical stretching
Imide II	1722	Imide C=O symmetric stretching
Imide III	1374	Imide C-N stretching
Imide IV	739	Imide C=O bending
Crosslinking Reaction	2213	C≡C bond absorption

As shown in Figure 10.7(b), the peak resolution at 2213 cm^{-1} becomes weak, which was the reason for employing the DSC isothermal kinetics technique. A plot of T_g as a function of the degree of cure was also obtained

from the FTIR data (Figure 10.9), but significant scatter was observed, resulting from (i) non-uniform equilibration of the furnace during opening and closing the door to remove samples and (ii) scatter in the infrared data. This data is useful in the future development of time-temperature-transformation (TTT) diagrams for processing of these polyimides. The data in Figure 10.9 can be modeled by relationships presented by Venditti and Gillham [145] based on heat capacity measurements, which have proven to be accurate for a variety of polyimides. Future studies at Air Force Research Laboratory will investigate the aforementioned methods to obtain more accurate results.

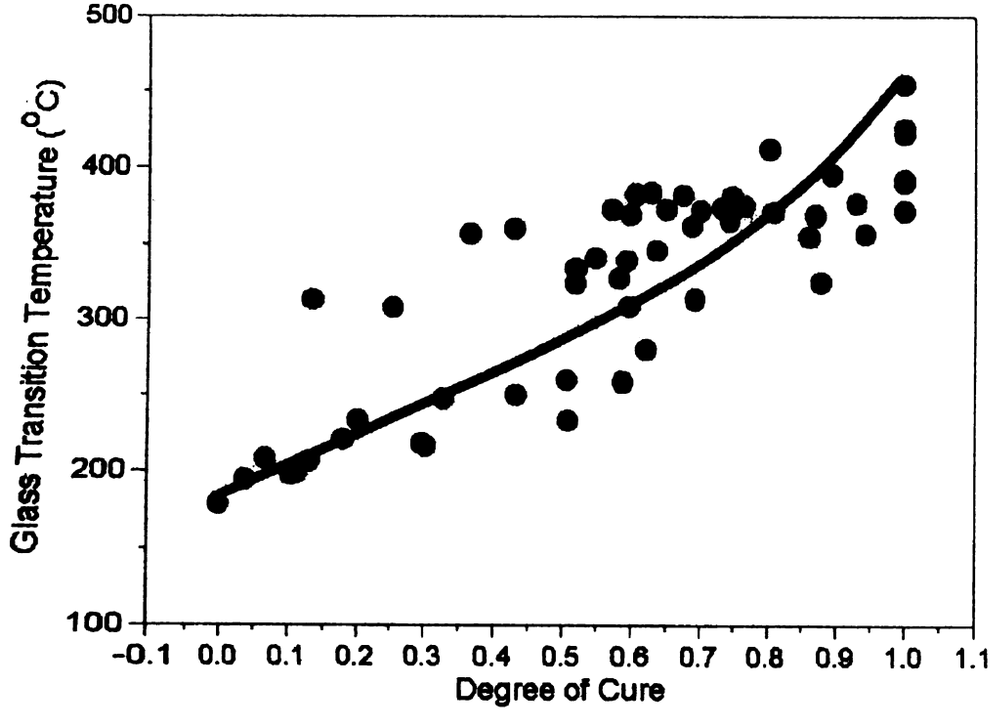

Figure 10.9: T_g as a function of the degree of cure for AFR-PEPA-2.

Degree of cure was also monitored using isothermal DSC kinetics and application of Equation 4.1. A typical degree of cure versus time plot is shown in Figure 10.10. Assuming n^{th} order kinetics, the rate equation can be written

$$\frac{d\alpha}{dt} = k(1-\alpha)^n \tag{10.4}$$

where n is the reaction order, t is time, and k is the rate constant. The rate constant is a function of the cure temperature by the Arrhenius relationship

$$k = k_o \exp\left(-\frac{E}{RT}\right) \tag{10.5}$$

where k_o is a frequency factor and E is the activation energy.

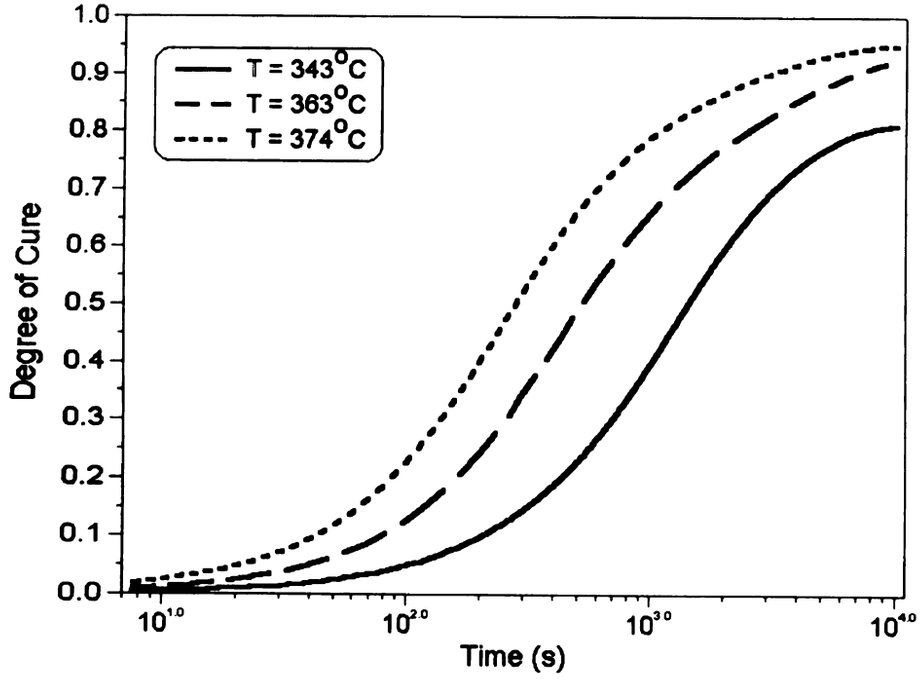

Figure 10.10: Degree of cure as a function of time for AFR-PEPA-2, determined from isothermal DSC experiments.

Table 10.5 displays the kinetic parameters for the polyimides calculated from Equations 10.4 and 10.5. The data suggests that the N = 2 system cures more rapidly than the N = 8 system, most likely due to diffusion control. Also, the N = 8 system displays higher values of reaction order and activation energy due to the lower concentration of phenylethynyl groups for the N = 8 polyimide oligomer.

Table 10.5: Cure kinetic parameters for AFR-PEPA-N polyimides.

Polyimide	**Activation Energy (kJ/mol)**	**ln (k_o) (1/min)**	**Reaction Order**
AFR-PEPA-2	80.3 ± 12	5.66 ± 0.99	1.24 ± 0.090
AFR-PEPA-8	104 ± 5.2	7.41 ± 0.43	1.87 ± 0.061

Lastly, Figure 10.11 displays the glass transition temperature of the polyimides after 8 h cure times at various temperatures. These results are consisted to those reported by Rice [164] of 455°C, 445°C, and 435°C for AFR-PEPA-N polyimides 2, 4, and 8, respectively. Therefore, T_g values equivalent or greater than AFR700B can be achieved. This is coupled with (i) improved hydrolytic stability and high temperature strength reported by Rice [164], and (ii) lower viscosity and possible RTM processability reported in this study.

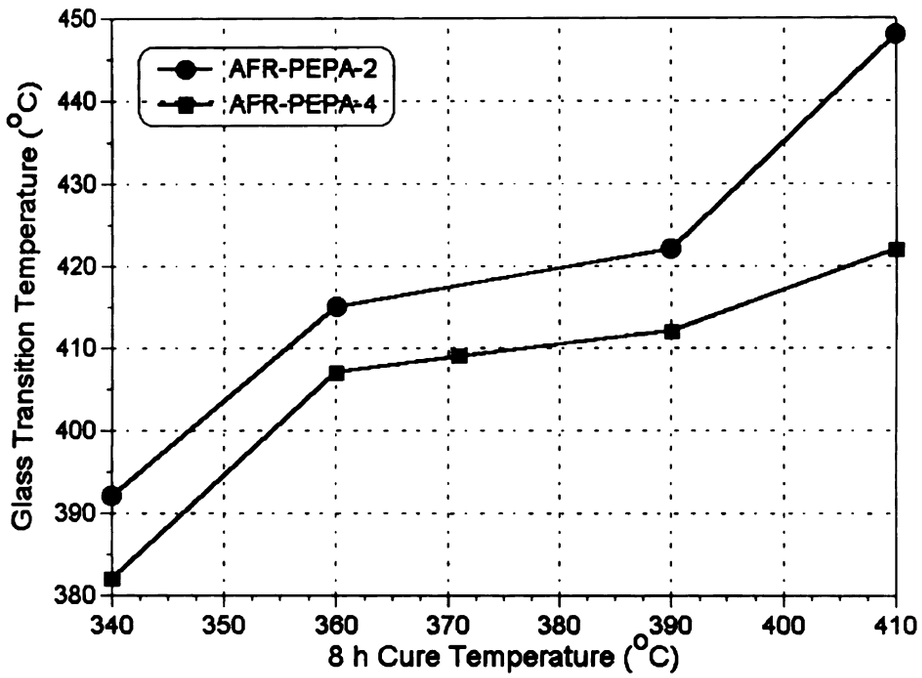

Figure 10.11: Glass transition temperature as a function of 8 h cure time for AFR-PEPA-N polyimides.

10.3.4 Mechanical Properties

Mechanical properties of partially cured polyimides are shown in Table 10.6. Also shown are the measured glass transition temperatures and possible melting temperatures. Indeed these materials also crystallize, which was observed for phenylethynyl terminated PETI-5 in Chapter 5. Also, the influence on mechanical properties appears to be similar. For example, the 360°C cured AFR-PEPA-4 displayed a sharp melting peak in the DSC trace and subsequently had a higher mass density and higher Young's modulus than the

N = 4 polyimides cured at higher temperatures. This suggests that the higher degree of crystallinity resulted in a higher modulus and higher mass density, as reported for PETI-5 in Chapter 5.

Table 10.6: Mechanical properties of AFR-PEPA-N polyimides.

AFR-PEPA-2						
Cure Temperature (°C)	**T_g (°C)**	**T_m (°C)**	**Mass Density (g/cm^3)**	**Young's Modulus (MPa)**	**Tensile Strength (MPa)**	**Failure Strain (%)**
360	370	432	1.354 ± 0.009	3665 ± 174	50.22 ± 6.63	1.54 ± 0.25
371	359	434	1.362 ± 0.008	3509 ± 336	66.27 ± 10.3	2.02 ± 0.35
390	382	438	1.360 ± 0.002	3347 ± 148	63.88 ± 3.93	2.19 ± 0.21
AFR-PEPA-4						
360	326	422*	1.421 ± 0.005	3516 ± 268	--	--
371	347	438	1.392 ± 0.007	3393 ± 259	72.0 ± 11.0	2.41 ± 0.54
390	350	438	1.396 ± 0.004	3249 ± 298	82.8 ± 7.35	3.22 ± 0.62

* Very sharp melting peak

Additional trends in the data show that the N = 8 system has a slightly higher toughness than the N = 2 system, which was expected since the N = 2 system is of higher crosslink density. Also, the toughness improved with the degree of cure because network defects in the form of unreacted groups are removed. The mechanical properties are satisfactory, even though the systems are not completely cured. Fully cured systems should provide better mechanical toughness, based on the study presented in Chapter 5 and data reported by Rice [164] on completely cured systems.

10.3.5 Thermal Stability

A representative TGA scan is shown in Figure 10.12. The onset of thermal decomposition (thermal decomposition temperature) as a function of the heating rate is tabulated in Table 10.7. All of the three imide oligomers have similar thermal decomposition temperatures as a function of the different heating rates, indicating the thermal stability for the three polyimides are similar.

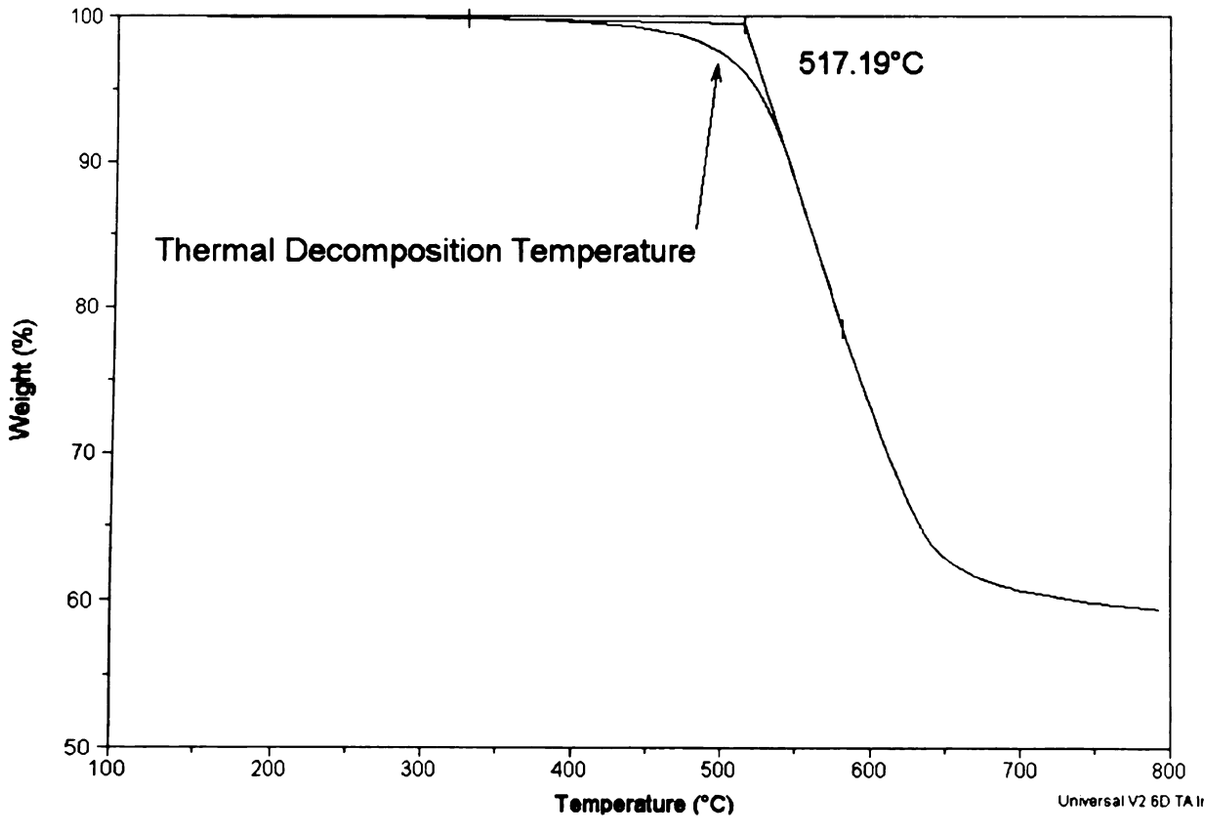

Figure 10.12: Representative TGA scan of AFR-PEPA-N polyimides showing determination of the thermal decomposition temperature.

Table 10.7: Thermal decomposition temperatures for polyimides at various heating rates.

Heating Rate (°C/min)	**Thermal Decomposition Temperature (°C)**		
	AFR-PEPA-2	AFR-PEPA-4	AFR-PEPA-8
1	499	489	493
2	504	500	505
5	527	515	524
10	546	529	539
20	568	548	557

Activation energies for degradation are shown in Table 10.8 (determined from plots similar to Figure 10.13), and lifetime model predictions generated using Equations 10.1 and 10.2 are shown for the three polyimides in Figure 10.14. Specific service temperature and the associated lifetime model prediction time based on weight loss are depicted in Table 10.9. It should be reiterated (based on the results obtained in Chapter 6) that lifetime models based on weight loss are only accurate for screening purposes and to meet specifications. These numbers do not necessarily correlate directly with mechanical properties, and the actual weight loss associated with mechanical property deterioration is material dependent. Still, the information provides useful initial screening information for the thermal stability of polyimides.

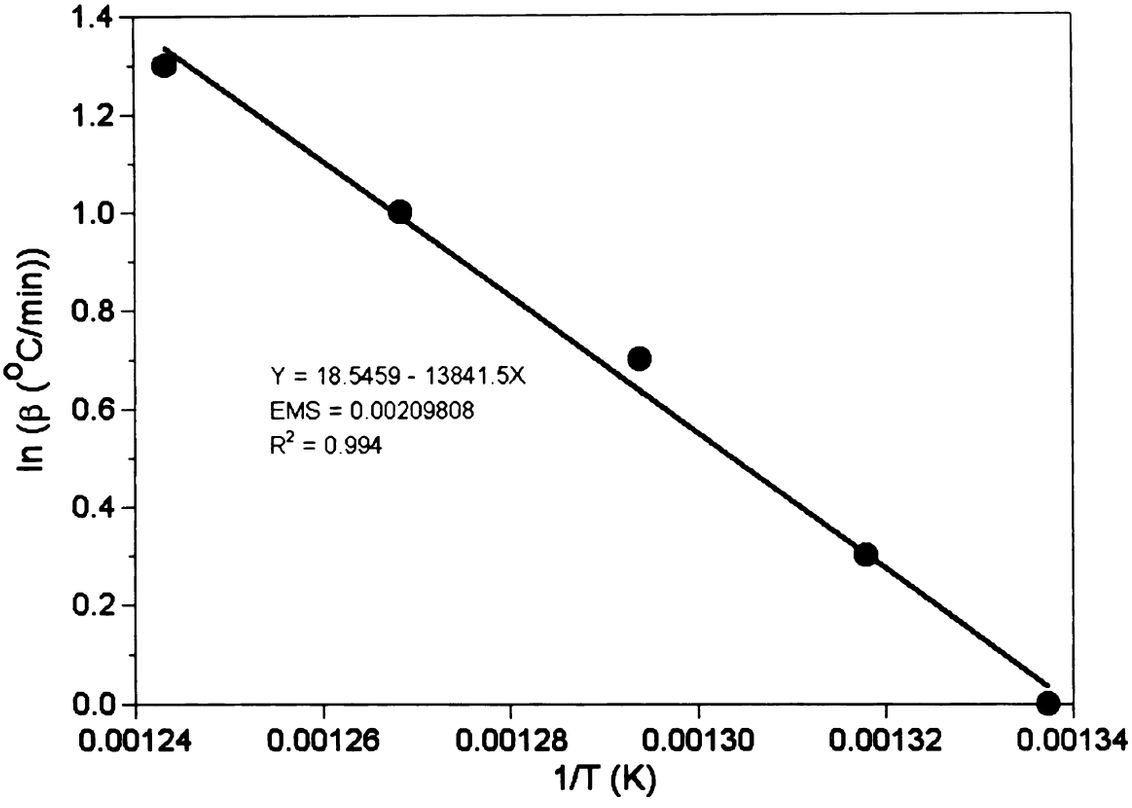

Figure 10.13: Determination of the activation energy for thermal degradation by plotting Equation 10.2.

Table 10.8: Activation energies of thermal degradation for AFR-PEPA-N polyimides at various weight loss values.

Weight Loss (%)	**Activation Energy (kJ/mole)**		
	AFR-PEPA-2	AFR-PEPA-4	AFR-PEPA-8
1	227	258	252
2	238	279	255
5	227	281	247
10	229	293	240
20	261	337	253
Average	236 ± 14	290 ± 29	249 ± 6

From Table 10.8, the activation energies for these polyimides are generally higher than reported for other phenylethynyl terminated systems

[212], indicating that the thermal stability is satisfactory. Lifetime model predictions at various service temperatures also indicate excellent thermal stability. For example, infinite lifetimes (greater than 1 million years) are predicted for 177°C use temperatures, and nearly infinite lifetimes (based on 2% weight loss) are predicted for 250°C service temperatures. All of the polyimides displayed similar thermal stability based on these studies.

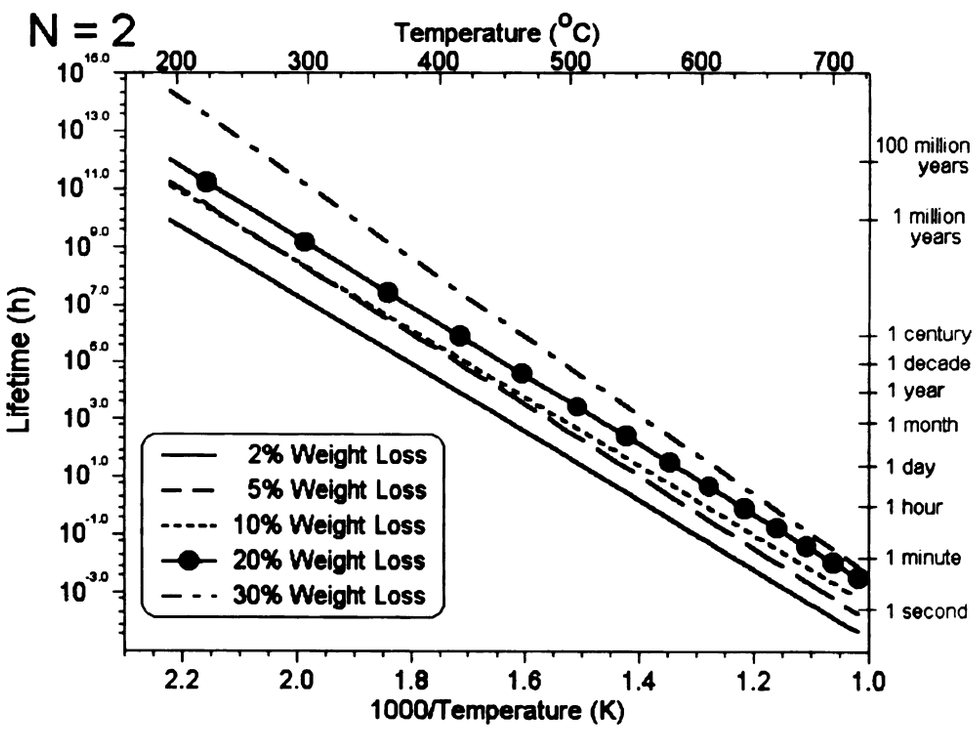

Figure 10.14(a): Lifetime thermal stability model prediction based on weight loss for AFR-PEPA-2.

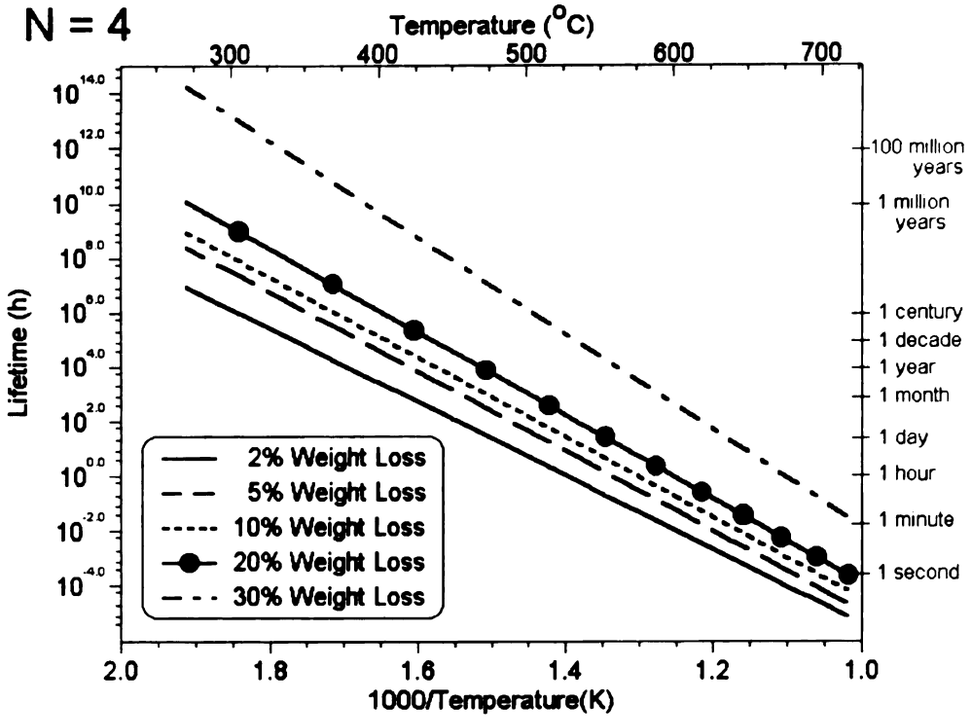

Figure 10.14(b): Lifetime thermal stability model prediction based on weight loss for AFR-PEPA-4.

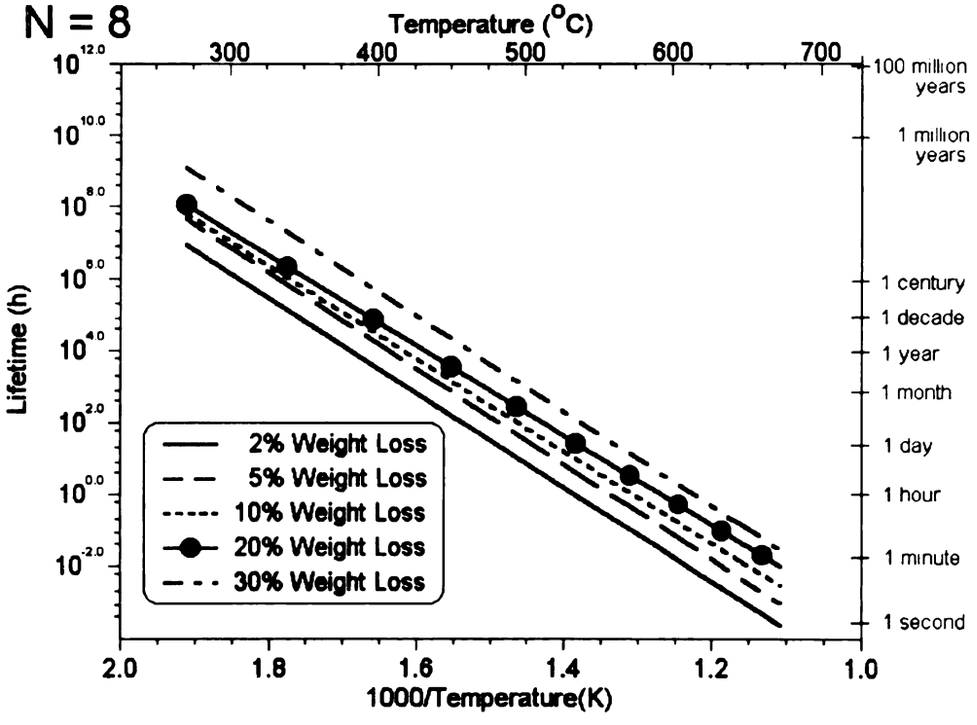

Figure 10.14(c): Lifetime thermal stability model prediction based on weight loss for AFR-PEPA-8.

Table 10.9: TGA lifetime model predictions at various service temperatures.

Service Temperature (°C)	Weight Loss (%)	TGA Lifetime Model Prediction		
		AFR-PEPA-2	AFR-PEPA-4	AFR-PEPA-8
177	ALL	∞	∞	∞
250	2	1.8×10^6 h	8.7×10^6 h	8.4×10^6 h
	5	2.4×10^7 h	2.5×10^8 h	4.4×10^7 h
	10	2.8×10^7 h	8.7×10^8 h	6.1×10^7 h
	20	1.8×10^8 h	∞	1.1×10^8 h
	30	∞	∞	∞
310	2	8.8×10^3 h	1.9×10^4 h	2.2×10^4 h
	5	8.7×10^4 h	3.3×10^5 h	1.1×10^5 h
	10	1.3×10^5 h	1.1×10^6 h	1.8×10^5 h
	20	8.0×10^5 h	1.1×10^7 h	3.8×10^5 h
	30	2.8×10^7 h	∞	3.0×10^6 h
371	2	9.6×10^1 h	1.3×10^2 h	1.7×10^2 h
	5	8.4×10^2 h	1.4×10^3 h	7.2×10^2 h
	10	1.6×10^3 h	4.7×10^3 h	1.4×10^3 h
	20	8.8×10^3 h	3.7×10^4 h	3.5×10^3 h
	30	1.7×10^5 h	8.1×10^7 h	2.1×10^4 h

"∞" indicates service life is predicted greater than 1 million years

10.4 Conclusions

Initial characterization of the structure-property-processing relationships for AFR-PEPA-N imide oligomers and their crosslinked polyimides was presented. These results represent portion of the initial development of a new polyimide, AFR700C, which provides RTM processability and improved hydrolytic stability relative to AFR700B.

Data presented in this Chapter demonstrated that (i) viscosity near the values desirable for RTM processing can be achieved, even without the

addition of reactive diluents or other chemical modification, (ii) mechanical properties on partially cured AFR-PEPA-N polyimides were satisfactory, and (iii) the thermal stability based on weight loss appears promising. From this research, significant knowledge was gained on which direction to proceed for the development of a new AFR700C polyimide.

Future research at Air Force Research Laboratory will attempt to optimize the structure-property-processing conditions of the AFR-PEPA-N systems, possibly by the addition of reactive diluents, which can decrease the viscosity and increase the mechanical toughness. Ultimately, from the data presented here and reported by Rice [164] and Scola *et al.* [217], it appears certain that an AFR700C material that meets the requirements discussed in this chapter can be achieved.

Chapter 11

Conclusions and Recommendations

11.1 Primary Findings

- For BMPM/DABPA BMI resins, the critical structure-property-processing relationships are associated with the formation of ether crosslinks by hydroxyl dehydration, which are unstable and rearrange to form less flexible segments. For example, after all of the C=C bonds of the 'ene' molecule have been consumed, the following property modifications were observed: (i) ~0.2% density decrease, (ii) a ~100°C increase in T_g, (iii) a ~20% increase in equilibrium moisture content, (iv) a ~36% increase in the diffusion coefficient, (v) a 25-40% ductility loss as a function of temperature and monomer composition, and (vi) an increased tendency towards microcracking in IM7/BMI laminates.
- Cure induced microcracking can be prevented in IM7/BMI cross-ply composite laminates by an extended initial cure time (8 h) at 177°C prior to higher temperature postcure due to a reduction in composite residual stress and an associated improved interphase.
- Studies on the deformation behavior of BMI, POPPI, PEI, and PETI-5 polyimides demonstrated that for highly crosslinked polyimides the

deformation and failure behavior is controlled by network defects in the form of unreacted groups, crosslink heterogeneities, etc., and network packing efficiency. For PETI-5, which is highly chain extended, deformation is controlled by network defects, free volume, and crystallinity that likely results from liquid crystal ordering of the phenylethynyl terminated oligomers in the melt. Thermoplastic deformation and toughness is controlled primarily by free volume.

- Hydrolytic degradation of polyimides generally occurs via attack of the imide ring, reducing the polyimide to a polyamic acid. The polyamic acid species is then 550 times more susceptible to hydrolysis than the imide. Residual amide groups present in the absence of complete imidization reduce the hydrolytic stability of polyimides. Also, acidic environments were shown to accelerate the hydrolysis of polyimides, based on molecular weight studies of degradation.
- Thermooxidative stability based on weight loss was shown to be useful primarily as a screening method and for specification requirements, since (i) rapid changes in mechanical properties were observed after only small increments in weight loss and (ii) thermooxidative thresholds based on weight loss are material dependent.

- Comparative hydrolytic degradation studies of AFR700B, PETI-5, and K3B demonstrated that the hygrothermal durability inequality PETI-5 > K3B > AFR700B exists. This was due to (i) the hydrolytic instability of the Michael addition crosslinks in AFR700B, (ii) higher moisture absorption parameters for AFR700B, and (iii) the hydrolytic stability of the phenylethynyl crosslinks in PETI-5.
- Based on the aforementioned studies, a series of phenylethynyl terminated polyimides, AFR-PEPA-N, were synthesized and characterized. Based on the research conducted here and from collaborators at Air Force Research Laboratory and the University of Dayton Research Institute, these systems were shown to (i) have extremely high T_gs (435–455°C), (ii) have hydrolytic stability comparable to PETI-5, (iii) be processable by resin transfer molding after minor chemical modifications, (iv) exhibit high toughness for a high temperature polyimide, and (v) display good thermal stability.

11.2 Suggestions for Future Work

- Minor modifications to the DABPA monomer in BMPM/DABPA monomers may prevent the hydroxyl dehydration reaction, which leads to embrittlement and associated composite service environment induced microcracking.

- The crystallization phenomena of phenylethynyl terminated polyimides is not well understood, but from the data presented strongly influences the overall mechanical response. This subject should be investigated in future studies to properly ascertain the relationships between crystallinity and properties on a fundamental level.
- Optimization of structure-property-processing relationships the AFR-PEPA-N imide oligomers and resulting polyimides needs to be completed for the development of a new, hydrolytically stable, RTM processable polyimide, AFR700C. Suggestions for improving toughness and lowering the melt viscosity involve the addition of low viscosity reactive diluents and/or minor chemical modifications to the existing structure, such as the incorporation of groups containing meta-substituted amines.

APPENDICES

APPENDIX 1 - Calculation of Laminate Stress Distribution

Consider the flexural deformation of a composite rectangular beam subjected to the loading condition displayed in Figure A.1, with depth h and width w. If the following assumptions are made, the proceeding analysis is valid [95]:

- planes initially normal to the longitudinal axis of the beam remain plane and normal during bending
- each ply of the laminate is linearly elastic with no shear coupling, meaning the ply axes are either 0° or 90°
- the plys are symmetrically arranged about the x-y plane
- perfect interlaminar bonding
- only two stress components are present, σ_x and τ_{xy}

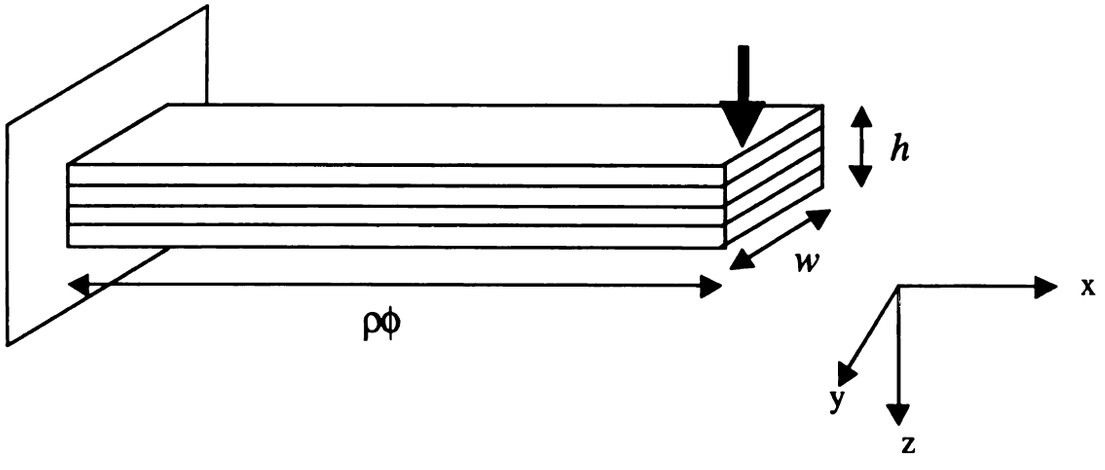

Figure A.1: Laminated cantilever beam.

The following variable definitions are required:

ρ = radius of curvature of the neutral surface during flexure
ϕ = angle of curvature defined in the figure above
z = distance from the neutral surface defined by the x-y plane
E_a = Young's modulus in the direction a
σ_a = normal stress in the direction a
ε_a = strain in the direction a
M = bending moment induced by applied load
j = ply number from laminate midplane ($z_0 = 0$)
N = number of plys

During flexural deformation, since the plane sections initially normal to the longitudinal axis of the beam remain plane and normal, the longitudinal normal strain at some distance z from the neutral surface (laminate midplane) is given by equation A.1 from strength of materials.

$$\varepsilon_x = \frac{(\rho + z)\phi - \rho\phi}{\rho\phi} = \frac{z}{\rho} \tag{A.1}$$

Because the laminate is assumed to have a balanced configuration with no shear coupling, the longitudinal stress in the jth ply is given by

$$(\sigma_x)_j = (E_x)_j (\varepsilon_x)_j \tag{A.2}$$

Combination of the above two equations yields another representation of the longitudinal stress:

$$(\sigma_x)_j = (E_x)_j \frac{z}{\rho} \tag{A.3}$$

From statics, the bending moment is related to the longitudinal stress by

$$M = 2 \int_0^{h/2} \sigma_x w z \, dz \tag{A.4}$$

where the symmetry assumption about the ply midplane has been used. Again, substitution of the previous two equations gives

$$M = \frac{2w}{3\rho} \sum_{j=1}^{N/2} (E_x)_j \left(z_j^3 - z_{j-1}^3\right) \tag{A.5}$$

Since we are assuming an even number of plys of uniform thickness, $z_j = jh/N$ and the previous equation becomes modified to

$$M = \frac{2wh^3}{3\rho N^3}\sum_{j=1}^{N/2}(E_x)_j\left(3j^2 - 3j + 1\right) \tag{A.5}$$

Next, for a homogenous isotropic rectangular beam, the moment is related to the curvature by the familiar equation

$$M = \frac{E_f I_{yy}}{\rho} = \frac{E_f wh^3}{12\rho} \tag{A.6}$$

where I_{yy} is the moment of inertia of cross section about the neutral y-axis and E_f is the effective flexural modulus of the beam. By once again combining the previous two equations, the effective flexural modulus of a laminated beam with an even number of plys can be written as

$$E_f = \frac{8}{h^3}\sum_{j=1}^{N/2}(E_x)_j\left(3j^2 - 3j + 1\right) \tag{A.7}$$

Note that the value for E_x for an individual unidirectional lamina can be approximated by the rule of mixtures. These formulas are given in A.8 and A.9 for longitudinal and transverse fiber directions, respectively.

$$E_{11} = V_{\text{fiber}}E_1^{\text{fiber}} + \left(1 - V_{\text{fiber}}\right)E_1^{\text{matrix}} \tag{A.8}$$

$$E_{22}^{-1} = V_{\text{fiber}}/E_2^{\text{fiber}} + \left(1 - V_{\text{fiber}}\right)/E_2^{\text{matrix}} \tag{A.9}$$

Above, 1 and 2 are the fiber and transverse directions, respectively, whereas V_{fiber} represents the fiber volume fraction.

Finally, to determine the normal stress distribution in a mathematical form that is simple to calculate, equations A.3 and A.6 can be combined to give

$$(\sigma_x)_j = \frac{M}{E_f I_{yy}}(E_x)_j z = \frac{Mz}{I_{yy}}\left[\frac{(E_x)_j}{E_f}\right] = \frac{12Mz}{wh^3}\left[\frac{(E_x)_j}{E_f}\right] \qquad (A.10)$$

In the case of the interlaminar stresses, a similar approach is used, recalling that the bending moment is related to the transverse shear force, v, by

$$\frac{dM}{dx} = v \qquad (A.11)$$

By applying simple static analysis to the stresses in the laminate, the equations below for the shearing stress, τ_{xz} can be obtained.

$$(\tau_{xz})_k = \frac{3v}{2wh}\left[\frac{C}{E_f}\right] \qquad (A.12)$$

$$C = \frac{4}{N^2}\sum_{j=k}^{N/2}(E_x)_j(2j-1) \qquad (A.13)$$

Note again that these equations apply only to a rectangular laminate that meets all of the assumptions discussed above and has an even number of plies of uniform thickness. A complete account of the above derivations can be found in Reference [95].

APPENDIX 2 - Attenuated Total Reflectance Fourier Transform Infrared Spectroscopy (ATR-FTIR)

When an organic material is irradiated with photons, it can transmit, scatter, or absorb the incident radiation. Absorbed infrared radiation usually excites molecules into higher-energy vibrational states. This occurs when the energy (frequency) of the photons matches the energy difference between two vibrational states (frequency corresponding to molecular vibration). That is, the molecule exhibits a change in dipole moment in one of its vibrational modes upon exposure to photons in the infrared region.

Infrared spectroscopy traditionally involves transmission of infrared light through a specimen, measuring the light intensity at the detector, and comparing it to the intensity obtained with no specimen present. These instruments usually operate in the infrared region between 2.5 - 25μm, or 4000 – 400 cm^{-1}, where the latter units are preferred and appellated wavenumbers. This region is where the most fundamental vibrational modes occur and thus the most useful for material characterization.

A typical data output involves a plot of percent transmittance, %T, or absorbance, A, where the latter is used for quantification calculations. If I is the energy detected with a sample present, and I_o with no specimen in the detector, the following relationships hold:

$$\%T = 100\frac{I}{I_o} \tag{A.14}$$

$$A = \log\left(\frac{1}{T}\right) \tag{A.15}$$

Note again that absorbance units are used in quantification, but this holds only in the case where these units are proportional to concentration. In some infrared techniques, other units may need to be used for quantitative analysis.

In Fourier transform infrared spectroscopy (FTIR), an interferometer is used to modulate the intensity of each wavelength of light at a different audio frequency. A beam splitter breaks the light (broad-band infrared source) into two optical paths and recombination at the beam splitter generates a modulated optical path difference [146]. The recombined beam undergoes constructive and destructive interference, and several techniques are possible for generating the optical path difference [146]. Regardless of the technique, a signal interferogram is generated which is Fourier transformed by a computer into the single-beam infrared spectrum.

Attenuated Total Reflectance (ATR) spectroscopy is a reflection technique used to generate an infrared spectrum. ATR is similar in principle to the traditional transmission technique discussed above. In this case, however, an ATR plate or internal reflection element (IRE) is constructed of some infrared transparent material of high refractive index (>2). Often germanium

or zinc selenide are used. Infrared radiation enters the IRE and is internally reflected at the IRE/specimen interface. The specimen can be in any physical form, and for solids is clamped to the IRE. Infrared radiation becomes totally internally reflected because the angle of incidence of the interface exceeds the critical angle. At each internal reflectance point, a standing wave is generated that penetrates a short distance (roughly the wavelength of light) into the sample. The instrument detector senses intensity loss due to absorption of the standing wave by the material being analyzed. Finally, the signal obtained is Fourier transformed into the spectrum.

Useful information, such as depth profiling, can be obtained using this technique, but there are some drawbacks. Most importantly, the spectrum of the sample component closest to the interface is weighted most heavily, so surface effects may be a problem. The other possible drawback is that since the technique is a reflection technique, other intensity units than absorbance may provide a more precise correlation between intensity and concentration. The reader is referred to Reference [146] for further discussion.

APPENDIX 3 - Lifetime Model Predictions and Accelerated Test Methodology Using Thermogravimetric Analysis

The theory of lifetime model predictions using TGA is based on the work of Toop [147]. Below, the fundamental equations used for analysis with respect to this dissertation will be discussed.

In order to generate lifetime models using the respective methodology, a number of samples (20-60 mg, each) are sectioned from the material of interest. Each specimen is scanned at different heating rates, often 1 – 20°C/min, and the weight loss recorded as a function of temperature. From the resultant thermal curves, the temperatures for a constant decomposition level are determined. Assuming the decomposition follows an Arrhenius, first order kinetics behavior,

$$Q = -\frac{R}{C}\left[\frac{d\log_{10}\beta}{d(1/T)}\right] \tag{A.16}$$

where Q is the activation energy (J/mol), R is the universal gas constant (8.314 J/mol-K), T is the absolute temperature at a constant decomposition (fixed value of weight loss), β is the heating rate (K/min), and C is a constant (0.457), then the activation energy can be determined from the slope of the logarithm of the heating rate versus the reciprocal of the temperature at constant decomposition level.

The value of the activation energy is the most critical, since this value can next be used to (i) calculate estimated lifetime at a given temperature or (ii) calculate the maximum operating temperature for a given estimated lifetime. For the current document, the latter prediction was generated. An important parameter to note is that the approximation C = 0.4569 holds to within ±1% only for values of $29 \leq x' \leq 46$. Additional iterations are used to generate the final curve if necessary.

Finally, Toop [147] has postulated that the relationships between activation energy and estimated lifetime (or maximum use temperature) can be written as follows:

$$\ln t_f = \frac{Q}{RT_f} + \ln\left[\frac{Q}{\beta R} \times p\left(\frac{Q}{RT_c}\right)\right] \tag{A.17}$$

$$T_f = \frac{Q/R}{\ln t_f - \ln\left[\frac{Q}{\beta R} \times p\left(\frac{Q}{RT_c}\right)\right]} \tag{A.18}$$

Above, t_f is the estimated time to failure (min), T_f is the failure temperature (K), $p\left(\frac{Q}{RT}\right)$ is a value from the integral,

$$p\left(\frac{Q}{RT_c}\right) = \int_{\frac{Q}{RT_c}}^{+\infty} \theta^{-2} e^{-\theta}\, d\theta \tag{A.19}$$

and T_c is the temperature at the constant conversion point for a particular heating rate. Table A.1 is taken from Toop [147] and displays the data for the solution to the above integral in the form

$$-\log_{10}[p(x')] = -\log_{10}\left[\frac{1}{x'e^{x'}} - \int_{x'}^{\infty}\frac{dx}{xe^{x}}\right] \qquad (A.20)$$

Table A.1: Tabulation of integral A.20 taken from Toop [147].

		0.1	0.2	0.3	0.4	0.5	0.6	0.7	0.8	0.9
10	6.4157	0.0515	0.1030	0.1544	0.2057	0.2569	0.3081	0.3591	0.4101	0.4611
11	6.9276	0.0508	0.1015	0.1522	0.2028	0.2533	0.3038	0.3542	0.4046	0.4549
12	7.4327	0.0502	0.1003	0.1504	0.2004	0.2504	0.3004	0.3502	0.4001	0.4499
13	7.9323	0.0497	0.0993	0.1489	0.1985	0.2480	0.2975	0.3469	0.3963	0.4456
14	8.4273	0.0493	0.0985	0.1477	0.1968	0.2459	0.2950	0.3440	0.3930	0.4420
15	8.9182	0.0489	0.0978	0.1466	0.1954	0.2441	0.2929	0.3415	0.3902	0.4388
16	9.4056	0.0486	0.0971	0.1456	0.1941	0.2425	0.2910	0.3393	0.3877	0.4360
17	9.8900	0.0483	0.0965	0.1448	0.1930	0.2411	0.2893	0.3374	0.3855	0.4336
18	10.3716	0.0480	0.0960	0.1440	0.1919	0.2399	0.2878	0.3356	0.3835	0.4313
19	10.8507	0.0478	0.0956	0.1433	0.1910	0.2387	0.2864	0.3341	0.3817	0.4293
20	11.3277	0.0476	0.0951	0.1427	0.1902	0.2377	0.2852	0.3326	0.3801	0.4275
21	11.8026	0.0474	0.0948	0.1421	0.1895	0.2368	0.2841	0.3314	0.3786	0.4259
22	12.2757	0.0472	0.0944	0.1416	0.1888	0.2359	0.2831	0.3302	0.3733	0.4244
23	12.7471	0.0471	0.0941	0.1411	0.1881	0.2351	0.2821	0.3291	0.3760	0.4230
24	13.2170	0.0469	0.0938	0.1407	0.1876	0.2344	0.2813	0.3281	0.3749	0.4217
25	13.6855	0.0468	0.0935	0.1403	0.1870	0.2338	0.2805	0.3272	0.3730	0.4205
26	14.1527	0.0467	0.0933	0.1399	0.1865	0.2331	0.2797	0.3263	0.3729	0.4194
27	14.6187	0.0465	0.0931	0.1396	0.1861	0.2326	0.2791	0.3255	0.3720	0.4184
28	15.0836	0.0464	0.0928	0.1393	0.1857	0.2320	0.2784	0.3248	0.3711	0.4175
29	15.5474	0.0463	0.0926	0.1390	0.1853	0.2315	0.2778	0.3241	0.3704	0.4166
30	16.0103	0.0462	0.0925	0.1387	0.1849	0.2311	0.2773	0.3235	0.3696	0.4158
31	16.4722	0.0461	0.0923	0.1384	0.1845	0.2306	0.2768	0.3229	0.3689	0.4150
32	16.9333	0.0461	0.0921	0.1382	0.1842	0.2302	0.2763	0.3223	0.3683	0.4143
33	17.3936	0.0460	0.0920	0.1379	0.1839	0.2299	0.2758	0.3217	0.3677	0.4136
34	17.8532	0.0459	0.0918	0.1377	0.1836	0.2295	0.2754	0.3212	0.3671	0.4130
35	18.3120	0.0458	0.0917	0.1375	0.1833	0.2292	0.2750	0.3208	0.3666	0.4124
36	18.7701	0.0458	0.0916	0.1373	0.1831	0.2288	0.2746	0.3203	0.3661	0.4118
37	19.2276	0.0457	0.0914	0.1371	0.1828	0.2285	0.2742	0.3199	0.3656	0.4112
38	19.6845	0.0457	0.0913	0.1370	0.1826	0.2282	0.2739	0.3195	0.3651	0.4107
39	20.1408	0.0456	0.0912	0.1368	0.1824	0.2280	0.2735	0.3191	0.3647	0.4102
40	20.5966	0.0455	0.0911	0.1366	0.1822	0.2277	0.2732	0.3187	0.3642	0.4098
41	21.0519	0.0455	0.0910	0.1365	0.1820	0.2274	0.2729	0.3184	0.3638	0.4093
42	21.5066	0.0455	0.0909	0.1363	0.1818	0.2272	0.2726	0.3181	0.3635	0.4089
43	21.9609	0.0454	0.0908	0.1362	0.1816	0.2270	0.2724	0.3177	0.3631	0.4085
44	22.4184	0.0454	0.0907	0.1361	0.1814	0.2268	0.2721	0.3174	0.3628	0.4081
45	22.8682	0.0453	0.0906	0.1359	0.1812	0.2265	0.2718	0.3171	0.3624	0.4077
46	23.3212	0.0453	0.0906	0.1358	0.1811	0.2264	0.2716	0.3169	0.3621	0.4074
47	23.7738	0.0452	0.0905	0.1357	0.1809	0.2262	0.2714	0.3166	0.3618	0.4070
48	24.2260	0.0452	0.0904	0.1356	0.1808	0.2260	0.2712	0.3163	0.3616	0.4067
49	24.6779	0.0452	0.0903	0.1355	0.1806	0.2258	0.2709	0.3161	0.3612	0.4064
50	25.1294	0.0451	0.0903	0.1354	0.1805	0.2256	0.2707	0.3159	0.3610	0.4061

Example of Integral Table Use

Assume an activation energy, Q = 226.8 kJ/mole is calculated from dynamic heating rate experiments described above and the temperature of interest was 583.95°C. Then, using the integral table,

$$x' = \frac{Q}{RT} = \frac{226800\ J/mol}{(8.314\ J/mol - K)(857.10\ K)} = 31.83$$

$$-\log_{10}(p(31.83)) = 16.4722 + 0.3689 + 0.01384$$

$$-\log_{10}(p(31.83)) = 16.85494$$

$$(p(31.83)) = 1.396561 \times 10^{-17}$$

The final value can then be used in equations A.17 and A.18 to make lifetime model predictions.

REFERENCES

1. R. J. Morgan, R. J. Jurek, A. Yen, and T. Donnellan, *Polymer,* **34,** 835 (1993)

2. J. Choi, A. Lee, E. E. Shin, and R. J. Morgan, *Proc. 28th Central Region ACS Meeting,* Dayton, OH, June 1996

3. R. J. Morgan, E. E. Shin, B. Rosenberg, and A. Jurek, *Polymer,* **38,** 639 (1997)

4. E. E. Shin, R. Jurek, L. T. Drzal, R. J. Morgan, J. Choi, and A. Lee, *Proc. ASME Materials Division,* **69,** 183 (1995)

5. E. E. Shin, C. Dunn, E. Fouch, R. J. Morgan, M. Wilenski, and L. T. Drzal, *Proc. of the ASME Materials Division,* **69,** 191 (1995)

6. E. E. Shin, R. J. Morgan, M. Wilenski, J. Zhou, J. E. Lincoln, and L. T. Drzal, *28th Int. SAMPE Tech. Conf.*, November 4-7, 225 (1996)

7. R. J. Morgan, E. E. Shin, J. E. Lincoln, J. Choi, and A. Lee, *28th Int. SAMPE Tech. Conf.*, November 4-7, 213 (1996)

8. E. E. Shin, R. J. Morgan, J. Zhou, J. E. Lincoln, R. J. Jurek, and D. B. Curliss, *Proc. American Soc. for Compos., 12th Tech. Conf.,* October 6-8, 1113 (1997)

9. E. E. Shin and R. J. Morgan, *ANTEC SPE Conf.,* 1357 (1993)

10. R. J. Morgan, "Thermal Characterization of Composites," in Thermal Characterization of Polymeric Materials, Second Edition, Academic Press, 2091-2261 (1997)

11. A. Yee and C. Soles, Personal Communication, (1997)

12. J. B. Enns and J. K. Gillham, *J. Appl. Polym. Sci.,* **28,** 2831 (1983)

13. N. D. Danieley and E. R. Long Jr., *J. Polym. Sci.: Polym. Chem. Edtn.*, **19,** 2443 (1981)

14. Y. Diamant, G. Marom, and L.J. Broutman, *J. Appl. Polym. Sci.,* **26** 3015 (1981)

15. R. Pethrick, E. Hollins, I. McEwan, E. Pollock, D. Hayward, and P. Johncock, *Polym. Int.*, **39**, (1996)

16. V.B. Gupta, L.T. Drzal, and M.J. Rich, *J. Appl. Polym. Sci.*, **30**, 4467 (1985)

17. T. M. Donnellan and D. Roylance, *Polym. Eng. Sci.,* **32**, 409 (1992)

18. T. M. Donnellan and D. Roylance, *Polym. Eng. Sci.,* **32**, 415 (1992)

19. R.E. Allred, T.M. Donnellan, R. Cochran, and K. Miller, *Proc. High Temple Workshop XVII,* Monterey, CA, Paper R (1997)

20. R. J. Morgan, E. E. Shin, J. E. Lincoln, and J. Zhou, *Proc. 43rd SAMPE Symp.,* Anaheim, CA, May/June, 106 (1998)

21. R. J. Morgan, F-M. Kong, and C. M. Walkup, *Polymer*, **25**, 375 (1984)

22. J. M. Barton, *Polymer*, **20**, 1018 (1979)

23. Y. Diamant, G. Marom, and L.J. Broutman, *J. Appl. Polym. Sci.,* **26**, 3015 (1981)

24. G. A. Gordon and A. Ravve, *Polym. Eng. Sci.*, **20**, 70 (1980)

25. J. E. Lincoln, R. J. Morgan, and E. E. Shin, *J. Adv. Mater.*, **32**, 24 (2000)

26. M.S. Wilenski, *The Improvement of the Hygrothermal and Mechanical Properties of Bismaleimide and K3B/IM7 Carbon Fiber Composites Through a Systematic Study of the Interphase*, Ph.D. Thesis, Michigan State University (1997)

27. M. S. Wilenski, E. E. Shin, R. J. Morgan, and L. T. Drzal, *Unpublished* (1996)

28. D. A. Scola, M. Bak, and D. J. Parker, *SAMPE J.*, March/April, 47 (1986)

29. D. Wilson, J. K. Wells, J.N. Hay, D. Lind, G. A. Owens, and F. Johnson, *SAMPE J.*, May/June, 35 (1987)

30. X. Huang, R. F. Eduljee, and J.W. Gillespie, Jr., *Composites, Part B*, **29B**, 391 (1998)

31. A. P. C. Furrow and D. A. Dillard, *J. Compos. Mater.*, **32**, 31 (1998)

32. A. S. Vallely and J. K. Gillham, *J. Appl. Polym. Sci.*, **64**, 39 (1997)

33. L. J. Burcham, R. F. Eduljee, and J.W. Gillespie, Jr., *Polym. Compos.*, **16**, 507 (1995)

34. C. L. Pederson, J.W. Gillespie, Jr., and R.L. McCullough, *Polym. Compos.*, **16**, 154 (1995)

35. P. Le Coustumer, K. Lafdi, and A. Oberlin, *Compos. Sci. and Tech.*, **52**, 433 (1994)

36. S. G. Lim and C. S. Hong, *J. Compos. Mater.*, **23**, 695 (1989)

37. R. Talreja, *J. Compos. Mater.*, **19**, 355 (1985)

38. R. B. Stout, *J. Eng. Mater. Tech.*, **109**, 259 (1987)

39. Y. M. Han, H. T. Hahn, and R. B. Croman, *Composites Sci. and Tech.*, **31**, 165 (1988)

40. G.-P. Fang, R. A. Schapery, and Y. Weitsman, *Eng. Fracture Mechanics*, **33**, 619 (1989)

41. L. N. McCartney, *J. Mech. Phys. Solids*, **40**, 27 (1992)

42. D. L. Hiemstra and N. R. Sottos, *J. Compos. Mater.*, **27**, 1030 (1993)

43. G. A. Schoeppner and N. J. Pagano, *Int. J. Structures*, **35**, 1025 (1998)

44. N. J. Pagano, G. A. Schoeppner, R. Kim, and F. L. Abrams, *Compos. Sci. and Tech.*, **58**, 1811 (1998)

45. L.E. Asp, L.A. Berglund, and R. Talreja, *Compos. Sci. and Tech.*, **56**, 1089 (1996)

46. J. A. Nairn, *J. Appl. Mech.*, **64**, 804 (1997)

47. L. D. Landro, A. Palonca, and G. Sala, *Polym. Compos.*, **16**, 276 (1995)

48. D. F. Adams, *J. Reinforced Plastics and Composites*, **6**, 66 (1987)

49. C. A. Bigelow, *J. Compos. Tech. Research*, **14**, 211 (1992)

50. B. Cunningham, J. P. Sargent, and K. H. G. Ashbee, *J. Mater. Sci.*, **16**, 620 (1981)

51. F. R. Jones, M. Mulheron, J.E. Bailey, *J. Mater. Sci.*, **18**, 1533 (1983)

52. M. Simpson, P. M. Jacobs, and F. R. Jones, *Composites*, **22**, 89 (1991)

53. M. Simpson, P. M. Jacobs, and F. R. Jones, *Composites*, **22**, 99 (1991)

54. M. Simpson, P. M. Jacobs, and F. R. Jones, *Composites*, **22**, 105 (1991)

55. J. Boyd, *SAMPE J.*, **35**, 13 (1999)

56. V. Korotkov, Y. Chekanov, and B. Rozenberg, *Proc. ICCM-10, Whistler, B.C., Canada*, **3**, 165 (1995)

57. V. N. Korotkov, Y. A. Chekanov, and B. A. Rozenber, *J. Mater. Sci. Letters*, **10**, 806 (1991)

58. Yu. A. Chekanov, V. N. Korotkov, B. A. Rozenberg, and E. A. Dhzavadyan, *Polymer*, **36**, 2013 (1995)

59. R. F. Boyer, *Polym. Eng. Sci.*, **8**, 161 (1968)

60. J. Heijboer, *J. Polym. Sci.: Part C*, **16**, 3755 (1968)

61. R. J. Morgan and L. E. Nielsen, *J. Macromol. Sci. – Phys.*, **B9**, 239 (1974)

62. J. A. Sauer, In *Molecular Order – Molecular Motion* (H. H. Kausch, ed.), Interscience Publishers, 69 (1971)

63. R. D. Adams, In *Engineered Materials Handbook* (T.J. Reinhart, ed.), ASM Int., **1**, 206 (1987)

64. R. G. Ni and R. D. Adams, *J. Compos. Mater.*, **18**, 104 (1984)

65. D. A. Saravanos, *Dynamic Characterization of Adv. Mater., NCA/AMD*, **16/172**, 11 (1993)

66. R. F. Gibson, *Proc. 6th Annul. American Society of Metals/Eng. Society of Detroit (ASM/ESD) Adv. Compos. Conf.*, Detroit, MI, 441 (1990)

67. S. A. Suarez, R. F. Gibson, C. T. Sun, and S. K. Chaturvedi, *Exp. Mech.*, **26**, 175 (1986)

68. R. D. Adams and D. G. C. Bacon, *J. Compos. Mater.*, **7**, 53 (1973)

69. R. F. Gibson, V. S. Rao, and P. R. Mantena, *Int. SAMPE Symp. Exhib.*, **32**, 231 (1987)

70. P. Ghosh, N. R. Bose, B. C. Mitra, and S. Das, *J. Appl. Polym. Sci.*, **64**, 2467 (1997)

71. P. K. Sengupta and D. Mukhopadhyay, *J. Appl. Polym. Sci.*, **51**, 831 (1994)

72. R. J. Armstrong, A. Wolfenden, S. S. Vinson, and R. C. Knight, *18th Int. SAMPE Tech. Conf.*, October 7-9, 372 (1986)

73. K.E. Reed, *Polym. Compos.*, **1**, 44 (1980)

74. J. L. Thomason, *Polym. Compos.*, **11**, 105 (1990)

75. N. R. Sottos, D. L. Hiemstra, and W. R. Scott, *Fracture Mech., ASTM STP 1220.*, **25**, 140 (1995)

76. H. F. Wu, W. Gù, G. –Q. Lu, and S. L. Kampe, *J. Mater. Sci.*, **32**, 1795 (1997)

77. J. L. Thomason, *Composites*, **26**, 487 (1995)

78. D. E. Burton and D. M. Blackketter, *Dynamic Characterization of Adv. Mater., NCA/AMD*, **16 / 172**, 23 (1993)

79. S. Dong and R. Gauvin, *Polym. Compos.*, **14**, 414 (1993)

80. R. F. Gibson, *M³D: Mechanics and Mechanisms of Material Damping, ASTM STP 1169*, (V. K Kinra and A. Wolfenden, eds.), 60 (1992)

81. I. C. Finegan and R. F. Gibson, *Compos. Structures*, **44**, 89 (1999)

82. S.J. Hwang and R. F. Gibson, *Compos. Sci. Tech.*, **41**, 379 (1991)

83. Y. Gu, R. F. Gibson, and S.J. Hwang, *Advanced Composite Materials: New Developments and Applications Conference Proceedings, Detroit, MI*, 507 (1991)

84. G. A. Lesleutre, *Advanced Composite Materials: New Developments and Applications Conference Proceedings, Detroit, MI*, 513 (1991)

85. S.J. Hwang and R. F. Gibson, *Advanced Composite Materials: New Developments and Applications Conference Proceedings, Detroit, MI*, 519 (1991)

86. S.J. Hwang, R. F. Gibson, and J. Singh, *Compos. Sci. Tech.*, **43**, 159 (1992)

87. T. Murayama, Dynamic Mechanical Analysis of Polymeric Materials, Elsevier, Amsterdam (1978)

88. C. T. Sun, J. K. Wu, and R. F. Gibson, *J. Mater. Sci.*, **22**, 1006 (1987)

89. P. S. Chua, *Polym. Compos.*, **8**, 308 (1987)

90. D. J. Nelson and J. W. Hancock, *J. Mater. Sci.*, **13**, 2429 (1978)

91. N. N. Kishore, A. Ghosh, and B. D. Agarwal, *J. Reinforced Plastics and Composites*, **1**, 40 (1982)

92. N. N. Kishore, A. Ghosh, and B. D. Agarwal, *J. Reinforced Plastics and Composites*, **1**, 64 (1982)

93. R. Mantena, T. A. Place, and R. F. Gibson, *Proc., Symp. on the Role of Surfaces and Interfaces in Material Damping*, ASM International (1985)

94. J. N. Hay, J. D. Boyle, S. F. Parker, and D. Wilson, *Polymer*, **30**, 1032 (1989)

95. R. F. Gibson, Principles of Composite Material Mechanics, McGraw-Hill, (1994)

96. J. E. Lincoln, *Effects of Cure and Initial Monomer Stoichiometry on the Physical, Thermal, and Mechanical Properties of Bismaleimide Resins*, B.S. Thesis, Michigan State University (1998)

97. M. K. Ghosh and K. L. Mittal, Polyimides: Fundamentals and Applications, Marcel Dekker, Inc., New York, (1996)

98. R. H. Pater, *SAMPE J.*, **30**, 29 (1994)

99. P. M. Hergenrother, *SAMPE J.*, **36**, 30 (2000)

100. G. Stoller, *USA Today*, Cover Story, November (1998)

101. R. J. Morgan, R. Jurek, D. E. Larive, and E. J. English, *22nd Int. SAMPE Tech. Conf.*, 145 (1990)

102. T.K. Tsotsis, *J. Compos. Mater.*, **29**, 410 (1995)

103. C. Conreur, J. Francillette, and F. Laupretre, *J. Polym. Sci.: Part A: Polym. Chem.*, **35**, 123 (1997)

104. A. Skontorp, S.-S. Wang, *Proc. 28th Central Region ACS Meeting*, Dayton, OH, 1203, (1996)

105. I. Jangchud, R. K. Eby, A. M. Serrano, and M. A. Meador, *J. Adv. Mater.*, 19, (1996)

106. K. Jordan and J. O. Iroh, *Polym. Eng. Sci.*, **36**, 2550 (1996)

107. K. N. Ninan, K. Krishnan, and J. Mathew, *J. Appl. Polym. Sci.*, **32**, 6033 (1986)

108. L. Guozheng, G. Aijuan, and L. Liwen, *J. Adv. Mater.*, 61, January (1996)

109. A. Skontorp, S.-S. Wang, *Proc. 28th Central Region ACS Meeting*, Dayton, OH, 1203, June (1996)

110. D. A. Scola, *ANTEC*, 2404, (1992)

111. T. S. Gates and M. Feldman, *J. Compos. Tech. Research*, **17**, 33 (1995)

112. H. L. McManus, R. A. Cunningham, *High Temperature and Environmental Effects on Polymeric Composites: 2nd Volume, ASTM STP 1302*, T. S. Gates, A.-H. Zureick, eds., American Society for Testing and Materials, 1 (1997)

113. J. D. Russell and J. L. Kardos, *Polym. Compos.*, **18**, 64 (1997)

114. J. D. Russell and J. L. Kardos, **18**, 595 (1997)

115. A. Apicella, L. Nicolais, and C. de Cataldis, *Adv. Polym. Sci.*, **66**, 189 (1985)

116. F. N. Kelly and F. Bueche, *J. Polym. Sci.*, **50**, 2549 (1968)

117. H. G. Carter and K. G. Kibler, *J. Compos. Mater.*, **11**, 265 (1977)

118. G. S. Springer, ed., Environmental Effects on Composite Materials, Technomic Publishing Co., 16 (1981)

119. K. E. G. Thorp and A. S. Crasto, *Proc. American Soc. Compos. 10th Tech. Conf.*, 601 (1995)

120. M. R. VanLandigham, R.F. Eduljee, and J.W. Gillespe, Jr., *High Temperature and Environmental Effects on Polymeric Composites: 2nd Volume, ASTM STP 1302*, T.S. Gates, A.-H. Zureick, eds., American Society for Testing and Materials, 50 (1997)

121. H.T. Hahn, *J. Eng. Mater. Tech.*, **109**, 3 (1987)

122. A. W. Obst, M. R. VanLandingham, R. F. Eduljee, and J. W. Gillespie, Jr., *28th Int. SAMPE Tech. Conf.*, 994 (1996)

123. L. J. Burchan, M. R. Vanlandingham, R. F. Eduljee, and J. W. Gillespie, Jr., *Polym. Compos.*, **17**, 682 (1996)

124. J. L. Vasat, J. L. Kardos, and M. P. Dudukovic, *27th Int. SAMPE Tech. Conf.*, 843 (1995)

125. B. P. Rice, *28th Int. SAMPE Tech. Conf.*, 778 (1996)

126. D. B. Curliss, *28th Int. SAMPE Tech. Conf.*, 790 (1996)

127. D. Cornelia, *39th Int. SAMPE Symp.*, 917 (1994)

128. D. R. Gaskell, Introduction to the Thermodynamics of Materials, 3rd Edition, Taylor and Francis (1995)

129. C. L. Leung and K. C. Leung, *PSME-ACS*, **74**, 348 (1996)

130. M. L. Rommel, A. S. Postyn, and T. A. Dyer, *SAMPE J.*, **29**, 19 (1993)

131. D. Mitramajumdar and H. Aglan, *Polymer*, **33**, 1855 (1992)

132. Publication of the United States Air Force, "Project Saves Millions in F-117A Replacement Parts", USAF Materials Technology Highlights, 2, (Spring 1999)

133. E. E. Shin, R. J. Morgan, and J. Zhou, *Proc. 45th SAMPE Symp.*, 352 (2000)

134. R. J. Morgan, E. E. Shin, J. E. Lincoln, and J. Zhou, *Proc. 45th SAMPE Symp.*, 345 (2000)

135. D. B. Curliss, *High Temple Workshop XX*, San Diego, CA (January 2000)

136. D. A. Scola and J. H. Vontell, *Polym. Compos.*, **9**, 443 (1988)

137. T. S. Chow, *Polym. Eng. Sci.*, **24** (1984)

138. A. D'Amore, G. Caprino, L. Nicolars, and G. Marino, *Compos. Sci. Tech.*, **59**, 1993 (1999)

139. P. Geldermans, C. Goldsmith, and F. Bedetti, Polyimides: Synthesis, Characterization, and Applications, Vol. 2, Plenum Press, 695 (1982)

140. R. DeIasi and J. Russell, *J. Appl. Polym. Sci.*, **15**, 2965 (1971)

141. R. DeIasi, *J. Appl. Polym. Sci.*, **16**, 2909 (1972)

142. M.I. Bessonov, M. M. Koton, V. V. Kudryavtsev, and L. A. Laius, eds., Polyimides: Thermally Stable Polymers, Plenum Publishing, New York, Chapter 2 (1987)

143. L. Fengcai, L. Desheng, L. Zhugen, B. Luna, and G. Yuanming, *Scientia Sinica (Series B)*, **39**, 345 (1986)

144. L. V. Ivanova, *Polym. Sci. Ser. A (Russian)*, **40**, 663 (1998)

145. R. A. Venditti and J. K. Gillham, *J. Appl. Polym. Sci.*, **64**, 3 (1997)

146. P. R. Griffiths, Chemical Infrared Fourier Transform Spectroscopy, John Wiley and Sons (1975)

147. D. J. Toop, *IEEE Trans. Elec. Ins., EI-6,* **2** (1971)

148. J. E. Lincoln, R. J. Morgan, and E. E. Shin, *Polym. Compos.*, **22** (2001)

149. J. E. Lincoln, R. J. Morgan, and E. E. Shin, *Proc. American Soc. Compos. 15th Tech. Conf.*, 1103 (2000)

150. R. J. Morgan, E. E. Shin, J. E. Lincoln, and J. Zhou, *Proc. American Soc. Compos. 15th Tech. Conf.*, 1061 (2000)

151. J. E. Lincoln, R. J. Morgan, and E. E. Shin, *J. Polym. Sci. Part B: Polym. Phys. Ed.*, Submitted (2001)

152. J. E. Lincoln, W. A. Price, D. B. Curliss, and R. J. Morgan, *High Temple XXI*, Paper I (2001)

153. R. J. Morgan, E. E. Shin, and J. E. Lincoln, *High Temple XXI*, In Press (2001)

154. R. J. Morgan, R. J. Jurek, A. Yen, and T. Donnellan, *Polymer,* **34**, 835 (1993)

155. E. E. Shin, R. J. Morgan, J. Zhou, J. E. Lincoln, R. J. Jurek, and D. B. Curliss, *Proc. American Soc. Compos. 12th Tech. Conf.*, 1113 (1997)

156. R. J. Morgan, E. E. Shin, J. E. Lincoln, J. Zhou, L. T. Drzal, A. Lee, and D. B. Curliss, *High Temple Workshop XVIII* (1998)

157. R. J. Morgan, E. E. Shin, J. Zhou, J. E. Lincoln, and B. Rozenberg, *High Temple Workshop XIX* (1999)

158. R. J. Morgan, J. E. Lincoln, and E. E. Shin, *High Temple Workshop XX*, Paper 8, Section H (2000)

159. E. E. Shin, R. J. Morgan, J. Zhou, J. E. Lincoln, R. J. Jurek, and D. B. Curliss, *J. Thermoplastic Compos. Mater.*, **13**, 40 (2000)

160. J. E. McGrath, B. Tan, V. Vasudevan, G. W. Meyer, A. C. Loos, and T. Bullions, *28th Int. SAMPE Tech. Conf.*, 29 (1998)

161. A. Ayambem, S. J. Mecham, and Y. Sun, Glass, T. E.; McGrath, J. E. *Polymer*, **41**, 5109 (2000)

162. G. W. Meyer, S. J. Pak, Y. J. Lee, and J. E. McGrath, *Polymer*, **36**, 2303 (1995)

163. D. W. Cho and L. T. Drzal, *J. Appl. Polym. Sci.*, **75**, 1278 (2000)

164. B. P. Rice, *High Temple Workshop XVII*, Paper J (1997)

165. J. G. Smith, J. W.Connell, and P. M. Hergenrother, *Polymer*, **38**, 4657 (1997)

166. P. M. Hergenrother, J. W. Connell, and J. G. Smith Jr., *Polymer*, **41**, 5073 (2000)

167. J. A. Johnston, F. M. Li, F. W. Harris, and T. Takekoshi, *Polymer*, **35**, 4865 (1994)

168. T. V. Holland, T. E. Glass, and J. E. McGrath, *Poymer*, **41**, 4965 (2000)

169. P. M. Hergenrother, R. G. Bryant, B. J. Jensen, and S. J. Havens, *J. Polym. Sci. Part A: Polym. Chem.*, **32**, 3061 (1994)

170. D. Cho and L. T. Drzal, *J. Appl. Polym. Sci.*, **76**, 190 (2000)

171. B. J. Jensen and A. C. Chang, *High Perform. Polym.*, **10**, 175 (1998)

172. R. G. Bryant, B. J. Jensen, and P. M. Hergenrother, *J. Appl. Polym. Sci.*, **59**, 1249 (1996)

173. X. Fang, D. F. Rogers, D. A. Scola, and M. P. Stevens, *J. Polym. Sci. Part A: Polym. Chem.*, **36**, 461 (1998)

174. R. DeIasi and J. Russell, *J. Appl. Polym. Sci.*, **15**, 2965 (1971)

175. R. DeIasi, *J. Appl. Polym. Sci.*, **16**, 2909 (1972)

176. P. S. Wang, T. N. Wittberg, and J. D. Wolf, *J. Mater. Sci.*, **23**, 3987 (1998)

177. L. Guozheng, G. Aijuan, and L. Liwen, *J. Adv. Mater.*, 61 (1996)

178. A. Gu and L. Guozheng, *Plast. Rubber Compos. Process. Appl.*, **25**, 437 (1996)

179. R. Chandra and L. Rajabi, *J. Macromolecular. Sci., Rev. Macromolecular Chem. Phys.*, **1**, 61 (1997)

180. A. D. Gupta and D. Kumar, *J. Appl. Polym. Sci.*, **30**, 3879 (1985)

181. L. Zhang, Q. Jiang, L. Yiang, and X. Cai, *Polym. Int.*, **39** (1996)

182. K. N. Ninan, K. Krishnan, and J. Mathew, *J. Appl. Polym. Sci.*, **32**, 6033 (1986)

183. J. E. Lincoln, R. J. Morgan, and E. E. Shin, *J. Adv. Mater.*, **32**, 24 (2000)

184. J. E. Lincoln, R. J. Morgan, and E. E. Shin, *Polym. Compos.*, **22** (2001)

185. L. M. Nicholson, K. S. Whitley, T. S. Gates, and J. A. Hinkley, *44th Int. SAMPE Tech. Conf.*, 794 (1999)

186. E. A. DiMarzio, *J. Res. Nat. Bureau Stds. A. Phys. Chem.*, **6**, 611 (1964)

187. D. R. Miller and C. W. Macosko, *Maromolecules*, **9**, 206 (1976)

188. T. H. Hou, B. J. Jensen, and P. M. Hergenrother, *J. Compos. Mater.*, **30**, 109 (1996)

189. J. W. Connell, *Proc. 21st Annu. Adhesion Soc. Meet.*, 15 (1998)

190. R. J. Morgan, J. E. O'Neal, *J. Mater. Sci.*, **12**, 1338 (1977)

191. L. Bao and A. Lee, *High Temple XX*, Paper T (2000)

192. N. Brown, *Mater. Sci. Eng.*, **8**, 69 (1971)

193. S. S. Labana, S. Newman, and A. J. Chompff, *Proc. ACS Symp. Highly Crosslinked Polym. Networks*, 453 (1970)

194. J. E. Lincoln, W. A. Price, D. B. Curliss, and R. J. Morgan, *Polymer*, To be Submitted (2001)

195. S. W. Lambert, P. J. Phillips, and S. J. Lin, *Polymer*, **35**, 1809 (1994)

196. P. J. Hendra, A. J. Peacock, and H. A. Willis, *Polymer*, **29**, 49 (1988)

197. M. Shibayama, H. Takahashi, H. Yamaguchi, S. Sakurai, and S. Nomura, *Polymer*, **35**, 2944 (1994)

198. T. P. Russell and H. R. Brown, *J. Polym. Sci. Part B: Polym. Phys.*, **25**, 1129 (1987)

199. P. M. Hergenrother, R. G. Bryant, B. J. Jensen, and S. J. Havens, *J. Polym. Sci. Part A: Polym. Chem.*, **32**, 3061 (1994)

200. T. Vu-Khanh and S. Frikha, *J. Thermoplastic Compos. Mater.*, **12**, 84 (1999)

201. J. Denault and T. Vu-Khanh, *Polym. Compos.*, **13**, 361 (1992)

202. A. J. Hsieh, C. R. Desper, and N. S. Schneider, *Polymer* (1992)

203. R. J. Morgan and J. E. O'Neal, *J. Polym. Sci. Polym. Phys. Ed.*, **14**, 1053 (1976)

204. R. J. Morgan and J. E. O'Neal, *Polymer*, **20**, 375 (1979)

205. A. P. Perrella, *24th Int. SAMPE Tech. Conf.*, T711 (1992)

206. S. Sacks and W. S. Johnson, *J. Thermoplastic Compos. Mater.*, **11**, 429 (1998)

207. A. R. Wedgewood, *24th Int. SAMPE Tech. Conf.*, T385 (1992)

208. J. A. Cella, *Polym. Degra. Stabil.*, **36**, 99 (1992)

209. J. H. Flynn, In Thermal Methods in Polymer Analysis, S. W. Shalaby, ed., 163 (1977)

210. C. S. Siat, S. Bourbigot, and M. Le Bras, *Polym. Degra. Stabil.*, **58**, 303 (1997)

211. M. J. Turk, A. S. Ansari, W. B. Alston, G. S. Gahn, A. A. Frimer, and D. A. Scheiman, *J. Polym. Sci.: Part A: Polym. Chem.*, **37**, 3943 (1999)

212. R. F. Boswell, S. J. Claus, and F. Arnold, *44th Int. SAMPE Symp.*, 714 (1999)

213. C. Marais and G. Villoutreix, *Polymers* (France), **3-4**, 26 (1996)

214. K. C. Chuang and J. E. Waters, *40th Int. SAMPE Symp.*, 1113 (1995)

215. H. Tang, L. Dong, J. Zhang, M. Ding, and Z. Feng, *Macromol. Chem. Phys.*, **197**, 543 (1996)

216. J. Yin, Y-F. Ye, and Z-G Wang, *Eur. Polym. J.*, **34**, 1839 (1998)

217. D. A. Scola and C. Leung, *AFOSR Polym. Matrix Compos. Prog. Rev.* (2000)

218. B. Rice, *PVAMU Annul. Report for Sept. 95 – Aug. 96*, (1996)

219. B. Rice, *PVAMU Annul. Report for Sept. 96 – Aug. 97*, (1997)

220. J. A. Johnson, F. M. Li, F. W. Harris, and T. Takekoshi, *Polymer*, **35**, 4865 (1994)

221. M. Bruma, E. Hamciue, B. Schulz, T. Kopnick, B. Stiller, and F. Mercer, *Polymer*, **40**, 6865 (1999)

222. J. –C. Mileo, *Revue De L'Institut Francais Du Petrole*, **48**, 61 (1993)

223. K. Thorp and D. Curliss, *High Temple XXI*, Paper L (2001)

224. R. M. Ikeda, *J. Appl. Polym. Sci.*, **47**, 619 (1993)

225. M. Sabasivam, A. Klein, and L. H. Sperling, *J. Appl. Polym. Sci.*, **65**, 1001 (1997)

226. Y. Tang, Y. Xie, and W-P. Pan, *Proc. 26th NATAS Conf.*, 584 (1998)

227. F. E. Arnold and A. Guy, *44th Int. SAMPE Symp.*, 1576 (1999)

228. R. J. Cano, H. L. Belvin, E. S. Weiser, and D. M. McGowen, *43rd Int. SAMPE Symp.*, 144 (1998)

229. X. Fang, D. A. Scola, and C. DiFrancia, *Proc. ACS Div. Polym. Mater.*, **78**, 7 (1998)

230. F. Li, S. Fang, J. J. Ge, P. S. Honigfort, J. –C. Chen, F. W. Harris, and S. Z. D. Cheng, *Polymer*, **40**, 4571 (1999)

231. M. L. Rommel, L. Konopka, and P. M. Hergenrother, *28th Int. SAMPE Tech. Conf.*, 22 (1996)

232. K. A. Harrington, R. Orwoll, B. J. Jensen, and P. R. Young, *41st Int. SAMPE Symp.*, 135 (1996)

233. J. G. Smith, J. W. Connell, and P. M. Hergenrother, *43rd Int. SAMPE Symp.*, 93 (1998)

234. P. M. Hergenrother and M. L. Rommel, *41st Int. SAMPE Symp.*, 1061 (1996)

235. J. W. Connell, J. G. Smith, P. M. Hergenrother, and M. Rommel, *28th Int. SAMPE Tech. Conf.*, 14 (1996)

236. T. H. Hou, R. J. Cano, and B. J. Jensen, *High Perform. Polym.*, **10**, 181 (1998)

237. B. J. Jensen, S. E. Lowther, and A. C. Chang, *Polym. Preprints*, **38**, 305 (1997)

238. P. M. Hergenrother, R. G. Bryant, B. J. Jensen, J. G. Smith, and S. P. Wilkinson, *39th Int. SAMPE Symp.*, 961 (1994)

239. R. J. Cano, B. J. Jensen, and J. E. Bennett, *44th Int. SAMPE Symp.*, 1780 (1999)

240. L. Fengcai, L. Desheng, L. Zhugen, B. Luna, and G. Yuanming, *Scientia Sinica: Series B*, **39**, 345 (1986)

241. K. T. Kern, P. C. Stancil, W. L. Harries, E. R. Long, and S. A. Thibeault, *SAMPE J.*, **29**, 29 (1993)

242. X. Huang, J. W. Gillespie Jr., and R. F. Eduljee, *Compos. Part B*, **28B**, 419 (1997)

243. H. Chung, Y. Joe, and H. Han, *J. Appl. Polym. Sci.*, **74**, 3287 (1999)

244. P. I. Karkanas and I. K. Partridge, *J. Appl. Polym. Sci.*, **77**, 1419 (2000)

245. S. L. Simon and J. K. Gillham, *J. Appl. Polym. Sci.*, **46**, 1245 (1992)

246. M. R. Keenan, *J. Appl. Polym. Sci.*, **33**, 1725 (1987)

247. J. Ampudia, E. Larrauri, E. M. Gil, M. Rodriguez, and L. M. Leon, *J. Appl. Polym. Sci.*, **71**, 1239 (1999)

248. J. K. Gillham In The Role of the Polymeric Matrix in the Processing and Structural Properties of Composite Materials, J. C. Seferis and L. Nicolais, eds., Plenium Press, 127 (1983)

249. J. P. Pascault and R. J. J. Williams, *J. Polym. Sci.: Part B: Polym. Phys.*, **28**, 85 (1990)

250. J. Lange, *Polym. Eng. Sci.*, **39**, 1651 (1999)

251. G. Wisanrakkit and J. K. Gillham, *J. Coatings Tech.*, **62**, 35 (1990)

252. R. A. Vendittit and J. K. Gillham, *J. Appl. Polym. Sci.*, **64**, 3 (1997)

253. J. W. Connell, J. G. Smith Jr., and P. M. Hergenrother, *United States Patent*, **5,689,004** (1997)

254. R. H. Vora, *United States Patent*, **4,973,651** (1990)

255. P. M. Hergenrother and J. G. Smith Jr., *United States Patent*, **5,760,168** (1998)

256. R. G. Bryant, B. J. Jensen, and P. M. Hergenrother, *United States Patent*, **5,446,204** (1995)

257. R. N. Griffin and R. A. Gray, *United States Patent*, **5,177,180** (1993)

258. P. M. Hergenrother, R. G. Bryant, B. J. Jensen, and S. J. Havens, *United States Patent*, **5,599,993** (1997)

259. D. Cornelia, *High Temple Workshop XV*, Paper C-1 (1995)

260. D. Cornelia, *High Temple Workshop XVI*, Paper W-1 (1996)

261. B. Hoogstenden and R. Kuhbander, *High Temple Workshop XV*, Paper U-1 (1995)

262. W. A. Price and D. B. Curliss, *High Temple Workshop XX*, Paper V (2000)

263. B. P. Rice and C. W. Lee, *29th Int. SAMPE Tech. Conf.*, 675 (1997)

264. A. Lee, *High Perform. Polym.*, **8**, 475 (1996)

265. P. P. Nechaev, Y. V. Moiseev, Y. S. Vygodskii, and G. E. Zaikov, *Int. J. Chem. Kinetics*, **6**, 245 (1974)